Physics of microparticle acoustophoresis
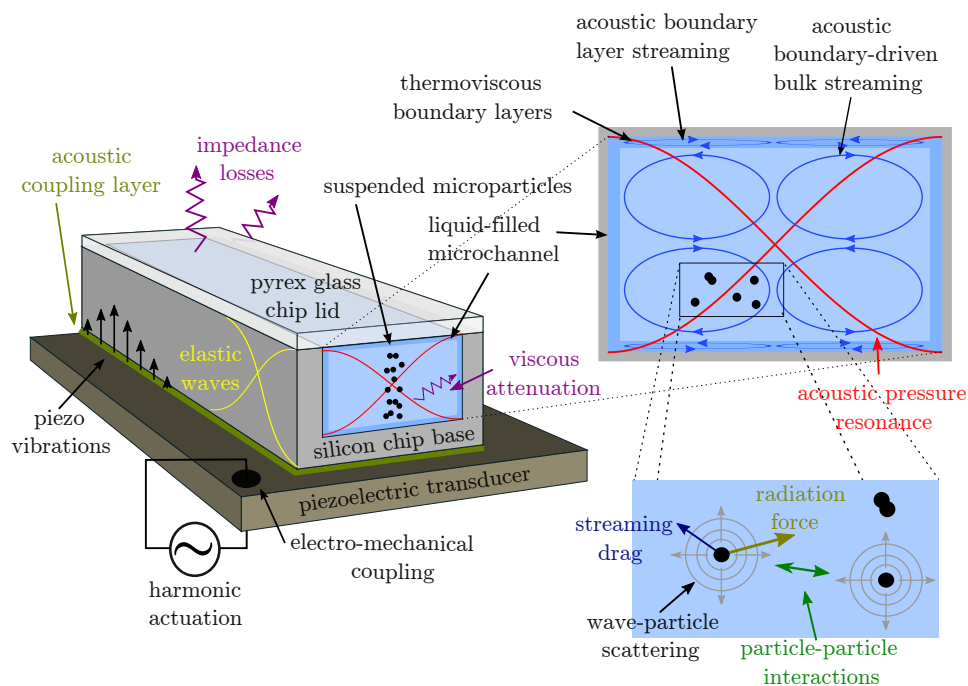
Bridging theory and experiment

Rune Barnkob

PhD thesis, 31 August 2012

Advised by Professor Henrik Bruus

Physics of microparticle acoustophoresis — Bridging theory and experiment

http://www.nanotech.dtu.dk/microfluidics
http://rune.barnkob.com

Til min mor,
som gav mig øjne og øre

Abstract

This thesis presents studies of microparticle acoustophoresis, a technique for manipulation of particles in microsystems by means of acoustic radiation and streaming forces induced by ultrasound standing waves. The motivation for the studies is to increase the theoretical understanding of microparticle acoustophoresis and to develop methods for future advancement of its use.

Throughout the work on this thesis the author and co-workers[1] have studied the physics of microparticle acoustophoresis by comparing quantitative measurements to a theoretical framework consisting of existing hydrodynamic and acoustic predictions. The theoretical framework is used to develop methods for *in situ* determination of acoustic energy density and acoustic properties of microparticles as well as to design a microchip for high-throughput microparticle acoustophoresis.

An experimental model system is presented. This system is the center for the theoretical framework, and its underlying assumptions, of the acoustophoretic microparticle motion in a suspending liquid subject to harmonic ultrasound actuation of the surrounding microchannel.

Based directly on the governing equations a numerical scheme is set up to study the transient acoustophoretic motion of the microparticles driven by the acoustic radiation force from sound scattered of the particles and the Stokes drag force from the induced acoustic streaming. The numerical scheme is used to predict the acoustophoretic particle motion in the experimental model system and to study the transition in the motion from being dominated by streaming-induced drag to being dominated by radiation forces as function of particle size, channel geometry, and suspending medium.

Next, is presented an automated and temperature-controlled platform for reproducible acoustophoresis measurements suitable for direct comparison to the theoretical framework. The platform was used to examine in-plane acoustophoretic particle velocities by micro particle imaging velocimetry. The in-plane particle velocities are analyzed as function of spatial position revealing the complexity of the underlying acoustic resonances. The resonances and hence the acoustic particle motion are investigated to determine the dependency on driving voltage,

---

[1]See the list of publications, Section 1.3, and the introduction to each chapter, Section 1.2.

driving frequency, and resonator temperature. Furthermore, the in-plane velocity measurements form the basis for a systematic investigation of the acoustic radiation- and streaming-induced particle velocities as function of the particle size, the actuation frequency, and the suspending medium. These measurements are compared to theoretical predictions showing good agreement.

The acoustophoretic particle motion, and in particular the acoustic streaming, possesses a three-dimensional character. By using the experimental platform in combination with the Astigmatism micro-PTV technique, preliminary results are presented of the out-of-plane acoustophoretic velocities displaying close similarities to the analytical and numerical predictions of the theoretical framework.

One of the key problems in microchannel acoustophoresis is to measure the absolute size of the acoustic energy density, an important parameter when designing and optimizing acoustophoresis devices. To facilitate this development, a number of methods are presented to *in situ* determine the acoustic energy densities by means of acoustophoretic particle motion measured either as particle trajectories, particle velocities, or particle depletion in terms of light-intensity.

Other key parameters when designing acoustophoresis devices for particle manipulation are the acoustic properties, density and compressibility of the subject particles. For cells these parameters are widely distributed and are seldom known. For this a method is proposed to *in situ* determine the density and compressibility of a single particle undergoing acoustophoretic motion in an arbitrary acoustic field.

Finally, the theoretical framework was used as an essential parameter when designing an acoustophoresis microchip allowing for high-throughput particle separation larger than 1 Liter per hour for a single separation chamber. The design is based on previously reported design of acoustophoretic separators but expanded with temperature control allowing for high-power acoustic actuation.

Resumé

Afhandlingen *Physics of microparticle acoustophoresis – Bridging theory and experiment, Fysikken bag mikropartikel-akustoforese – sammenkobling af teori og eksperiment*, er et studie af mikropartikel-akustoforese. Mikropartikel-akustoforese er en teknik til manipulering af partikler og væsker i mikrosystemer ved hjælp af akustiske strålings- og strømningskræfter induceret af stående ultralydsbølger. Motivationen for dette studie har været at øge den, ind til dato, begrænsede teoretiske forståelse indenfor mikropartikel-akustoforese, samt at udvikle metoder til fremtidig forbedring inden for dette område.

Gennem ph.d.-projektet har forfatteren og dennes samarbejdspartnere[2] studeret tidligere beskrivelser af mikropartikel-akustoforese. På baggrund af disse teoretiske forudsigelser – numeriske såvel som analytiske – har vi foretaget kvantitative målinger med det formål at validere og forbedre de eksisterende forudsigelser på feltet. Derudover anvendes de eksisterende teoretiske forudsigelser til at udvikle en række metoder til *in situ* karakterisering af eksperimentelle akustoforetiske opstillinger og i et enkelt tilfælde til at designe et akustoforetisk separationssystem.

Mere konkret præsenteres der i afhandlingen et eksperimentelt model system, hvor der opsættes en teoretisk beskrivelse af mikropartiklernes akustoforetiske hastighed i en væskefyldt mikrokanal med stående ultralydsbølger. Baseret på de styrende ligninger beskrives en numerisk model til studie af den akustoforetiske bevægelse af mikropartikler induceret af den akustiske strålingskraft, samt viskøst træk fra den akustiske strømning. Den numeriske model bruges til at beskrive overgangen i partiklernes akustoforetiske bevægelse fra at være domineret af det akustiske strømningstræk til at blive domineret af den akustiske strålingskræft. Denne overgang studeres som funktion af partikelstørrelse, kanalgeometri og den omgivende væske.

Hernæst præsenteres en automatiseret og temperaturstyret opstilling til reproducerbare akustoforese-målinger, hvilket er velegnet til sammenligning med de teoretiske forudsigelser. I kombination med mikro-PIV teknikken bruges opstillingen til at undersøge de akustoforetiske plane partikelhastigheder. Disse partikelhastigheder udersøges som funktion af position i kanalen som afslører den rumlige

---

[2]See publikationslisten, afsnit 1.3, samt introduktionen til de enkelte kapitler, afsnit 1.2.

kompleksitet af de underliggende akustiske resonanser. Ydermere undersøges det hvordan den påtrykte resonans, og dermed de akustiske partikelbevægelser, responderer som funktion af den påtrykte drivspænding, frekvens og temperatur. Endvidere bruges denne type hastighedsmålinger i en systematisk undersøgelse af de inducerede partikelhastigheder, fra at være domineret af den akustiske strålingskraft til at være domineret af den akustiske strømning, som funktion af partikelstørrelse, resonansfrekvens og egenskaberne af den omgivende væske.

Den akustoforetiske partikelbevægelse har en tredimensional karakter, især den akustiske strømning, og ved at bruge den eksperimentelle platform i kombination med Astigmatisk mikro-PTV teknikken, præsenteres der foreløbige resultater af de tre-dimensionelle akustoforetiske partikelhastigheder som udviser lighed med de præsenterede analytiske og numeriske forudsigelser.

Et af de centrale problemer i mikropartikel-akustoforese er at måle den absolutte størrelse på den akustiske energitæthed. Dette er en essentiel parameter ved optimering og design af akustoforetiske anvendelser. For at lette denne udvikling, præsenteres der i afhandlingen en række metoder til *in situ* bestemmelse af den akustiske energitæthed ved udelukkende at studere akustoforetisk partikelbevægelse, enten målt som partikelbaner, partikelhastigheder eller partiklers skyggevirkning.

Andre vigtige parametre, når man skal designe akustoforetisk udstyr til partikelmanipulation, er de akustiske egenskaber, densitet og kompressibilitet, af de manipulerede partikler, fx celler, for hvilke disse parametre sjældent er kendt. I afhandlingen foreslås der en metode til bestemmelse af densitet og kompressibilitet af en enkelt partikel, som undergår akustoforetisk bevægelse i et vilkårligt akustisk felt. Der præsenteres de næste nødvendige skridt for at realisere denne metode.

Endelig bruger vi den teoretiske indsigt til at designe en akustoforese-mikrochip, som tillader separationshastigheder på over 1 Liter i timen. Mikrochippens udformning er baseret på tidligere forskningsresultater, men ved at bruge en temperaturstyring til sikring af stabile akustiske resonanser, har vi kunnet benytte høj akustisk aktueringsspænding.

Preface

This thesis is submitted as partial fulfillment for obtaining the degree of Doctor of Philosophy (PhD) at the Technical University of Denmark (DTU). The PhD project was financed by the Danish Council for Independent Research, Technology and Production Sciences, Grant No. 274-09-0342. The project was carried out at the Department of Micro- and Nanotechnology, DTU Nanotech, as a member of the Theoretical Microfluidics Group (TMF) during a three-year period from September 2009 to August 2012. The project was supervised by Professor Henrik Bruus, leader of the TMF group at DTU Nanotech. During many short visits throughout all three project years and in the period from September to November 2010 I worked in the lab of Professor Thomas Laurell at Lund University, Sweden. During the period from February to July 2010, I visited the University of California, Santa Barbara, CA, USA, together with the rest of the TMF group and I worked with the group of Professor Tom Soh, and in August 2010 I visited the group of Professor Steve Wereley for a week at Purdue University, IN, USA. Lastly, in the period from November to December 2010 I worked in the lab of Martin Wiklund, Royal Institute of Technology, Stockholm, Sweden.

As evident from the many above-mentioned visits to experimental research groups this thesis is the outcome of fruitful collaborations with many smart people, whom I will like to acknowledge. Primarily and firstly, I will like to thank Professor Henrik Bruus for always being there to make sure that I grew up as a scientist with no compromises when it comes to scientific detail and accuracy. Henrik has been a superb supervisor and mentor as well as a good friend. We have had many great times academically as well as less academically ranging from altitude, latitude, and longitude bets in the Ecuadorian jungle to lots of visits to cafés around the world and in particular in Copenhagen.

Next, I will like to thank Thomas Laurell and the rest of Elmät for always keeping a door open for me. In particular, I will like to thank Per Augustsson for a fruitful collaboration, academically as well as personally and for always being (too) skeptical — I cross my fingers that our collaboration continues somehow. Thanks to Martin Wiklund for good discussions and for inviting me to the capital of Scandinavia, and Ida Iranmanesh for good collaboration and Fesenjun. Thanks to Tom Soh for hosting me in sunny California, Lore Dobler for flowers, and the

Kongens Lyngby, 31 August 2012

Rune Barnkob

Contents

List of Figures

List of Tables

List of Symbols and Acronyms

Symbol	Description	Unit
a	Microparticle radius	m
BAW	Bulk Acoustic Wave	
c	Isentropic speed of sound	$\mathrm{m\,s^{-1}}$
C	Particle concentration	$\mathrm{m^{-3}}$
$C\,(g)$	Relative convergence parameter	
C_{corr}	PIV cross-correlation function	
C_p	Specific heat capacity, constant pressure	$\mathrm{J\,kg^{-1}\,K^{-1}}$
C_v	Specific heat capacity, constant volume	$\mathrm{J\,kg^{-1}\,K^{-1}}$
$D_{\mathrm{th}} \equiv \frac{k_{\mathrm{th}}}{\rho C_p}$	Thermal diffusivity	$\mathrm{m^2\,s^{-1}}$
E_{ac}	Time-average acoustic energy density	$\mathrm{J\,m^{-3}}$
f	Frequency	$\mathrm{s^{-1}}$
f_1	Compressibility factor in $\boldsymbol{F}^{\mathrm{rad}}$	
f_2	Density factor in $\boldsymbol{F}^{\mathrm{rad}}$.	
$\boldsymbol{F}^{\mathrm{drag}}$	Viscous Stokes drag force	N
$\boldsymbol{F}^{\mathrm{rad}}$	Acoustic radiation force	N
i	Unit imaginary number	
$K = \kappa^{-1}$	Bulk modulus	Pa
$k = \frac{2\pi}{\lambda} = \frac{f}{c}$	Acoustic wavenumber	$\mathrm{m^{-1}}$
k_{th}	Thermal conductivity	$\mathrm{W\,m^{-1}\,K^{-1}}$
l, w, h	Microchannel length, width, and height	m
$\boldsymbol{n}$	Outward-pointing normal vector	
p	Pressure	Pa
piezo (or PZT)	Piezoelectric transducer	
PID	Proportional–Integral–Derivative controller	
PIV	Particle Image Velocimetry	
PTV	Particle Tracking Velocimetry	
PZT	Lead Zirconate Titanate	
s	Entropy per unit mass	$\mathrm{J\,K^{-1}\,kg^{-1}}$
S	PIV interrogation window side length	pixels
SAW	Surface Acoustic Wave	
t	Time	s
T	Temperature	K
$\boldsymbol{u}$	Acoustophoretic particle velocity	$\mathrm{m\,s^{-1}}$
U_{pp}	Piezo peak-to-peak voltage	V
$\boldsymbol{v}$	Fluid velocity vector	$\mathrm{m\,s^{-1}}$
v	Fluid velocity magnitude	$\mathrm{m\,s^{-1}}$
$\langle \boldsymbol{v}_2 \rangle$	Steady acoustic streaming velocity	$\mathrm{m\,s^{-1}}$
V	Volume	$\mathrm{m^3}$

Symbol	Description	Unit
α	Isobaric thermal expansion	K^{-1}
$\beta = 1/3$	Viscosity ratio	
δ	Viscous boundary layer thickness	m
$\tilde{\delta} = \delta/a$	Normalized viscous boundary layer thickness	
δ_{th}	Thermal boundary layer thickness	m
δ_{ij}	Kronecker's delta	
ϵ	Internal energy per unit mass	$\mathrm{J\,kg}^{-1}$
η	Dynamic viscosity	$\mathrm{Pa\,s}$
$\gamma = C_p/C_v$	Specific heat ratio	
γ_{att}	Viscous attenuation factor	
Γ	Viscous correction factor to $\boldsymbol{F}^{\mathrm{rad}}$	
$\kappa = K^{-1}$	Isothermal compressibility	Pa^{-1}
$\tilde{\kappa} = \kappa_{\mathrm{p}}/\kappa_0$	Compressibility ratio for particle and liquid	
λ	Acoustic wavelength	m
ν	Kinematic viscosity (momentum diffusivity)	$\mathrm{m^2\,s^{-1}}$
$\omega = 2\pi f$	Angular frequency	s^{-1}
Ω	Domain	
$\partial\Omega$	Domain boundary	
Φ	Acoustic contrast factor in $\boldsymbol{F}^{\mathrm{rad}}$	
ρ	Mass density	$\mathrm{kg\,m}^{-3}$
$\tilde{\rho} = \rho_{\mathrm{p}}/\rho_0$	Mass density ratio for particle and liquid	
$\boldsymbol{\sigma}'$	Viscous stress tensor	Pa
ζ	Second coefficient of viscosity	$\mathrm{Pa\,s}$
$\bar{\square}$	Complex conjugate of the function $\square$	
$\square_i$	i'th component of the function $\square$, $i = x, y, z$	
$\square_0, \square_1, \square_2$	1st-, 2nd-, and 3rd-order perturbations of $\square$	
$\square_{\mathrm{a}}$	Amplitude of the first-order field $\square$	
$\langle\square\rangle = \frac{1}{\tau}\int_t^{t+\tau}\square\,\mathrm{d}t,$	Time average of function $\square$	
$\langle\square\rangle_\triangle$	Average of function $\square$ taken over $\triangle$	
$\partial_\square$	Partial derivative with respect to $\square$	
(x, y, z)	Cartesian coordinates	m

List of Material Parameters

All material parameters are listed at 25 °C unless otherwise stated.

Polystyrene				
Density	ρ_p	1050	kg m^{-3}	Ref. [1]
Speed of sound (at 20 °C)	c_p	2350	m s^{-1}	Ref. [2]
Poisson's ratio	σ_p	0.35		Ref. [3]
Compressibility	κ_p	249	TPa^{-1}	See a.
Polyamide				
Density	ρ_p	1030	kg m^{-3}	See d.
Speed of sound (for Nylon)	c_p	2660	m s^{-1}	Ref. [1]
Compressibility	κ_p	137	TPa^{-1}	See b.
Water				
Density	ρ_0	997	kg m^{-3}	Ref. [1]
Speed of sound	c_0	1497	m s^{-1}	Ref. [1]
Charact. acoustic impedance	Z_0	1.49	$\times 10^6\,\text{kg m}^{-2}\,\text{s}^{-1}$	$Z_0 = \rho_0 c_0$
Viscosity	η	0.890	mPa s	Ref. [1]
Viscous boundary layer, 1.940 MHz	δ	0.38	µm	Eq. (3.15b)
Viscous boundary layer, 3.900 MHz	δ	0.27	µm	Eq. (3.15b)
Compressibility	κ_0	448	TPa^{-1}	See b.
Compressibility factor (polystyrene)	f_1	0.444		Eq. (3.30a)
Density factor (polystyrene)	f_2	0.034		Eq. (3.30b)
Contrast factor (polystyrene)	Φ	0.165		Eq. (3.33)
Normalized momentum diffusivity	ν/Φ	5.25	$\text{mm}^2\,\text{s}^{-1}$	
Thermal conductivity	k_th	0.603	$\text{W m}^{-1}\,\text{K}^{-1}$	Ref. [4]
Specific heat capacity	C_p	4183	$\text{J kg}^{-1}\,\text{K}^{-1}$	Ref. [4]
Specific heat capacity ratio	γ	1.014		Eq. (3.10)
Thermal diffusivity	D_th	1.43	$\times 10^{-7}\,\text{m}^2\,\text{s}^{-1}$	Eq. (3.13)
Thermal expansion coefficient	α	2.97	$\times 10^{-4}\,\text{K}^{-1}$	Ref. [1], c.
0.75:0.25 mixture of water and glycerol				
Density	ρ_0	1063	kg m^{-3}	Ref. [5]
Speed of sound	c_0	1611	m s^{-1}	Ref. [6]
Viscosity	η	1.787	mPa s	Ref. [5]
Viscous boundary layer, 2.027 MHz	δ	0.51	µm	Eq. (3.15b)
Compressibility	κ_0	363	TPa^{-1}	See b.
Compressibility factor (polystyrene)	f_1	0.313		Eq. (3.30a)
Density factor (polystyrene)	f_2	-0.008		Eq. (3.30b)
Contrast factor (polystyrene)	Φ	0.10		Eq. (3.33)
Normalized momentum diffusivity	ν/Φ	16.8	$\text{mm}^2\,\text{s}^{-1}$	
0.50:0.50 mixture of water and glycerol				
Density	ρ_0	1129	kg m^{-3}	Ref. [5]
Speed of sound	c_0	1725	m s^{-1}	Ref. [6]
Viscosity	η	5.00	mPa s	Ref. [5]
Viscous boundary layer, 2.270 MHz	δ	0.79	µm	Eq. (3.15b)
Compressibility	κ_0	298	TPa^{-1}	See b.
Compressibility factor (polystyrene)	f_1	0.164		Eq. (3.30a)

Density factor (polystyrene)	f_2	-0.049		Eq. (3.30b)
Contrast factor (polystyrene)	Φ	0.030		Eq. (3.33)
Normalized momentum diffusivity	ν/Φ	146	$\mathrm{mm^2\,s^{-1}}$	
Thermal conductivity (at 20 °C)	k_th	0.416	$\mathrm{W\,m^{-1}\,K^{-1}}$	Ref. [7]
Specific heat capacity (at 1.7 °C)	C_p	3360	$\mathrm{J\,kg^{-1}\,K^{-1}}$	Ref. [8]
Specific heat capacity ratio	γ	1.04		Eq. (3.10)
Thermal diffusivity	D_th	1.10	$\times 10^{-7}\,\mathrm{m^2\,s^{-1}}$	Eq. (3.13)
Thermal expansion coefficient	α	4.03	$\times 10^{-4}\,\mathrm{K^{-1}}$	Ref. [1], c.
Air				
Density	ρ_air	1.16	$\mathrm{kg\,m^{-3}}$	Ref. [1]
Speed of sound	c_air	343.4	$\mathrm{m\,s^{-1}}$	Ref. [1]
Charact. acoustic impedance	Z_air	3.99	$\times 10^{5}\,\mathrm{kg\,m^{-2}\,s^{-1}}$	$Z_\mathrm{air} = \rho_\mathrm{air} c_\mathrm{air}$
Pyrex glass				
Density	ρ_py	2230	$\mathrm{kg\,m^{-3}}$	Ref. [1]
Charact. acoustic impedance	Z_py	1.25	$\times 10^{7}\,\mathrm{kg\,m^{-2}\,s^{-1}}$	$Z_\mathrm{py} = \rho_\mathrm{py} c_\mathrm{py}$
Young's modulus	Y_py	62.6	GPa	[4]
Poisson's ratio	σ_py	0.225		[4]
Speed of sound, longitudinal	c_py	5640	$\mathrm{m\,s^{-1}}$	See e.
Silicon				
Density	ρ_si	2331	$\mathrm{kg\,m^{-3}}$	Ref. [1]
Speed of sound, longitudinal	c_si	8490	$\mathrm{m\,s^{-1}}$	
Charact. acoustic impedance	Z_si	1.98	$\times 10^{7}\,\mathrm{kg\,m^{-2}\,s^{-1}}$	$Z_\mathrm{si} = \rho_\mathrm{si} c_\mathrm{si}$

[a]Calculated as $\kappa_\mathrm{p} = \frac{3(1-\sigma_\mathrm{p})}{1+\sigma_\mathrm{p}} \frac{1}{\rho_\mathrm{p} c_\mathrm{p}^2}$ from Ref. [9].

[b]Calculated as $\kappa_0 = 1/\left(\rho_0 c_0^2\right)$.

[c]Calculated as $\alpha = -\left(1/\rho\right)\left(\partial_T \rho\right)_p$.

[d]ORGASOL1 5 mm: http://r427a.com/technical-polymers/orgasol-powders/ technical-data-sheets.

[e]Calculated as $c_\mathrm{L} = \sqrt{\frac{1-\sigma}{(1+\sigma)(1-2\sigma)} \frac{Y}{\rho}}$ from Ref. [9].

CHAPTER 1

Introduction

Manipulation and separation of particles and fluids are used in a broad range of research. Especially the manipulation, separation, purification, and isolation of bioparticles and cells in complex biofluids are becoming essential within the areas of biology and medicine. For this, the technology of lab-on-a-chip and microfluidics provides a large potential for creating high performance manipulation and separation applications due to precise and accurate control of the forces driving the manipulation [10–12]. Typically, such forces are hydrodynamic, electric, dielectric, magnetic, and mechanical contact forces. Acoustic forces are also being used for the manipulation of fluids and suspended particles, where the migration due to sound are often termed acoustophoresis.

The ability to use acoustic forces for manipulation of particles and fluids are well-known and has a long history dating back to scientists including Chladni, Savart, Faraday, Kundt, and Rayleigh. It is thus a classical field that has now found new life in the modern research in the form of acoustofluidics, the use of ultrasound acoustic fields for application in microfluidics. The acoustofluidics research field has received increasing interest since the early 90s by work of Mandralis and Feke [13, 14], Yasuda *et al.* [15], Johnson and Feke [16], and Hawkes and Coakley [17][1]. Excellent acoustofluidics reviews are given by Friend and Yeo in *Review in Modern Physics* with the emphasis on surface acoustic wave devices [19] and in the on-going 23-articles-long tutorial series in *Lab on a Chip* focusing on bulk acoustic wave devices [20].

The research field of acoustofluidics is now expanding rapidly as scientists realize its high potential for gentle, label-free, and purely mechanical manipulation of particles and fluids. During the last decade acoustofluidics has been applied to numerous useful purposes, such as medium exchange of yeast cells [21], separation of lipids from blood cells [22], phage display selection [23], selective bioparticle retention [24], raw milk control [25], whole-blood plasmapheresis [26], forensic

---

[1]An excellent historic review are given in the PhD thesis of Per Augustsson [18].
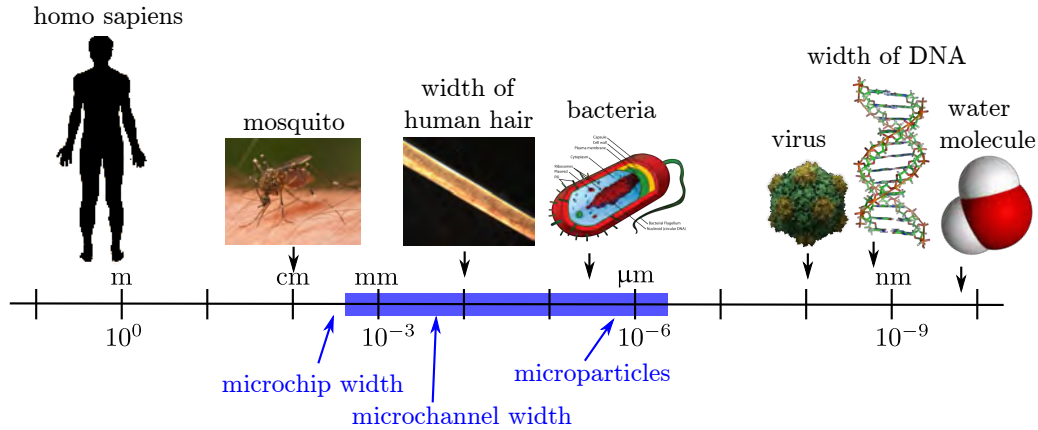
Figure 1.1: Length scales treated in this thesis (blue) in context to other length scales. The lengths are all approximate and are inspired by numerous sources on Wikipedia.

analysis of sexual assault evidence [27], cell cycle synchronization of mammalian cells [28], enrichment of prostate cancer cells from blood [29], study of natural killer cells [30], single-cell manipulation [31], and trapping of bacteria [32]. In addition, acoustophoresis is being used commercially for the acoustic focusing cytometer from Life Technologies.

However, for future development, the research of acoustofluidics faces crucial challenges, including the increase of separation and manipulation throughput, the ability to handle suspensions of physiological relevant concentrations, and the separation and manipulation of sub-micrometer particles such as small bacteria, vira, and biomolecules.

To date acoustofluidics has mainly been driven by applications often leaving room for improvements regarding the understanding of the underlying physical phenomena. Hence, the motivation for this thesis is to increase the theoretical understanding of microparticle acoustophoresis. To do this we carry out theoretical and experimental analyses to validate and expand existing predictions and to develop methods for future enhancement of acoustofluidics.

1.1 Length scales and frequencies

The thesis involves the science of sound (ultrasound) in small mm-sized systems, and in Fig. 1.1 and Fig. 1.2 are shown the length scales and acoustic frequencies treated in this work, respectively.

1.2 Thesis outline

This thesis consists of 8 chapters, whereof most of the content included is already published (or sent for publication) in journals and conference proceedings as listed in Section 1.3. The thesis is naturally built around the six journal papers, which are all enclosed in the appendices Chapters A to F, and the thesis constitutes
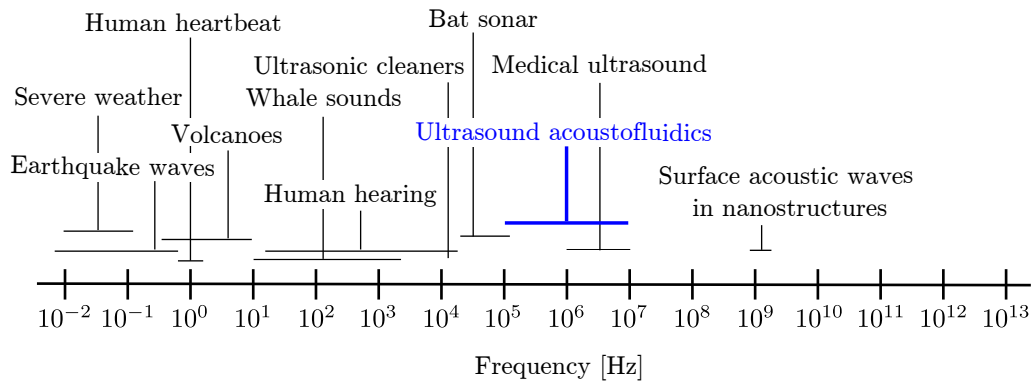
Figure 1.2: Acoustic frequencies of "Ultrasound acoustofluidics" (blue) in the context of acoustic frequencies encountered in modern human life. The frequencies are all approximate and are inspired by Ref. [33] and various sources on the world wide web.

a combined presentation connecting the various parts of the work. Most of the work is part of collaborations with colleagues and therefore each chapter starts with a list of relevant collaborators.

Here follows as list of all the chapter titles and brief outlines of their content.

Chapter 2 — Physics of acoustophoresis. This chapter provides an introduction to the physics of microparticle acoustophoresis. We introduce our experimental model system representing the class of hard-material acoustic devices for generation of bulk acoustic resonances driven by an attached piezoelectric transducer. With the experimental model system in mind, we map the acoustic and hydrodynamic effects important for understanding the acoustophoretic microparticle motion, and we state the primary assumptions constituting the basis of the theoretical descriptions in this thesis.

Chapter 3 — Theory of acoustophoresis. We set up the mathematical framework for this thesis based on the phenomena and approximations presented in Chapter 2. We introduce the governing equations for a thermoviscous fluid and we derive the acoustic wave equation for the isentropic assumption which is suitable when investigating the underlying eigenmodes of the acoustic resonator. We further describe the time-averaged second-order phenomena of the acoustic radiation force acting on suspended particles as well as the boundary-induced acoustic streaming flow. Finally, we set up the equation of motion for suspended microparticles as they undergo acoustophoresis.

Chapter 4 — Numerics of acoustophoresis. We set up a numerical model for the microparticle acoustophoresis in the experimental model system presented in Chapter 2. The model is based directly on the governing equations presented in Chapter 3 implemented and solved using the commercial finite element software COMSOL Multiphysics. Using the model we show the transition in the

microparticle acoustophoresis from being dominated by the streaming-induced drag forces to being dominated by the acoustic radiation forces. Furthermore we demonstrate how this transition depends on particle size, channel geometry, and suspending medium. This chapter is based on the journal paper appended in Chapter E.

Chapter 5 — Acoustophoresis analyzed by micro-PIV. We present an automated and temperature-controlled experimental platform for analyzing the experimental model system in a stable and reproducible manner. The platform was used to carry out micro-PIV measurements of the in-plane acoustophoretic microparticle motion. The measurements were carried out for a large fraction of the investigated microchannel providing insight in the complexity of the acoustophoretic motion. Moreover, the actuation frequency and temperature are scanned in order to investigate the peak widths and temperature sensitivities of the underlying acoustic resonances. Finally, we use the micro-PIV setup to investigate the interplay between the radiation- and streaming-induced forces on microparticles. We verify a theoretical prediction of the ratio of the radiation- and streaming-induced particle velocities and we demonstrate control over this ratio by adjusting the particle size, the actuation frequency, and the suspending medium. This chapter is based on the journal papers appended in Chapters B and F.

Chapter 6 — Acoustophoresis analyzed by Astigmatism micro-PTV. In order to measure the out-of-plane velocity components of the acoustophoretic microparticle motion, we extend the automated and temperature-controlled acoustophoresis platform presented in Chapter 5 for use in combination with the Astigmatism micro-PTV technique. We show the transition in the acoustophoretic particle motion from being dominated by the streaming-induced drag for small particles to being dominated by the radiation forces for larger particles. From the motion of the smallest particles we compare the measured acoustic streaming to analytical predictions. This chapter is based on preliminary work to be presented at the "µFlu2012" conference [34].

Chapter 7 — Applications of acoustophoresis. We present three applications of microparticle acoustophoresis: (*i*) In order to improve the development and optimization of acoustophoresis microdevices we propose a set of methods for *in situ* determination of the acoustic energy density. All methods are based on the assumption of a locally well-known transverse resonance but they rely on different measurement probes such as particle trajectories, particle velocities, and light intensities. (*ii*) Using a theoretical expression for the acoustic radiation force and the measurements of acoustophoretic particle motion as presented in Chapter 5 and 6 we propose a method for determination of the density and compressibility of individual microparticles. (*iii*) We present a high-throughput acoustophoresis chip based on maintaining a stable resonance by use of temperature control allowing for large actuation voltages enabling high-throughput separation of cells

in suspension. This chapter is based on the journal papers appended in Chapters A, C, and D.

Chapter 8 — Conclusions and outlook. We end the thesis with a summation of our findings and give an outlook for further suitable routes of physics studies of microparticle acoustophoresis to advance the development of the acoustofluidics research field.

1.3 Publications during the PhD studies

During my PhD studies I have co-authored 6 peer-reviewed journal publications, 12 peer-reviewed conference proceedings, and 5 conference abstracts.

1.3.1 Peer-reviewed journal publications

1. R. Barnkob, P. Augustsson, T. Laurell, and H. Bruus, *Measuring the local pressure amplitude in microchannel acoustophoresis*, Lab on a Chip **10**, 563-570 (2010). Front-page cover. Enclosed in Chapter A.

2. P. Augustsson[†], R. Barnkob[†], S. T. Wereley, H. Bruus, and T. Laurell, *Automated and temperature-controlled micro-PIV measurements enabling long-term-stable microchannel acoustophoresis characterization*, Lab on a Chip **11**, 4152-4164 (2011). Front-page cover. Enclosed in Chapter B.

3. R. Barnkob, I. Iranmanesh, M. Wiklund, and H. Bruus, *Measuring acoustic energy density in microchannel acoustophoresis using a simple and rapid light-intensity method*, Lab on a Chip **12**, 2337-2344 (2012). Promoted as a 'HOT' article. Enclosed in Chapter C.

4. J. D. Adams[†], C. L. Ebbesen[†], R. Barnkob, A. H. J. Yang, H. T. Soh, and H. Bruus, *Liter-per-hour-throughput cell separation of whole human blood by temperature-controlled microchannel acoustophoresis*, J Micromech Microeng **22**, 075017 (2012). Enclosed in Chapter D.

5. P. B. Muller, R. Barnkob, M. J. H. Jensen, and H. Bruus, *A numerical study of microparticle acoustophoresis driven by acoustic radiation forces and streaming-induced drag forces,* Lab on a Chip **12**, 4617–4627 (2012). Enclosed in Chapter E.

6. R. Barnkob, P. Augustsson, T. Laurell, and H. Bruus, *Acoustic radiation- and streaming-induced microparticle velocities determined by micro-PIV in an ultrasound symmetry plane*, Physical Review E **86**, 056307 (2012). Enclosed in Chapter F.

† Authors 1 and 2 share first authorship.

1.3.2 Peer-reviewed conference proceedings

1. <u>R. Barnkob</u>, P. Augustsson, T. Laurell, and H. Bruus, *Measurement of acoustic resonance line shapes by microbead acoustophoresis in straight microchannels*, USWNet 2009, 7th annual meeting, KTH-AlbaNova, 30 November – 1 December 2009, Stockholm, Sweden.

2. P. Augustsson, <u>R. Barnkob</u>, C. Grenvall, T. Deierborg, P. Brundin, H. Bruus, and T. Laurell, *Microchannel for measurements of acoustic properties of living cells*, USWNet 2010, 8th annual meeting, 2-3 October 2010, Groningen, The Netherlands.

3. <u>R. Barnkob</u>, P. Augustsson, T. Laurell, and H. Bruus, *Quantifying acoustic streaming in large-particle acoustophoresis*, USWNet 2010, 8th annual meeting, 2-3 October 2010, Groningen, The Netherlands.

4. <u>R. Barnkob</u>, P. Augustsson, T. Laurell, and H. Bruus, *An automated full-chip micro-PIV setup for measuring microchannel acoustophoresis: Simultaneous determination of forces from acoustic radiation and acoustic streaming*, Proc. 14th MicroTAS, 3-7 October 2010, Groningen, The Netherlands (S. Verporte, H. Andersson, J. Emneus, and N. Pamme, eds.), pp. 1247-49, CBMS, 2010.

5. P. Augustsson, <u>R. Barnkob</u>, C. Grenvall, T. Deierborg, P. Brundin, H. Bruus, and T. Laurell, *Measuring the acoustophoretic contrast factor of living cells in microchannels.* Proc. 14th MicroTAS, 3-7 October 2010, Groningen, The Netherlands (S. Verporte, H. Andersson, J. Emneus, and N. Pamme, eds.), pp. 1337-39, CBMS, 2010.

6. C. L. Ebbesen, J. D. Adams, <u>R. Barnkob</u>, H. T. Soh, and H. Bruus, *Temperature-controlled high-throughput (1 L/H) acoustophoretic particle separation in microchannels*, Proc. 14th MicroTAS, 3-7 October 2010, Groningen, The Netherlands (S. Verporte, H. Andersson, J. Emneus, and N. Pamme, eds.), pp. 728-30, CBMS, 2010.

7. <u>R. Barnkob</u>, P. Augustsson, S. T. Wereley, H. Bruus, and T. Laurell, *Microchannel acoustophoresis: continuous flow focusing efficiency compared to full-chip high-resolution micro-PIV measurements of the acoustic radiation force*, International Congress on Ultrasonics, 5-8 September 2011, Gdansk, Poland.

8. <u>R. Barnkob</u>, P. Augustsson, C. Magnusson, H. Lilja, H. Bruus, and T. Laurell, *Measuring density and compressibility of white blood cells and prostate cancer cells by microchannel acoustophoresis.* Proc. 15th MicroTAS, 2-6 October 2011, Seattle (WA), USA (J. Landers, A. Herr, D. Juncker, N. Pamme, and J. Bienvenue, eds.), pp. 127-129, CBMS, 2011.

9. <u>R. Barnkob</u>, P. Augustsson, T. Laurell, and H. Bruus, *Controlling the ratio of radiation and streaming forces in microparticle acoustophoresis*, USWNet 2012, 10th annual meeting, 21-22 September 2012, Lund, Sweden.

10. P. Augustsson, <u>R. Barnkob</u>, H. Bruus, C. J. Kähler, T. Laurell, Á. G. Marín, P. B. Muller and M. Rossi, *Measuring the 3D motion of particles in microchannel acoustophoresis using astigmatism particle tracking velocimetry*, Proc. 16th MicroTAS, 28 October - 1 November 2012, Okinawa, Japan.

11. M. Khoury, <u>R. Barnkob</u>, L. Laub Busk, P. Tidemand-Lichtenberg, H. Bruus, K. Berg-Sørensen, *Optical stretching on chip with acoustophoretic prefocusing*, SPIE Optics+Photonics, 12 - 16 August 2012, San Diego Convention Center, San Diego, California, USA.

12. M. Rossi, <u>R. Barnkob</u>, P. Augustsson, Á. Márin, P. B. Muller, H. Bruus, T. Laurell and C. J. Kähler, *Experimental and numerical characterization of the 3D motion of particles in acoustofluidic devices*, 3rd European Conference on Microfludics, 3-5 December 2012, Heidelberg, Germany.

1.3.3 Conference abstracts

1. <u>R. Barnkob</u>, P. Augustsson, T. Laurell, and H. Bruus, *Decomposition of acoustophoretic velocity fields into contributions from acoustic radiation and acoustic streaming*, DFS 2011, Danish Physical Society, 21-22 June 2011, Nyborg, Denmark

2. <u>R. Barnkob</u>, P. Augustsson, T. Laurell, and H. Bruus, *Particle-size dependent cross-over from radiation-dominated to streaming-dominated acoustophoresis in microchannels*, APS 2011, The 64th Annual Meeting of the Division of Fluid Dynamics, 20-22 November 2011, Baltimore, Maryland, USA.

3. M. J. H. Jensen, P. B. Muller, <u>R. Barnkob</u>, and H. Bruus, *Numerical study of acoustic streaming and radiation forces on micro particles*, BNAM 2012, Joint Baltic-Nordic Acoustics Meeting, June 18-20 2012, Odense, Denmark.

4. H. Bruus, P. B. Muller, <u>R. Barnkob</u>, and M. J. H. Jensen, *COMSOL analysis of acoustic streaming and microparticle acoustophoresis*, COMSOL Conference Europe 2012, 10-12 October 2012, Milan, Italy.

5. <u>R. Barnkob</u>, P. B. Muller, H. Bruus, and M. J. H. Jensen, *Numerical analysis of radiation- and streaming-induced microparticle acoustophoresis*, APS 2012, The 65th Annual Meeting of the Division of Fluid Dynamics, 18-20 November 2012, San Diego, California, USA.

Physics of acoustophoresis

This chapter introduces the experimental acoustophoresis model system. This system represents a class of hard-material acoustic devices for generation of bulk acoustic resonances and it constitutes the basis for the analyses presented in this work. With the experimental model system in mind we describe the phenomena essential for understanding the acoustophoretic motion of microparticles. This chapter provides an overview of the phenomena and their assumptions described in a qualitative manner rather than a more quantitative, mathematical description which is given in the following Chapter 3.

2.1 Experimental model system

Our experimental acoustophoresis model system was developed and is located in the lab of Professor Thomas Laurell, Lund University, Sweden, and all experiments presented in this thesis using this system is carried out by or in collaboration with Dr. Per Augustsson. The core of the acoustophoresis system is a silicon/glass microchip attached to a piezoelectric transducer (piezo) responsible for the ultrasound actuation. The silicon/glass microchip is designed and fabricated by Dr. Per Augustsson and the reader is referred to his PhD thesis [18] and the Lab Chip Acoustofluidics 5 tutorial by Lenshof *et al.* for descriptions on the realization of such acoustophoresis devices [35].

The experimental model system is shown in Fig. 2.1 and consists of a silicon/glass microchip translational invariant along its length $L = 35\,\mathrm{mm}$ with an etched microchannel that can be loaded with particle suspension through silicone tuning at its ends. The chip is glued to and acoustically actuated by a piezo of dimension $35\,\mathrm{mm} \times 5\,\mathrm{mm} \times 1\,\mathrm{mm}$ of the type Pz26 from Ferroperm Piezoceramics, Denmark. In Fig. 2.1(a) is shown a section along the length of the microchip showing the silicon chip (gray) of width $W = 2.52\,\mathrm{mm}$ and height $h_{\mathrm{si}} = 350\,\mathrm{\mu m}$.
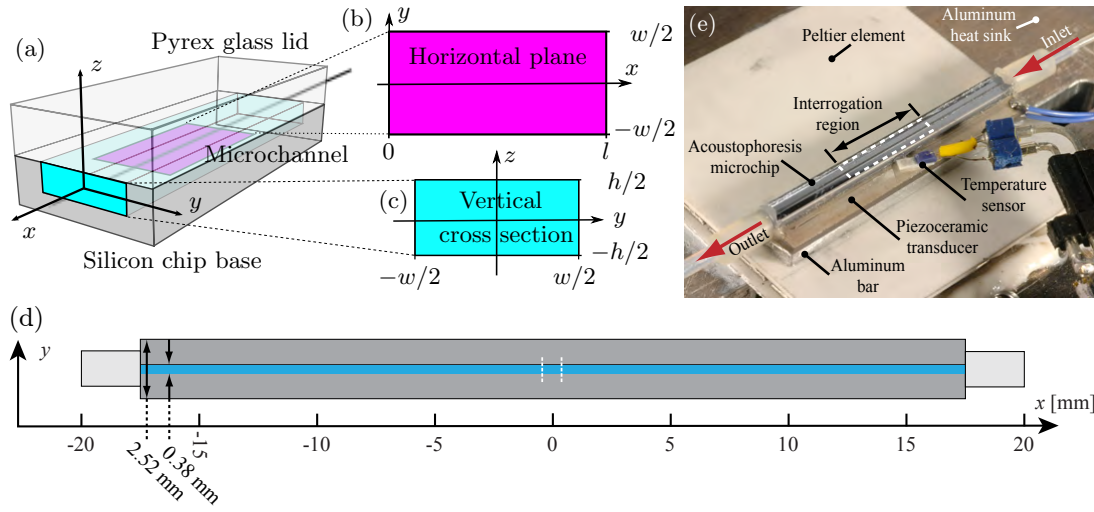
Figure 2.1: Experimental acoustophoresis model system located in the lab of Professor Thomas Laurell, Lund University, Sweden, and developed and fabricated by Dr. Augustsson [18]. (a) A section of the acoustophoresis chip translational invariant along its length L consisting of a silicon chip base of width W and height h_{si}, with an etched microchannel of width w and height h, and anodically bonded with a Pyrex glass lid of width W and height h_{py}. All chip and channel dimensions are listed in Table 2.1. (b) Horizontal xy plane section (magenta) at the channel mid height $z = 0$ of dimension $l \times w$. (c) Vertical yz microchannel cross section (cyan) of dimension $w \times h$. (d) Top view of the silicon chip base (dark gray), microchannel (blue), microscope field of view of length l (dashed white lines), and inlet and outlet tubing (light gray). (e) Photograph of the experimental model system placed in the automated and temperature-controlled micro-PIV setup described in Section 5.1. Particle suspensions are infused into the microchannel via the inlet and outlet silicone tubing and the chip is acoustically actuated by the piezoelectric transducer glued to the chip bottom. Adapted from Refs. [36, 37].

The microchannel (light cyan) of width $w = 377\,\mu\mathrm{m}$ and height $h = 157\,\mu\mathrm{m}$ is etched into the silicon. The chip is anodically bonded with a Pyrex glass lid (transparent gray) of height $h_{\mathrm{py}} = 1.13\,\mathrm{mm}$. All chip and channel dimensions are summarized in Table 2.1. Throughout this thesis we place the origo O of the spatial xyz coordinate system at the center of the microchannel such that x always points along the channel length, y along the transverse channel width, and z along the channel height. Fig. 2.1(b) shows the horizontal xy plane (magenta) of dimension $l \times w$ at the channel mid height $z = 0$, where the length l refers to the width of a given microscope field of view. Fig. 2.1(c) shows the vertical yz microchannel cross section (cyan) of dimension $w \times h$, while Fig. 2.1(d) shows a xy top view schematic of the silicon chip base (dark gray) and microchannel (blue).

Fig. 2.1(e) shows a photograph of the experimental model system as it is placed in an automated and temperature-controlled setup described in Section 5.1. More information on the chip and setup can be found in Ref. [36] appended in Chap-

Table 2.1: Dimensions of the experimental model system shown in Fig. 2.1.

Description		Value	Description		Value
Width, channel	w	377 μm	Width, chip	W	2.52 mm
Height, channel	h	157 μm	Height, silicon base	h_{si}	350 μm
Length, channel	L	35 mm	Height, Pyrex glass lid	h_{gl}	1.13 mm
Length, chip	L	35 mm	Height, chip	$h_{\mathrm{si}} + h_{\mathrm{gl}}$	1.48 mm
Piezo transducer (Pz26, Ferroperm, Denmark)				$35\,\mathrm{mm} \times 5\,\mathrm{mm} \times 1\,\mathrm{mm}$	

ter B.

2.2 Acoustic actuation

Basically, two ultrasound driving mechanisms are commonly used in acoustofluidics: (*i*) the generation of standing ultrasound bulk acoustic waves (BAW) driven by a piezo attached to the microchip acting as a resonator, see Fig. 2.1, and (*ii*) the generation of surface acoustic waves (SAW) by an interdigitated transducer on a piezoelectric substrate, see Refs. [19, 38, 39]. The two driving mechanisms are fundamentally different and each have their advantages, however, in this work we focus on BAW-driven acoustophoresis. Nevertheless, much of the fundamental physics remains the same, and it is the author's hope that also researchers working on SAW-driven acoustophoresis can benefit from this thesis.

As described in Section 2.1 our experimental model system supports BAW-driven acoustophoresis. The piezo is driven with a harmonic electric signal at low MHz frequencies sending MHz vibrations into the chip and the surroundings. These vibrations result in mm-wavelength acoustic resonances in the chip and its liquid-filled cavities. These resonances lead to nonlinear interactions driving phenomena such as acoustic streaming of the suspending fluid and radiation forces on the suspended particles. In Fig. 2.2 is sketched the experimental model system and the involved phenomena arising from acoustically driving the system via the piezo. In the following we set out to describe these phenomena aiming at stating the underlying assumptions used in this thesis work to describe microparticle acoustophoresis. The primary assumptions are listed in Table 2.2.

2.2.1 Piezoelectric actuation

A piezoelectric material transforms energy between electrical and mechanical forms such that an applied electric field generates mechanical stress and vice versa. At low voltages piezoelectric materials exhibit a linear relationship between electrical and mechanical energy and depending on the type of motion, scale of device, and material, it can be used to generate static and dynamic vibrations of up to hundreds of megahertz. Reviews on the use of piezoelectric transducers in acoustofluidics systems are given by Friend and Yeo [19] and in

Table 2.2: Primary theoretical assumptions used throughout the thesis.

Microchannel fluid	The microchannel contains a Newtonian and isotropic liquid.
Piezo transducer	The geometry and resonance modes of the piezoelectric transducer are not treated and we assume harmonic time dependence of the lowest -order acoustic fields in the liquid.
Low amplitudes	All acoustic amplitudes are low, i.e. the perturbation scheme is assumed to be valid.
Isentropic oscillations	The acoustic oscillations of the microchannel liquid are assumed to be isentropic (adiabatic and reversible) processes [40].
Microchip	The geometry of the silicon/glass microchip has no influence on the acoustic resonances inside the liquid-filled microchannel, and instead the chip is modeled as hard-walled boundary conditions for the acoustic eigenmodes of the liquid-filled microchannel.
Bulk acoustic waves	The waves are bulk acoustic waves (BAW), i.e. all forms of surface acoustic waves (SAW) are neglected.
Standing waves	The harmonic MHz actuation leads to the build-up of acoustic resonances sufficiently fast to neglect the transient acoustic waves.
Microparticles	All particles are spherical with radius a much smaller than the acoustic wavelength λ, i.e. $a \ll \lambda$.
Single microparticles	The particle suspensions are dilute enough to neglect any hydrodynamic as well as acoustic particle-particle interactions.
Viscosity	Viscosity is considered to be negligible in the bulk of the fluid, but non-negligible near solid surfaces such as particles and walls, where the fluid velocity gradients are large inside the viscous boundary layers.
Acoustic streaming	We only treat boundary-driven acoustic streaming and hence we neglect other types of acoustic streaming such as bulk attenuation-driven streaming and cavitation microstreaming around bubbles.
Constant parameters	The following parameters are assumed to be constant: • viscosity η, • heat conductivity k_th, • specific heats C_p and C_v, • compressibility κ, • thermal expansion α.
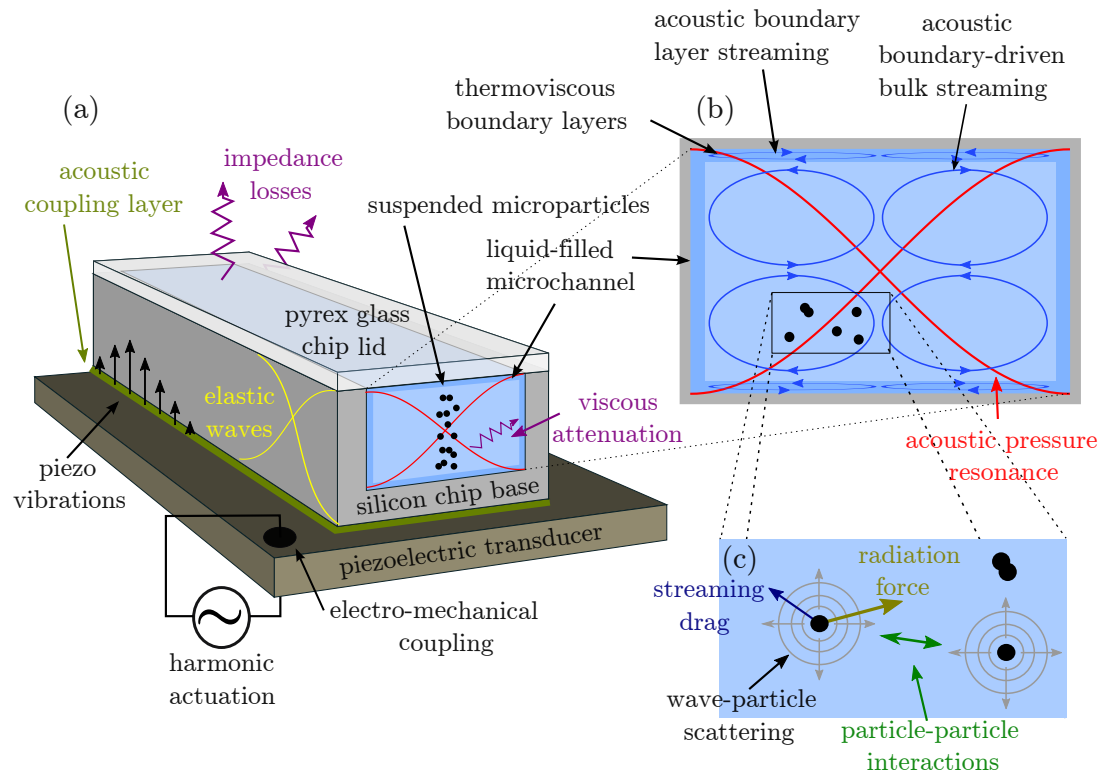
Figure 2.2: Sketch of the physics of acoustophoresis in our experimental model system shown in Fig. 2.1. (a) The microchip (gray) is attached to the piezo (brown) via an acoustic coupling layer (green). The piezo is driven harmonically at MHz frequencies giving rise to resonances building up in the bulk of the chip and inside the liquid-filled microchannel. (b) Zoom-in on the liquid-filled microchannel (light blue) with an imposed acoustic transverse standing half wave (red). The liquid oscillations must fulfill the no-slip condition at the solid walls resulting in the creation of a thin thermoviscous boundary layer (intermediate blue). Inside the boundary layer arise acoustic streaming rolls (dark blue) which drive acoustic streaming rolls in the bulk liquid (dark blue). (c) Microparticles (•) suspended in the channel is primarily subject to two forces (*i*) drag forces from the induced acoustic streaming and (*ii*) acoustic radiation forces emanating from the scattering of waves.

the tutorial paper by Dual and Möller [41] outlining the piezoelectric theory and its applicability when designing acoustofluidic devices.

As pointed out in the reviews, the electric actuation of the piezoelectric material is complicated, making model predictions difficult. In piezoelectric materials the mechanical and electrical behavior are coupled such that a change in electrical boundary conditions will change the material's mechanical behavior and vice versa, e.g. mechanical loading or damping of a piezoelectric material will tend to increase its electrical impedance. The mechanical loading depends on all connected device elements, and in our systems, in particular, the coupling glue layer between chip and transducer. This glue layer is often more or less of random homogeneity and thickness making theoretical predictions of the coupling difficult.

Moreover, theoretical predictions could also take into account the damping of the piezoelectric transducer due to the surrounding air and experimental platform on which it rests. On the other hand, due to the electromechanical coupling one can use electrical measurements like admittance curves to experimentally characterize acoustofluidics devices as described by Dual *et al.* [42]. Admittance curves can be used for e.g. detecting resonance frequencies if the system and transducer resonances match reasonably well [41].

In this work we do not try to predict the behavior of the piezoelectric element as this would require a better control of the actual coupling layer between chip and transducer and the damping from the experimental platform consisting of temperature control elements etc. should then be taken into account. Instead we simply assume that the liquid-filled microchannel experiences a harmonic acoustic actuation in its bulk, disregarding any boundary actuation effects which would be the result of a deeper analysis of the piezoelectric actuation and the mechanics of the solid chip materials. Furthermore, we assume the harmonic actuation to be of reasonably low amplitude[1] in order to apply a perturbation scheme in the mathematical analysis described in Chapter 3.

2.2.2   Ultrasound resonances

The microchip sketched in Fig. 2.2 forms an acoustic resonator implying that acoustic resonances occurs at specific frequencies f_j. Here a resonance is the tendency of the system to oscillate at greater amplitudes at some frequencies f_j than at other frequencies $f \neq f_j$, such that the acoustic energy density inside the resonator becomes several orders of magnitude larger at resonance. Besides oscillating at large amplitudes, the resonance modes are usually both stable and reproducible and their spatial pattern are set by the geometry of the system [43]. Hence, the piezoelectric transducer is operated at frequencies f close to the system's resonance frequencies f_j and as close as possible to the resonances of the piezo to allow optimal coupling of the transmitted acoustic energy. The microchannel in the experimental model system is therefore designed to support a horizontal transverse resonance at 2 MHz, which is the resonance frequency of the piezo.

To understand this type of systems it is important to avoid thinking in terms of traveling waves. For example, in glass a 2-MHz ultrasound wave propagates for around 200 µs corresponding to a length of 1.1 m before it dies out due to intrinsic attenuation. Thus, in our mm-sized microchip this wave experiences ∼1000 reflections and the spatial pattern of a resonance mode is therefore set by the geometry and frequency rather than the spatial behavior of the actuation.

The precise frequency of a desired microchannel resonance mode depends on the whole surrounding system and the coupling to the piezo. Such models are described in the recent tutorial by Dual and Möller [41], where they establish a

---

[1]Using the Ferroperm Piezoelectric calculator (http://www.ferroperm-piezo.com/) we obtain a 7-nm actuation amplitude when exciting an unloaded 35 mm×5 mm×1 mm-large Pz26 element at 20 V peak-to-peak voltage.

numerical model integrating the piezoelectric theory with the elastic wave theory for the solid chip materials [9, 44], and the acoustic fluid waves inside the microchannel [43, 45]. However, such fully-integrated models are numerically time-consuming for realistic system dimensions and furthermore some experimental conditions, such as the coupling glue layer thickness and homogeneity, are too ill-defined.

In this work we will use first-order linear fluid theory to analyze the acoustic resonances (eigenmodes) of the microchannel and represent the surrounding chip by approximate boundary conditions. Furthermore, the bulk viscous (and thermal) attenuation is negligible and we therefore treat inviscid bulk acoustics [43]. Contrary in the bulk liquid, viscosity does play a significant role near the solid boundaries where the fluid must satisfy the no-slip velocity condition resulting in the presence of a sub-µm-thin thermoviscous boundary layer containing large fluid velocity gradients [45].

2.2.3 Non-linear effects

As sketched in Fig. 2.2 the acoustic resonances in the fluid drive two non-linear effects known as acoustic streaming and acoustic radiation forces. While the linear effects of the acoustic resonance time averages to zero (average over one period of harmonic oscillation, typically ~ 1 µs), the non-linear effects lead to non-zero time-averaged forces on the fluid and the suspended particles.

2.2.3.1 Acoustic streaming

Acoustic streaming is the generation of flow from sound and is a well-known phenomenon within the studies of acoustics. Acoustic streaming appears in different forms, but common to all of them is the appearance of a steady fluid flow driven by viscous attenuation of acoustic waves. In viscous fluids the viscous attenuation causes a net displacement of fluid particles resulting in streaming flows. For an ideal inviscid fluid the small acoustic oscillations of the fluid are reversible and hence the time-average net flow is zero.

In acoustofluidic systems the viscous attenuation driving the streaming often takes place in either the bulk fluid or in the viscous boundary layers near solid walls. Other forms are the cavitation microstreaming driven by bubble oscillations [46] and streaming driven in surface acoustic wave systems [47]. In this work we deal only with boundary-induced acoustic streaming as we treat bulk acoustic waves in a system with ideally no bubbles and a length scale much smaller than the viscous attenuation length required for bulk-induced streaming [11]. For more information on the applications of the different forms of streaming in microsystems, the reader is referred to Refs. [11, 47], while a more thorough theoretical review can be found in Refs. [48–50]. To clarify, in this thesis we only consider boundary-induced acoustic streaming and the term *acoustic streaming* refers to this streaming form only.

Boundary-induced acoustic streaming is a steady rotational motion of an oscillating fluid close to a solid boundary. At the solid boundaries the oscillating fluid velocity must go to zero to fulfill the no slip condition from molecular forces between the solid boundary and the molecules of the fluid. This decay of the oscillating fluid velocity happens on a length scale denoted the viscous acoustic boundary layer thickness δ. For a standing wave parallel to a solid plane boundary, the viscous attenuation drives a momentum flux close to the boundary from the pressure antinodes to the pressure nodes [47] resulting in a steady vorticity inside the viscous boundary layer termed inner streaming rolls (also Schlichting rolls), which were first treated by Schlichting in 1932 based on Prandtl's boundary-layer theory [51]. The inner streaming rolls drive the counter-rotating streaming rolls in the bulk fluid referred to as the outer streaming rolls (or Rayleigh rolls), which were first described theoretically by Rayleigh in 1884, who derived the expression for the fluid slip velocity just outside the viscous boundary layer [52]. Both the inner and outer streaming rolls are sketched in Fig. 2.2.

2.2.3.2   Acoustic radiation forces

The acoustic radiation force is the key parameter in most acoustofluidic applications and in particular when dealing with acoustic particle and cell manipulation. The acoustic radiation force arises from scattering of the acoustic waves on particles suspended in a fluid with an imposed acoustic field. This scattering causes a momentum transfer from the acoustic wave to the suspended particles resulting in a net radiation force that cause a migration of the particles relative to the suspending fluid.

2.2.4   Acoustophoretic particle motion

As illustrated in Fig. 2.2(c) particles suspended in the liquid inside the microchannel are influenced by the acoustic actuation as they become subject to streaming-induced drag forces from the suspending liquid and the acoustic radiation forces acting directly on them due to scattering. Throughout the thesis, we base our analysis on these two effects. We neglect any particle-particle effects, hydrodynamic as well as acoustic. Regarding the hydrodynamic interactions, Mikkelsen and Bruus [53] reported that hydrodynamic effects become significant for inter-particle distances below 2 particle diameters and hence we will keep the experiments well above this threshold. The acoustically induced inter-particle effects arise from waves that scatters from one particle onto another and hence it is often denoted the secondary radiation force or Bjerknes forces. However, for solid particles (and not bubbles) the Bjerknes forces are negligible in comparison to the primary radiation force and the hydrodynamic particle-particle effects [54]. A primary assumption is therefore that we consider particle suspensions such dilute that particle-particle effects are negligible. Also, where not otherwise stated, the influence of the walls on the viscous drag coefficients is neglected.

2.3   Concluding remarks

This chapter introduced the experimental model system that forms the basis for the analyses in the thesis. With the experimental model system in focus, the phenomena arising from acoustic actuation were introduced and in Table 2.2 the primary theoretical assumptions were summarized and used to establish the theoretical framework presented in the next Chapter 3.

Chapter 3

Theory of acoustophoresis

In this chapter the theoretical framework for the thesis is introduced, namely the theory of the involved physics and approximations described in the former Chapter 2. The presented theory is classical and well known dating back to the time of Helmholtz and Lord Rayleigh, and the approach presented here is inspired mainly by Landau and Lifshitz [45, 55], Pierce [40], and Bruus [43, 56].

Vectors, tensors, and derivatives

All symbols and acronyms are listed in the List of Symbols and Acronyms on page xiv. However, parts of the notation require a little more description:

Vectors and tensors. Vectors are represented as bold symbols or by index notation and the Einstein summation convention, e.g., v_i, where i is the i'th spatial vector component (x, y, and z) and where repeated indices indicate a summation over the index. Especially, we mostly represent tensors using the index notation for clarity about which index a given operater acts on.

Derivatives. Derivatives are represented by the short notation, i.e. $\partial_i \equiv \frac{\partial}{\partial i}$.

3.1 Governing equations of a thermoviscous fluid

We study the motion of a Newtonian fluid. The fluid is regarded as a continuous medium, i.e. we consider the motion of fluid particles that contain a large number of molecules (continuum hypothesis). In order to describe this motion, we use the Eulerian description of any fluid field $F = F(\boldsymbol{r}, t)$, i.e., the position $\boldsymbol{r}$ and time t are independent variables.

The state of a moving, compressible, and thermoviscous fluid is completely determined by the three components of the fluid velocity $\boldsymbol{v}$, and any two of the thermodynamic quantities, e.g., the temperature T and the pressure p [45]. All

the remaining thermodynamic quantities are thus to be determined through the equations of state. The mathematical description of the state of the moving fluid is therefore fully described by the equations of conservation of mass, momentum and energy.

Conservation of mass. The mass conservation equation of the fluid is the continuity equation [45]

$$\partial_t \rho = -\boldsymbol{\nabla} \cdot (\rho \boldsymbol{v}), \tag{3.1}$$

where ρ is the fluid mass density. In this thesis we deal with acoustics which is essentially propagation of compression and decompression, hence the fluid is treated as compressible $\boldsymbol{\nabla} \cdot \boldsymbol{v} \neq 0$.

Conservation of momentum. The equation for conservation of momentum is the Navier–Stokes equation [45]

$$\rho \left[\partial_t v_i + (v_j \partial_j) v_i \right] = -\partial_i p + \partial_j \sigma'_{ij}, \tag{3.2}$$

where we have neglected any external forces, and where we have introduced the viscous stress tensor $\boldsymbol{\sigma}'$ with the ij'th component

$$\sigma'_{ij} = \eta \left(\partial_j v_i + \partial_i v_j \right) + (\beta - 1)\eta \left(\partial_k v_k \right) \delta_{ij}. \tag{3.3}$$

Here δ_{ij} is the Kronecker delta and η is the fluid dynamic viscosity. Moreover, we have introduced the compressional viscosity ratio $\beta = \zeta/\eta + 1/3$, where ζ is the so-called second coefficient of viscosity, also called the bulk viscosity or expansion viscosity (losses due to compression and expansion of the fluid). In this work we use $\zeta = 0 \ \Rightarrow \ \beta = 1/3$ as of simple liquids [57].

Conservation of energy. The law of conservation of energy is governed by the so-called heat-transfer equation [45]

$$\partial_t \left(\tfrac{1}{2}\rho v^2 + \rho\epsilon \right) = -\boldsymbol{\nabla} \cdot \left[\boldsymbol{v} \left(\tfrac{1}{2}\rho v^2 + \rho\epsilon + p \right) - \boldsymbol{v} \cdot \boldsymbol{\sigma}' - k_{\text{th}} \boldsymbol{\nabla} T \right], \tag{3.4}$$

where ϵ is the internal energy per unit mass, T is the temperature, and k_{th} is the thermal conductivity. In terms of the entropy per unit mass s, the equation can be rewritten as [45]

$$\rho T \left[\partial_t s + (\boldsymbol{v} \cdot \boldsymbol{\nabla}) s \right] = \sigma'_{ik} \partial_i v_k + \boldsymbol{\nabla} \cdot (k_{\text{th}} \boldsymbol{\nabla} T). \tag{3.5}$$

Defining constants. As described in the assumptions in Table 2.2 we neglect any spatial variations in the fluid viscosities η and thermal conduction k_{th} as well as any variations in the fluid's compressibility κ, speed of sound c, heat capacities C_p and C_v, and thermal expansion α. However, for second-order acoustics, it turns out that the variations in viscosity with temperature plays a significant role for, e.g. acoustic streaming, as discussed in Section 3.4 and Ref. [58]. With constant viscosity and thermal conductivity, the governing equations of conservation become

$$\partial_t \rho = -\boldsymbol{\nabla} \cdot (\rho \boldsymbol{v}), \tag{3.6a}$$

$$\rho \left[\partial_t \boldsymbol{v} + (\boldsymbol{v} \cdot \boldsymbol{\nabla}) \boldsymbol{v} \right] = -\boldsymbol{\nabla} p + \eta \nabla^2 \boldsymbol{v} + \beta \eta \boldsymbol{\nabla} (\boldsymbol{\nabla} \cdot \boldsymbol{v}), \tag{3.6b}$$

$$\rho T \left[\partial_t s + (\boldsymbol{v} \cdot \boldsymbol{\nabla}) s \right] = \sigma'_{ik} \partial_i v_k + k_{\text{th}} \nabla^2 T. \tag{3.6c}$$

3.1.1 Thermodynamic relations

We describe the thermodynamic quantities by means of the temperature T and the pressure p, and thus we can describe the changes in the density $\rho = \rho\left(T, p\right)$ and entropy per mass $s = s\left(T, p\right)$ as

$$\mathrm{d}\rho = \left(\partial_T \rho\right)_p \mathrm{d}T + \left(\partial_p \rho\right)_T \mathrm{d}p, \tag{3.7a}$$

$$\mathrm{d}s = \left(\partial_T s\right)_p \mathrm{d}T + \left(\partial_p s\right)_T \mathrm{d}p. \tag{3.7b}$$

Here, $\left(\partial_p \rho\right)_T = \gamma \left(\partial_p \rho\right)_s = \left(\gamma/c^2\right) = \gamma \rho \kappa$, where $\gamma = C_p/C_v$ is the ratio of the specific heats C_p at constant pressure and C_v at constant volume, $1/c^2 = \left(\partial_p \rho\right)_s$ is one over the square of the isentropic speed of sound, and $\kappa = 1/\left(\rho c^2\right)$ is the isentropic compressibility [40]. Further, we use the definition of the isobaric thermal expansion $\alpha = -\left(1/\rho\right)\left(\partial_T \rho\right)_p$ to write $\left(\partial_T \rho\right)_p = -\alpha \rho$, the definition of the specific heat C_p to get $\left(\partial_T s\right)_p = C_p/T$ and lastly the Maxwell relation $\left(\partial_p s\right)_T = -\left[\partial_T \left(\frac{1}{\rho}\right)\right]_p = -\left(\alpha/\rho\right)$ [55]. We thus end up with the two general thermodynamic identities

$$\mathrm{d}\rho = \gamma \rho \kappa \, \mathrm{d}p - \alpha \rho \, \mathrm{d}T, \tag{3.8a}$$

$$\mathrm{d}s = \frac{C_p}{T} \, \mathrm{d}T - \frac{\alpha}{\rho} \, \mathrm{d}p. \tag{3.8b}$$

In the isentropic case $\mathrm{d}s = 0$, the identities reduce to

$$\mathrm{d}p = \frac{\rho C_p}{\alpha T} \mathrm{d}T = c^2 \mathrm{d}\rho, \tag{3.9}$$

where we have used the thermodynamic identity [55]

$$\gamma = \frac{T\alpha^2}{\rho C_p \kappa} + 1. \tag{3.10}$$

3.1.2 Perturbation scheme

As described in Table 2.2, we assume an acoustic wave to constitute tiny perturbations to a zeroth-order state of the liquid. At its zeroth-order state the liquid is homogeneous, quiescent, and in thermal equilibrium, such that the zeroth-order fields become T_0, p_0, $\boldsymbol{v}_0 = \boldsymbol{0}$, ρ_0, and s_0. By taking first- and second-order perturbations (subscript 1 and 2, respectively) into account, we write the perturbation series as

$$p = p_0 + p_1 + p_2, \quad \boldsymbol{v} = \boldsymbol{0} + \boldsymbol{v}_1 + \boldsymbol{v}_2, \quad T = T_0 + T_1 + T_2, \tag{3.11a}$$

$$\rho = \rho_0 + \rho_1 + \rho_2, \quad s = s_0 + s_1 + s_2, \tag{3.11b}$$

where the perturbation parameter is implicitly assumed, i.e. $T_0 \gg T_1 \gg T_2$.

3.1.3   Thermoviscous first-order equations

To first order in the acoustic perturbations we use the thermodynamic identities in Eqs. (3.8a) and (3.8b) to eliminate ρ_1 and s_1 resulting in the following expressions for the continuity equation expressed in terms of p_1, the Navier–Stokes equation for $\boldsymbol{v}_1$, and the thermodynamic heat-transfer equation for T_1

$$\partial_t p_1 = \frac{1}{\gamma\kappa}\left(\alpha\partial_t T_1 - \boldsymbol{\nabla}\cdot\boldsymbol{v}_1\right), \tag{3.12a}$$

$$\rho_0\partial_t\boldsymbol{v}_1 = -\boldsymbol{\nabla}p_1 + \eta\nabla^2\boldsymbol{v}_1 + \beta\eta\boldsymbol{\nabla}\left(\boldsymbol{\nabla}\cdot\boldsymbol{v}_1\right), \tag{3.12b}$$

$$\partial_t T_1 = D_{\text{th}}\nabla^2 T_1 + \frac{\alpha T_0}{\rho_0 C_p}\partial_t p_1, \tag{3.12c}$$

where we have introduced the thermal diffusivity

$$D_{\text{th}} = \frac{k_{\text{th}}}{\rho_0 C_p}. \tag{3.13}$$

As outlined in Chapter 2 we assume all first-order fields to be harmonic in time, i.e. $F(\boldsymbol{r},t) = F(\boldsymbol{r})\exp(-\mathrm{i}\omega t)$. We get $\partial_t p_1 = -\mathrm{i}\omega p_1$ and we can eliminate p_1 from Eq. (3.12)

$$\mathrm{i}\omega\boldsymbol{v}_1 + \nu\nabla^2\boldsymbol{v}_1 + \left[\nu\beta + \frac{\mathrm{i}}{\gamma\rho_0\kappa\omega}\right]\boldsymbol{\nabla}\left(\boldsymbol{\nabla}\cdot\boldsymbol{v}_1\right) = \frac{\alpha}{\gamma\rho_0\kappa}\boldsymbol{\nabla}T_1, \tag{3.14a}$$

$$\mathrm{i}\omega T_1 + \gamma D_{\text{th}}\nabla^2 T_1 = \frac{\gamma-1}{\alpha}\boldsymbol{\nabla}\cdot\boldsymbol{v}_1. \tag{3.14b}$$

From Eq. (3.14) arise the thermal and the viscous boundary layer thicknesses δ_{th} and δ [45], respectively (values for 2-MHz ultrasound waves in water at $25\,°\mathrm{C}$),

$$\delta_{\text{th}} = \sqrt{\frac{2\gamma D_{\text{th}}}{\omega}} = 0.15\,\mu\mathrm{m}, \tag{3.15a}$$

$$\delta = \sqrt{\frac{2\nu}{\omega}} = 0.38\,\mu\mathrm{m}. \tag{3.15b}$$

These are the length scales over which the acoustic fields change from their values in the bulk to their values at rigid boundaries.

3.1.4   Isentropic first-order equations

Throughout the thesis (except Chapter 4) we assume the acoustic oscillations to be isentropic, such that $\mathrm{d}s = 0$ [40] and Eq. (3.12) reduces to

$$\rho_0\partial_t\boldsymbol{v}_1 = -\boldsymbol{\nabla}p_1 + \eta\nabla^2\boldsymbol{v}_1 + \beta\eta\boldsymbol{\nabla}\left(\boldsymbol{\nabla}\cdot\boldsymbol{v}_1\right), \tag{3.16a}$$

$$\frac{1}{c^2}\partial_t p_1 = -\rho_0\boldsymbol{\nabla}\cdot\boldsymbol{v}_1, \tag{3.16b}$$

$$\rho_1 = \frac{1}{c^2}p_1, \tag{3.16c}$$

$$T_1 = \frac{\alpha T_0}{\rho_0 C_p}p_1. \tag{3.16d}$$

Thus, we can solve Eqs. (3.16a) and (3.16b) for $\boldsymbol{v}_1$ and p_1, and ρ_1 and T_1 are then given by inserting p_1 into Eqs. (3.16c) and (3.16d), respectively.

3.1.4.1   Acoustic wave equation

If we take the time derivative of Eq. (3.16b) and insert Eq. (3.16a) we obtain for p_1 the acoustic wave equation (with an extra term due to viscous attenuation)

$$\frac{1}{c^2}\partial_t{}^2 p_1 = \left[1 - \frac{(1+\beta)\,\eta}{\rho_0 c^2}\partial_t\right]\nabla^2 p_1. \tag{3.17}$$

Further, with the harmonic time dependence of p_1 we get the so-called lossy Helmholtz wave equation

$$\nabla^2 p_1 = -k^2\left(1 + \mathrm{i}\gamma_{\mathrm{att}}\right)p_1, \tag{3.18a}$$

$$\gamma_{\mathrm{att}} = \frac{(1+\beta)\,\eta\omega}{2\rho_0 c^2}, \tag{3.18b}$$

where we have introduced the wavenumber $k = \omega/c$ and the viscous damping coefficient γ_{att} which is assumed to be small since $\gamma_{\mathrm{att}} \approx 10^{-6}$ for 2-MHz ultrasound oscillations in water at $25\,°\mathrm{C}$. Possible solutions to the lossy Helmholtz wave equation are damped plane waves

$$p_1\left(\boldsymbol{r}, t\right) = p_{\mathrm{a}}\mathrm{e}^{\mathrm{i}(\boldsymbol{k}\cdot\boldsymbol{r} - \omega t)}\mathrm{e}^{-\gamma_{\mathrm{att}}\boldsymbol{k}\cdot\boldsymbol{r}}, \tag{3.19}$$

where p_{a} is the undamped amplitude of the wave and where the real exponential term with γ_{att} constitutes the damping of the wave. The characteristic damping length $1/\left(\gamma_{\mathrm{att}}k\right) \approx 36\,\mathrm{m}$ is very long for our microfluidic system and hence we neglect all bulk viscous attenuation. Thus, in the invicid case Eq. (3.17) reduces to the wave equation $\nabla^2 p_1 = (1/c^2)\partial_t^2 p_1$ with the general 1D solution $p_1 = p_1\left(x \pm ct\right)$ showing that c is indeed the (isentropic) speed of sound of the fluid. The inviscid case further leads to $\boldsymbol{v}_1$ being irrotational and hence being the gradient of a potential $\boldsymbol{v}_1 \equiv \boldsymbol{\nabla}\phi$, and we can relate the velocity $\boldsymbol{v}_1$, the pressure p_1, density ρ_1, and the temperature T_1 as

$$\boldsymbol{v}_1 = -\frac{\mathrm{i}}{\rho_0\omega}\boldsymbol{\nabla}p_1 = -\frac{\mathrm{i}c^2}{\rho_0\omega}\boldsymbol{\nabla}\rho_1 = -\frac{\mathrm{i}c^2 C_p}{\omega\alpha T_0}\boldsymbol{\nabla}T_1. \tag{3.20}$$

3.1.5   Second-order equations

In the linear first-order theory all fields are harmonically varying in time resulting in no time-average contribution. Therefore in order to obtain time-averaged effects we go to the second-order perturbations, where we for simplicity neglect the second-order temperature T_2 and stay in the isentropic regime. Hence, we are left with the time-averaged second-order continuity equation and Navier–Stokes equation [59]

$$\rho_0\boldsymbol{\nabla}\cdot\langle\boldsymbol{v}_2\rangle = -\boldsymbol{\nabla}\cdot\langle\rho_1\boldsymbol{v}_1\rangle, \tag{3.21a}$$

$$\eta\nabla^2\langle\boldsymbol{v}_2\rangle + \beta\eta\boldsymbol{\nabla}\left(\boldsymbol{\nabla}\cdot\langle\boldsymbol{v}_2\rangle\right) - \langle\boldsymbol{\nabla}p_2\rangle = \langle\rho_1\partial_t\boldsymbol{v}_1\rangle + \rho_0\langle\left(\boldsymbol{v}_1\cdot\boldsymbol{\nabla}\right)\boldsymbol{v}_1\rangle. \tag{3.21b}$$

Notice that the products of first-order fields act as source terms for the second-order fields $\boldsymbol{v}_2$ and p_2. The second-order pressure p_2 contributes to the acoustic radiation forces and the second-order velocity $\boldsymbol{v}_2$ is responsible for the acoustic streaming as described later in Sections 3.3 and 3.4, respectively.

3.1.6 Acoustic energy density

The acoustic energy density is an essential parameter in microparticle acoustophoresis as it sets the scale for the acoustic radiation forces and streaming flows. The energy transported with acoustic waves is composed of the kinetic energy of the moving fluid elements and the potential energy of the compressed fluid. The kinetic energy density is given by the standard formulation $E_{\mathrm{kin}} = (1/2)\rho_0 v_1^2$, while the potential energy density is derived from the energy stored due to compression and expansion $E_{\mathrm{pot}} = -\int_{V_0}^{V}(p_1/V)\mathrm{d}V = (1/2)\kappa p_1^2$ [60]. Hence, the total time-averaged acoustic energy density $E_{\mathrm{ac}}(\boldsymbol{r})$ becomes

$$E_{\mathrm{ac}}(\boldsymbol{r}) = \frac{1}{2}\rho_0\langle v_1^2\rangle + \frac{1}{2}\kappa\langle p_1^2\rangle = \frac{1}{4}\left(\rho_0 v_1^2 + \kappa p_1^2\right), \tag{3.22}$$

where we have used the relation of the time average of the product of two time-harmonic fields $\langle A(t)B(t)\rangle = \frac{1}{2}\mathrm{Re}\left\{A(0)\bar{B}(0)\right\}$, where the bar represents complex conjugation.

3.2 Resonances

As discussed in Chapter 2 the resonances in the microchannel of our experimental model system depends on the actuation of the piezo, the coupling glue layer between piezo and chip, the mechanical loading of the piezo, and the chip and channel materials and geometries. In this work, however, we use a simple model to describe the resonances inside the liquid-filled microchannel neglecting any interaction with the bulk chip and the spatial behavior of the piezo actuation.

Mathmatically, resonance means that a system gets into its eigenmode where the acoustic energy density becomes unbounded, but if small losses are present the energy density will be bounded but be very large. In the following we study the eigenmodes for the liquid-filled microchannel and describe the associated resonance spectrum.

3.2.1 Eigenmodes for a liquid rectangular cuboid

In the following we model the liquid-filled microchannel of experimental model system as a liquid-filled rectangular cuboid where its boundary conditions represent the surrounding chip. Furthermore, we presume that the chip materials are
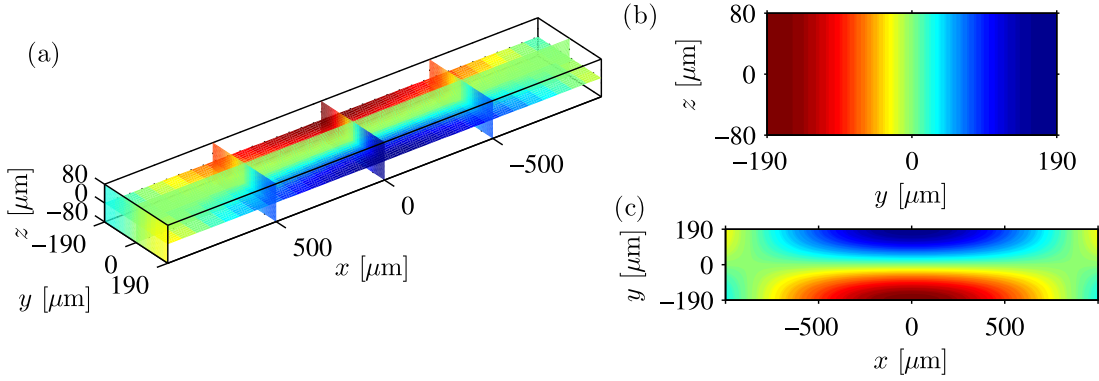
Figure 3.1: Pressure eigenmode p_1 (from p_a (dark red) to $-p_a$ (dark blue)), Eq. (3.24), for a liquid rectangular cuboid surrounded by infinitely hard walls and dimensions similar to the microchannel in the experimental model system, Fig. 2.1. The eigenmode has $\left(n_x, n_y, n_z\right) = (20, 1, 0)$ and only the channel fraction of 2 mm around $x = 0$ is shown. (a) 3D slice plot of the eigenmode p_1. (b) The eigenmode pressure in the vertical yz microchannel cross section at $x = 0$. (c) The eigenmode pressure in the horizontal xy plane at channel mid height $z = 0$.

acoustically infinitely hard in comparison to the liquid channel[1] to apply hard wall conditions at all boundaries, i.e. $\boldsymbol{n} \cdot \boldsymbol{\nabla} p|_{y=\pm w/2} = \boldsymbol{n} \cdot \boldsymbol{\nabla} p|_{z=\pm h/2} = \boldsymbol{n} \cdot \boldsymbol{\nabla} p|_{x=\pm L/2} = 0$. By solving the Helmholtz wave equation Eq. (3.18a) ($\gamma_{\mathrm{att}} = 0$) with these conditions, we get the following eigenfrequencies

$$f_{n_x, n_y, n_z} = \frac{c_0}{2} \sqrt{\frac{n_x^2}{l^2} + \frac{n_y^2}{w^2} + \frac{n_z^2}{h^2}}, \quad \text{with } n_x, n_y, n_z = 0, 1, 2, 3, \ldots, \qquad (3.23)$$

where the three indexes n_x, n_y, n_z are the number of half-wavelengths along x, y, and z, respectively. The corresponding eigenfunction p_1 becomes

$$p_1(x, y, z) = p_a \cos\left[k_x\left(x + \frac{L}{2}\right)\right] \cos\left[k_y\left(y + \frac{w}{2}\right)\right] \cos\left[k_z\left(z + \frac{h}{2}\right)\right], \quad (3.24)$$

where p_a is the pressure amplitude and where $k_j = n_j \pi / L_j$ is the wavenumber in each of the three spatial directions.

In Fig. 3.1 we plot the $(20, 1, 0)$-mode for the microchannel dimensions of the experimental model system but only for a section along x of 2 mm around the channel center $x = 0$. In most of the analyses throughout the thesis we assume $n_x < 20$ and hence within a microscope field of view smaller than $900\,\mu\text{m}$ we deal with a nearly purely transversal mode as described by

$$p_1 = p_a \cos\left[k_y\left(y + \frac{w}{2}\right)\right]. \qquad (3.25)$$

---

[1]For a silicon/water interface modelled as a liquid-liquid interface the reflection coefficient becomes $R = (Z_{\mathrm{si}} - Z_{\mathrm{wa}})/(Z_{\mathrm{si}} + Z_{\mathrm{wa}}) \approx 86\,\%$, where $Z_n = \rho_n c_n$ is the characteristic impedance of the material n as listed in the List of Material Parameters on page xvi [60].

By inserting Eq. (3.25) into Eq. (3.22) we get the 1D acoustic energy density E_{ac} for the purely transverse mode

$$E_{\text{ac}} = \frac{p_{\text{a}}^2}{4\rho_0 c_0^2} = \frac{1}{4}\kappa_0 p_{\text{a}}^2 = \frac{1}{4}\rho_0 v_{\text{a}}^2, \tag{3.26}$$

where $\kappa_0 = 1/\left(\rho_0 c_0^2\right)$ is the fluid compressibility and where v_{a} is the amplitude of the oscillation velocity.

3.2.2 Resonance spectra

As for the harmonic oscillator and as described in Ref. [43] we can to a good approximation describe an acoustic resonance by Lorentzian line shapes close to its resonance frequency f_0, i.e. the acoustic energy density E_{ac} for f sufficiently close to f_0 becomes

$$E_{\text{ac}}(f) = \frac{E_0}{\left[\frac{2Q}{f_0}\left(f - f_0\right)\right]^2 + 1}, \tag{3.27}$$

where $Q = f_0/\Delta f_0 = 1/\left(2\gamma_{\text{damp}}\right)$ is the resonance quality factor, γ_{damp} is the damping coefficient, and where Δf_0 is the full width at half maximum of the resonance such that $E_{\text{ac}}\left(f_0 \pm \Delta f_0/2\right) = E_0/2$.

3.3 Acoustic radiation force on a microparticle

The acoustic radiation force was treated theoretically by King in 1934 for the case of incompressible particles suspended in an inviscid fluid [61] and in 1955 this analysis was extended to the case of compressible particles by Yosioka and Kawasima [62]. In 1962 these results were summarized and generalized by Gorkov resulting in a formulation for the acoustic radiation force acting on compressible particles suspended in an inviscid fluid with an imposed acoustic field of wavelength λ much longer than the particle radius a [63]. Recently, following the approach of Gorkov, Settnes and Bruus extended the analysis to include the viscosity of the suspending fluid [64].

In this section we present the theoretical expression for the acoustic radiation force acting on a compressible, spherical, small particle of radius a freely suspended in a viscous fluid with an imposed acoustic field of wavelength λ much longer than a. For more information on the derivation of the force expressions the reader is referred to Refs. [54, 64, 65] for a thorough mathematical treatment, while the force is derived based on scaling arguments in Ref. [66].

3.3.1 General viscous expression

A small particle suspended in a fluid with an imposed acoustic field will act as a weak point scatterer which motivates the use of first-order scattering theory.

Therefore, if the incoming and scattered waves are sufficiently weak, the total first-order acoustic field is given by the sum of the two. Thus, for a given incoming field, knowing the scattered field will give the momentum transferred to the particle from the wave. The time-averaged force $\boldsymbol{F}^{\mathrm{rad}}$ on the particle is therefore equal to the average flux of momentum through any closed surface $\partial\Omega$ that encloses the particle. The fluid viscosity is negligible in the far-field (far from the viscous boundary layer surrounding the particle) and hence the average flux is the sum of the time-average second-order pressure $\langle p_2 \rangle$ and the momentum flux tensor $\rho_0 \langle \boldsymbol{v}_1 \boldsymbol{v}_1 \rangle$, and $\boldsymbol{F}^{\mathrm{rad}}$ becomes

$$\boldsymbol{F}^{\mathrm{rad}} = -\int_{\partial\Omega} \mathrm{d}a \, \left[\langle p_2 \rangle \boldsymbol{n} + \rho_0 \langle \boldsymbol{n} \cdot \boldsymbol{v}_1 \rangle \boldsymbol{v}_1 \right]. \tag{3.28}$$

As $\langle p_2 \rangle$ can be written in terms of the first-order field for the inviscid case of Eq. (3.21b), the rest of the derivation simply relies on determining the first-order scattered fields. Briefly, the scattering is weak and we neglect higher-order scattering terms resulting in a single monopole term and a single dipole term. The monopole describes a compressible and stationary particle that causes scattering because of compressibility differences between particle and fluid, while the dipole expresses a moving, incompressible particle resulting in scattering due to the density difference between particle and fluid. The scattering coefficients are found by matching the first-order pressure and velocity of the fluid with the proper boundary conditions in the near-field of the particle, where viscosity does play a role because of the viscous boundary layer surrounding the particle. In result, the time-averaged acoustic radiation force $\boldsymbol{F}^{\mathrm{rad}}$ on a single small spherical particle of radius a, density ρ_{p}, and compressibility κ_{p} in a viscous fluid is given by [64]

$$\boldsymbol{F}^{\mathrm{rad}} = -\pi a^3 \left\{ \frac{2\kappa_0}{3} \mathrm{Re} \left[\bar{f}_1 \bar{p}_1 \boldsymbol{\nabla} p_1 \right] - \rho_0 \mathrm{Re} \left[\bar{f}_2 \bar{\boldsymbol{v}}_1 \cdot \boldsymbol{\nabla} \boldsymbol{v}_1 \right] \right\}, \tag{3.29}$$

where the prefactors f_1 and f_2 are given by

$$f_1 \left(\tilde{\kappa} \right) = 1 - \tilde{\kappa}, \quad \text{with} \quad \tilde{\kappa} = \frac{\kappa_{\mathrm{p}}}{\kappa_0}, \tag{3.30a}$$

$$f_2 \left(\tilde{\rho}, \tilde{\delta} \right) = \frac{2 \left[1 - \Gamma\left(\tilde{\delta} \right) \right] \left(\tilde{\rho} - 1 \right)}{2\tilde{\rho} + 1 - 3\Gamma\left(\tilde{\delta} \right)}, \quad \text{with} \quad \tilde{\rho} = \frac{\rho_{\mathrm{p}}}{\rho_0}, \tag{3.30b}$$

$$\Gamma\left(\tilde{\delta} \right) = -\frac{3}{2} \left[1 + \mathrm{i} \left(1 + \tilde{\delta} \right) \right] \tilde{\delta}, \quad \text{with} \quad \tilde{\delta} = \frac{\delta}{a}. \tag{3.30c}$$

In Eq. (3.29) the first term with prefactor f_1 arises from the monopole scattering, while the second term with prefactor f_2 arises from the dipole scattering. Note that viscosity only give a significant correction for a particle with density ρ_{p} differing greatly from the density ρ_0 of the suspending fluid resulting in viscosity being negligible for near-neutral buoyancy particles.

3.3.2   Standing wave

In the case of a standing wave the spatial part of p_1 and v_1 is real and the radiation force expressed in Eq. (3.29) becomes a gradient force of the form

$$\boldsymbol{F}^{\mathrm{rad}} = -\boldsymbol{\nabla}U^{\mathrm{rad}}, \tag{3.31a}$$

$$U^{\mathrm{rad}} = \frac{4\pi}{3}a^3\left[f_1\frac{\kappa_0}{2}\langle p_1^2\rangle - \mathrm{Re}\,[f_2]\,\frac{3\rho_0}{4}\langle v_1^2\rangle\right], \tag{3.31b}$$

where U^{rad} is the force potential which for $\tilde{\delta} = 0$ reduces to the classical inviscid expression by Gorkov [63].

3.3.2.1   Transverse one-dimensional wave

For the special case of the horizontal transverse pressure resonance, Eq. (3.25), the radiation force reduces to [62]

$$F^{\mathrm{rad}} = 4\pi a^3 \Phi\left(\tilde{\kappa}, \tilde{\rho}, \tilde{\delta}\right) k_y E_{\mathrm{ac}} \sin\left[2k_y\left(y + \frac{w}{2}\right)\right], \tag{3.32}$$

where

$$\Phi\left(\tilde{\kappa}, \tilde{\rho}, \tilde{\delta}\right) = \frac{1}{3}f_1\left(\tilde{\kappa}\right) + \frac{1}{2}\mathrm{Re}\left[f_2\left(\tilde{\rho}, \tilde{\delta}\right)\right] \tag{3.33}$$

is the so-called acoustic contrast factor. In this work we treat light polymer particles making the viscous radiation force corrections negligible as we find $\left|\Phi\left(\tilde{\kappa}, \tilde{\rho}, \tilde{\delta}\right)/\Phi\left(\tilde{\kappa}, \tilde{\rho}, 0\right) - 1\right| < 0.4\,\%$.

3.4   Boundary-induced acoustic streaming

As described in Chapter 2 the boundary-induced acoustic streaming is driven by viscous attenuation inside the viscous boundary layer of thickness $\delta = \sqrt{2\nu/\omega}$. In the following we present the result of Rayleigh followed by the more recent results of Muller, Rednikov, and Sadhal.

3.4.1   Parallel-plate channel with $\lambda \gg h \gg \delta$

In 1884 Lord Rayleigh published his now classical expression for the boundary-driven acoustic streaming velocity $\langle\boldsymbol{v}_2\rangle$ in an infinite parallel-plate channel of height h imposed with a first-order bulk velocity field having a horizontal y-component of the form $v_{1y} = v_{\mathrm{a}}\sin\left[k_y\left(y + \frac{w}{2}\right)\right]$ corresponding to the first-order pressure p_1 given in Eq. (3.25) and illustrated in Fig. 3.1(b). For an isothermal fluid and with the assumption $\lambda \gg h \gg \delta$, Rayleigh found the components $\langle v_{2y}\rangle$
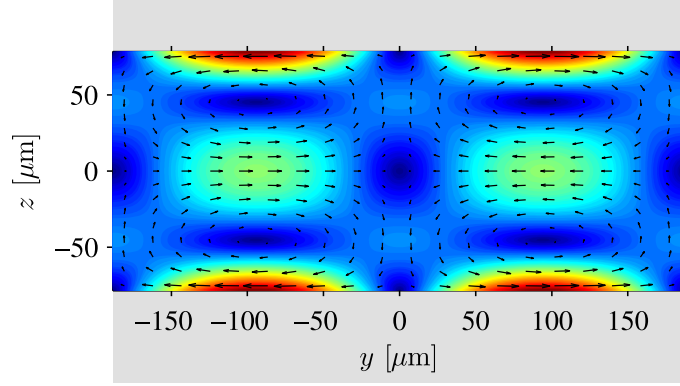
Figure 3.2: Vector plot (black arrows) of the acoustic streaming $\langle \boldsymbol{v}_2 \rangle$ and colorplot of its magnitude $\langle v_2 \rangle$ from zero (dark blue) to maximum (dark red) given by Rayleigh's result in Eq. (3.34) and valid for an isothermal liquid sandwiched between two parallel plates (gray) of height h and the assumption $\lambda \gg h \gg \delta$. The streaming is driven by a standing ultrasound pressure wave $p_1 = p_a \cos[k_y(y + w/2)]$ of wavelength $\lambda_y = 2\pi/k_y = 2w$ or $k_y = \pi/w$ for $n_y = 1$. Here w and h are those of our experimental model system described in Section 2.1. Adapted from Ref. [37].

and $\langle v_{2z} \rangle$ of $\langle \boldsymbol{v}_2 \rangle$ outside the boundary layers to be [52]

$$\langle v_{2y} \rangle = \frac{3}{16} \frac{v_a^2}{c_0} \sin\left[2k_y\left(y + \frac{w}{2}\right)\right] Y(z) \quad \text{with} \quad Y(z) = \left[1 - 3\frac{z^2}{(h/2)^2}\right], \quad (3.34a)$$

$$\langle v_{2z} \rangle = \frac{3}{16} \frac{v_a^2}{c_0} k_y h \cos\left[2k_y\left(y + \frac{w}{2}\right)\right] Z(z) \quad \text{with} \quad Z(z) = \left[\frac{z^3}{(h/2)^3} - \frac{z}{(h/2)}\right]. \quad (3.34b)$$

This result of $\langle \boldsymbol{v}_2 \rangle$ is plotted in Fig. 3.2 for the microchannel cross section of our experimental model system for the transverse half-wave resonance in Eq. (3.25) and Fig. 3.1(b). At the plates $z = \pm h/2$, the z-component $\langle v_{2z} \rangle$ of $\langle \boldsymbol{v}_2 \rangle$ vanishes resulting in the often-cited streaming velocity $\langle v_{2y}^{\text{bnd}} \rangle$ just outside the viscous boundary layer

$$\langle v_{2y}^{\text{bnd}} \rangle = -\Psi \frac{v_a^2}{c_0} \sin\left[2k_y\left(y + \frac{w}{2}\right)\right], \quad \Psi = \frac{3}{8} \approx 0.375. \quad (3.35)$$

At the mid height $z = 0$ of the channel $\langle v_{2z} \rangle$ vanishes as well and we get

$$\langle v_{2y}^{\text{mid}} \rangle = s_{\lambda \gg h}^0 \frac{v_a^2}{c_0} \sin\left[2k_y\left(y + \frac{w}{2}\right)\right], \quad s_{\lambda \gg h}^0 = \frac{3}{16} \approx 0.188, \quad (3.36)$$

where the sub- and superscripts in the streaming coefficient $s_{\lambda \gg h}^0$ refer to the geometry and the isothermal assumptions, respectively. Note that due to the assumption of $\lambda \gg h$, the channel ratio $k_y h$ does not enter the magnitude of $\langle v_{2y}^{\text{mid}} \rangle$. We expect this expression to deviate from measurements in our experimental model system as instead of $\lambda \gg h$ we have $\lambda \approx 4.8h$ for $\lambda = 2w$. Moreover, the microchannel does indeed have side walls and, moreover, the effects of the acoustic temperature dependence of the viscosity cannot be neglected [58].

3.4.2 Parallel-plate channel with λ, $h \gg \delta$

Recently, Muller extended Rayleigh's parallel-plate analysis by calculating $\langle \boldsymbol{v}_2 \rangle$ with the assumption of λ, $h \gg \delta$ [67]. This analytical expression for $\langle \boldsymbol{v}_2 \rangle$ has the same form as Eq. (3.34) but the z-dependent coefficients $Y(z, k_y h)$ and $Z(z, k_y h)$ are now functions of $k_y h$ such that

$$Y(z, k_y h) = \tilde{\Gamma} \left\{ \left[1 - k_y h \coth\left(k_y h\right) \right] \cosh\left(2k_y z\right) + 2k_y z \sinh\left(2k_y z\right) \right\}, \quad (3.37a)$$

$$Z(z, k_y h) = 2\tilde{\Gamma} \left\{ k_y h \coth\left(k_y h\right) \sinh\left(2k_y z\right) - 2k_y z \cosh\left(2k_y z\right) \right\}, \quad (3.37b)$$

$$\text{with } \tilde{\Gamma} = \frac{\sinh\left(k_y h\right)}{\sinh\left(k_y h\right) \cosh\left(k_y h\right) - k_y h}.$$

In the limiting case $\lambda \gg h$ ($k_y h = 2\pi \frac{h}{\lambda} \to 0$), the $k_y h$-dependent coefficients reduce to $Y(z)$ and $Z(z)$ in Eq. (3.34). Using the result of Muller with the dimensions of our experimental microchannel, we find that $\langle v_{2y}^{\mathrm{mid}} \rangle$ described in Eq. (3.36) is suppressed by a factor of 0.82 such that $\langle v_{2y}^{\mathrm{mid}} \rangle$ now becomes

$$\langle v_{2y}^{\mathrm{mid}} \rangle = s_{\lambda \approx 5h}^0 \frac{v_a^2}{c_0} \sin\left[2k_y\left(y + \frac{w}{2}\right)\right], \quad s_{\lambda \approx 5h}^0 \approx 0.158. \quad (3.38)$$

3.4.3 Thermoviscous correction

The streaming expressions in the former sections do not account for the temperature dependence of the viscosity η as they are derived based on the governing equations given in Eq. (3.18). However, it was recently shown theoretically by Rednikov and Sadhal that thermoviscous effects do play a role for the streaming amplitude [58]. For the parallel-plate geometry they found an overall correction factor multiplying $s_{\lambda \gg h}^0$,

$$s_{\lambda \gg h}^T = \left(1 + \frac{2}{3} B_T\right) s_{\lambda \gg h}^0 = 1.26 \, s_{\lambda \gg h}^0, \quad (3.39)$$

$$B_T = (\gamma - 1) \left[1 - \frac{(\partial_T \eta)_p}{\eta \alpha}\right] \frac{\sqrt{\nu D_{\mathrm{th}}}}{\nu + D_{\mathrm{th}}}, \quad (3.40)$$

where the coefficient 1.26 is found for water at $T_0 = 25\,^\circ\mathrm{C}$ using the parameters listed in the List of Material Parameters on page xvi.

Combining the reduction factor 0.82 from results of Muller given in the former section with the correction factor 1.26 from thermoviscous effects for $\eta(T)$ and $\lambda \approx 5h$, we get $s_{\lambda \approx 5h}^T \approx 1.03 s_{\lambda \gg h}^0$ and

$$\langle v_{2y}^{\mathrm{mid}} \rangle = s_{\lambda \approx 5h}^T \frac{v_a^2}{c_0} \sin\left[2k_y\left(y + \frac{w}{2}\right)\right], \quad s_{\lambda \approx 5h}^T \approx 0.194, \quad (3.41)$$

at the mid plane of a parallel-plate channel.

3.5 Acoustophoretic single-particle velocities

In the latter sections we have presented the governing acoustic equations and how the first-order acoustic resonances lead to the time-averaged second-order effects of the acoustic radiation force and the acoustic streaming. However, in experiments we observe these effects indirectly through the acoustophoretic motion of microparticles, which is the focus of this section.

As sketched in Fig. 2.2 a particle undergoing single-particle acoustophoresis is directly acted upon by the acoustic radiation force $\boldsymbol{F}^{\mathrm{rad}}$, while the acoustic streaming of velocity $\langle \boldsymbol{v}_2 \rangle$ contributes with a force on the particle through the viscous Stokes drag from the suspending liquid. If the particle is moving with velocity $\boldsymbol{u}$ sufficiently far from the channel walls [68], the drag force $\boldsymbol{F}^{\mathrm{drag}}$ is the well-known expression

$$\boldsymbol{F}^{\mathrm{drag}} = 6\pi\eta a \left(\langle \boldsymbol{v}_2 \rangle - \boldsymbol{u} \right), \tag{3.42}$$

and the equation of motion for the particle becomes

$$\frac{4\pi}{3} a^3 \rho_{\mathrm{p}} \partial_t \boldsymbol{u} = \boldsymbol{F}^{\mathrm{rad}} + 6\pi\eta a \left(\langle \boldsymbol{v}_2 \rangle - \boldsymbol{u} \right). \tag{3.43}$$

In this work the inertial effects can be neglected as the characteristic time $\tau \sim \rho_{\mathrm{p}} a^2 / \eta$ of acceleration ($< 1\ \mu\mathrm{s}$) is minute in comparison to the time scale of the motion of particles ($> 1\ \mathrm{ms}$) treated experimentally in this work. Hence, the quasi steady-state acoustophoretic particle velocity $\boldsymbol{u}$ becomes

$$\boldsymbol{u} = \frac{\boldsymbol{F}^{\mathrm{rad}}}{6\pi\eta a} + \langle \boldsymbol{v}_2 \rangle. \tag{3.44}$$

3.5.1 Acoustophoretic velocities at the channel mid height

In Chapter 5 the usefulness of the µPIV technique for measuring acoustophoretic particle velocities is demonstrated. However, this technique only allows for in-plane measurements of the particle velocities and are poor near walls. We therefore analyze the acoustophoretic microparticle velocity $\boldsymbol{u}$ at the mid plane $z = 0$ far from the walls and where $\langle v_{2z} \rangle = 0$. Moreover, we treat a purely transverse resonance, Eq. (3.25). Inserting Eqs. (3.32) and (3.41) into Eq. (3.44) we obtain the horizontal particle component u_y of amplitude u_{a},

$$u_y = u_{\mathrm{a}} \sin \left[2 k_y \left(y + \frac{w}{2} \right) \right] = u_y^{\mathrm{rad}} + u_y^{\mathrm{str}}, \tag{3.45a}$$

$$u_{\mathrm{a}} = u_0 \left(\frac{a}{a_0} \right)^2 + u_0 s_{\lambda \approx 5h}^T, \tag{3.45b}$$

where we define the amplitudes $u_{\mathrm{a}}^{\mathrm{rad}} = u_0 \left(a/a_0 \right)^2$ and $u_{\mathrm{a}}^{\mathrm{str}} = u_0 s_{\lambda \approx 5h}^T$ induced by radiation and streaming, respectively, and where we have introduced the charac-
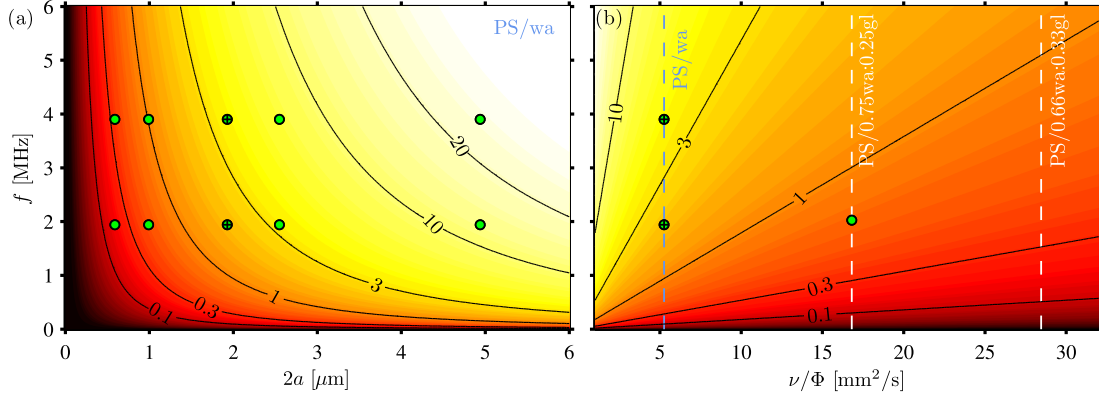
Figure 3.3: Theoretical prediction of the ratio $u^{\text{rad}}/u^{\text{str}}$, Eq. (3.47), of radiation- and streaming-induced velocities in the ultrasound symmetry plane at $z = 0$ of the microchannel (magenta plane in Fig. 2.1) at 25 °C. (a) Contour plot of $u^{\text{rad}}/u^{\text{str}}$ as function of particle diameter $2a$ and ultrasound frequency f for an aqueous suspension of polystyrene particles (PS) in pure water. (b) Contour plot of $u^{\text{rad}}/u^{\text{str}}$ as function of f and the rescaled momentum diffusivity ν/Φ for fixed particle diameter $2a = 2$ µm. The green dots indicate the cases studied experimentally in Section 5.5. Suspensions of polystyrene particles in three different liquids are indicated by dashed lines: pure water (light blue) as well as 0.75:0.25 and 0.67:0.33 mixtures of water:glycerol (white). Adapted from Ref. [37].

teristic velocity amplitude u_0 and the characteristic particle radius a_0 as

$$u_0 = \frac{v_{\text{a}}^2}{c_0} = \frac{4E_{\text{ac}}}{\rho_0 c_0} = \frac{4E_{\text{ac}}}{Z_0} \approx 27 \ \text{µm s}^{-1}, \tag{3.46a}$$

$$a_0 = \sqrt{\frac{6\nu}{\Phi}\frac{1}{\omega}} = \delta\sqrt{\frac{3}{\Phi}} \approx 1.6 \ \text{µm}. \tag{3.46b}$$

Here, Z_0 is the characteristic acoustic impedance of the suspending medium, and the numerical values are calculated for polystyrene particles suspended in water using the parameter values listed in the List of Material Parameters on page xvi with actuation frequency $f = 2$ MHz and a typical experimental energy density $E_{\text{ac}} = 10 \ \text{J m}^{-3}$ [69]. The ratio of the radiation- and streaming-induced velocity amplitudes becomes

$$\frac{u^{\text{rad}}}{u^{\text{str}}} = \frac{1}{6s^T_{\lambda \approx 5h}}\frac{\Phi}{\nu}\omega a^2, \tag{3.47}$$

which scales linearly with the angular frequency ω and the square of the particle radius a^2, but inversely with the streaming coefficient $s^T_{\lambda \approx 5h}$ and the momentum diffusivity rescaled by the acoustic contrast factor ν/Φ. In Fig. 3.3(a) we show a contour plot of the ratio $u^{\text{rad}}/u^{\text{str}}$ for polystyrene particles suspended in water at 25 °C as function of the particle diameter $2a$ and the ultrasound frequency f, while we in Fig. 3.3(b) show a similar plot but where $u^{\text{rad}}/u^{\text{str}}$ is plotted as

function of the rescaled momentum diffusivity ν/ϕ for fixed particle diameter $2a = 2\,\mu m$. The green dots indicate experiments presented in Section 5.5.

We define the mid-plane critical particle diameter $2a_c^{\mathrm{mid}}$ for cross-over from radiation-dominated to streaming-dominated acoustophoresis as the particle diameter for which $u^{\mathrm{rad}}\!\left(a_c^{\mathrm{mid}}\right)\!=\!u^{\mathrm{str}}\!\left(a_c^{\mathrm{mid}}\right)$. This results in

$$2a_c^{\mathrm{mid}} = 2a_0\sqrt{s_{\lambda\approx 5h}^{T}} = \sqrt{\frac{24\nu}{\omega}\frac{s_{\lambda\approx 5h}^{T}}{\Phi}} = \sqrt{12\frac{s_{\lambda\approx 5h}^{T}}{\Phi}}\delta = 1.40\,\mu m, \qquad (3.48)$$

where the numerical value is calculated for polystyrene particles suspended in water ($\Phi = 0.17$) actuated at 2 MHz. For $a = a_c^{\mathrm{mid}}$ the ratio of the velocity amplitudes $u^{\mathrm{rad}}/u^{\mathrm{str}}$ is unity, and consequently the unity contour line in Fig. 3.3(a) represents $2a_c^{\mathrm{mid}}$ as function of driving frequency f. Similarly, we perform the same analysis at the channel walls obtaining

$$2a_c^{\mathrm{bnd}} = 2a_0\sqrt{\Psi} = \sqrt{\frac{24\nu}{\omega}\frac{\Psi}{\Phi}} = \sqrt{12\frac{\Psi}{\Phi}}\delta = 1.94\,\mu m. \qquad (3.49)$$

The expression for the critical cross-over particle diameter, Eqs. (3.48) and (3.49), are important for designing experiments. In the expressions enters the channel geometry through the factors Ψ and $s_{\lambda\approx 5h}^{T}$, particle and liquid material parameters through Φ, and liquid parameters and frequency through the acoustic boundary layer thickness δ.

3.5.2   Radiation-force-dominated acoustophoresis

This thesis primarily treats 5-μm-diameter polystyrene particles suspended in water at 25 °C and acoustically actuated at frequency $f \approx 2$ MHz. In this case the ratio of the radiation- and streaming-induced particle velocities (at $z = 0$) becomes $u^{\mathrm{rad}}/u^{\mathrm{str}} \approx 13$ and consequently the influence from the acoustic streaming is negligible. This reduces the acoustophoretic particle velocity, i.e. $\boldsymbol{u} = \boldsymbol{F}^{\mathrm{rad}}/\left(6\pi\eta a\right)$, and using the transverse radiation force F^{rad}, Eq. (3.32), we obtain the transverse particle velocity u_y,

$$u_y = \frac{2\Phi}{3\eta}a^2 k_y E_{\mathrm{ac}}\sin\left[2k_y\left(y + \frac{w}{2}\right)\right]. \qquad (3.50)$$

This expression is later essential in Section 7.1.2 for the *in situ* determination of the acoustic energy density E_{ac}. From Eq. (3.50) and $u_y = \mathrm{d}y/\mathrm{d}t$, we can obtain an expression for the transverse path $y(y_0, t)$ of a particle starting at position $y_0 \equiv y(0)$ at time $t = 0$ [69, 70]

$$y(y_0, t) = \frac{1}{k_y}\arctan\left\{\tan\left[k_y\left(y_0 + \tfrac{w}{2}\right)\right]\exp\left(\frac{t}{t^*}\right)\right\} - \frac{w}{2}, \qquad (3.51a)$$

$$t^* = \frac{3\eta}{4\Phi\left(k_y a\right)^2}\frac{1}{E_{\mathrm{ac}}}, \qquad (3.51b)$$

Figure 3.4: Transverse particle path $y(y_0 - w/t, t) + w/2$, Eq. (3.51a), as function of normalized time t/t^*, Eq. (3.51b) . For given fixed parameters, the particle paths (black lines) are plotted for three different starting positions y_0. For use in Section 7.1.3 the channel is divided into two regions: The interrogation area of relative width α (green), and the center band of relative width $1 - \alpha$ (magenta). Adapted from Ref. [72].
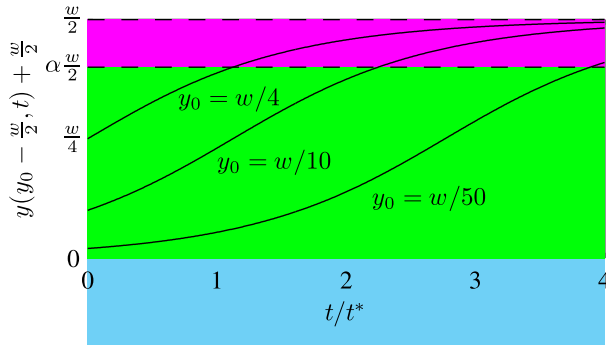
where the characteristic time scale t^* is introduced, which is inversely proportional to the acoustic energy density E_{ac}. Like the expression for the transverse velocity u_y, the expression for $y(y_0, t)$ can be used to determine the acoustic energy density E_{ac} as described in Section 7.1.1. Fig. 3.4 shows the transverse particle path $y(y_0, t)$ as function of normalized time t/t^* for three starting positions y_0 and a half-wave resonance $k_y = \pi/w$. By inversion of Eq. (3.51a), we obtain the time t it takes a particle to traverse from any initial position $-w/2 < y_0 < 0$ to any final position y at $y_0 < y < 0$ [69, 71],

$$ t = t^* \ln \left[\frac{\tan \left[k_y \left(y + \frac{w}{2} \right) \right]}{\tan \left[k_y \left(y_0 + \frac{w}{2} \right) \right]} \right]. \qquad (3.52) $$

3.5.3 Wall corrections to single-particle drag

The presence of the rectangular microchannel walls enhance the hydrodynamic drag on the microparticles as they undergo radiation-dominated acoustophoresis, moving relative to the suspending liquid. This problem was treated by Faxén for of a sphere moving parallel to a planar wall or in between a pair of parallel planar walls [73] and later extended by Brenner [74] to the sphere moving perpendicular to a single planar wall, as summarized by Happel and Brenner [68]. In general the wall-corrections enter the Stokes drag force $\boldsymbol{F}^{\mathrm{drag}}$, Eq. (3.42), in a non-trivial manner, however for the pure one-dimensional motion described in Section 3.5.1, the correction to the Stokes drag can be described as the dimensionless correction factor $\chi(a)$ which modifies the transverse acoustophoretic particle motion, Eq. (3.45),

$$ u_y = \left[\frac{1}{\chi(a)} \frac{a^2}{a_0^2} + s^T_{\lambda \approx 5h} \right] u_0 \sin \left[2k_y \left(y + \frac{w}{2} \right) \right]. \qquad (3.53) $$

No general analytical form exists for χ, so we list the result for three specific cases. For a particle moving parallel to the surface in the symmetry plane $z = 0$

Table 3.1: Wall drag-correction factors χ for particle sizes treated in the thesis.

2a	$\chi_{z=0}^{\text{paral}}$	$\chi_{z=\pm h/4}^{\text{paral}}$	$\chi_{\Delta y=w/4}^{\text{perp}}$
0.6 µm	1.004	1.005	1.004
1.0 µm	1.006	1.008	1.006
1.9 µm	1.012	1.016	1.011
2.6 µm	1.017	1.022	1.016
4.9 µm	1.032	1.042	1.030
10.2 µm	1.070	1.092	1.065

in the gap of height h between two parallel planar walls, χ is

$$\chi_{z=0}^{\text{paral}} \approx \left[1 - 1.004(2a/h) + 0.418(2a/h)^3\right]^{-1} \approx 1.070, \qquad (3.54)$$

while for motion in the planes at $z = \pm h/4$ it is

$$\chi_{z=\pm h/4}^{\text{paral}} \approx \left[1 - 1.305(2a/h) + 1.18(2a/h)^3\right]^{-1} \approx 1.092. \qquad (3.55)$$

Here the numerical values refer to a particle with diameter $2a = 10$ µm moving in a gap of height $h = 157$ µm. Similarly, for particle motion perpendicular to a single planar wall, the correction factor is

$$\chi^{\text{perp}} = \frac{4}{3}\sinh(\alpha)\sum_{j=1}^{\infty}\frac{j(j+1)}{(2j-1)(2j+3)} \qquad (3.56)$$

$$\times \left[\frac{2\sinh[(2j+1)\alpha] + (2j+1)\sinh(2\alpha)}{4\sinh^2[(j+\frac{1}{2})\alpha] - (2j+1)^2\sinh^2(\alpha)} - 1\right] \approx 1.065 \qquad (3.57)$$

where $\alpha = \cosh^{-1}(\Delta y/a)$ and Δy is the distance from the center of the particle to the wall. The numerical value refers to a 10-µm particle located at $\Delta y = w/4$. The values of the wall correction factor χ for all the particle sizes used in this work are summarized in Table 3.1.

In all parts of the thesis, except Section 5.5 and Chapter 6, we do not consider the drag-enhancing wall correction. However, the correction is significant for particles close to the walls and hence implementation of these corrections in acoustophoresis predictions will be beneficial.

3.6 Concluding remarks

This chapter presented the theoretical framework of thesis with the primary assumptions introduced and summarized in Table 2.2 in the former Chapter 2. The governing equations of the framework were introduced and the first- and second-order perturbations were presented. These form the basis for the next Chapter 4, where a numerical scheme is established. Moreover, simple eigenmodes of a rectangular cuboid were presented as well as the expressions for the particle

trajectory, Eq. (3.51a), and velocity profile, Eq. (3.50), of a particle undergoing radiation-dominated acoustophoresis in a pure transverse resonance. These expressions is the core in Section 7.1 where we present a set of methods for *in situ* determination of the acoustic energy density. Also, we presented a prediction of the acoustophoretic particle velocity at the channel mid height, Eq. (3.53), experimentally validated in Section 5.5.

Numerics of acoustophoresis

This chapter presents a numerical scheme for the analysis of the microparticle acoustophoresis for enabling improved design of acoustofluidic devices and studies of the basic physical aspects. The analysis is based directly on the governing hydrodynamic equations and by resolving the acoustic boundary layers. The numerical scheme utilizes the finite element method and is carried out using the software COMSOL Multiphysics 4.2a.

The numerical scheme is applied to analyze the microparticle acoustophoresis in the vertical microchannel cross section in the experimental model system presented in Section 2.1. The analysis demonstrates the acoustophoretic microparticle motion driven by the boundary-induced acoustic streaming and the acoustic radiation forces, and it constitutes as a good calibration of the acoustophoresis intuition before reaching the experimental results in the remaining thesis chapters.

The chapter starts with a description of the exact model system, the numerical implementation, and mesh convergence analysis followed by a presentation of the results for the first-order fields, the time-averaged second-order fields, and the microparticle velocities and positions as function of particle size, channel geometry, and suspending medium.

This chapter is based on work done in collaboration with PhD student Peter Barkholt Muller and Professor Henrik Bruus, DTU Physics, and Dr. Mads Jakob Herring Jensen, COMSOL A/S. The work is published in Lab on a Chip and the paper is appended in Chapter E. In the following, part of the paper is reproduced in a slightly modified version to align with the rest of the thesis, and in particular the introductory Chapters 1-3.

4.1 Numerical model

In this section we present the numerical model and how we implement and solve the governing equations introduced in Chapter 3 in the finite element software

COMSOL Multiphysics 4.2a, see Ref. [75]. This thesis will not treat the fundamentals of the finite element method, but the interested reader is referred to two great introductions in Refs. [76, 77].

4.1.1   Model system

The model system is an idealization of the straight liquid-filled microchannel described in Section 2.1. We neglect the structure of the actual silicon/glass chip and simply represent it as hard-wall isothermal boundary conditions as

$$T = T_0, \text{ on all walls,} \tag{4.1a}$$

$$\boldsymbol{v} = \boldsymbol{0}, \text{ on all non-actuated walls.} \tag{4.1b}$$

We further neglect any axial dynamics in the x direction along the microchannel and only consider the vertical cross section shown in Fig. 2.1(c) with $w = 380\,\mu\text{m}$ and $h = 160\,\mu\text{m}$. Finally, we represent the ultrasonic piezo transducer by the velocity boundary condition

$$\boldsymbol{n} \cdot \boldsymbol{v}_1 = v_{\text{bc}}(y, z)\mathrm{e}^{-\mathrm{i}\omega t}, \text{ added to actuated walls,} \tag{4.2}$$

where $\boldsymbol{n}$ is the outward pointing normal vector. In the analyses we excite the transverse half-wavelength resonance shown in Fig. 3.1(b) by the harmonic angular actuation $\omega = 2\pi f_{0,1,0}$ of frequency $f_{0,1,0} = c_0/(2w)$ from Eq. (3.23).

   We treat microparticle suspensions of spherical, and non-interaction polystyrene particles with mono-disperse diameters 0.5, 1.0, 2.0, 3.0, or 5.0 µm, respectively. The suspending liquid is water, but in a single case we investigate a 0.50:0.50 mixture of water:glycerol. All analyses are for temperature $T_0 = 25\,^{\circ}\text{C}$ and all material parameters are listed in the List of Material Parameters on page xvi.

4.1.2   Particle tracing module

In Chapters 5 and 6 we measure the acoustophoretic microparticle motion by particle tracking and particle image velocimetry. To mimic these experiments we model the acoustophoretic motion of N particles by applying the COMSOL Particle Tracing Module. The module uses a Lagrangian description of the motion of the particles, where each particle is treated as a point particle governed by Newton's second law resulting in a total of $2N$ ODEs in this analysis. The particles are subject to the acoustic radiation force $\boldsymbol{F}^{\text{rad}}$, Eq. (3.29), and the streaming-induced drag force $\boldsymbol{F}^{\text{drag}}$, Eq. (3.42), and consequently the module solves the equation of motion, Eq. (3.43), for each particle. We further neglect gravitation and any particle-wall interactions.

4.1.3   Numerical procedure

We implement the following numerical proceduce in COMSOL:

1. The first-order acoustic fields p_1, $\boldsymbol{v}_1$, and T_1 are calculated using the predefined Thermoacoustic Physics Interface solving Eq. (3.12) with the boundary conditions of Eqs. (4.1) and (4.2).

2. The time-averaged second-order pressure $\langle p_2 \rangle$ and the time-averaged second-order flow $\langle \boldsymbol{v}_2 \rangle$ are calculated by implementing Eq. (3.21) by modifying the Laminar Flow Physics Interface to include the addition of the time-averaged first-order products solved in Step 1. The right-hand side of Eq. (3.21a) is included as a mass source term by adding a so-called weak contribution to the governing equations, $-\frac{1}{2} \int_\Omega \left[\partial_x \mathrm{Re} \left(\rho_1 \bar{v}_{1x} \right) + \partial_y \mathrm{Re} \left(\rho_1 \bar{v}_{1y} \right) \right] \tilde{p}_2 \, \mathrm{dV}$ ($\tilde{p}_2$ is the pressure test function), while the right-hand side of Eq. (3.21b) is added as a body force term. Furthermore, for numerical stability, we keep the fourth-order non-linear term $\rho_0 \left(\langle \boldsymbol{v}_2 \rangle \cdot \boldsymbol{\nabla} \right) \langle \boldsymbol{v}_2 \rangle$ in the laminar flow equations.

3. The acoustic radiation forces are calculated from the first-order fields obtained in Step 1 by use of Eq. (3.29).

4. The COMSOL Particle Tracing Module is used to determine the time-dependent motion of the N suspended particles, where the drag force is calculated from the streaming flow $\langle \boldsymbol{v}_2 \rangle$ calculated in Step 2 and where the radiation force is calculated in Step 3.

The numerical proceduce was carried out using a computational mesh fine enough for all dependent variables to reach convergence, while ensuring that the acoustic boundary layers were properly resolved, see Section 4.1.3.1. This fine mesh was used when determining the first-order fields and the time-averaged second-order fields. In the simulation of the time-dependent particle motion, the flow field and radiation forces were interpolated to a coarser mesh to speed up the solving procedure substantially.

4.1.3.1 Mesh convergence analysis

The finite element mesh is created with a maximum element size length d_{mesh} at the channel boundaries and a maximum element size $10 d_{\mathrm{mesh}}$ in the bulk of the channel. In Fig. 4.1(a) is shown such a (coarse) mesh with 1204 elements and $d_{\mathrm{mesh}} = 20\delta$, or $\delta / d_{\mathrm{mesh}} = 0.05$, where $\delta = \sqrt{2\nu/\omega}$ is the viscous boundary layer thickness. When utilizing the finite element method it is crucial to use a mesh fine enough for the solution of all fields to reach convergence and to verify this a mesh-convergence analysis is made. We compare the solutions for decreasing d_{mesh} in order to determine the point at which the solution is independent of the number of mesh elements, and we define the relative convergence parameter $C(g)$ for a solution g with respect to a converged reference solution g_{ref},

$$C(g) = \sqrt{\frac{\int \left(g - g_{\mathrm{ref}} \right)^2 \, \mathrm{d}y \, \mathrm{d}z}{\int \left(g_{\mathrm{ref}} \right)^2 \, \mathrm{d}y \, \mathrm{d}z}}. \tag{4.3}$$

Figure 4.1: (a) The finite element mesh for a maximum element size of $d_\text{mesh} = 20\delta$ at the boundaries, resulting in a coarse mesh with only 1204 triangular elements. (b) Semi-logarithmic plot of the relative convergence parameter C, Eq. (4.3), for the acoustic fields p_1, T_1, $\boldsymbol{v}_1$, and $\langle v_2 \rangle$ as function of decreasing element size d_mesh/δ. The convergence threshold is chosen as $C = 0.002$ (dashed line), which is a trade off between accuracy and computational time. For all fields to convergence below this threshold, we need a maximum element size at the boundaries of $d_\text{mesh} = 0.5\delta$ or $\delta/d_\text{mesh} = 2.0$ (dash-dotted line). Adapted from [78].
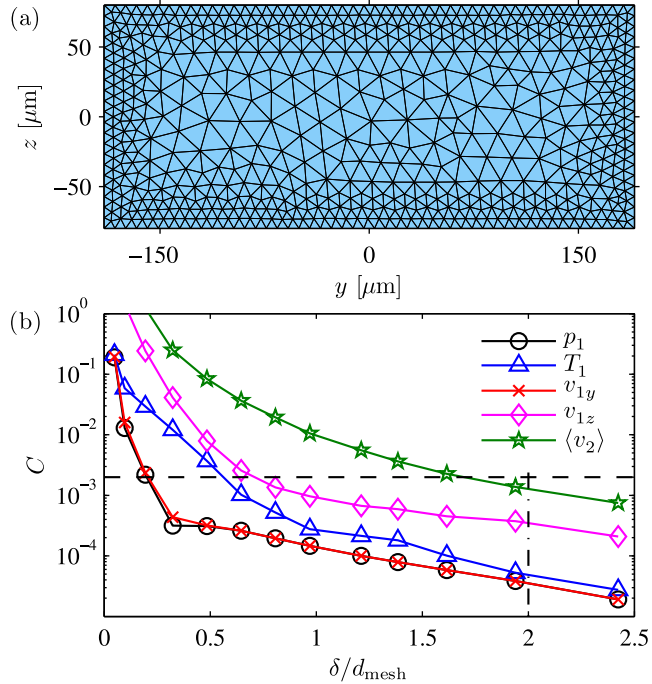
For g_ref we use the solution for the smallest value of d_mesh, namely $d_\text{mesh} = 0.3\delta$ or $\delta/d_\text{mesh} = 3.3$ resulting in 2.6×10^5 triangular mesh elements.

In Fig. 4.1(b) we have shown a semi-logarithmic plot of the exponential convergence of $C(g)$ for both first- and second-order fields. The time-averaged second-order velocity field $\langle v_2 \rangle$ converges noticeably slower than the first-order fields, as it depends on the gradients of the first-order fields and their convergence. In this work we define our point of convergence for $C(g) = 0.002$ (dashed line), which is reached for all fields at $d_\text{mesh} = 0.5\delta$ or $\delta/d_\text{mesh} = 2.0$. This mesh size, with 1.2×10^5 triangular elements, is used throughout the rest of the numerical analysis.

4.1.3.2   Computational requirements

The analysis requires an above-average workstation and in this work we have used a DELL precision 7500 workstation equipped with 48 GB RAM and two hexa-core Intel Xeon X5650 processors. When calculating the first-order acoustic fields in the numerical procedure Step 1, we used the mesh ($d_\text{mesh} = 0.5\delta$ or $\delta/d_\text{mesh} = 2.0$) found by the mesh-convergence analysis, which resulted in about 3×10^6 degrees of freedom, a calculation time of 4.5 minutes, and a peak RAM usage of 64 % or 31 GB. The calculation of the second-order acoustic fields in the numerical procedure Step 2 required around 5×10^5 degrees of freedom and took 2 minutes, while having a peak RAM usage of 19 % or 9 GB. The computation time for steps 3 and 4 was less than 15 seconds for calculation of 144 particle trajectories of 100 time steps and solved on a coarser mesh resulting in about 9×10^4 degrees
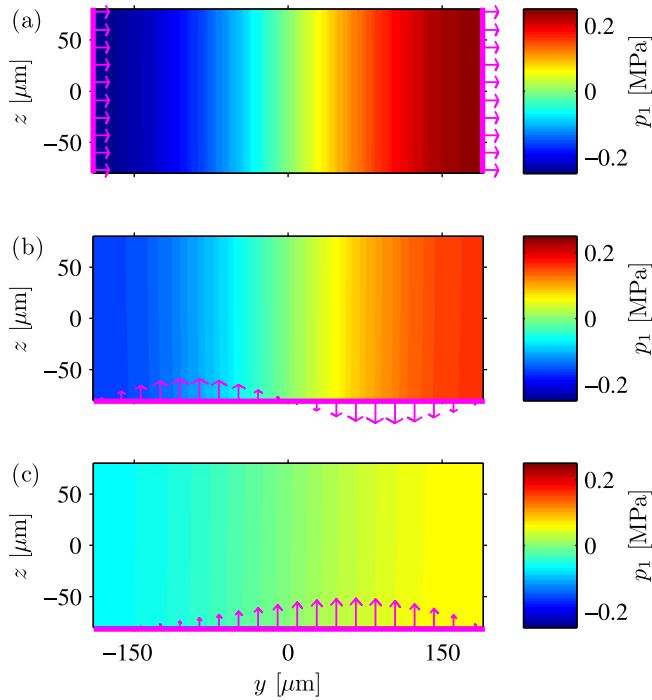
Figure 4.2: Colorplot of the first-order pressure field p_1 for three different actuation modes (magenta arrows) as of Eq. (4.4). The actuation frequency is $f_{0,1,0}$ for all modes and it is seen that regardless of the spatial actuation all three actuation modes excite the transverse half-wave resonance, but of different coupling strengths, such that the pressure amplitude becomes (a) 0.24 MPa with side-wall actuation, (b) 0.16 MPa with anti-symmetric bottom-wall actuation, and (c) 0.06 MPa with non-symmetric bottom-wall actuation. Adapted from Ref. [78].

of freedom. In summary, the scheme is solvable within computational reach in this two-dimensional analysis, while a future extension to three dimension might be limited by its computational requirement.

4.2 Numerical results

This section presents the numerical results for the first-order fields, the time-averaged second-order fields, and the microparticle velocities and positions as function of particle size, channel geometry and suspending medium. We aim at illustrating the versatility of the numerical scheme and its potential for use to study the basic physical aspects and as a tool to design of new acoustofluidic devices.

4.2.1 Actuation mode

The ultrasound actuation is modeled using the velocity boundary condition in Eq. (4.2) at the frequency $f_{0,1,0} = c_0/(2w) = 1.97\,\text{MHz}$ to excite the transverse half-wave resonance, Eq. (3.25). In the following we examine the excitation for the following three actuation modes of the velocity boundary condition v_{bc} in

Figure 4.3: Colorplots of the amplitudes of the first-order acoustic fields in the water-filled channel with the imposed horizontal half-wave resonance of frequency $f_{0,1,0}$ excited by the velocity boundary condition Eq. (4.4a): (a) pressure p_1 which is identical to panel (a) in Fig. 4.2, (b) temperature T_1, (c) horizontal velocity v_{1y}, and (d) vertical velocity v_{1z}. The sub-micrometer thin viscous boundary of width $\delta = 0.38 \, \mu$m is too small to be seen. The dashed white lines indicate the position for the line plots in Fig. 4.4. Adapted from Ref. [78].
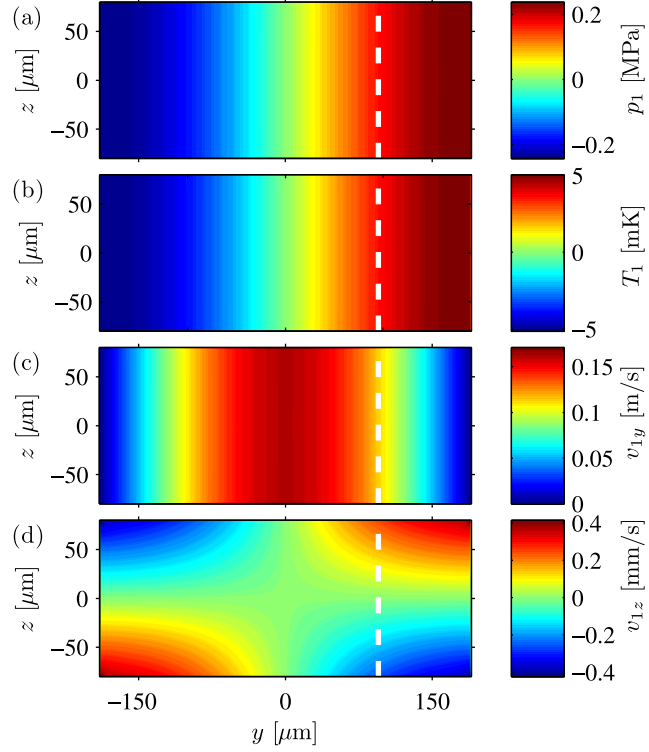
Eq. (4.2),

$$v_{\text{bc}}^A \left(\pm \tfrac{w}{2}, z \right) = \pm v_{\text{bc},0}^A, \tag{4.4a}$$

$$v_{\text{bc}}^B \left(y, -\tfrac{h}{2} \right) = v_{\text{bc},0}^B \sin \left(2\pi \frac{y}{w} \right), \tag{4.4b}$$

$$v_{\text{bc}}^C \left(y, -\tfrac{h}{2} \right) = v_{\text{bc},0}^C \left(\frac{1}{2} - \frac{y}{w} \right) \left(\frac{1}{2} + \frac{y}{w} \right)^2. \tag{4.4c}$$

To compare the three actuation modes, we chose the amplitude of the oscillation such that the line integral of the absolute value $|v_{\text{bc}}|$ of the velocity along the boundary perimeter $\partial\Omega$ of the domain Ω is given in terms of the angular frequency ω and a characteristic value d_0 of the displacement of an actuated boundary,

$$\oint_{\partial\Omega} \left| v_{\text{bc}}^X \right| \mathrm{d}\ell = 2h\omega d_0, \quad X = A, \, B, \, C, \tag{4.5}$$

where the normalization constant $2h$ is chosen such that $v_{\text{bc}}^A = \omega d_0$. For the characteristic displacement amplitude we use $d_0 = 0.1 \, \text{nm}$, which is a typical value for the loaded piezo displacement [44] and in this work it results in acoustic energy densities typical for experiments [69, 72, 79, 80] as discussed in Section 7.1.

The first-order pressure fields p_1 resulting from the three different actuation modes are shown in Fig. 4.2. It is seen that all actuation modes excite the $f_{0,1,0}$ resonance regardless of the detailed spatial dependence, but the coupling strength varies and the resonance amplitude is different for each of the three actuation modes. For simplicity, we use the v_{bc}^A velocity boundary condition, Eq. (4.4a) and Fig. 4.2(a), throughout the remaining sections in this chapter.
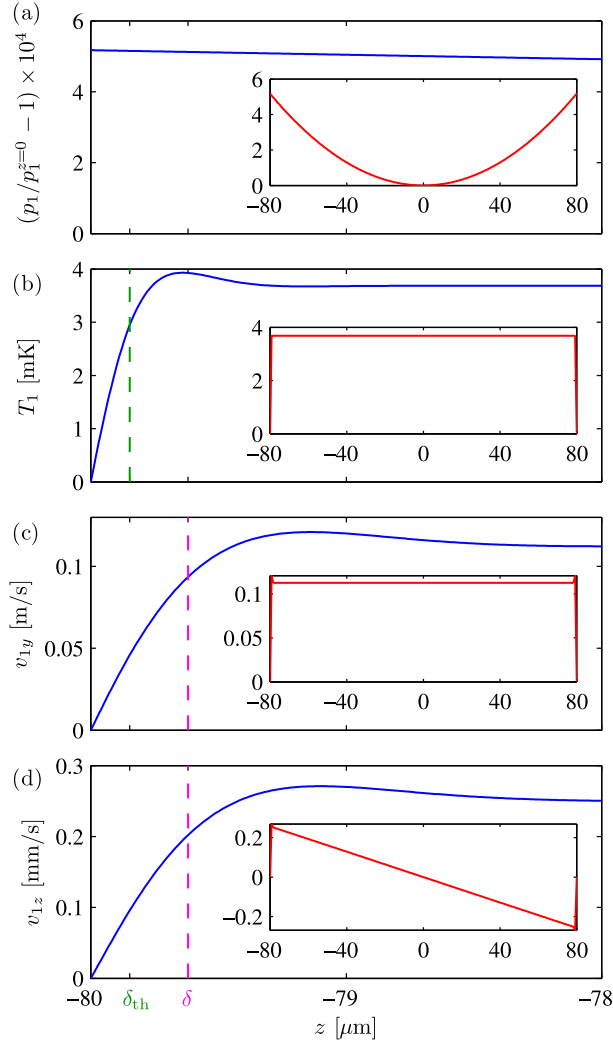
Figure 4.4: Lineplots at $y = w/4$ of the amplitudes of the first-order fields: (a) Relative pressure change $p_1/p_1^{z=0} - 1$, (b) temperature T_1, (c) horizontal velocity v_{1y}, and (d) vertical velocity v_{1z}. The main plots (blue curves) show the field amplitudes close to the bottom wall, while the insets (red curves) show the field amplitudes across the entire channel height. The characteristic length scales of the thermal and viscous boundary layers, δ_{th} and δ as of Eq. (3.15), are indicated by the green and magenta dashed lines, respectively. Both T_1, v_{1y}, and v_{1z} show marked variations on the length scale of the boundary layer, while only Δp_1 and v_{1z} show variations across the full height of the domain. Adapted from Ref. [78].

4.2.2 First-order fields

In Fig. 4.3 we show color plots of the pressure p_1, temperature T_1, horizontal velocity v_{1y}, and vertical velocity v_{1z}, resulting from the actuation mode shown in Eq. (4.4a) and Fig. 4.2(a). The amplitudes and structures of p_1, T_1, and v_{1y} relate strongly to the excited acoustic resonance, whereas v_{1z} arises due to bulk transverse resonance interacting with the viscous boundary layers at top and bottom walls. As consequence the non-resonant amplitude of v_{1z} is a factor of 10^3 smaller than the resonant amplitude of v_{1y}. We notice that T_1 and p_1 are proportional with proportionality factor $\approx (5 \text{ mK}) / (0.23 \text{ MPa}) = 2.2 \times 10^{-8} \text{ K Pa}^{-1}$ matching well with the theoretical prediction $\alpha T_0 / (\rho_0 C_p) \approx 2.1 \times 10^{-8} \text{ K Pa}^{-1}$ of Eq. (3.16d). Moreover, v_{1y} is shifted horizontally by $\lambda/4$ with respect to T_1 and p_1.
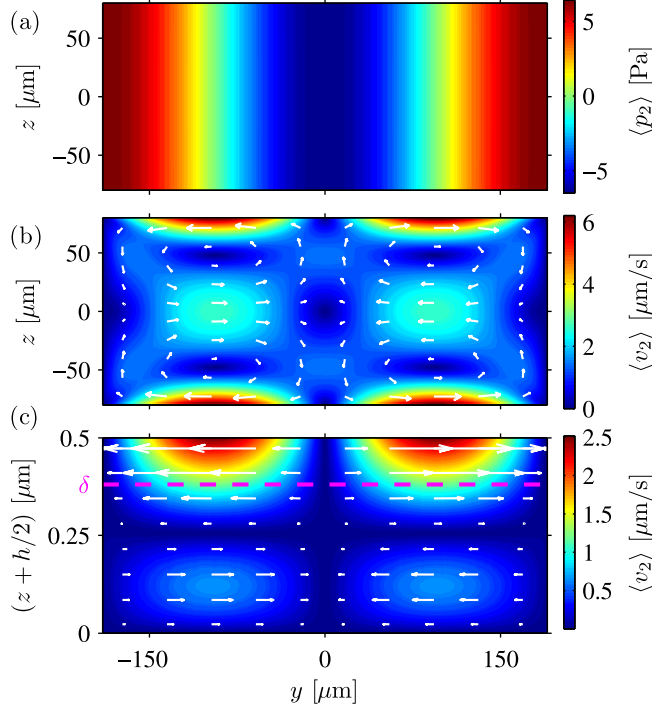
Figure 4.5: Time-averaged second-order fields in the water-filled channel excited in the horizontal half-wave resonance of frequency $f_{0,1,0}$ by the side-wall actuation shown in Fig. 4.2(a) and driven by the first-order fields plotted in Fig. 4.3. (a) Color plot of the time-averaged second-order pressure $\langle p_2 \rangle$ with a magnitude approximately 2.5×10^{-5} times smaller than the amplitude of the oscillating first-order pressure p_1 in Fig. 4.3(a). (b) Vector plot (white arrows) of the time-averaged second-order streaming velocity $\langle \boldsymbol{v}_2 \rangle$ and color plot of its magnitude $\langle v_2 \rangle$. Four bulk (Rayleigh) streaming rolls are clearly seen having the maximum speed near the top and bottom walls. (c) Zoom-in on the 0.4-µm-thick boundary layer near the bottom wall exhibiting the two boundary (Schlichting) streaming rolls that drive the bulk (Rayleigh) streaming rolls. Adapted from Ref. [78].

In Fig. 4.4 we plot the amplitudes of the first-order fields along the dashed white lines at $y = w/4$ shown in Fig. 4.3. Panel (a) shows the relative pressure change, $p_1/p_1^{z=0} - 1$ to the the pressure amplitude at $(y, z) = (w/4, 0)$, illustrating that p_1 only varies weakly along z and in particular not on the length scale of the boundary layers δ_{th} and δ as the velocities v_{1y} and v_{1z}, and temperature T_1 plotted in panels (b-d). Furthermore, T_1 and v_{1y} do not vary along z outside the boundary layers, while p_1 and v_{1z} do.

4.2.3   Second-order fields

As described in Section 2.2.3 and as evident from Eq. (3.21) the first-order acoustic fields drive time-averaged non-linear effects, namely a static pressure field $\langle p_2 \rangle$ and a steady velocity field $\langle \boldsymbol{v}_2 \rangle$ as shown in Fig. 4.5. The time-averaged second-

order fields exhibit a spatial oscillation in the horizontal y-direction of wavelength $\lambda/2$ because of the spatial period doubling in relation to the driving first-order fields as shown by the classical streaming prediction in Fig. 3.2.

The magnitude of the time-averaged second-order pressure $\langle p_2 \rangle$ in Fig. 4.5(a) is approximately 2.5×10^{-5} times smaller than the amplitude of the oscillating first-order pressure in Fig. 4.3(a). Moreover, the time-averaged velocity field $\langle \boldsymbol{v}_2 \rangle$ in Fig. 4.5(b) contains four bulk streaming rolls. The streaming velocity is maximum close to the top and bottom wall and has two local maxima on the horizontal center axis $z = 0$, where opposite pairs of bulk rolls meet. The solution in Fig. 4.5(b) is similar to Rayleigh's analytical solution given in Eq. (3.34) and plotted in Fig. 3.2. However, Rayleigh's solution deviates on the following two points: (i) the numerical solution is for a rectangular geometry and not parallel plates resulting in lower velocities close to the side walls, and (ii) as we are not in the limit $\lambda \gg h$ but have $\lambda \approx 4.8h$, the strength of the streaming rolls decreases slightly before meeting in the center of the channel resulting in a lower velocity $\langle v_{2y}^{\text{mid}} \rangle$ in the horizontal center plane. More precisely, Rayleigh's prediction in Eq. (3.36) gives $\langle v_{2y}^{\text{mid}} \rangle = \frac{1}{2} \langle v_{2y}^{\text{bnd}} \rangle$, while the numerical result gives $\langle v_{2y}^{\text{mid}} \rangle = 0.4097 \langle v_{2y}^{\text{bnd}} \rangle$. However, the analytical prediction by Muller without assuming $\lambda \gg h$, Eq. (3.38), gives $\langle v_{2y}^{\text{mid}} \rangle = 0.4194 \langle v_{2y}^{\text{wall}} \rangle$ and matches well with the numerics.

Fig. 4.5(c) shows a zoom-in on the 0.4-µm-thick viscous boundary layer close to the bottom wall containing two boundary (Schlicting) streaming rolls. Note that the boundary layer rolls are very elongated in the horizontal direction as the z-axis in Fig. 4.5(c) is stretched almost a factor 10^3 relative to the y-axis. The time-averaged second-order velocity $\langle \boldsymbol{v}_2 \rangle$ is zero at the bottom wall, thus fulfilling the boundary conditions Eq. (4.1b), while the maximum of its horizontal component $\langle v_{2y}^{\text{bnd}} \rangle = 6.42$ µm s^{-1} is reached at a distance of approximately 3δ from the wall. The maximum bulk amplitude $v_{1y}^{\text{max}} = 0.162$ m s^{-1} of the horizontal first-order velocity component, v_{1y} shown in Fig. 4.3(c), is reached at the channel center $y = 0$. From this we can calculate the velocity ratio $\Psi = c_0 \langle v_{2y}^{\text{bnd}} \rangle / \left(v_{1y}^{\text{max}} \right)^2 = 0.367$, which deviates less than 3 % from the value $\Psi = 3/8 = 0.375$ of Eq. (3.35).

4.2.4   Particle tracing simulations

We now turn to study the acoustophoretic motion of 144 polystyrene microparticles suspended in water and distributed evenly at the initial time $t = 0$ as shown in Fig. 4.6(a). In Fig. 4.6(b)-(f) we show the particle trajectories after 10 s of acoustic actuation. Within each panel all particles have the same diameter $2a$, but the particle size is increased from one panel to the next: (b) 2a = 0.5 µm, (c) 1 µm, (d) 2 µm, (e) 3 µm, and (f) 5 µm. For the smallest particles, panel (b) and (c), the drag force from the acoustic streaming dominates the particle motion, and the characteristic streaming flow rolls are clearly seen. For the larger particles, panel (e) and (f), the acoustic radiation force dominates the particle
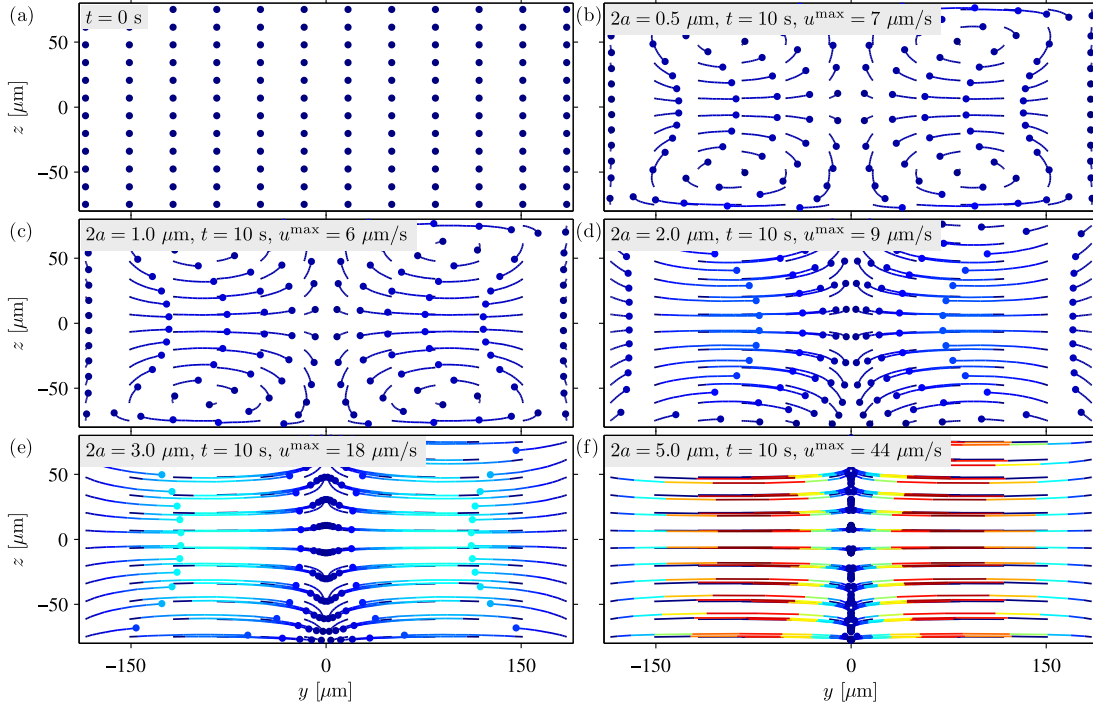
Figure 4.6: (a) The starting positions (●) of 144 evenly distributed particles at $t = 0$ s in the computational domain at the onset of the horizontal half-wave $f_{0,1,0}$ resonance shown in Figs. (4.3) and (4.5). In the following five panels are shown the trajectories (colored lines) and positions (●) that the particles have reached by acoustophoresis at $t = 10$ s for five different particle diameters: (b) 0.5 µm, (c) 1 µm, (d) 2 µm, (e) 3 µm, and (f) 5 µm. The colors indicate the instantaneous particle velocity u ranging from $0\,\mu\text{ms}^{-1}$ (dark blue) to $44\,\mu\text{ms}^{-1}$ (dark red). The lengths of the trajectories indicate the distance covered by the particles in 10 s. Streaming-induced drag dominates the motion of the smallest particles, which consequently are being advected along the acoustic streaming rolls of Fig. 4.5(b). In contrast, the acoustic radiation force dominates the motion of the larger particles, which therefore are forced to the vertical nodal plane at $y = 0$ of the first-order pressure p_1 shown in Fig. 4.3(a). Adapted from Ref. [78].

motion, and the particle velocity $\boldsymbol{u}$ is almost horizontal with the sinusoidal spatial dependence given by $u_y(y) = F^{\text{rad}}(y)/(6\pi\eta a)$ as predicted in Section 3.5.2. Panel (d) shows an intermediate regime where drag and radiation forces are of the same order of magnitude. At the nodal plane $y = 0$ the radiation forces are zero, and consequently for times t larger than 10 s all particles in panel (f) that have reached $y = 0$ ends up at $(y, z) = (0, \pm h/2)$ due to the weak but non-zero streaming-induced drag forces.

At the top and bottom walls the streaming-induced drag force and the radiation force counteract each other and by comparing the length of the trajectories near the top and walls we find the 2-µm diameter is closest to the critical diameter (at the walls), which matches well with the prediction $2a_{\text{c}}^{\text{bnd}} = \sqrt{12\frac{\Psi}{\Phi}}\delta = 1.94\,\mu\text{m}$ in Eq. (3.49).
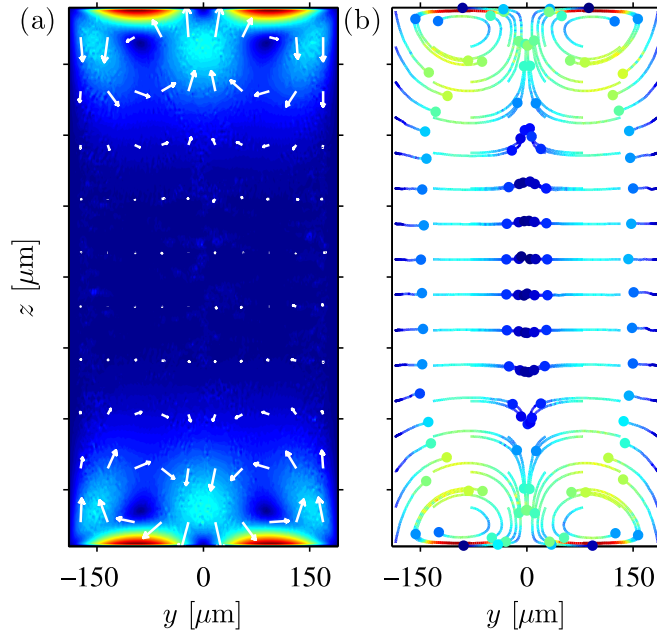
Figure 4.7: Acoustophoresis in a high-aspect-ratio channel. The model is identical to Fig. 4.2(a), but the channel is vertically elongated for fixed width $w = 0.38$ mm, so the channel aspect ratio becomes $h/w = 2$. (a) Vector plot (white arrows) similar to Fig. 4.5(b) of the time-averaged second-order streaming velocity $\langle \boldsymbol{v}_2 \rangle$ and color plot [from 0 µm/s (dark blue) to 4.2 µm/s (dark red)] of its magnitude. (b) Particle tracing plot for 1-µm-diameter polystyrene particles corresponding to Fig. 4.6(c) but for time $t = 100$ s, aspect ratio $h/w = 2$, and velocity ranging from 0 µm/s (dark blue) to 3.3 µm/s (dark red). In this high aspect-ratio geometry the acoustic streaming flow rolls are located near the top and bottom walls leaving the center region nearly streaming free. Adapted from Ref. [78].

4.2.5 Changing the channel aspect ratio

We now examine how a vertical elongation to change the channel aspect ratio from $h/w = 0.42$ to 2 affects the microparticle acoustophoresis if all other parameters remain unchanged. The results are shown in Fig. 4.7 and panel (a) shows that the streaming is only significant near the top and bottom of the channel with aspect ratio $h/w = 2$. This is because the vertical extension Δ of the streaming roll is identical to the horizontal one, which is $\Delta = \lambda/4$. Therefore with the horizontal half-wave resonance in a channel of aspect ratio $h/w = 2$, we obtain a streaming-free region with an vertical extent of $h - 2(h/4) = h/2$ around the center of the channel, which indeed is seen in Fig. 4.7(a).

As a consequence, the acoustophoretic motion of particles in the center region is controlled by the radiation force. This is illustrated in Fig. 4.7(b), where trajectories of small 1-µm-diameter particles are shown. For $-h/4 < z < h/4$ their motion is similar to the radiation-force dominated motion of the larger 5-µm-diameter particles moving in the shallow channel with $h/w = 0.42$ as shown in Fig. 4.6(f). Near the top and bottom walls, the 1-µm-diameter particles exhibit

the usual small-particle streaming-induced motion as shown in Fig. 4.6(b).

Clearly, geometry can be used to obtain more control of the acoustophoretic motion of suspended particles in microchannels. However, note that the example shown in Fig. 4.7 requires that there are no resonance dynamics along the height of the channel, which might be complicated to realize experimentally.

4.2.6   Changing the suspending medium

As described in Eq. (3.47) the ratio of radiation- and streaming-induced acoustophoresis is inversely proportional to the liquid momentum diffusivity ν rescaled with the acoustic contrast factor Φ. We therefore examine the change in acoustophoretic motion by changing the suspending liquid from water ($\nu/\Phi = 5.25 \text{ mm}^2\,\text{s}^{-1}$) to a 0.50:0.50 mixture water:glycerol ($\nu/\Phi = 146 \text{ mm}^2\,\text{s}^{-1}$). The material parameters for the 0.50:0.50 mixture water:glycerol are listed in the List of Material Parameters on page xvi.

First, in order to excite the same horizontal half-wave resonance we need to change the frequency of actuation as the speed of sound of the glycerol mixture is about 15 % larger than that of water, i.e. we get $f_{0,1,0} = c_0/(2w) = 2.27$ MHz. This frequency and the usual actuation condition Eq. (4.2) are used to calculate the results shown in Fig. 4.8 for the first-order pressure field p_1, the time-averaged second-order streaming velocity $\langle \boldsymbol{v}_2 \rangle$, and the particle velocities u and particle trajectories for 5-µm-diameter polystyrene particles.

The ultrasound actuation amplitude remains the same as previously, but from Fig. 4.8 we notice that p_1 is a factor of 2.6 smaller (from 0.243 MPa to 0.094 MPa) in the high-viscosity glycerol mixture than in the low-viscosity water of Fig. 4.3(a). Clearly, the difference in viscosity leads to different acoustic responses. Likewise, the induced streaming velocity $\langle v_{2y}^{\text{bnd}} \rangle$ near the boundary, is reduced by a factor of 15 from 6.42 µm/s in water, Fig. 4.5(b), to 0.43 µm/s in the glycerol mixture, Fig. 4.8(b). Given the validity of Rayleigh's streaming theory, the velocity ratio $\Psi = c_0 \langle v_{2y}^{\text{bnd}} \rangle / \left(v_{1y}^{\text{max}} \right)^2$ should be independent of viscosity. However, for the glycerol mixture we obtain a value of 0.336 deviating 8 % from the value in water, see Section 4.2.3, and 10 % from Rayleigh's value 3/8 of Eq. (3.35).

In Fig. 4.8(c) is shown that the viscous boundary-layer thickness in the glycerol-in-water mixture at 2.27 MHz is $\delta = 0.79$ µm, a factor 2.08 larger than the value $\delta = 0.38$ µm in water at 1.97 MHz shown in Fig. 4.5(c). As the two resonance frequencies only differ by 10 %, the change in the boundary-layer thickness is mainly due to the viscosity ratio, $\sqrt{5 \text{ mPa s}}/\sqrt{1 \text{ mPa s}} \approx 2.2$.

Finally, from Eq. (3.35) using $\Psi = 3/8$ and $\Phi = 0.03$, we calculate the critical particle diameter to be $2a_c^{\text{bnd}} = 9.6$ µm for the cross-over from radiation-dominated to streaming-dominated acoustophoretic motion in the glycerol-in-water system. This value explains why the particle trajectories for the 5-µm-diameter polystyrene particles in Fig. 4.8(d) appear to be much more influenced by the acoustic streaming rolls, compared to the same-sized particles in water, Fig. 4.6(f). Instead, Fig. 4.8(d) resembles more the motion of the 1-µm-diameter particles in water, Fig. 4.6(c). This resemblance can be quantified by the ratio
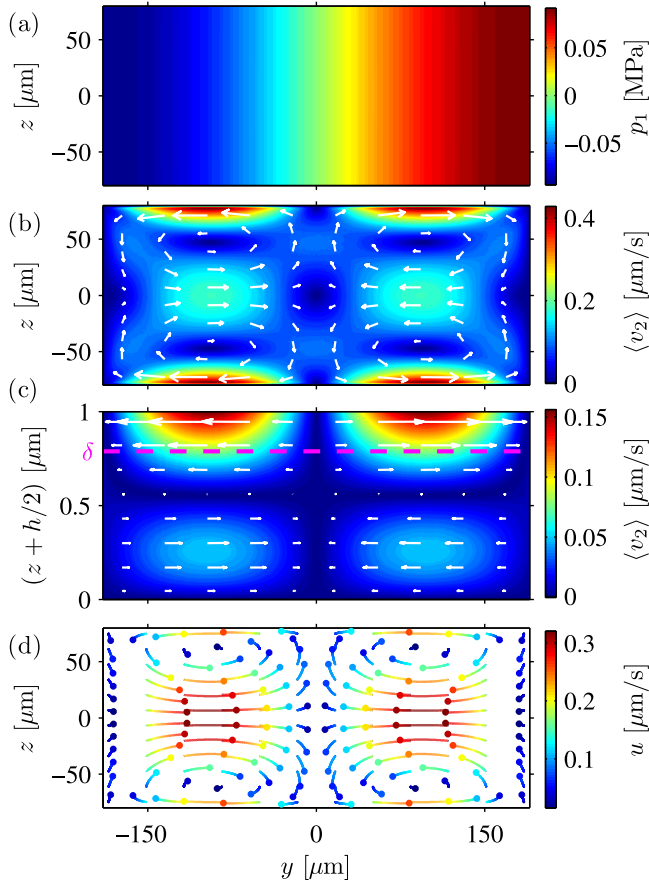
Figure 4.8: Acoustophoresis in a 0.50:0.50 mixture water:glycerol. The setup is identical to Fig. 4.2(a) except that the resonance frequency is increased to $f = c_0/(2w) = 2.27$ MHz. (a) Color plot of the pressure p_1 showing the horizontal half-wave resonance. (b) Vector plot (white arrows) of the time-averaged second-order streaming velocity $\langle \boldsymbol{v}_2 \rangle$ and color plot of its magnitude corresponding to Fig. 4.5(b). (c) Zoom-in on the now 0.79-µm-thick boundary layer near the bottom wall exhibiting the two boundary (Schlichting) streaming rolls that drive the bulk (Rayleigh) streaming rolls. (d) Particle tracing plot for 5-µm-diameter polystyrene particles corresponding to Fig. 4.6(f) but for 150 s of acoustic actuation. Adapted from Ref. [78].

a/a_c^{bnd}: for 5-µm-diameter particles in the glycerol-in-water mixture it is 0.52, while for 1-µm-diameter particles in pure water it is 0.50, only 4 % lower. Note that because of the reduction in streaming velocity by the above-mentioned factor of 15 we have chosen to follow the particles in the glycerol-in-water mixture for 150 s and in water only for 10 s.

4.3 Concluding remarks

We have successfully utilized the finite element method using the software COMSOL Multiphysics to model the microparticle acoustophoresis inside the microchannel in our experimental model system, Section 2.1, subject to a transverse horizontal half-wave resonance. The motion is due to the combined effect of Stokes drag from the time-averaged second-order streaming flow and the acoustic radiation forces.

Based directly on the governing equations, the model described the boundary layer streaming rolls and bulk streaming rolls as predicted analytically by Schlichting and Rayleigh, respectively. The model was used to characterize the cross over from streaming-dominated to radiation-dominated acoustophoretic microparticle motion as function of particle diameter, channel geometry, and sus-

pending medium. By increasing the height-to-width ratio, we demonstrated how to get rid of streaming effects in the center region of a microchannel given that it supports a purely transverse resonance. Further, by changing suspending medium from water to a 0.50:0.50 glycerol:water mixture, we demonstrated how to enhance the streaming effects. The former study may form a good starting point for designing streaming-free devices for handling of sub-micrometer particles, such as small cells, bacteria, and vira, and thus supporting concurrent experimental efforts to suppress streaming, e.g., through averaging over alternating actuation frequencies [81]. The latter study is pointing in the direction of developing devices with improved mixing capabilities by enhancing streaming [82, 83]. We have thus shown that our simulation tool has a great potential for enabling improved design of acoustofluidic devices.

The numerical model can be extended in a number of obvious directions: (*i*) make a full 3D-model taking the elastic properties of the chip surrounding the microchannel into account, (*ii*) include gravitation, (*iii*) include full thermoviscous effects taking into account e.g. the temperature dependency of the viscosity [58], (*iv*) implement wall-enhancement of the drag forces, and (*iv*) particle-particle interactions, hydrodynamic as well as acoustic.

An important next step is to create a basis for experimental verification of our numerical modeling, which is the topic of the next Chapters 5 and 6, where we present a temperature-stable acoustophoresis platform to use for high-resolution 2D and 3D characterization of the acoustophoretic particle motion.

Acoustophoresis analyzed by micro-PIV

An important step for improving the fundamental understanding of microparticle acoustophoresis is to produce reliable, high-resolution experiments for the comparison and validation of existing analytical and numerical predictions as those presented in Chapters 3 and 4. In 2007 Hagsäter *et al.* showed that full-chip micro-particle image velocimetry (micro-PIV or µPIV) is a strong tool for analyzing the in-plane acoustophoretic particle motion [84]. However, the lack of stable devices, the time-dependent inhomogeneous particle distributions, and the time-consuming process associated with high-precision µPIV have hurdled systematic measurements of microparticle acoustophoresis.

This chapter presents a µPIV platform for automated, temperature-controlled, long-term-stable, and full-channel velocity measurements of microparticle acoustophoresis. The platform is located in the laboratory of Professor Thomas Laurell, Lund University, and was developed in close collaboration with his PhD student Per Augustsson. Using this platform, measurements were carried out of the acoustophoretic particle velocities at the horizontal microchannel plane of the experimental model system in Fig. 2.1(b).[1] These measurements are presented for a 15-mm-long section revealing the complexity of the global spatial structure of the underlying acoustic resonances. Further, the acoustophoretic particle velocities are examined as function of the driving frequency, voltage, and resonator temperature. Finally, the chapter ends with a systematic investigation of the acoustophoresis radiation-to-streaming transition as function of particle size, actuation frequency, and suspending medium.

Sections 5.1–5.4 are based on work carried out in collaboration with Professor Thomas Laurell and his PhD student Per Augustsson, Lund University, Profes-

---

[1]In this chapter all measurements are carried at the horizontal xy plane shown in Fig. 2.1(b). However, in Section 5.2–5.4 the transverse origo $y = 0$ is placed at the microchannel wall and not at the microchannel center as illustrated in Fig. 2.1(b).

sor Steven T. Wereley, Purdue University, and Professor Henrik Bruus, Technical University of Denmark. The work is published in Lab on a Chip and the paper is appended in Chapter B. In Sections 5.1–5.4, part of the paper is reproduced in a slightly modified version to align with the rest of the thesis, and in particular the introductory Chapters 1-3. The reader is referred to Chapter B for more details on the actual experimental setup and procedure, and the presentation of an analysis of the connection between the presented acoustophoretic particle velocities and continuous flow-mode acoustophoresis typically used in acoustophoretic separation applications.

Section 5.5 is based on work done in collaboration with Professor Thomas Laurell and Dr. Per Augustsson, Lund University, and Professor Henrik Bruus, Technical University of Denmark. The work is submitted for publication in Physical Review E and the paper and supplemental information are appended in Chapter F. In Section 5.5, part of the paper is reproduced in a slightly modified version to align with the rest of the thesis, and in particular the introductory Chapters 1-3.

5.1 Automated and temperature-controlled acoustophoresis platform

In order to achieve high-precision acoustophoresis measurements that are reproducible and reliable the underlying acoustic resonances need to be stable. This allows the possibility of carrying out a large number of repeated measurements ensuring a large statistical basis and provides a base for investigating a large parameter space in a reliable manner. In this section we describe an automated and temperature-controlled platform for obtaining such stable measurements and this platform is the central groundwork for our 2D μPIV and 3D A-μPTV acoustophoresis characterization measurements presented in this chapter, in Chapter 6, in Section 5.5, and in Section 7.2.

5.1.1 Experimental setup

To obtain a strong and stable acoustic resonance for a given piezo transducer we take the following points into consideration. (i) The electronic signal that drives the transducer must have a stable frequency f and peak-to-peak voltage U_{pp}. (ii) The acousto-mechanical contact between the transducer and the chip must be stable and ideally acoustically loss-free, preferably by using a hard epoxy glue. (iii) The amount of silicon/glass surrounding the microchannel should be minimized to maximize the ratio of acoustic energy inside the microchannel compared to the acoustic energy in the bulk of surrounding materials. (iv) The use of soft materials connected to the chip (as e.g. fluidic tubing) must be kept to a minimum to reduce acoustic loses. (v) The temperature of the chip must be kept constant as the temperature dependence of the mechanical properties of the chip (speed of sound, density, Young's modulus, and Poisson's ratio) translate into a
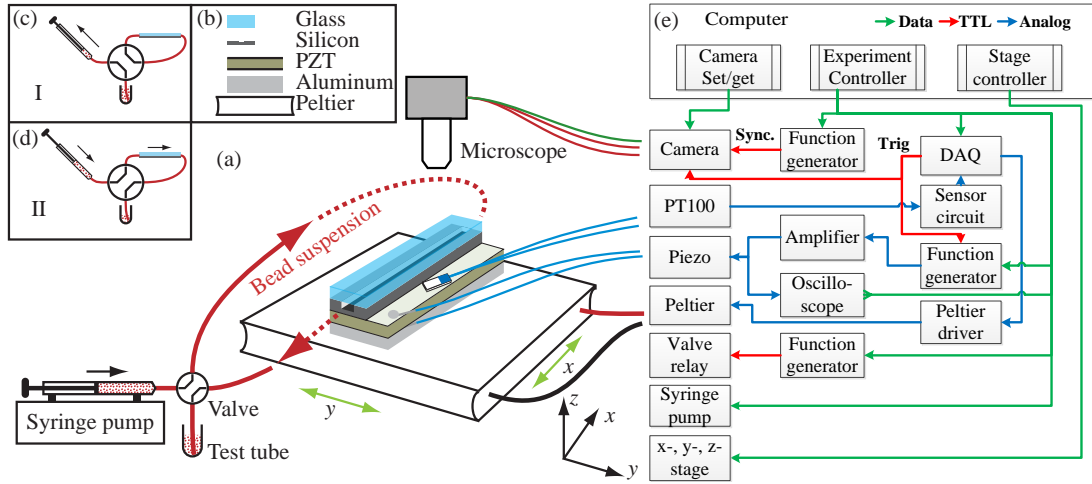
Figure 5.1: (a) Schematic of the acoustophoresis model chip, Section 2.1, as it is placed in the automated and temperature-controlled acoustophoresis platform located in the Laurell laboratory, Lund University, Sweden. (b) The chip is glued to the piezoelectric transducer (PZT) ensuring a fixed and stable acoustic coupling and the transducer is sandwiched and glued together with an aluminum slab and Peltier element resting on the microscope stage. (c-d) The chip is connected to the sample test tube with a motorized 4-diagonal valve allowing loading and reloading of newly stirred suspension. (e) Diagram of the software and hardware configuration controlling the temperature and experimental timing sequence, positioning of the channel, and the camera setup. More details are given in Ref. [36] appended in Chapter B. Adapted from Ref. [36].

temperature dependence of the resonance frequency, and hence of the acoustic energy in the microchannel. In the following we give a brief introduction to our acoustophoresis platform shown in Fig. 2.1(e) and sketched in Fig. 5.1.

Assembly. In the platform we use the experimental model chip described in Section 2.1. The chip is interfaced with pieces of silicone tubing glued to the chip inlet and outlet at each end, oriented along the channel axis and in order to achieve good long term stability, the chip and all platform parts are glued together. From bottom and up the parts are: an aluminum mounting plate also serving as heat sink, a Peltier element (40 mm × 40 mm), an aluminum bar, the piezoelectric transducer (piezo) covering the entire bottom of the chip, and the chip. A Pt100 thermo-resistive element for temperature measurement was glued onto the piezo alongside the acoustophoresis chip, see Fig. 2.1(e) and Fig. 5.1.

Actuation and temperature control. The piezo was driven by a function generator at a frequency f close to 2 MHz via a power amplifier circuit and the peak-to-peak voltage amplitude U_{pp} over the piezo was recorded with an oscilloscope. The temperature of the setup was controlled using a PID control loop using the Pt100 and the Peltier element to probe and regulate the temperature T, respectively.

Loading and reloading of particle suspension. The microchip is loaded

and reloaded via a syringe pump and a motorized 2-position 4-way diagonal valve. When the valve is in its initial position, microparticle suspension can be withdrawn from a test tube into a 1-mL syringe, while the inlet and outlet of the microchannel is short circuited, abruptly stopping flow in the channel. Switching the valve connects the syringe to the chip inlet, while the outlet connects to the test tube. The configuration has two main advantages: microbeads can be reused for several passages through the microchannel, and the repeated loading and unloading of sample at high flow rates induces the stirring of microparticles in the test tube avoiding microparticles sedimenting at the bottom of the test tube.

Imaging. To record the motion of suspended microparticles in the chip we used a bright field microscope equipped with a high-speed camera with frame rates ranging from 50 to 800 Hz. The image size was 1280×640 pixels corresponding to 0.88 mm $\times 0.44$ mm in the xy object plane (i.e. 1 pixel ~ 0.69 µm), i.e. in Fig. 2.1(b) the length l becomes 0.88 mm. The image of a 5-µm-diameter particle is thus $\sim 7 \times 7$ pixels.

Automation. The entire acoustophoresis platform is controlled by a Lab-View program such that a sequence of predefined experiments can be run in an automated manner. The program regulates the temperature in a PID-loop, creates the gate signal to actuate ultrasound and trig the camera, it reads off the voltage over the piezo from an oscilloscope, and it further controls the syringe pump and the motorized valve.

5.1.2 Experimental procedure

The acoustophoresis platform is designed primarily for carrying out stop-flow experiments with the ultrasound as the only driving force. To set up a given experiment one needs to provide the following parameters to the control software: ultrasound frequency f and amplitude U_{pp}, oscilloscope measurement range, camera frame rate, temperature set point T_0, ultrasound gate time, temperature settling time, and number of repeats $n_{\mathrm{tot}}^{\mathrm{pair}}$. Once initiated, the software automatically executes the timing of events for each individual acoustophoretic focusing experiment throughout the experimental series in the following order, Fig. 5.1(e):

1. The valve is switched to position I, Fig. 5.1(c), and bead suspension is withdrawn from the test tube into the syringe.

2. The valve is switched to position II, Fig. 5.1(d), and bead suspension is injected through the chip into the test tube.

3. The valve is switched back to position I to stop the flow in the microchannel, and the remaining bead suspension is emptied into the test tube to induce mixing.

4. The system is idle for about 10 s to allow the temperature to stabilize to within ± 0.1 °C of the preset value.

5. A gate signal activates the ultrasound for ~ 100 ms and triggers the camera to capture a predefined number of frames.
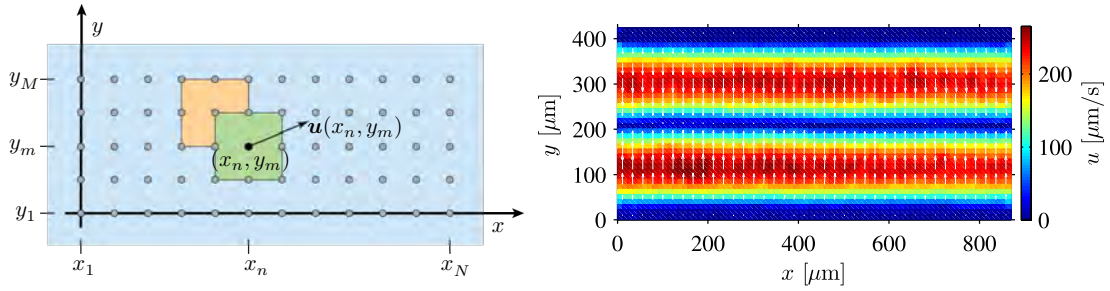
Figure 5.2: (a) Sketch of a given µPIV image frame (blue rectangle) divided into $N \times M$ interrogation windows (green square) of size $S \times S$ pixels and centered around the discrete grid points (x_n, y_m) (gray circles). The interrogation windows overlap they neighbours by 50 % (light orange square). The µPIV interrogation window at each grid point results in a 2D velocity vector $\boldsymbol{u}(x_n, y_m)$ (black arrow). (b) µPIV measurement of the acoustophoretic velocity $\boldsymbol{u}$ (white arrows) and its magnitude (colorplot) of 5-µm polystyrene beads suspended in water and driven at frequency $f = 1.940$ MHz, voltage $U_{\mathrm{pp}} = 1$ V, and temperature $T = 25°$. Adapted from Refs. [36, 37].

6. The piezo voltage amplitude U_{pp} is registered via the oscilloscope. It has an uncertainty of 5 %.

Throughout this chapter we use the above-described procedure to investigate various aspects of acoustophoretic motion in stop-flow mode using a water suspension of polystyrene particles with the addition of 0.01 % of surfactant Tween20. In Sections 5.2 to 5.4, we investigate particles of diameter $2a = (5.16 \pm 0.08)$ µm, while in Section 5.5 we investigate particles of diameters ranging from 0.6-10 µm. The particle concentration is kept low to avoid particle-particle interactions to ensure the validity of the single-particle theory presented in Section 3.5.

Having now established the acoustophoresis platform and measurement procedures we move to the µPIV analysis of the experimental image data to determine the acoustophoretic microparticle velocities.

5.2 µPIV for acoustophoresis measurements

µPIV is a flow measurement technique for detailed determination of the velocities of groups of tracer particles in microfluidic systems [85–89]. The technique is based on digital image frames that are sub-divided into interrogation windows centered around (x_n, y_m) and containing $S \times S$ pixels (rectangular area can be chosen) at positions $\boldsymbol{r}$ with intensity $I(x_n, y_m, t, \boldsymbol{r})$ at time t, see the sketch in Fig. 5.2(a). The core of the µPIV technique is the discrete cross-correlation function C_{corr} formed by the pixel intensities I from two interrogation windows

(denoted an image pair), separated by a short time interval Δt,

$$C_{\text{corr}}\left(x_n, y_m, t, \Delta t, \Delta \boldsymbol{r}\right) = \frac{1}{S^2} \sum_{\boldsymbol{r}^{\text{pix}}}^{S^2} I\left(x_n, y_m, t, \boldsymbol{r}_{\text{pix}} + \Delta \boldsymbol{r}\right) I\left(x_n, y_m, t + \Delta t, \boldsymbol{r}_{\text{pix}}\right).$$

(5.1)

The pixel off-set $\Delta \boldsymbol{r}$ is varied until a maximum value of C_{corr} is found, i.e. $\max_{\Delta \boldsymbol{r}}(C_{\text{corr}}) = C_{\text{corr}}(\Delta \boldsymbol{r}_{\text{max}})$. This pixel displacement is then a measure of the local displacement of the tracer particles, and the corresponding particle velocity is given by $\boldsymbol{u}(x_n, y_m) = \Delta \boldsymbol{r}_{\text{max}}/\Delta t$.

High-quality µPIV analysis with good statistics is achieved by repetitive measurements and subsequent averaging of the correlation function C_{corr}, a procedure known as correlation average [90]. In this work, all acoustophoretic experiments were repeated between 25 and 100 times using the automation of the experimental platform. The following procedure was adopted to obtain good µPIV measurements of microparticle acoustophoresis: In a given time-sequence of image frames recorded immediately after the onset of ultrasound, the first frame was discarded to ensure that the acoustic resonance was fully developed; only the second and third frame was analyzed, as the particle distribution for large radiation-dominated particles rapidly becomes inhomogeneous due to the spatial dependence of the acoustic radiation force, Eq. (3.29). Furthermore, we obtained better statistics and sub-pixel resolution by using an iterative window shifting algorithm based on a smoothed continuum version of the discrete correlation function [91]. Finally, the accuracy of the analysis was refined by use of a central difference interrogation window method and a four-point image correction [86].

The µPIV analysis was carried out using the software *EDPIV - Evaluation Software for Digital Particle Image Velocimetry* (http://www.edpiv.com). As part of the analysis, the recorded bright-field images were inverted and the background was subtracted. The background was derived by finding the lowest pixel intensity in the whole data set for each pixel position. To ensure convergence of the µPIV algorithm 20 window-shifting iterations was employed. Unless otherwise stated, the interrogation window size $S \times S$ was set to $S = 64$ pixels, and we used a 50 % overlap such that the side length in the square grid (x_n, y_m) of Fig. 5.2(a) is $S/2 = 32$ pixels. Search radius for the shift-vector $\Delta \boldsymbol{r}$ was set to 20 pixels.

Depth of correlation. In µPIV all the particles in the volume are illuminated, and the thickness of the measurement plane is therefore defined by the depth of field of the microscope objective. This thickness of the measurement plane, denoted the depth of correlation (DOC), was defined by Meinhart *et al.* [92] as twice the distance from the object plane to the nearest plane for which the particles are sufficiently defocused such that they no longer contributes significantly to the cross-correlation analysis. The first analytical expression for the DOC was derived by Olsen and Adrian [93], an expression later improved by

Particle diameter $2a$	DOC, Eq. (5.2)
0.6 µm	14 µm
1.0 µm	16 µm
1.9 µm	22 µm
2.6 µm	27 µm
5.1 µm	47 µm
10.2 µm	94 µm

Table 5.1: Depth of correlation (DOC) for some particle diameters $2a$ used throughout this thesis. Numerical aperture $NA = 0.4$, Magnication $M = 20$, and Optical wavelength $\lambda_{\mathrm{opt}} = 520$ nm.

Rossi *et al.* [94] as

$$\mathrm{DOC} = \frac{n_{\mathrm{w}}}{n_0} \left\{ \frac{1 - \sqrt{\epsilon}}{\sqrt{\epsilon}} \left(\frac{n_0^2}{NA^2} - 1 \right) \times \left[d_{\mathrm{p}}^2 + 1.49\lambda_{\mathrm{opt}}^2 \left(\frac{n_0^2}{NA^2} - 1 \right) \right] \right\}^{1/2}, \qquad (5.2)$$

where n_{w} and n_0 is the index of refraction for water and air, respectively, NA is the numerical aperture of the objective, M is the objective magnification, λ_{opt} is the optical wavelength, and ϵ is the threshold parameter for which a particle's contribution to the correlation function can be neglected. $\epsilon = 0.01$ is a reasonable choice. The estimated DOC for six particles sizes are listed in Table 5.1, where we have used a wavelength $\lambda_{\mathrm{opt}} = 520$ nm, which is the wavelength at which the microscope objective is most sensitive.

Discrete acoustophoretic velocity field. From the µPIV analysis we obtain the acoustophoretic velocity field of the tracer particles

$$\boldsymbol{u} = \boldsymbol{u}\left(x_n, y_m\right) = \begin{pmatrix} u_x\left(x_n, y_m\right) \\ u_y\left(x_n, y_m\right) \end{pmatrix}, \qquad (5.3)$$

on the discrete lattice (x_n, y_m) with indices $1 \leq n \leq N$ and $1 \leq m \leq M$, see Fig. 5.2(a). The rectangular lattice has the lengths $L_x = x_N$ and $L_y = y_M$ along the x- and y-direction, respectively. For quantitative comparisons of acoustophoretic velocity fields $\boldsymbol{u}$, we use both the local speed $u(x_n, y_m) = |\boldsymbol{u}(x_n, y_m)|$ and the L^2-norm $||\boldsymbol{u}||$. The square of the L^2-norm is defined as

$$||\boldsymbol{u}||^2 = \frac{1}{NM} \sum_{n=1}^{N} \sum_{m=1}^{M} \left| \boldsymbol{u}\left(x_n, y_m\right) \right|^2. \qquad (5.4)$$

Note that $||\boldsymbol{u}||$ can be thought of as an area-average speed, while $||\boldsymbol{u} - \boldsymbol{u}_{\mathrm{ref}}||^2$ is the variance of $\boldsymbol{u}$ around $\boldsymbol{u}_{\mathrm{ref}}$.

The uncertainty in terms of standard deviation in the velocity fields obtained by µPIV was minimized by optimizing three parameters: the displacement of the tracer particles between the two images in an image pair, the number of repeated measurements, and the size S of the interrogation window. This is the subject for the following three sections.

5.2.1   Optimizing the time-shift for an image pair

In µPIV the best results are obtained if the maximum displacement of the tracer particles within an image pair is about one to a few times the diameter of the particles. To verify this, the image frame was positioned in the channel center ($x = 0$ in Fig. 2.1(d)) with $T = 25$ °C, $f = 1.968$ MHz, and $U_{\mathrm{pp}} = 2.95$ V. We carried out 100 acoustophoresis measurements each recorded with 10 time frames at a frame rate of 800 Hz. From the data, nine different µPIV image pairs can be constructed by pairing frame 1 with frame $1 + n$ (for $n = 1, 2, \ldots, 9$), and this leads to the nine possible time shifts $\Delta t = n \times 1.25$ ms, see Eq. (5.1).

The maximum acoustophoretic velocity in this experiment was measured to be 1 mm/s corresponding to a maximum particle displacement of $n \times 1.8$ pixels for the nine different image-pair time shifts. In Fig. 5.3(a) we plot the normalized area-average acoustophoretic speed $||\boldsymbol{u}||$ as a function of this maximum pixel displacement. A distinct maximum is seen around 7 pixels corresponding to the tracer-particle diameter of 5 µm. In all of the µPIV analysis the piezo voltage U_{pp} was therefore set to achieve this displacement as accurate as possible.

The image-pair time-shift is only one of many parameters of the µPIV analysis we need to optimize. In practice, the determination the acoustophoretic velocity field is a trade-off between the desired velocity accuracy and the time it takes to carry out the experiment and µPIV analysis. For a given microparticle concentration, a certain velocity accuracy requires a minimum number of uncorrelated image pairs $n_{\mathrm{tot}}^{\mathrm{pair}}$ and a maximum interrogation window size $S \times S$. If the interrogation window size is too large, the resolution of the velocity field is too low to resolve the dynamics, but the smaller the window gets, the more experimental repetitions $n_{\mathrm{tot}}^{\mathrm{pair}}$ are needed to ensure a proper bead coverage and thus sufficient statistics in the µPIV analysis. Therefore, it is important to carry out a parametric study of the µPIV analysis settings and number of experimental repetitions for a certain set of experimental parameters, such as camera frame rate and microparticle velocities.

5.2.2   Estimation of the standard deviation

One way to estimate the µPIV standard deviation is to repeat a measurement to obtain $n_{\mathrm{tot}}^{\mathrm{pair}}$ uncorrelated image pairs, and then sub-divide this series into N_{group} groups each containing $n_{\mathrm{group}}^{\mathrm{pair}}$ image pairs ($n_{\mathrm{tot}}^{\mathrm{pair}} = N_{\mathrm{group}} n_{\mathrm{group}}^{\mathrm{pair}}$). For each group a µPIV analysis involving averaging over the $n_{\mathrm{group}}^{\mathrm{pair}}$ cross-correlation functions is performed resulting in N_{group} velocity fields $\boldsymbol{u}_i$. The vector average $\langle \boldsymbol{u} \rangle_{\mathrm{vec}} = \sum_{i=1}^{N_{\mathrm{group}}} \boldsymbol{u}_i / N_{\mathrm{group}}$ is calculated, and the relative standard deviation $\Delta(\boldsymbol{u}, \boldsymbol{u}_{\mathrm{ref}})$ of $\boldsymbol{u}$ around the reference field $\boldsymbol{u}_{\mathrm{ref}} = \langle \boldsymbol{u} \rangle_{\mathrm{vec}}$ can be estimated from the variance $||\boldsymbol{u} - \boldsymbol{u}_{\mathrm{ref}}||^2$, see Eq. (5.4), and the maximum speed u_{max} of $\boldsymbol{u}$, as

$$\Delta\left(\boldsymbol{u}, \boldsymbol{u}_{\mathrm{ref}}\right) = \sqrt{\frac{1}{N_{\mathrm{group}}} \sum_{i=1}^{N_{\mathrm{group}}} \frac{||\boldsymbol{u} - \boldsymbol{u}_{\mathrm{ref}}||^2}{u_{\mathrm{max}}^2}}. \tag{5.5}$$
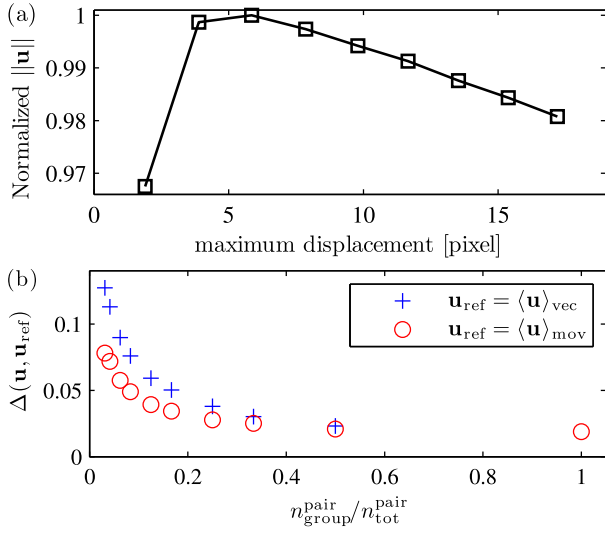
Figure 5.3: (a) Area-average acoustophoretic speed $||\boldsymbol{u}||$ as function of maximum particle displacement in a single-image frame using $n_{\text{tot}}^{\text{pair}} = 100$ and $S = 32$ pixels. (b) Relative standard deviation $\Delta(\boldsymbol{u}, \boldsymbol{u}_{\text{ref}})$ of the acoustophoretic particle velocities $\boldsymbol{u}$ determined by µPIV as function of the amount of correlation averaging $n_{\text{group}}^{\text{pair}}/n_{\text{tot}}^{\text{pair}}$ for a total of $n_{\text{tot}}^{\text{pair}} = 96$ image pairs. $\boldsymbol{u}_{\text{ref}}$ is calculated using either the vector average $\langle\boldsymbol{u}\rangle_{\text{vec}}$ (blue +) or the moving average $\langle\boldsymbol{u}\rangle_{\text{mov}}$ (red ∘), see Eq. (5.5). Adapted from Ref. [36].

In Fig. 5.3(b) is shown the result of this vector-average estimate (blue +) of the relative standard deviation $\Delta(\boldsymbol{u}, \langle\boldsymbol{u}\rangle_{\text{vec}})$ versus $n_{\text{group}}^{\text{pair}}/n_{\text{tot}}^{\text{pair}}$ for $n_{\text{tot}}^{\text{pair}} = 96$. In the limit where the sub-groups contain a single image pair ($n_{\text{group}}^{\text{pair}} = 1$) each of which leads to a µPIV velocity field by a single cross-correlation function Eq. (5.1), the method corresponds to pure vector averaging of the resulting $N_{\text{group}} = n_{\text{tot}}^{\text{pair}} = 96$ velocity vector fields. In the opposite limit ($n_{\text{group}}^{\text{pair}} = n_{\text{tot}}^{\text{pair}}$), the average of the correlation functions of all 96 image pairs is used to calculate a single µPIV velocity field ($N_{\text{group}} = 1$), and the method corresponds to pure correlation function averaging. For intermediate values $1/96 < n_{\text{group}}^{\text{pair}}/n_{\text{tot}}^{\text{pair}} < 1$, the method is a combination of vector averaging and correlation averaging. In Fig. 5.3(b) it is seen that for the given 96 image pairs, $\Delta(\boldsymbol{u}, \langle\boldsymbol{u}\rangle_{\text{vec}})$ decreases monotonically from 12 % for $n_{\text{group}}^{\text{pair}}/n_{\text{tot}}^{\text{pair}} = 0.01$ to below 3 % for $n_{\text{group}}^{\text{pair}}/n_{\text{tot}}^{\text{pair}} = 0.5$ supporting the fact [87] that correlation average yields better precision in µPIV than vector average. Although viable, the vector-averaging method is a time-consuming way (24 h to obtain the results for $\Delta(\boldsymbol{u}, \langle\boldsymbol{u}\rangle_{\text{vec}})$ to obtain the standard deviation as it requires additional µPIV analysis and additional number of experimental repeats. A more efficient way is to use the 3-by-3-point moving-average method, where $\Delta(\boldsymbol{u}, \boldsymbol{u}_{\text{ref}})$ is calculated using for each point (x_n, y_m) in the grid the nearest-neighbor average $\boldsymbol{u}_{\text{ref}}(x_n, y_m) = \langle\boldsymbol{u}\rangle_{\text{mov}}(x_n, y_m)$ of the velocity $\boldsymbol{u}_i$ of the 3×3 points having (x_n, y_m) in the center. It is seen in Fig. 5.3(b) that the moving-average estimate $\Delta(\boldsymbol{u}, \langle\boldsymbol{u}\rangle_{\text{mov}})$ (red ∘) agrees well with the vector-average method, settling around 2 % for $n_{\text{group}}^{\text{pair}}/n_{\text{tot}}^{\text{pair}} = 1$. No additional effort is needed when using the moving-average method and thus it is used in the rest of the chapter to evaluate the standard deviation $\Delta(\boldsymbol{u}, \boldsymbol{u}_{\text{ref}})$.
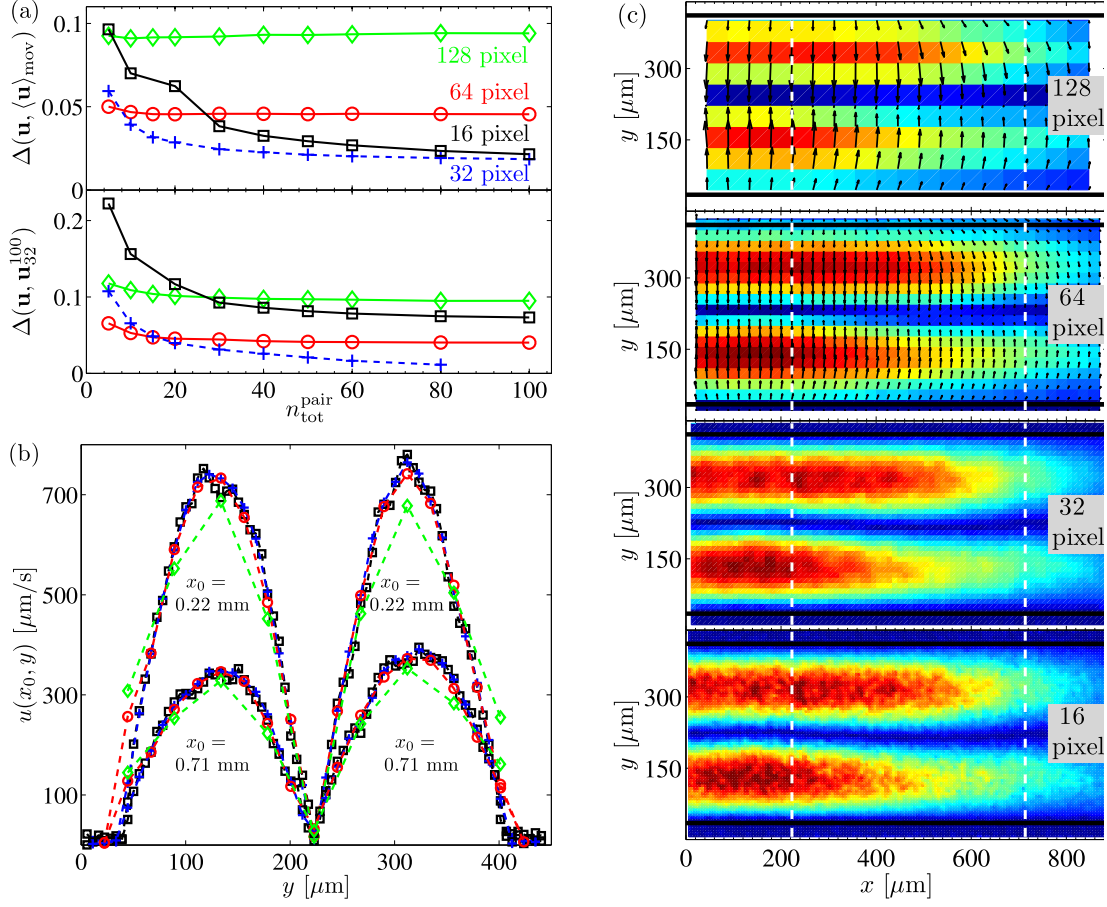
Figure 5.4: µPIV measurements in a single image frame of fixed position of the acoustophoretic particle velocities versus the number $n_{\text{tot}}^{\text{pair}}$ of uncorrelated image pairs and of the interrogation window size S. Experimental parameters are $T = 25$ °C, $f = 1.968$ MHz, and $U_{\text{pp}} = 1.89$ V. (a) The relative deviation $\Delta(\boldsymbol{u}, \boldsymbol{u}_{\text{ref}})$ of the velocity $\boldsymbol{u}$ relative to reference velocities $\langle \boldsymbol{u} \rangle_{\text{mov}}$ (moving average) and $\boldsymbol{u}_{32}^{100}$ ($S = 32$ pixels and $n_{\text{tot}}^{\text{pair}} = 100$) as a function of $n_{\text{tot}}^{\text{pair}}$ and S. (b) Line plots of the velocity magnitude $u(x_0, y)$ along the transverse y-direction at $x_0 = 223$ µm and $x_0 = 713$ µm with $n_{\text{tot}}^{\text{pair}} = 100$. (c) Acoustophoretic particle velocity $\boldsymbol{u}$ (black arrows) and its magnitude u (colors from 0 µm s^{-1} (dark blue) to 800 µm s^{-1} (dark red)). The white dashed lines indicate the two line plots shown in panel (b). Adapted from Ref. [36].

5.2.3 Optimizing interrogation window size and number of image pairs

Next step is to investigate how the quality of the µPIV results depends on the number $n_{\text{tot}}^{\text{pair}}$ of uncorrelated image pairs (number of repeats) and the pixel size S of the quadratic $S \times S$ interrogation window. Other more detailed studies of additional µPIV parameters such as the search radius, number of window shifting iterations, and various central-difference schemes are not treated here.

In Fig. 5.4(a) is shown plots of the relative standard deviation $\Delta(\boldsymbol{u}, \boldsymbol{u}_{\text{ref}})$ of the velocity field $\boldsymbol{u}$ as a function of $n_{\text{tot}}^{\text{pair}}$ and S using the moving-average method

$\boldsymbol{u}_{\mathrm{ref}} = \langle \boldsymbol{u} \rangle_{\mathrm{mov}}$ with $n_{\mathrm{group}}^{\mathrm{pair}} = n_{\mathrm{tot}}^{\mathrm{pair}}$ and $N_{\mathrm{group}} = 1$. As the number of uncorrelated image pairs $n_{\mathrm{tot}}^{\mathrm{pair}}$ increases, $\Delta\left(\boldsymbol{u}, \langle \boldsymbol{u} \rangle_{\mathrm{mov}}\right)$ decreases. The high uncertainty $\sim 10\ \%$ for $S = 128$ pixels is also visible in the line and color plots of the speed u in panel (b) and (c), respectively. The effect of the low tracer particle concentration used, is reflected in the observation that the lowest standard deviation is obtained for $S = 32$ pixels. For the smallest interrogation window size $S = 16$ pixels the number of tracer particles per window is so low that the statistical fluctuations increase noticeably, compare 16 pixels and 32 pixels in panel (c). The relative standard deviation for $S = 32$ pixels drops below 3 % already for $n_{\mathrm{tot}}^{\mathrm{pair}} = 20$. This tendency is supported by the plot of $\Delta\left(\boldsymbol{u}, \boldsymbol{u}_{\mathrm{ref}}\right)$ using the velocity field $\boldsymbol{u}_{32}^{100}$ obtained for $S = 32$ pixels and $n_{\mathrm{tot}}^{\mathrm{pair}} = 100$ as $\boldsymbol{u}_{\mathrm{ref}}$ for all four values of S. This plot also shows that to obtain an uncertainty below 5 % it is thus sufficient to use $n_{\mathrm{tot}}^{\mathrm{pair}} = 20$ and $S = 64$ leading to a spatial resolution of 20 µm. In Sections 5.3 and 5.4 we use $S = 64$, while we in Section 5.5 primarily use $S = 32$ for most of the results.

In Fig. 5.4(b) are shown two line plots of the speed $u\left(x_0, y\right)$ along the transverse y-direction at $x_0 = 223$ µm and $x_0 = 713$ µm with $n_{\mathrm{tot}}^{\mathrm{pair}} = 100$ for the same data as in panel (a). Except for the most coarse-grained resolution ($S = 128$ pixels), the other three window sizes $S = 64$ pixels, 32 pixels, and 16 pixels agree well. However, close to the wall both $S = 128$ pixels and 64 pixels differs from $S = 32$ pixels and 16 pixels, because the large window sizes results in a significant overlap of windows with the channel walls, which results in an erroneous contribution of non-zero velocities outside the channel.

In Fig. 5.4(c) are shown plots of the acoustophoretic velocity field $\boldsymbol{u}$ (arrows) and speed u (colors) corresponding to the data in Fig. 5.4(b) using $n_{\mathrm{tot}}^{\mathrm{pair}} = 100$ and $S = 128$, 64, 32, and 16 pixels. The resolution clearly increases as S decreases, but simultaneously the noise increases because the number of tracer particles in each interrogation window decrease. In the color plots are marked the two x-coordinates, $x_0 = 223$ µm and $x_0 = 713$ µm corresponding to the two line plots in Fig. 5.4(b).

As observed, a lower standard deviation $\Delta\left(\boldsymbol{u}, \boldsymbol{u}_{\mathrm{ref}}\right)$ can be obtained by increasing $n_{\mathrm{tot}}^{\mathrm{pair}}$. However, the cost is an increased time t^* for data acquisition and analysis: $t^* = (\tilde{t}_{\mathrm{exp}} + \tilde{t}_{\mathrm{img}} + \tilde{t}_{\mathrm{PIV}})n_{\mathrm{tot}}^{\mathrm{pair}}$, where $\tilde{t}_{\mathrm{exp}}$ is the measurement time per image pair, $\tilde{t}_{\mathrm{img}}$ the image analysis time per image pair, and $\tilde{t}_{\mathrm{PIV}}$ the time for the total µPIV analysis per image pair. Rough estimates of the times per image pair are $\tilde{t}_{\mathrm{exp}} \sim 30$ s, $\tilde{t}_{\mathrm{img}} \sim 20$ s, and $\tilde{t}_{\mathrm{PIV}} \sim 60$ s, which for $n_{\mathrm{tot}}^{\mathrm{pair}} = 20$ results in a total time $t^* \sim 30$ min to run one set of parameters.

We have now established the temperature-stable acoustophoresis platform and µPIV analysis, and the following Sections 5.3 and 5.4 we investigate the particle velocities globally and as function of driving voltage, driving frequency, and resonator temperature, respectively.

Figure 5.5: Global acoustophoretic velocity structure for three acoustic resonance modes of frequency f = 1.940 MHz, 1.951 MHz, and 1.968 MHz, respectively. (a) Schematic of the chip. The global velocity structure is measured in the 12-mm-long section indicated with a dashed black rectangle, while the single-image frame investigated in Secs. 5.2 and 5.4 is indicated with dashed white lines. (b) Normalized acoustophoretic speed $u(x,y)/u_{\max}$ (colors from 0 (dark blue) to 1 (dark red)) measured by μPIV at $T = 25$ °C and the three frequencies f = 1.940 MHz, 1.951 MHz, and 1.968 MHz. For each frequency the data consists of 15 stitched image frames (white lines) each a result of 25 repeated measurements. (c) Color plot of the natural logarithm of $u(x,y)/u_{\max}$ from panel (b). Adapted from Ref. [36].
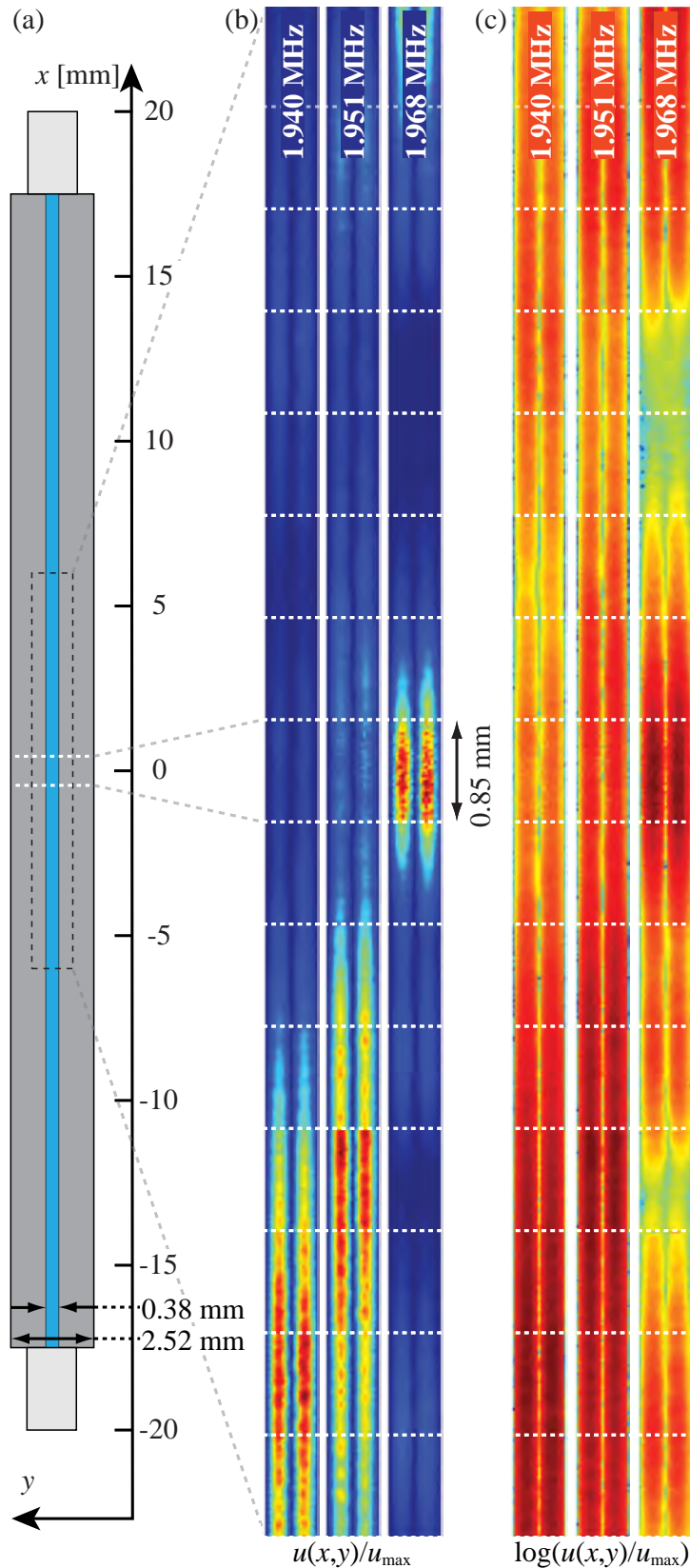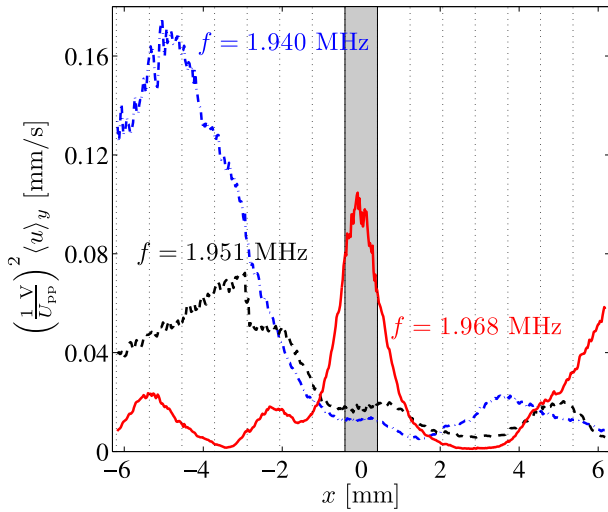
Figure 5.6: Average $\langle u \rangle_y$ along y, Eq. (5.6), of the acoustic velocities as function of the axial position x along the 12-mm channel section shown in Fig. 5.5 for the three resonance frequencies $f = 1.940$ MHz (dash-dotted blue line), 1.951 MHz (dashed black line), and 1.968 MHz (solid red line) at $T = 25$ °C. The borders between the 15 neighboring image frames are marked by vertical dashed black lines, while a light gray color indicate the single-image frame at the channel center $x = 0$ investigated in Secs. 5.2 and 5.4. Adapted from Ref. [36].

5.3   Global resonance structure

In Fig. 5.5 we plot the µPIV-determined particle velocities along a 12-mm-long section around the center of the 35-mm-long microchannel sketched in panel (a). The color plots in panel (b) show the speed u/u_{max} of the acoustophoretic velocities for the 5-µm-diameter polystyrene tracer particles normalized by the maximum speed u_{max}. For each frequency a total of 15 adjacent image frames each of 0.85-mm width were stitched together with an overlap of 10 %, and the acoustophoresis experiment was repeated 25 times for each position of the image frame. For all measurements the temperature was kept constant at 25 °C.

To accommodate for the high dynamic range in the acoustophoretic velocity of the tracer particles, the camera frame rate was set to either 400 Hz or 800 Hz. To achieve the same microbead displacement for each of the three frequencies as described in Section 5.2.1, the driving voltage was set to $U_{\text{pp}} = 2.00$ V at $f = 1.940$ MHz, 1.25 V at 1.951 MHz, and 0.75 V at 1.968 MHz. The interrogation window size was $S = 64$ pixels leading to a grid size of 32 pixels and thus a grid resolution of 22 µm.

In Fig. 5.5(c) more details in the spatial structure of the resonances are made visible by color plots of $\log(u/u_{\text{max}})$. This is particularly evident for $f = 1.968$ MHz, where four local maxima becomes visible. We notice that all three resonances yield acoustophoretic particle velocities $\boldsymbol{u}$ with a mirror symmetry around the center line in the transverse y-direction resulting in a almost perfect straight line pressure nodal-line with zero $\boldsymbol{u} = \boldsymbol{0}$. However, equally clear are the strong variations along the channel axis (x-direction) in the measured $\boldsymbol{u}$-field. Despite the near-perfect geometry, the present data does not exhibit the sinusoidal axial pressure distribution in the resonance predicted by the idealized hard-wall model discussed in Section 3.2.1. The reasons for this may be sought in the walls not being infinitely hard, the asymmetry due to the acoustical differ-

ences between the bottom silicon and top Pyrex layer, the presence of inlet/outlet tubing, and imprecise mounting of the chip, the piezo transducer, and the Peltier element.

To allow for quantitative comparisons between the three resonance modes, we do two things. First, we abandon the normalization used in Fig. 5.5(b), and instead use the absolute but voltage-calibrated, acoustophoretic velocities $\left(\frac{1\,\mathrm{V}}{U_{\mathrm{pp}}}\right)^2 \boldsymbol{u}$; and second, given the regular behavior in the transverse direction, we introduce the y-direction average $\langle u\rangle_y$ of the speed $u\left(x_n, y_m\right)$,

$$\langle u\rangle_y = \frac{1}{M}\sum_{m=1}^{M} u\left(x_n, y_m\right), \tag{5.6}$$

which is a function of axial coordinate x_n. In Fig. 5.6 we plot the voltage-corrected speed $\left(\frac{1\,\mathrm{V}}{U_{\mathrm{pp}}}\right)^2 \langle u\rangle_y$ versus axial position x for each of the three resonance frequencies at $T = 25\ °\mathrm{C}$. It is clear that globally the 1.940-MHz-mode (blue) leads to the highest acoustophoretic velocity, followed by 1.968 MHz (red), and 1.951 MHz (black) being lowest. Counting local maxima, the 1.940-MHz mode (blue) has two peaks (at -4.8 mm and 3.6 mm), the 1.951-MHz mode (black) three (at -2.8 mm, 0.8 mm and 4.6 mm), and the 1.968-MHz mode (red) four (at -5.2 mm, -2.2 mm, 0 mm, and > 6 mm).

If we restrict ourselves to observe the image frame in the center of the channel (gray box), we now find that the 1.940-MHz mode (blue) is the weakest. Moreover, if we in this single frame let the frequency increase from 1.940 MHz to 1.968 MHz, we see how the magnitude of the subsequent resonances increases. This is the spatial structure of the resonances corresponding to the frequency spectra in Fig. 5.7(b), where the normalized area-average speed increases from 0.05, via 0.3 to 0.6 for the three respective frequencies.

5.4 Frequency, voltage, and temperature

5.4.1 Voltage scan

The piezo driving voltage U_{pp} appears in the acoustic responses as $p_a \propto U_{\mathrm{pp}}$ and $u_y \propto U_{\mathrm{pp}}^2$. The latter is clear from Eq. (3.50) and the fact that $E_{\mathrm{ac}} \propto p_a^2$. U_{pp} therefore has a decisive influence of which frame rate to choose for the µPIV analysis. The dependence of the acoustophoretic velocity u on U_{pp} was evaluated for the three frequencies $f = 1.940$ MHz, 1.951 MHz, and 1.968 MHz, each identified as a local maximum of u in the recorded frequency spectrum at $T = 25°\mathrm{C}$. The maximum allowed driving voltage $U_{\mathrm{pp}}^{\mathrm{max}}$ was limited by the maximum camera frame rate of 800 Hz at the chosen image size. For each frequency, $U_{\mathrm{pp}}^{\mathrm{max}}$ was adjusted to obtain the optimal tracer particle displacement shown in Fig. 5.3(a), and then the acoustophoretic velocity field was acquired for seven driving voltages ranging from zero to $U_{\mathrm{pp}}^{\mathrm{max}}$.

From the analyses of the three resonance frequencies it was verified that the acoustophoretic velocity scales by U_{pp} to the power of 2. For each frequency, the measured data points $||\boldsymbol{u}||$ were fitted to a power law $(U_{pp})^\beta$ resulting in $\beta = 1.7$, 2.1 and 2.0, respectively (data not shown). Fitting instead the measured maximum speed u_{max} yielded the same behavior with a distribution of the power ranging from 1.87 to 2.09. These results agree well with the findings in Section 7.1.1 (Ref. [69]).

5.4.2 Frequency scan

The temperature and frequency dependence of the acoustophoretic velocity was studied within the channel-center single-image frame for actuation frequencies in the range from 1.930 MHz to 1.980 MHz in steps of 1 kHz. The frequency spectrum was scanned at three constant temperatures $T = 23$ °C, 25 °C, and 27 °C, and the spectrum at 25 °C was re-evaluated two days later to validate the reproducibility of the system, see Fig. 5.7.

As described in Section 5.4.1, for each setting of f and T we tune the transducer voltage U_{pp} to a value leading to the optimum pixel displacement in the µPIV analysis shown in Fig. 5.3(a). In Fig. 5.7(a) we plot the measured values of U_{pp} versus frequency f for the three selected temperatures. Together with the U_{pp}-square scaling of the acoustophoretic velocity, we can use this curve to calibrate for the different voltage amplitudes at the different measurements. This calibration has been performed in Fig. 5.7(b), where we plot the normalized area-average speed $\left(\frac{1\,\text{V}}{U_{pp}}\right)^2 ||\boldsymbol{u}||$, such that all values correspond to $U_{pp} = 1$ V and the maximum value in the plot is unity (for $T = 27$ °C and $f = 1.967\,\text{MHz}$). The recording time of each spectrum is ~ 6 hours, but in spite of this long time interval, the moving-average standard deviation $\Delta\left(\boldsymbol{u}, \langle\boldsymbol{u}\rangle_{mov}\right)$ is only of the order of 5 % (the size of the point symbols) in agreement with Fig. 5.3(b). Moreover, the relative difference between the day-1 and the day-3 spectrum at 25 °C is also only about 5 %.

In the frequency dependence of $||\boldsymbol{u}||$, we observe three peaks at the frequencies $f = 1.940$ MHz, 1.951 MHz, and 1.968 MHz. Measuring the shift in Lorentzian peaks fitted to the data points, the temperature sensitivity $\Delta f/\Delta T$ of the resonance frequency of the 1.940-MHz peak is found to be ≈ 1.25 kHz/°C, for the 1.951-MHz-peak ≈ 1.0 kHz/°C, and for the 1.968-MHz-peak ≈ 0.0 kHz/°C. These temperature-induced shifts of the resonance frequencies depend on the spatial distribution of the resonance mode in the full 3D structure of the system and the temperature coefficients of the system materials, and they are therefore difficult to determine, even using numerical simulation. However, the measured sensitivities are the right order of magnitude given the following estimates: If we assume that the entire mode is confined in the water, then from $f(T) = c_{wa}(T)/(2w)$ and the table values of $c_{wa}(T)$ we find $\Delta f/\Delta T \approx 3.5$ kHz/°C, while the sensitivity for Pyrex given $f(T) = c_{py}(T)/(2W)$ is $\Delta f/\Delta T \approx 0.1$ kHz/°C (for longitudinal

Figure 5.7: µPIV measurements of the particle velocities in channel-center single-image frame as function of frequency and temperature. (a) Transducer voltage U_{pp} versus frequency f used to maintain the particular maximum particle velocity which leads to the optimal maximum pixel displacement in the µPIV analysis, see Fig. 5.3(a), at temperatures $T = 23°$ (red ×), $25°$ (blue $\bigcirc$ for day 1, blue ● for day 3), and $27°$ (black △). (b) Semi-logarithmic plot of the area-averaged acoustophoretic speed $(\frac{1\,\mathrm{V}}{U_{pp}})^2\|\boldsymbol{u}\|$ versus f normalized to unity at $f = 1.967$ MHz and $T = 27°$. All data points are calibrated to correspond to $U_{pp} = 1$ V by use of panel (a) and the $(U_{pp})^2$-dependence. (c) Color plot of the velocity magnitude (dark blue 0 mm/s, dark red 0.12 mm/s) normalized to $U_{pp} = 1$ V as in the previous panel for 3×3 temperature and frequency values near the 1.951-MHz resonance. Adapted from Ref. [36].
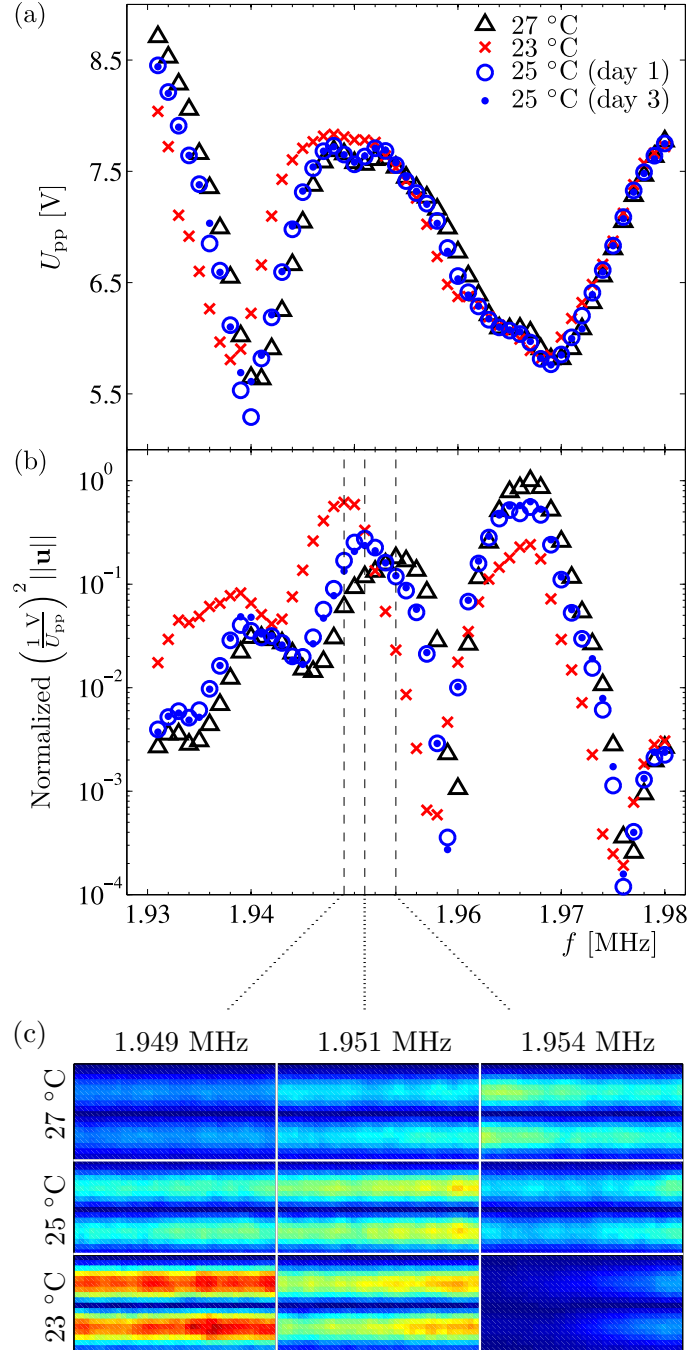
waves).

5.5 Determination of the radiation-to-streaming transition

This section is motivated by the push within contemporary acoustofluidics to control sub-micrometer particles such as small bacteria, vira, and biomolecules. Experimental work on acoustophoresis has primarily dealt with cases in the radiation-dominated regime, typically for particle diameters larger than 2 μm as estimated in Section 3.5. The cross-over from radiation-dominated to streaming-dominated acoustophoresis has been reported by several groups [47, 84, 95], but has not been fully understood. However, understanding and controlling the ratio of radiation- and streaming-induced acoustophoretic velocities may be the key for future realization of ultrasound manipulation of sub-micrometer particles.

In this section we use the experimental model system, the acoustophoresis platform, and the micro-PIV analysis, Secs. 2.1, 5.1, and 5.2, respectively, to make a detailed study of the cross-over from radiation-dominated to streaming-dominated acoustophoresis as function of decreasing particle size, actuation frequency, and suspending medium. The following is a reproduction of part of the paper appended in Chapter F, where more information may be found.

5.5.1 Experimental procedure

Experiments were carried out to test the validity of the theoretical predictions for the acoustophoretic particle velocity Eq. (3.53) in the horizontal ultrasound symmetry plane and for the ratio of the corresponding radiation and streaming-induced velocities, see Eq. (3.47) and Fig. 3.3.

Table 5.2: The nominal and the measured diameter of the polystyrene particles used in the experiment. Adapted from [37]

Nominal diameter	Measured diameter $(2a)$
591 nm	(0.59 ± 0.03) μm[a]
992 nm	(0.99 ± 0.05) μm[a]
2.0 μm	(1.91 ± 0.07) μm[b]
3.0 μm	(2.57 ± 0.07) μm[b]
5 μm	(5.11 ± 0.16) μm[b]
10 μm	(10.16 ± 0.20) μm[b]

[a]Value from manufacturer and assumed 5 % standard deviation.

[b]Measured by Coulter counter.

5.5.1.1   Microparticle suspensions

In this measurement series we examine two types of microparticle; polystyrene particles suspended in Milli-Q water and polystyrene particles suspended in a 0.75:0.25 mixture of Milli-Q water and glycerol. To each of the two suspending liquids was added 0.01 % w/V Triton-X surfactant. The material parameters of the suspensions are listed in the List of Material Parameters on page xvi. Note that the rescaled momentum diffusivity ν/Φ of the glycerol suspension is 3 times larger than that for the Milli-Q water suspension.

We analyzed 12 particle suspensions by adding particles of 6 different diameters $2a$ from 0.6 µm to 10 µm to the two liquids. The particle diameters were measured using a Coulter Counter (Multisizer 3, Beckman Coulter Inc., Fullerton, CA, USA) and fitting their distributions to Gaussian distributions, see Supplemental Material. The resulting diameters are listed in Table 5.2.

The concentration C of the particles were calculated based on the concentrations provided by the manufacturer and varies in this work from 10^{10} m^{-3} for the largest particles in the 0.75:0.25 mixture of water and glycerol to 10^{15} m^{-3} for the smallest particles in the pure water solution. The concentrations correspond to mean inter particle distances $C^{-1/3}$ ranging from 4 particle diameters for the largest 10-µm particle in water to 173 particle diameters for the smallest 0.6-µm particle in the 0.75:0.25 mixture of water and glycerol. Mikkelsen and Bruus [53] have reported that hydrodynamic effects become significant for inter-particle distances below 2 particle diameters. Thus we can apply the single-particle theory presented in Section 3.5.

5.5.1.2   Measurement series

We measured the acoustophoretic velocities of polystyrene microparticles in the following four series of experiments, the second being a repeat of the first:

MQ0: Milli-Q water, $f = 1.940$ MHz, $\lambda = 2w$,
  and $2a = 1.0, 1.9, 2.6,$ and 5.1 µm.
MQ1: Milli-Q water, $f = 1.940$ MHz, $\lambda = 2w$,
  and $2a = 0.6, 1.0, 1.9, 2.6, 5.1,$ and 10.2 µm.
MQ2: Milli-Q water, $f = 3.900$ MHz, $\lambda = w$,
  and $2a = 0.6, 1.0, 1.9, 2.6, 5.1,$ and 10.2 µm.
Gl2: 0.75:0.25 Milli-Q water:glycerol, $f = 2.027$ MHz, $\lambda = 2w$,
  and $2a = 0.6, 1.0, 1.9, 2.6, 5.1,$ and 10.2 µm.

Given the different particle diameters, we thus have the above-mentioned 22 sets of acoustophoretic particle-velocity measurements, each consisting of 50 to 250 measurement cycles. All experiments were carried out at a fixed temperature of 25 °C and the applied piezo voltage U_{pp}^*. The camera frame rate was chosen such that the particles would move at least a particle diameter between two consecutive images. The measurement field of view was 1280×640 pixels

corresponding to 892 µm × 446 µm. The imaging parameters were: optical wavelength 520 nm for which the microscope objective is most sensitive, numerical aperture 0.4, and magnification 20. See acquisition details in the Supplemental Information in Chapter F.

5.5.1.3 Micro-PIV analysis

For the MQ1, MQ2, and Gl1 series, the interrogation window size was 32 × 32 pixels with a 50 % overlap resulting in a 79 × 39 square grid with 16 pixels between each grid point. For the MQ0 series, the interrogation window size was 64 × 64 pixels with a 50 % overlap resulting in a 39 × 19 square grid with 32 pixels between each grid point.

5.5.2 Results

The core of our results is the 22 discrete acoustophoretic particle-velocity fields obtained by micro-PIV analysis of the 22 sets of acoustic focusing experiments and shown in the Supplemental Information in Chapter F. As in Section 5.2, the measured microparticle velocities $\boldsymbol{u}$ are thus represented on a discrete $x_n \times y_m$ micro-PIV grid, Eq. (5.3). All measured velocities presented in the following are normalized to their values at $U_{\mathrm{pp}} = 1$ V using the voltage-squared law [69],

$$\boldsymbol{u} = \left(\frac{1 \text{ V}}{U_{\mathrm{pp}}^*}\right)^2 \boldsymbol{u}^*, \tag{5.7}$$

where the asterisk denotes the actual measured values. As a result, the extracted velocity amplitudes and acoustic energy densities are normalized as well,

$$u_{\mathrm{a}} = \left(\frac{1 \text{ V}}{U_{\mathrm{pp}}^*}\right)^2 u_{\mathrm{a}}^*, \tag{5.8}$$

$$E_{\mathrm{ac}} = \left(\frac{1 \text{ V}}{U_{\mathrm{pp}}^*}\right)^2 E_{\mathrm{ac}}^*. \tag{5.9}$$

The actual peak-to-peak values of the applied voltage U_{pp}^* for all four experimental series are given in Chapter F (Supplemental Information).

5.5.2.1 Excitation of a 1D transverse standing wave

In Figs. 5.8 and 5.9 we verify experimentally that the acoustophoretic particle velocity is of the predicted sinusoidal form given in Eq. (3.45a) and resulting from a 1D transverse standing wave. For the actual applied voltage of $U_{\mathrm{pp}}^* = 7.94$ V the maximum velocity was measured to be 1.77 mm s^{-1}, which by Eq. (5.7) is normalized to the maximum velocity $u_{\mathrm{max}}^* = 28$ µm s^{-1} seen in Fig. 5.8.

A detailed analysis of the measured velocity field reveals three main points: (*i*) The average of the ratio of the axial to the transverse velocity component is
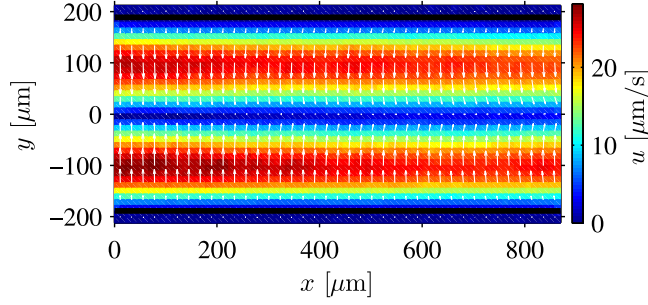
Figure 5.8: Experimental micro-PIV measurement of acoustophoresis in the horizontal ultrasound symmetry plane of 1-µm-diameter polystyrene particles suspended in water and driven at the piezo frequency $f = 1.940$ MHz corresponding to $\lambda/2 = w$, temperature 25 °C, and voltage $U_{pp}^* = 7.94$ V. The arrows represent the measured velocity vectors $\boldsymbol{u}$ and the colors their magnitude u normalized to U_{pp}^*, see Eq. (5.7). Adapted from Ref. [37].

practically zero, $\langle |u_x/u_y| \rangle < 5$ %, (*ii*) the maximum particle velocity along any line with a given axial grid point coordinate x_m varies less than 6 % as a function of x_m, and (*iii*) the axial average $\langle u_y \rangle_x$ of the transverse velocity component u_y is well fitted within small errorbars (< 1 %) by Eq. (3.45a).

5.5.2.2 Measuring the velocity amplitude

In Fig. 5.9(a) we plot the axial average $\langle u_y \rangle_x$ of the transverse velocity component u_y (black and red points) and its standard deviation $\sigma(\langle u_y \rangle_x)$ (error bars) for the velocity field shown in Fig. 5.8 at the standing half-wave resonance frequency $f = 1.940$ MHz for the 1-µm-diameter streaming-dominated particles (series MQ1). The measured velocities away from the side walls (red points) are fitted well by the predicted sinusoidal velocity profile $u_a \sin\left[2k_y\left(y + \frac{w}{2}\right)\right]$ (blue curve) Eq. (3.45a) for fixed wavelength $\lambda = 2\pi/k = 2w$ and using u_a as the only fitting parameter. Velocities close to the side walls (black points) are discarded due to their interaction with the side walls.

As shown in Fig. 5.9(b), the theoretical prediction also fits well the measured velocities for the large radiation-dominated 10-µm-diameter particles (series MQ1, $\lambda/2 = w$). Moreover, as seen in Fig. 5.9(c) a good fit is also obtained for the 1-µm-diameter particles at the standing full-wave frequency $f = 3.900$ MHz (series MQ2, $\lambda = w$).

Given this strong support for the presence of standing transverse waves, we use this standing-wave fitting procedure to determine the velocity amplitude u_a in the following analysis of the acoustophoretic particle velocity.

In spite of the normalization to the same driving voltage of 1 V, the velocity amplitude of the half-wave resonance in Fig. 5.9(a) is 400 times larger than that of the full-wave resonance in Fig. 5.9(c). This is due to a difference in coupling to the piezo and in dissipation.
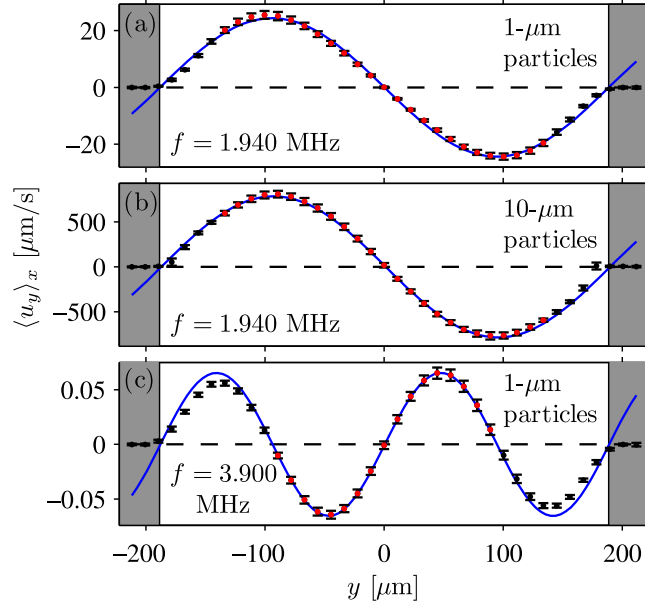
Figure 5.9: Measured average $\langle u_y \rangle_x$ (black and red points) and its standard deviation $\sigma(\langle u_y \rangle_x)$ (error bars) of the transverse velocity u_y of polystyrene particles in water. The sinusoidal prediction Eq. (3.45a) for u (blue line) is fitted to data points $\langle u_y \rangle_x$ away from the side walls (red points). (a) Streaming-dominated acoustophoresis for $2a = 1$ μm driven at $f = 1.940$ MHz ($\lambda/2 = w$, same data as in Fig. 5.8). (b) Radiation-dominated acoustophoresis for $2a = 10$ μm at $f = 1.940$ MHz ($\lambda/2 = w$). (c) Streaming-dominated acoustophoresis for $2a = 1$ μm at $f = 3.900$ MHz ($\lambda = w$). Adapted from Ref. [37].

5.5.2.3 Velocity as function of particle diameter

To analyze in detail the transverse velocity amplitude u_a in all four series MQ0, MQ1, MQ2, and Gl1, we return to the wall-enhanced drag coefficient χ of Section 3.5.3. In general, χ depends in a non-linear way on the motion and position of the particle relative to the rigid walls. However, from the DOC size Table 5.1 we can conclude that the majority of the observed particles reside in the middle half of the channel, and in our standing-wave fitting procedure for u_a in Section 5.5.2.2 we discarded particles close to the side walls. Consequently, given this and the values of χ in Table 3.1, it is a good approximation to assume that all involved particles have the same wall correction factor, namely the symmetry-plane, parallel-motion factor,

$$\chi \approx \chi_{z=0}^{\text{paral}}. \tag{5.10}$$

As the drag-correction only enters on the radiation-induced term in Eq. (3.53), we introduce a wall-drag-corrected particle size $a_{\text{wd}} = (\chi_{z=0}^{\text{paral}})^{-\frac{1}{2}} a$.

To determine the acoustic energy density E_{ac} and the streaming coefficient $s_{\lambda \approx 5h}^T$ we plot in Fig. 5.10, for each of the four experiment series, u_a/u_0 versus the particle diameter $2a$ (colored symbols) and wall-drag-corrected particle diameter $2a_{\text{wd}}$ (gray symbols). The characteristic velocity amplitude u_0 is determined
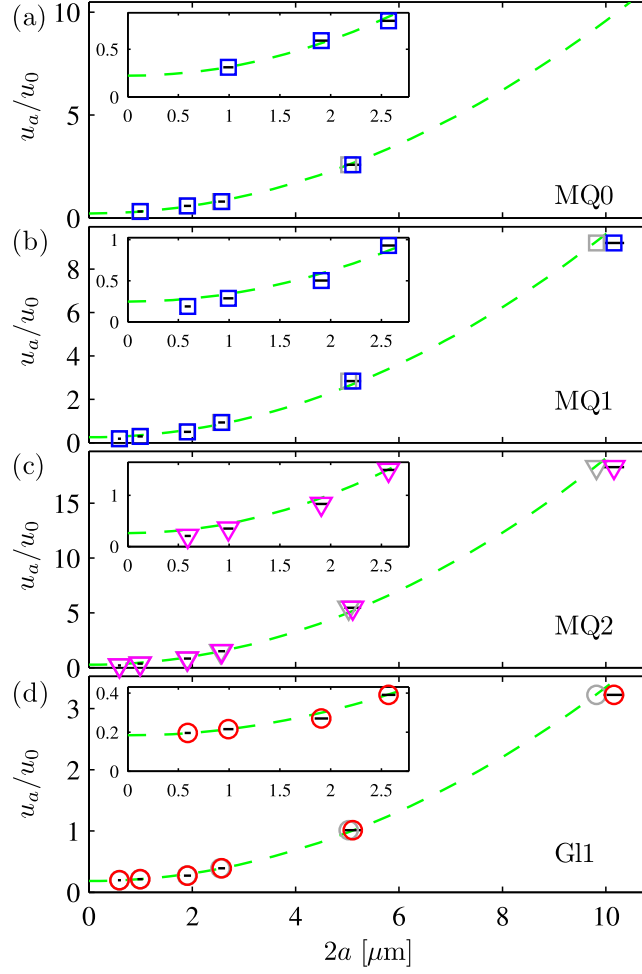
Figure 5.10: Measured and normalized acoustophoretic velocity amplitudes u_a/u_0 as function of particle diameter $2a$ (colored symbols) and wall-drag-corrected particle diameter $2a_{wd}$ (gray symbols) for the four experiment series (a) MQ0, (b) MQ1, (c) MQ2 and (d) Gl1 described in Section 5.5.1.2. The characteristic velocity amplitude u_0 is determined from fitting Eq. (3.45b) to the gray points in each series using E_{ac} and s as fitting parameters resulting in the values listed in Table 5.3(a) (green dashed lines). The standard deviation of u_a/u_0 is less than the symbol size and the standard deviations on the particle diameters are indicated as black lines. Adapted from Ref. [37].

in each series by fitting the wall-drag-corrected data points to Eq. (3.45b) using E_{ac} and $s_{\lambda \approx 5h}^T$ as fitting parameters. In all four experiment series, a clear a^2-dependence is seen. Notice further that the velocities follow almost the same distribution around the fitted line in all series. This we suspect may be due to systematic errors, e.g. that the 5-µm-diameter particles are slightly underestimated (see the Coulter data in Chapter F (Supplemental Information)). The resulting fitting parameters E_{ac} and $s_{\lambda \approx 5h}^T$ are listed in Table 5.3(a). The energy densities normalized to $U_{pp} = 1$ V, see Eq. (5.9) varies with more than a factor 700 due to a large difference in the strength of the excited resonances. According to the

Table 5.3: Measured acoustic energy densities E_{ac} normalized to $U_{\mathrm{pp}} = 1$ V and streaming coefficient $s^T_{\lambda \approx 5h}$. Adapted from Ref. [37].

(a) Un-weighted fit to all points, see Fig. 5.10.		
Susp., freq.	E_{ac} [J m^{-3}]	$s^T_{\lambda \approx 5h}$
MQ0, 1.940 MHz	52.306 ± 0.918	0.222 ± 0.025
MQ1, 1.940 MHz	31.807 ± 0.569	0.247 ± 0.071
MQ2, 3.900 MHz	0.070 ± 0.001	0.262 ± 0.125
Gl1, 2.027 MHz	2.420 ± 0.020	0.184 ± 0.012
(b) Based on particles with $2a = 0.6$ µm and $2a = 10$ µm		
Susp., freq.	E_{ac} [J m^{-3}]$^{\mathrm{a}}$	$s^T_{\lambda \approx 5h}$ $^{\mathrm{b}}$
MQ1, 1.940 MHz	32.436 ± 1.282	0.182 ± 0.008
MQ2, 3.900 MHz	0.071 ± 0.003	0.205 ± 0.008
Gl1, 2.027 MHz	2.559 ± 0.110	0.186 ± 0.008

$^{\mathrm{a}}$Eq. (5.11)
$^{\mathrm{b}}$Eq. (5.12)

predictions in Section 3.5 the streaming coefficient $s^T_{\lambda \approx 5h}$ should be constant, but experimentally it varies from 0.18 to 0.25. However, taking the fitting uncertainties into account in a weighted average, leads to $\langle s \rangle_{\mathrm{w}} = 0.192 \pm 0.010$ close to $s^T_{\lambda \approx 5h} \approx 0.194$ of Eq. (3.41).

Another approach for extracting E_{ac} and $s^T_{\lambda \approx 5h}$ is to assume that the smallest particles $2a = 0.6$ µm are influenced only by the streaming-induced drag. If so, the velocity of the largest $2a = 10$ µm particle has a streaming component of less than 6 %, see the measured ratios $u_{\mathrm{a}}^{0.6\ \mu\mathrm{m}}/u_{\mathrm{a}}^{10\ \mu\mathrm{m}}$ in Table 5.4. Therefore, we further assume that the 10 µm-diameter particles are influenced solely by the radiation force, and from $u_{\mathrm{a}}^{\mathrm{rad}} = u_{\mathrm{a}}(a/a_0)^2$ we determine the acoustic energy density as

$$E_{\mathrm{ac}} = \frac{3}{2} \frac{\eta c_0}{\Phi \omega} \frac{u_{\mathrm{a}}^{10\ \mu\mathrm{m}}}{a_{\mathrm{wd}}^2}. \tag{5.11}$$

Knowing the acoustic energy density, we use Eq. (3.41) to calculate the streaming coefficient $s^T_{\lambda \approx 5h}$ from $u_{\mathrm{a}}^{\mathrm{str}} = u_0 s$ as

$$s^T_{\lambda \approx 5h} = \frac{\rho_0 c_0}{4 E_{\mathrm{ac}}} u_{\mathrm{a}}^{0.6\ \mu\mathrm{m}}. \tag{5.12}$$

Assuming that the largest error is due to the dispersion in particle size, we obtain the results listed in Table 5.3(b). The acoustic energy densities are close to the ones extracted from the fits in Fig. 5.10 and the geometric streaming coefficient varies from 0.180 to 0.203 with an weighted average of $\langle s \rangle_{\mathrm{w}} = 0.191 \pm 0.005$. Note that using Eqs. (5.11) and (5.12), we only need to consider the dispersion of the 10-µm-diameter particles, which results in a more reliable estimate of $s^T_{\lambda \approx 5h}$.

We use the acoustic energy densities in Table 5.3(b) together with the material parameters list in the List of Material Parameters to calculate u_0 and a_0,
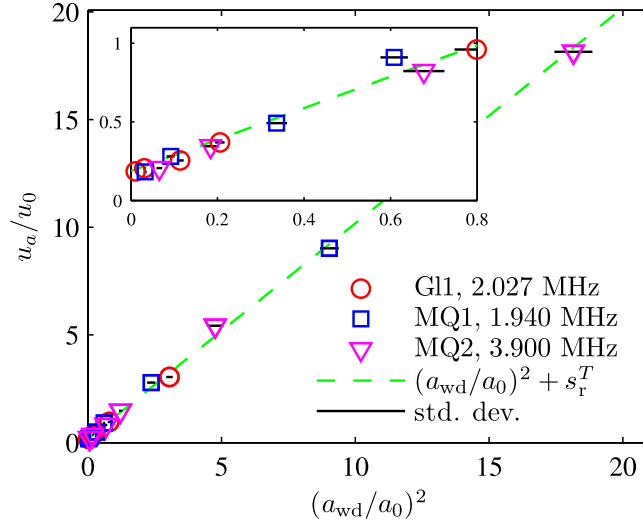
Figure 5.11: Normalized acoustophoretic particle velocities u_a/u_0 versus normalized particle size squared $(a_\mathrm{wd}/a_0)^2$. Adapted from Ref. [37].

Eq. (3.46), for each of the experiment series MQ1, MQ2, and Gl1. According to the theoretical prediction in Eq. (3.45b), all data points must fall on a straight line of unity slope and intersection $s^T_{\lambda\approx 5h}$ if plotted as the normalized velocity amplitude u_a/u_0 as function of the normalized particle radius squared $(a/a_0)^2$. The plot is shown in Fig. 5.11 showing good agreement with the theoretical prediction using $s^T_{\lambda\approx 5h} \approx 0.194$.

5.5.2.4 Velocity ratios

In Table 5.4 we list velocity ratios for different particle sizes in the experiment series MQ1, MQ2, and Gl1.

From Eq. (3.45b) we expect $u_\mathrm{a} - u^\mathrm{str}_\mathrm{a} \propto a^2$ leading to the prediction $(u^{5\ \mu\mathrm{m}}_\mathrm{a} - u^\mathrm{str}_\mathrm{a})/(u^{10\ \mu\mathrm{m}}_\mathrm{a} - u^\mathrm{str}_\mathrm{a}) = (5/10)^2 = 0.25$. If we assume that the smallest 0.6-µm-diameter particles are only influenced by the acoustic streaming, we have $u^\mathrm{str}_\mathrm{a} = u^{0.6\ \mu\mathrm{m}}_\mathrm{a}$. We can therefore test the just mentioned hypothesis by calculating $(u^{5\ \mu\mathrm{m}}_\mathrm{a} - u^{0.6\ \mu\mathrm{m}}_\mathrm{a})/(u^{10\ \mu\mathrm{m}}_\mathrm{a} - u^{0.6\ \mu\mathrm{m}}_\mathrm{a})$. The results are listed in the third column in Table 5.4, where we obtain values ranging from 0.27 to to 0.29, or a deviation of 8 to 18 %.

Assuming that the smallest 0.6-µm-diameter particles and the largest 10-µm-diameter particles are influenced only by the acoustic streaming and the acoustic radiation force, respectively, we can estimate the ratio of radiation- and streaming-induced velocities as $u^\mathrm{rad}_\mathrm{a}/u^\mathrm{str}_\mathrm{a} = u^{10\ \mu\mathrm{m}}_\mathrm{a}/u^{0.6\ \mu\mathrm{m}}_\mathrm{a}$, which are listed in the second column in Table 5.4. First, we notice that the ratio increases by a factor of $88.4/49.6 = 1.8$ as we increase the frequency by a factor of $3.900/1.940 = 2.0$. This agrees well with a linear increase with frequency as predicted by Eq. (3.47). Secondly, we notice that the ratio increases by a factor of $48.6/16.4 = 3.0$ as we change the suspending medium from a 0.75:0.25 mixture of water and glycerol to pure water. According to Eq. (3.47) $u^\mathrm{rad}_\mathrm{a}/u^\mathrm{str}_\mathrm{a}$ increases linearly with ν/Φ

Table 5.4: Measured relative particle velocities for different particle sizes. Adapted from Ref. [37].

Susp., freq.	$\dfrac{u_{\mathrm{a}}^{0.6\ \mu\mathrm{m}}}{u_{\mathrm{a}}^{10\ \mu\mathrm{m}}}$	$\dfrac{u_{\mathrm{a}}^{10\ \mu\mathrm{m}}}{u_{\mathrm{a}}^{0.6\ \mu\mathrm{m}}}$	$\dfrac{u_{\mathrm{a}}^{5\ \mu\mathrm{m}}-u_{\mathrm{a}}^{0.6\ \mu\mathrm{m}}}{u_{\mathrm{a}}^{10\ \mu\mathrm{m}}-u_{\mathrm{a}}^{0.6\ \mu\mathrm{m}}}$
MQ1, 1.940 MHz	0.020	49.6	0.294
MQ2, 3.900 MHz	0.011	88.4	0.291
Gl1, 2.027 MHz	0.061	16.4	0.270

and from the List of Material Parameters we obtain a predicted ratio increase of $16.8/5.25 = 3.2$, which matches well with the experimentally-estimated ratio. With these results we have gained experimental support for the theoretical prediction of the velocity ratio given in Eq. (3.47).

5.6   Concluding remarks

Sections 5.1-5.4.   We have presented an automated and temperature-controlled experimental platform for characterization of microchannel acoustophoresis by µPIV. The platform was operated in stop-flow mode.

The high mechanical, thermal, and electronic stability of the platform and the good reproducibility of the measurements provided acoustophoretic velocity data with a spatial resolution of about 20 µm and a relative uncertainty of the velocity measurements of about 5 %. The good experimental statistics was enabled by the system automation allowing individual experiments to be repeated 20 to 100 times. The standard deviation of the obtained data can be further reduced, but in practice this is balanced against the time it takes to acquire and analyze the data.

We have demonstrated both short-term stability of the order of 1 h (the time it takes to measure a single frame at a given frequency and temperature), and long-term stability over several days (the time it takes to make multi-frame scans over large sections of the microchannel).

We have further shown that temperature control is the key feature to obtain stable and reproducible resonant ultrasound modes in an acoustophoresis microchannel. For minute temperature changes ($\sim 2\ ^{\circ}\mathrm{C}$), the acoustic resonance peaks are shifted by ~ 1 kHz/$^{\circ}\mathrm{C}$. However, a temperature change of 5 $^{\circ}\mathrm{C}$ can lead to a complete change from one resonance mode into another.

We have investigated the global features of some resonant modes and it was found that the transverse velocity field varied greatly along the channel. The large spatial variation in velocity magnitude calls for some concern regarding the strategy that we employed for the frequency spectra data, where a single field of view was evaluated for a range of frequencies. The complexity of the acoustic resonance patterns in this type of resonator requires further studies of the frequency, temperature, and spatial domain. This calls for better theoretical predictions taking into account the solid chip structure and piezo actuation.

Section 5.5.   We have investigated the motion of microparticles due to acoustic radiation and acoustic streaming inside the microchannel of the experimental model system, Section 2.1. The results are found to be in excellent agreement with the theoretical prediction, Eq. (3.53), for the dependence of the radiation- and streaming-induced velocities on the size of the particles, the ultrasound frequency, the viscosity of the suspending liquid, and the acoustic contrast factor, as shown by the collapse after re-scaling of data from 22 different measurement on the same line in Fig. 5.11. The results have bearing on acoustophoretic manipulation strategies for sub-micrometer biological particles such as bacteria and vira, which are too small to be handled using the present manifestation of this technique. From this investigation, we can conclude that increasing the ultrasound frequency, increase of the channel aspect ratio, and lowering the viscosity of the suspending fluid is probably the most viable route to conduct such manipulation.

Acoustophoresis analyzed by Astigmatism micro-PTV

In Chapter 5 micro-PIV was successfully used to measure the in-plane acoustophoretic particle velocities in the horizontal xy-plane at the channel mid height of the experimental model system, Fig. 2.1(b). However, as shown numerical in Chapter 4, microparticle acoustophoresis is essential three-dimensional, e.g. for the 2-MHz transverse resonance the acoustic streaming will have non-zero velocity components across most of the vertical yz cross section. Moreover, the excited resonance can have features in all spatial directions leading to both radiation- and streaming-dominated acoustophoresis in three dimensions, and thus we must determine the three components (3C) of the particles velocities in a micro volume (3D) to obtain the full picture of microparticle acoustophoresis. This full three-dimensional picture is crucial for validating existing theoretical acoustofluidics predictions and to push the development of better predictions.

Our experimental model system does only allow optical top-view access along the z-direction setting the requirement for a velocimetry method capable of 3C3D measurements using a single camera. We have therefore initiated an expansion of the Lund-DTU collaboration to include the group of Christian J. Kähler, Bundeswehr Universität München, an leading expert in the simple but efficient velocimetry technique of Astigmatism Particle Tracking Velocimetry (A-µPTV). We have therefore extended the automated and temperature-controlled acoustophoresis platform presented in the former Chapter 5 to use the A-µPTV technique, and in this chapter we present full three-dimensional tracking of particles undergoing both radiation- and streaming-dominated acoustophoretic motion.

This chapter is based on recent and in progress work in collaboration with Dr. Massimiliano Rossi, Dr. Álvaro G. Marín, and Professor Christian J. Kähler, Bundeswehr Universität München, Germany, Professor Thomas Laurell and Dr. Per Augustsson, Lund University, Sweden, and PhD student Peter B. Muller and Professor Henrik Bruus, DTU Physics, Denmark. The current results are
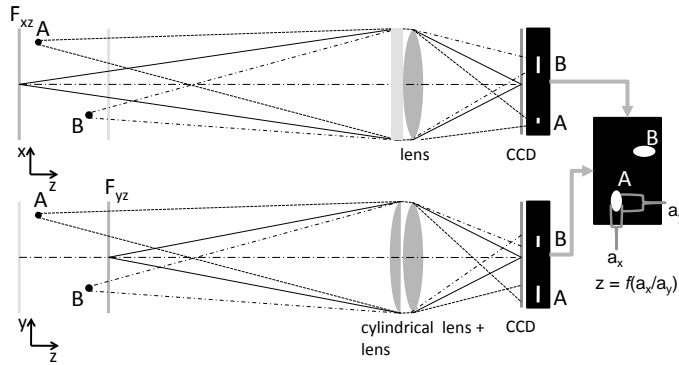
Figure 6.1: Working principle of the 3D Astigmatic micro-PTV technique (A-µPTV). A cylindrical lens is introduced directly in front of the camera CCD resulting in two different focal planes (xz and yz) such that the particles A and B appear as ellipses with elliptical axes (a_x, a_y) expressing the particle depth position along the z-direction. Reproduced with permission, Ref. [96]

submitted to the 3rd European Conference on Microfluidics 2012 "µFlu2012" in Heidelberg [34]. The current results are reproduced in the following. All experiments were carried out in Lund with all groups gathered, while the A-µPTV data analysis was carried out by the group of Kähler, and the theoretical analysis was conducted by the group of Bruus.

6.1 A short intro to Astigmatism µPTV

As pointed out in a recent review [97], it has become a great challenge in microfluidics to develop three-component, three-dimensional (3C3D) measurement approaches that work with a single optical access. Astigmatism particle tracking velocimetry (A-µPTV) is a reasonably new approach for measuring the 3C3D particle velocities in microfluidic systems [96, 98, 99] and it is particularly well-suited for measuring out-of-plane components such as streaming-induced acoustophoretic motion, and it does not suffer from some adverse effects as other 3C3D methods such as scanning µPIV and stereoscopic µPIV (S-µPTV) [97]. Furthermore, A-µPTV is based on particle tracking and does not suffer from averaging over interrogation windows and therefore gives a spatial resolution comparable to that obtained by the single-pixel evaluation approach [100]. Some examples of applying the A-µPTV are Kumar *et al.* who measured electro-thermally-driven microvortices [101] and Tschulik *et al.* who measured the flow field arising during electrochemical metal deposition in external magnetic fields [102].

In A-µPTV a cylindrical lens is introduced directly in front of the CCD sensor, which creates two different (xz and yz) focal planes perpendicular to the optical z-axis. Consequently, objects are defocused in the x-direction in the xz-plane while they are defocused in the y-direction in the yz-plane and particles will therefore appear as ellipses on the sensor with the elliptical axes (a_x, a_y)

relating to depth position along z, see Fig. 6.1. The method is accurate for low-concentration particle suspensions and it is being continuously developed, e.g. recently an easily-applicable intrinsic calibration procedure was developed to enhance the measurement depth and decrease the uncertainty of the technique making it a reliable tool for 3C3D velocity measurements [103].

6.2 Experimental setup

In this work we examined the experimental model system described in Section 2.1 implemented in the acoustophoresis platform described in Section 5.2, i.e. we used the same experimental setup as used for the μPIV analysis in Chapter 5. We used the same principal objective lens with 20× magnification and 0.4 numerical aperture, but in addition we introduced a cylindrical lens with focal length $f_{cyl} = 150$ mm right in front of the camera CCD in order to obtain astigmatic particle images [96]. Moreover, we used another CCD camera (12-bit, 1376×1040 pixels, Sensicam QE, PCO GmbH) and the illumination was provided by a continuous diode-pumped laser with 2 W at 532 nm wavelength. With this configuration a measurements volume of $900{\times}600{\times}120$ μm^3 was obtained so that a two-position scan along the z-direction was necessary to cover the whole cross-sectional area of the channel. The experiments were carried out using spherical polystyrene particles of diameters of 5.33 μm and 0.537 μm (Microparticles GmbH), all labeled with a proprietary fluorescent dye to be visualized with the epifluorescent microscopic system.

6.2.1 Experimental procedure

Two set of experiments series were carried out, one series measuring the 5.33-μm particles and another series measuring the 0.537-μm particles. Both series were measured at the same position in the microchannel and with the piezo transducer driven at frequency $f = 1.94$ MHz at temperature $T = 25$ °C, i.e. the same acoustic resonance was obtained for both series. The piezo transducer peak-to-peak voltage was $U_{pp} = 0.91$ V and $U_{pp} = 1.62$ V for the measurements of the 5.33-μm and 0.537 μm particles, respectively. The measurements of the 5.33-μm particles are based on 10 consecutive experiments resulting in a total of 111 valid particle trajectories, while the measurements of the 0.537-μm particles are based on four consecutive experiments resulting in an overall number of 500 valid trajectories.

6.3 Acoustophoresis measurements by Astigmatism μPTV

Radiation-dominated acoustophoresis. The trajectories of the 5-μm particles are plotted in Fig. 6.2(a). The motion of the particles are clearly dominated
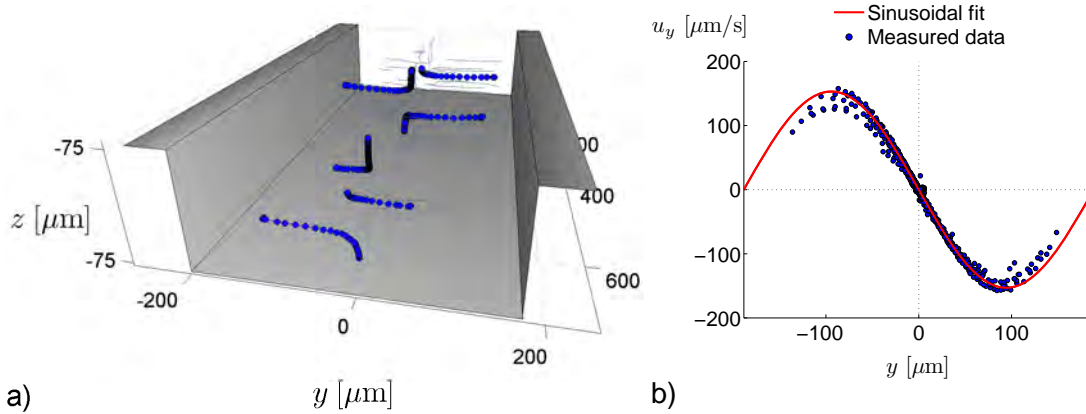
Figure 6.2: (a) Experimental 3D trajectory pathlines (thin gray lines) and positions (blue dots) measured by A-μPTV for six 5-μm polystyrene particles. (b) Transverse velocity component u_y (blue dots) as function of the transverse y-position for the six particle trajectories shown in panel (a). The prediction in Eq. (3.50) is fitted (red line) to u_y using the acoustic energy density as the only fitting parameter resulting in $E_{ac}^{0.91\,V} = 22.6\,\mathrm{J\,m^{-3}}$. Adapted from Ref. [34].

by the acoustic radiation force and they are focused to the pressure nodal plane at the channel center $y = 0$. Furthermore, we notice that the particles are pushed towards the top and bottom of the microchannel on a much longer timescale by the acoustic streaming exactly as predicted by the numerical simulations in Fig. 4.6. In Fig. 6.2(b) we plot the transverse velocity component u_y (blue dots) as function of the transverse y-position. The transverse velocity conforms well with the predicted sinusoidal profile in Eq. (3.50) (red line) fitted to data points using the acoustic energy density E_{ac} as the only fitting parameter as described later in Section 7.1.2. Thus, the acoustic energy density of the excited resonance driven at $U_{pp} = 0.91\,\mathrm{V}$ is estimated to $E_{ac}^{5\,\mu m} = 22.6\,\mathrm{J\,m^{-3}}$ (this value is corrected with 10 % according to the wall-drag corrections listed in Table 3.1). From the velocities in Fig. 6.2(b) it is evident that the particles are moving with different velocity amplitudes, which we suspect to be due to their movements are taking place at different z-positions and thus some are more effected by the presence of the walls than others, see Section 3.5.3.

Streaming-dominated acoustophoresis. The trajectories of the 0.537-μm particles are plotted in Fig. 6.3(a). The 0.5-μm particles do clearly not show the same motion as the 5-μm and instead they are carried around by bulk vortices by the acoustic streaming $\langle \boldsymbol{v}_2 \rangle$ as predicted in the numerical simulations in Fig. 4.6. An estimation of the cross-sectional velocity field (averaged along the x-axis) is shown in Fig. 6.3(b). The velocity in each grid point was calculated as a weighted average of the neighboring particle velocities, weighted according to the inverse of the distance between the grid point and the particle position. The experimental error on the measured z-position is approximately $\pm 1\,\mu m$, and since

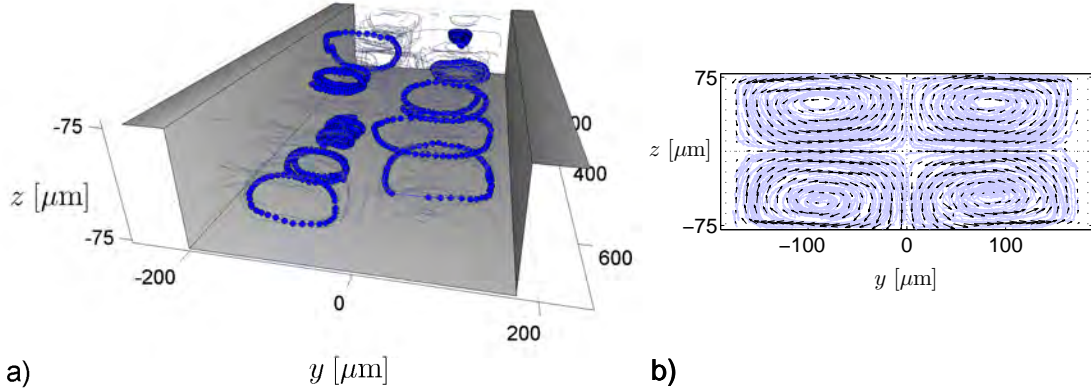a)   b)

Figure 6.3: (a) Experimental 3D trajectories (thin gray line) for 0.5-µm particles. For ten selected trajectories the pathlines and particle positions are shown in blue. (b) Measured cross-sectional particle velocities (black arrows) averaged along the x-axis. The velocity magnitudes range from 0 µm s^{-1} to 80 µm s^{-1}. The individual particle tracks are represented by light blue connected dots. Adapted from Ref. [34].

the acquisition rate is 4.5 Hz, a rough estimate of the experimental error on the particle velocities become $\pm 5\,\mu\mathrm{m\,s}^{-1}$.

6.3.1   Comparison to theoretical predictions

We now want to compare the velocity results for the small particles to a theoretical prediction of the acoustic streaming. The theoretical prediction is based on the Rayleigh's prediction in Eq. (3.34) extended with the prediction by Muller in Eq. (3.37) to cope with the height being comparable to the acoustic wavelength, i.e. $\lambda \approx 5h$. Furthermore, the theoretical prediction takes into account the effect of the no-slip condition on the vertical side walls [67]. Moreover, the prediction takes into account the correction for the temperature dependence of the viscosity inside the boundary layer as presented in Section 3.4.3, Ref. [58].

The scale of the streaming prediction we set by the acoustic energy density E_{ac} measured using the experimental data for the radiation-dominated 5-µm particles to be $E_{\mathrm{ac}}^{5\,\mu\mathrm{m}} = 22.6$ J/m^3. Taking the different voltages of the 5-µm and the 0.5-µm particle experiments into account, we arrive at the estimated acoustic energy density in the experiment with the small particles to be $E_{\mathrm{ac}}^{0.5\,\mu\mathrm{m}} = (1.62\,\mathrm{V}/0.91\mathrm{V})^2 E_{\mathrm{ac}}^{5\,\mu\mathrm{m}} = 71.6$ J/m^3.

To compare the experimental results and the analytical prediction we consider the 0.5-µm particle velocities in the vertical cross section of the channel (yz plane, see Figs. 6.4 and 6.5). In Fig. 6.4 is shown (a) the analytical prediction of the 0.5-µm particle velocities and (b) the experimental 0.5-µm particle velocities, both data sets are shown on the same 37×15 grid. As seen in Fig. 6.4, the topologies of the experimental and the analytical velocity fields are almost
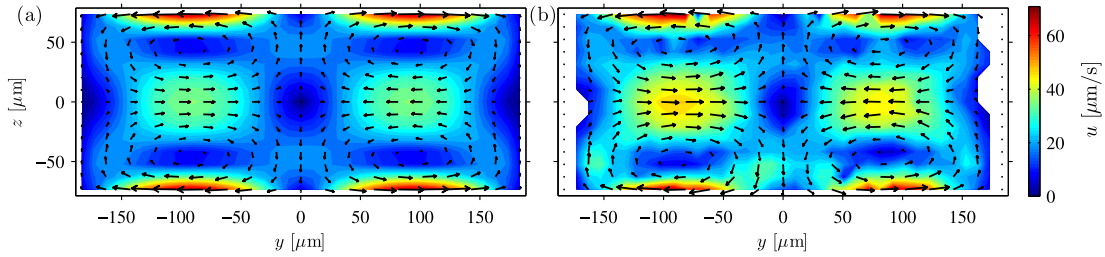
Figure 6.4: (a) Analytical prediction of the 0.5-µm particle velocity vectors $\boldsymbol{u}$ (black arrows) and magnitudes u (colors) plotted on the same grid as the experimental results. The analytical prediction takes into account both the dominant streaming-induced drag force and the minor acoustic radiation force on the 0.5-µm particles. (b) Experimental results for the 0.5-µm particle velocity vectors $\boldsymbol{u}$ (black arrows) and magnitudes u (colors). In several of the outer grid points there is no experimental data which is represented by a blank area and a dot. The figure axes coincide with the position of the channel walls. The topology of the experimental results are almost identical to the analytical prediction, while the magnitudes show some differences, predominantly in the center of the channel with up to 25 % difference. Adapted from Ref. [34].
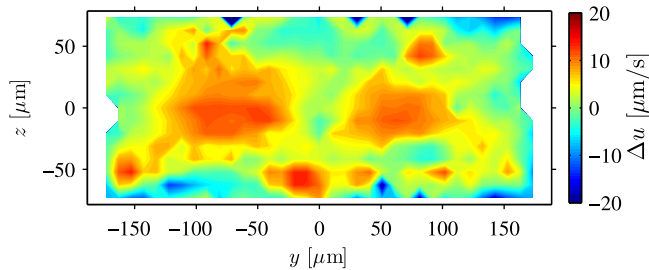
Figure 6.5: Difference between experimental and analytical particle velocities, $\Delta u = u_{\mathrm{exp}} - u_{\mathrm{ana}}$. The difference is greatest around the horizontal center axis, up to $\Delta u = 12$ µm s^{-1}, which is approximately 25 % difference relative to u_{exp}. Close to the boundaries local differences occur, presumably due to low statistics in the experimental data at these points Adapted from Ref. [34].

identical. However, there are some differences in the magnitude of the velocities. In Fig. 6.5 is shown the difference between the experimental and the analytical velocities, $\Delta u = u_{\mathrm{exp}} - u_{\mathrm{ana}}$. In most of the channel cross section the difference is within estimated experimental error of ± 5 µm s^{-1}. The experimental velocities tend to be somewhat larger than the analytical prediction, up to $\Delta u = 12$ µm s^{-1} in the center of the channel, which is approximately 25 % difference relative to u_{exp}. The local deviations close to the boundaries are ascribed to experimental error due to low statistics.

6.4 Concluding remarks

In this work we have presented preliminary results from an on-going collaboration between the groups of Laurell, Kähler, and Bruus. We have accurately measured

3D trajectories of microparticles of 0.5-µm and 5-µm diameter in experimental model system in Fig. 2.1. This allowed us to perform a quantitative comparison between theory and experiments of streaming-induced particle velocities in a rectangular channel. The analytical derivation successfully predicts the topology of the measured streaming-induced 0.5-µm particle velocities, with some localized differences in the magnitude, up to an absolute difference of 12 $\mu\mathrm{m\,s}^{-1}$ corresponding to 25 %. With the given experimental uncertainties, estimated to be $\pm 5\,\mu\mathrm{m\,s}^{-1}$, this is a good quantitative agreement. These preliminary results really stress the strength of three-dimensional velocimetry methods when analyzing microparticle acoustophoresis. Moreover, using this kind of technique, allows to investigate a whole range of acoustophoresis devices, where the particle motion is parallel to the optical axis.

CHAPTER 7

Applications of acoustophoresis

In the former chapters of the thesis, the focus was to deepen the understanding of microparticle acoustophoresis and to validate existing predictions. Contrary, this chapter presents three applications of acoustophoresis: (*i*) Use of microparticle acoustophoresis to *in situ* determine the acoustic energy density, (*ii*) use acoustophoresis for conducting measurements of the density and compressibility of individual microparticles, and (*iii*) use acoustophoresis for high-throughput particle separation. This chapter is based on the journal papers appended in Chapters A, C, and D.

7.1 Determination *in situ* of acoustic energy densities

One of the key problems in microchannel acoustophoresis is the prediction and measurement of the absolute size of the acoustic fields and forces. These are important parameters when designing a microchip for e.g. cell separation where the length of a given channel and the suspension flow rate must fit the transverse acoustic forces to obtain separation. As shown in Chapter 3 and in particular Section 3.5 the acoustic energy density E_{ac} is an essential parameter as both the acoustic radiation force and the acoustic streaming amplitudes are linearly proportional to E_{ac}. It is thus naturally to use E_{ac} as a figure of merit for the acoustophoretic performance. However, it is neither straightforward to theoretically predict, nor experimentally determine the energy density in an microchannel. As discussed in Section 2.2 and illustrated in the physics sketch in Fig. 2.2 the acoustic power sent from the transducer to the microchannel is subject to losses from thermal dissipation and acoustic radiation, making it difficult to predict the acoustic energies inside the microchannel from a given input power of the actuating transducer. Moreover, it is difficult to model the exact actuated acoustic

resonance and therefore difficult to predict the distribution of energy between the microchannel and the surrounding microchip.

Existing techniques for measuring the acoustic energy density (or acoustic pressure amplitude) mostly rely on external electric [79] or gravitational [80, 104] forces. However, based on the acoustophoretic alignment of particles advected along a microchannel, Wiklund *et al.* [105] estimated the acoustic pressure amplitude using the advection length and advection time needed to align the particles.

In this section we present methods for measuring the acoustic energy density relying solely on the acoustophoretic particle motion by using the acoustic energy density as a fitting parameter to fit experimental data to a theoretical prediction of either (*i*) the single-particle trajectory $y(y_0, t)$ in Eq. (3.51) (*ii*) the transverse velocity profile in Eq. (3.50), or (*iii*) a many-particle light-intensity model based on the expression for $y(y_0, t)$. All the presented methods estimates the acoustic energy density E_{ac} locally at the position of observing the particle motion and rely on the following assumptions:

1. The acoustic field must be purely one-dimensional, i.e. $\lambda_x \gg \lambda_y$ within the field-of-view.

2. The particle motion must be dominated by the acoustic radiation force and conform with the assumptions for the acoustic radiation force expression (3.32).

3. The investigated particle suspensions must be dilute enough to ensure negligible partice-particle hydrodynamic and acoustic interactions.

Note, in this section the transverse origo $y = 0$ is placed at the wall of the straight microchannel. That is, in the theory presented in Chapter 3, $y + w/2 \rightarrow y$ and $y_0 + w/2 \rightarrow y_0$.

7.1.1 Particle trajectory fitting

This section describes a method based on tracking individual microbeads as they traverse the microchannel and fitting the measured trajectories to a theoretical prediction using the acoustic energy density as a fitting parameter. This method is particularly suited for low particle concentrations and provides an important step in measuring compressibilities of individual cells using acoustophoresis [106–108]. Moreover, this section outlines how the extraction of the acoustic energy density as a function of frequency might be a suitable tool for investigation of the pressure amplitude, the resonance frequency and the Q factor of the associated ultrasound resonance by fitting the resonance spectra to a sum of Lorentzian response curves.

This chapter is based on work carried out in collaboration with Professor Thomas Laurell and his then PhD student Per Augustsson, Lund University, and Professor Henrik Bruus, Technical University of Denmark. The work is published in Lab on a Chip and the paper is appended in Chapter A. The experimental part of the work was carried out during the author's master thesis work, see Ref. [109], while the main part of the analysis and the writing of the paper was carried
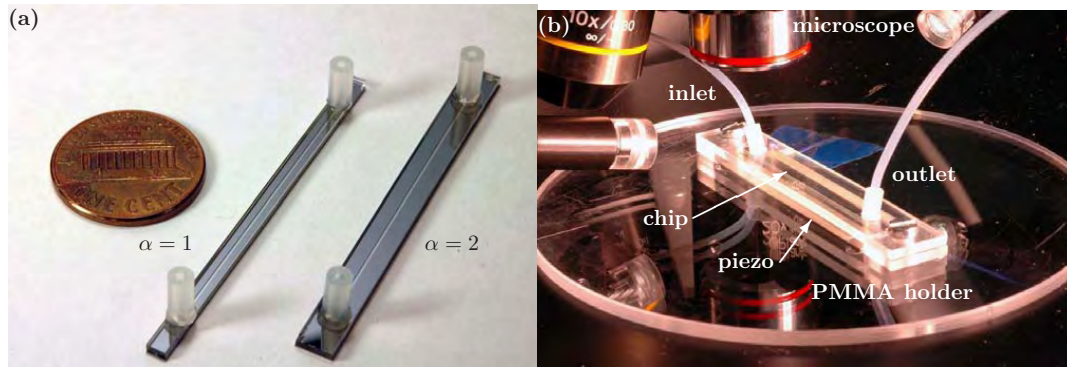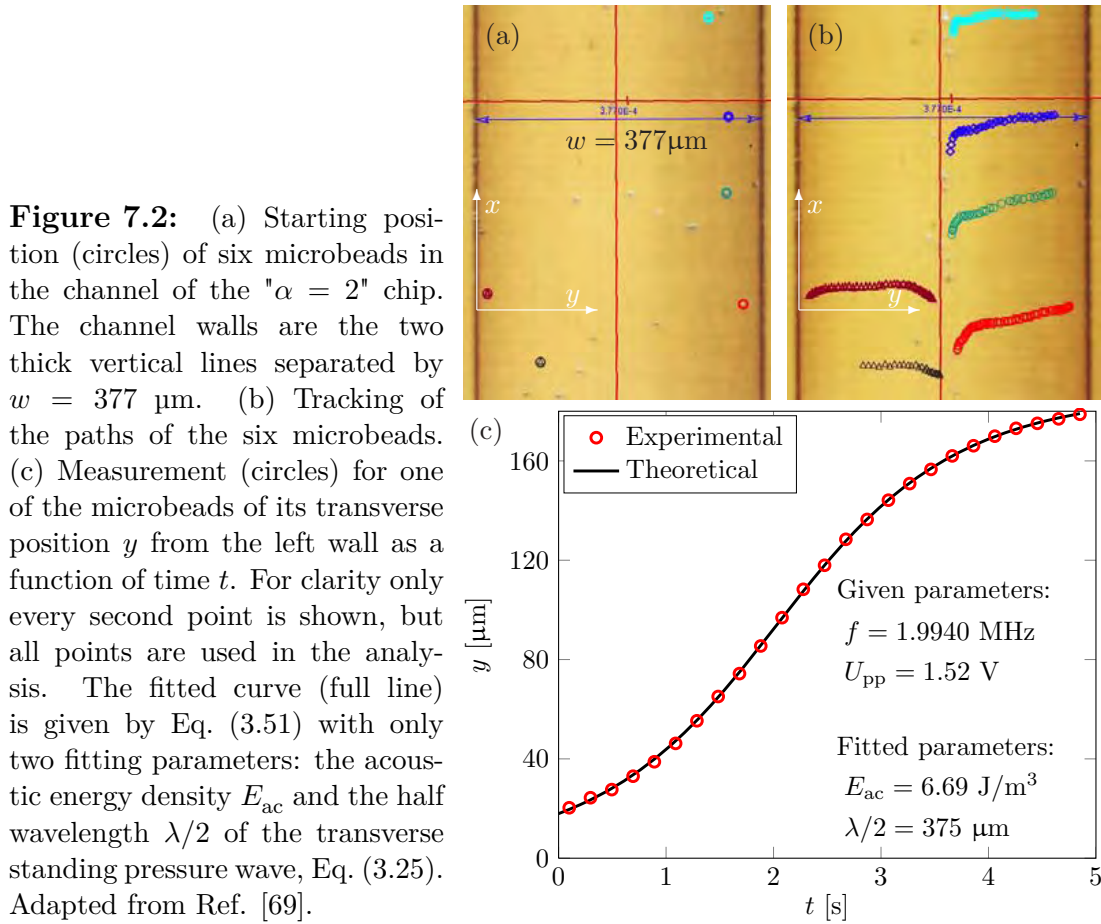
Figure 7.1: (a) The silicon/glass chips identical to experimental model chip described in Section 2.1, but differing on the following three points: (*i*) the chips are not translational invariant along their lengths and the channel is infused with particle suspension through holes in the Pyrex glass lid, (*ii*) the chip length is 50 mm and the channel length is 40 mm, and (*iii*) the chip width of the "$\alpha = 2$" is 4.67 mm. (b) A photograph of the experimental setup with the chip and the piezoelectric transducer mounted in a PMMA holder under a microscope and a CCD camera. Adapted from Ref. [69].

out during the first month of this PhD project. The following is a reproduction of parts of the published paper modified to align with rest of the thesis.

7.1.1.1 Experimental procedure

We used two different microfluidic chips denoted "$\alpha = 1$" and "$\alpha = 2$", respectively, as shown in Fig. 7.1(a). The chips are almost identical to the experimental model chip described in Section 2.1, but differing on the following three points: (*i*) the chips are not translational invariant along their lengths and thus the channel is infused with particle suspension through silicone tubing attached to drilled holes in the Pyrex glass lid, (*ii*) the chip length is 50 mm, while the channel length is 40 mm, and (*iii*) the chip width of the "$\alpha = 2$" is 4.67 mm and not 2.52 mm. Fig. 7.1(b) shows one of the chips mounted on the piezo with an intermediate thin glycerol layer for acoustic coupling. The two elements are fixed in a PMMA holder, such that the chip is only in contact with the holder through its inlet/outlet silicone tubing and via the piezo. The experimental platform and electronic driving are identical to the platform described in Section 5.1, but without any automation of the loading of the suspension, no valve for fully short-circuiting the flow, and no temperature control. Moreover, we carry out same type of experiments as described in Chapters 5 and 6, where we study the acoustophoretic motion of polystyrene microparticles suspended in water and without any external flow. For more details, the reader is referred to the paper appended in Chapter A.

Figure 7.2: (a) Starting position (circles) of six microbeads in the channel of the "$\alpha = 2$" chip. The channel walls are the two thick vertical lines separated by $w = 377$ μm. (b) Tracking of the paths of the six microbeads. (c) Measurement (circles) for one of the microbeads of its transverse position y from the left wall as a function of time t. For clarity only every second point is shown, but all points are used in the analysis. The fitted curve (full line) is given by Eq. (3.51) with only two fitting parameters: the acoustic energy density E_{ac} and the half wavelength $\lambda/2$ of the transverse standing pressure wave, Eq. (3.25). Adapted from Ref. [69].

7.1.1.2　Extracting the acoustic energy density

To determine the acoustic energy density we tracked the transverse path $y(y_0, t)$ of individual microparticles undergoing acoustophoresis by employing the free video analysis tool *Tracker 2.6* to perform manual tracking by mouse-clicking. Fig. 7.2(a) shows a microscope top view of the horizontal xy plane at the mid height $z = 0$ of the microchannel before the onset of the ultrasound. Fig. 7.2(b) shows the same view after ultrasonic actuation with driving frequency of $f = 1.9940$ MHz and a driving voltage $U_{pp} = 1.52$ V. Moreover, some microparticles paths are shown (colored points) and one of these are plotted in Fig. 7.2(c). The axial motion $x(t)$ seen in the last part of the paths shown in Fig. 7.2(b) is due to hydraulic compliance of the system leading to difficulties in keeping the liquid at complete rest.

Using the energy density E_{ac} and the half-wavelength $\lambda/2$ as the only fitting parameters, a curve of the form $y(y_0, t)$ given by Eq. (3.51) is fitted to the data points. As shown by the full curve in Fig. 7.2(c), this fitting procedure yields good results: the observed path has the theoretically predicted shape, and we can extract reliable values for the acoustic energy density E_{ac}. In the given case we found $E_{ac} = 6.69$ J m^{-3}, and we also note that the fitted value for $\lambda/2$
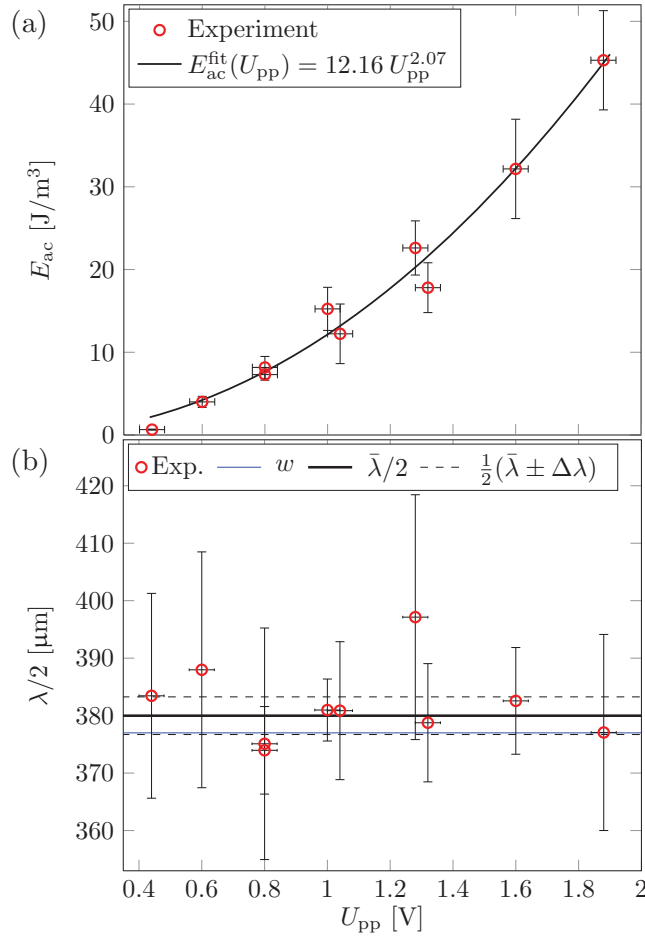
Figure 7.3: (a) Measured acoustic energy density E_{ac} versus applied peak-to-peak voltage U_{pp} on the piezo transducer (points) for the "$\alpha = 1$" chip. A power law fit (full line) to the data is close to the expected square law, $E_{ac} \propto (U_{pp})^2$. (b) The average value $\bar{\lambda}/2 = (380 \pm 3)$ µm of the fitted half wavelength is close to the expected value of $w = 377$ µm. Adapted from Ref. [69].

is 375 µm, very close to the expected value, namely the width of the channel $w = 377$ µm. From Eq. (3.26) we find the pressure amplitude in the "$\alpha = 2$" chip to be 0.242 MPa, which is 10^{-4} times the cohesive energy density 2.6 GPa of water. Equivalently, the density and temperature fluctuations are 10^{-4} times $\rho_0 = 997$ kg m^{-3} and $T_0 = 25$ °C, respectively, and thus the acoustic perturbation theory holds even at resonance.

In this series of low-voltage experiments we measured energy densities in the range $0.65 - 50$ J m^{-3} corresponding to pressure amplitudes in the range $0.08 - 0.66$ MPa. The upper range of these results are consistent with previously reported estimates in the literature for microbead acoustophoresis in microsystems. Using external electric forces, Wiklund *et al.* [79] measured energy densities in the range $65 - 650$ J m^{-3} corresponding to pressure amplitudes in the range $0.76 - 2.4$ MPa, while Hultstöm *et al.* [80] used force balance between gravity and acoustophoretic forces to measure energy densities in the range $37 - 82$ J m^{-3} corresponding to pressure amplitudes in the range $0.57 - 0.85$ MPa.

Figure 7.4: Measured acoustic energy density E_{ac} versus applied frequency f on the piezo transducer (circles) for the "$\alpha = 2$" chip for $U_{\text{pp}} = 1.48$ V. The data points are fitted by a sum (full line) of two Lorentzian peaks (dashed lines). The values of the fitting parameters for peak 1 are $f_1 = 1.9927$ MHz, $E_{\text{ac},1} = 3.3$ J/m^3, and $Q_1 = 577$. For peak 2 they are $f_2 = 2.0021$ MHz, $E_{\text{ac},2} = 15.5$ J/m^3, and $Q_2 = 209$. The peak spacing is $\Delta f_{12} = f_2 - f_1 = 9.4$ kHz, while the line widths are $\delta f_1 = 3.5$ kHz and $\delta f_2 = 9.6$ kHz. Adapted from Ref. [69].
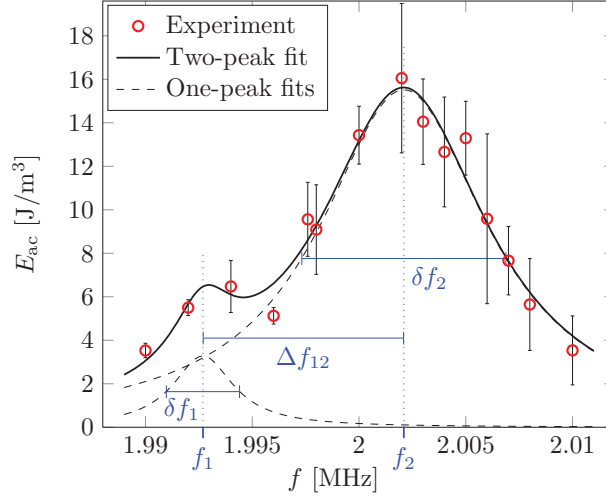
7.1.1.3 Energy densities versus driving voltage

We now use the procedure from the latter section to determine the acoustic energy density E_{ac} and half the wavelength $\lambda/2$ for typically 8 individual microbeads. In the following when we plot the results for a set of external parameters, each data point is a statistical average of these individual measurements, and the error bars are the associated standard deviations.

First, at the driving frequency $f = 1.9976$ MHz, we study the energy density and the half wavelength as a function of the peak-to-peak value U_{pp} of the driving voltage on the piezo transducer in the range from 0.5 V to 1.9 V. The results are shown in Fig. 7.3 and the ten $\left(U_{\text{pp}}, E_{\text{ac}}\right)$-points are well fitted by a power law of the form $E_{\text{ac}} \propto (U_{\text{pp}})^{2.07}$. This is close to a power of 2, which is expected since the acoustic pressure delivered by the piezo transducer is proportional to the applied voltage, and the acoustic energy density is proportional to the square of the pressure, see Eq. (3.26). We also note that the statistically determined error bars increase with increasing driving voltage and thus with increasing microbead velocity. This is as result of the decreased temporal resolution of the paths given the fixed rate of 16 CCD frames per second and the increased microbead velocity. Fig. 7.3(b) shows that for all voltages the average of the other fitting parameter, the half wavelength, is $\bar{\lambda}/2 \pm \Delta\lambda = (380 \pm 3)$ µm, which is very close to the expected value of $w = 377$ µm.

7.1.1.4 Resonance frequencies and Q factors

By measuring the acoustic energy density E_{ac} as a function of the applied frequency f across the piezo transducer, we have been able to characterize the acoustic resonances in more detail. The following results were obtained on the "$\alpha = 2$" chip of width $W = 4.67$ mm, see Fig. 7.1(a). The driving frequency

f was varied from 1.990 MHz to 2.010 MHz, while the tone generator and the amplifier were set to fixed values. However, due to the piezoelectric coupling of the transducer, the actual peak-to-peak voltage U_{pp} varied between 1.44 V and 1.60 V as a function of frequency. We used the quadratic dependency of E_{ac} on U_{pp} to correct all measured values of E_{ac} to correspond to the same average voltage 1.48 V.

The measured acoustic energy spectrum E_{ac} is shown in Fig. 7.4. A clear maximum is seen at $f_2 = 2.0021$ MHz while a smaller, less pronounced peak is seen at $f_1 = 1.9927$ MHz. According to Eq. (3.27), a simple acoustic resonance can be described by a Lorentzian line shape, and we therefore fit the measured spectrum by the sum of two Lorentzian line shapes. In this case we thus end up with six fitting parameters, three per peak, the energy density maxima $E_{ac,1}$ and $E_{ac,2}$, the resonance frequencies f_1 and f_2, and the Q factors Q_1 and Q_2. The values of these parameters are listed in the caption of Fig. 7.4, and from the energy densities we extract as in Eq. (3.26) the pressure amplitudes $p_{1,1} = 0.16$ MPa and $p_{1,2} = 0.37$ MPa.

The two resonance peaks in Fig. 7.4 are separated by a spacing $\Delta f_{12} = f_2 - f_1 = 9.4$ kHz, while the line width of the two peaks are of the same order of magnitude, namely $\delta f_1 = 3.5$ kHz and $\delta f_2 = 9.6$ kHz. These values emphasize, as is also seen directly on the graph, that the individual acoustic resonances are barely resolved.

The origin of the observed two-peak structure is explained qualitatively by the 2D pressure eigenmode simulations shown in Fig. 7.5. It is seen how axial modes appear and gives rise to close-lying resonances. While our non-shear-wave model does not allow for accurate determination of these resonance frequencies, it nevertheless provide a reliable order-of-magnitude estimate for the spacing between them, $\Delta f \approx 12$ kHz, close to the observed $\Delta f_{12} = 9.4$ kHz. Furthermore, we speculate that the difference in amplitude between the two peaks shown in Fig. 7.4 is mainly due to the shift in wave pattern going from one value n_x to the neighboring peak at $n_x + 1$ as illustrated by the thick, white, vertical lines in Fig. 7.5, consistent with the center position of the microscope field of view. For $n_x = 17$ the pressure amplitude along the vertical line is much smaller than that for $n_x = 18$. See Refs. [43, 109] for more details on axial modes and the model used for the results of Fig. 7.5.

7.1.1.5   Conclusions on the particle tracking method

We have established a new method to measure *in situ* the energy density, the local pressure amplitude, and the Q factor of ultrasound resonances in microfluidic chips by tracking individual polystyrene microbeads undergoing acoustophoresis in straight water-filled channels in silicon/glass chips. We have shown that, as expected, the acoustic energy density scales with applied piezo voltage to the power 2. Furthermore, by plotting the energy densities as a function of the applied ultrasound frequency, we have estimated the Q factors by fits to Lorentzian line

Figure 7.5: A top view color plot (blue negative, red positive) of the pressure field of three ultrasound resonances calculated in a simplified 2D model. For each resonance is shown the number of n_x of half wavelengths in the axial direction, the resonance frequency f, and the distance Δf in frequency space to the neighboring resonance. The thick white vertical lines mark the center position of the microscope field of view. Adapted from Ref. [69].
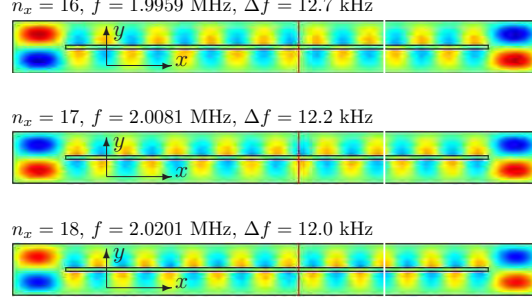
shapes. However, as shown in Section 5.3, this is not accurate due to the spatial complexity of the underlying resonances and care must be taken when estimating Q factors from such results. Nevertheless, the Q factors of 200-600 measured in this work, seem to be of reasonable order of magnitude, but high [43].

7.1.2   Velocity profile fitting

This section describes an approach based on fitting the theoretical expression of the acoustophoretic transverse velocity profile, Eq. (3.50), to experiments of the microparticles velocities. This approach was used earlier in the Chapters 5 and 6. The following presented results are part of the collaborative work presented in Chapter 5 and appended in Chapter B. The measurements were carried out using the experimental model system, Section 2.1, and we investigate a microscope field-of-view around $x = 0$ with the resonance mode at $f = 1.968$ MHz at $T = 25$ °C, which is nearly a straight 1D resonance within the channel-center single-image frame of Fig. 5.5.

By µPIV analysis with $n_{\text{tot}}^{\text{pair}} = 100$ we obtained the acoustophoretic velocity field $\boldsymbol{u}(x, y)$, the magnitude of which is shown as the color plot in Fig. 7.6(a). As it is a nearly perfect 1D transverse standing wave, it is meaningful to calculate the x-direction-average $\langle u_y \rangle_x$ of the y-component u_y of $\boldsymbol{u}(x, y)$,

$$\langle u_y \rangle_x = \frac{1}{N} \sum_{n=1}^{N} u_y(x_n, y_m), \tag{7.1}$$

which is a function of the transverse grid coordinate y_m. In Fig. 7.6(b), the analytical expression (3.50) for $u_y(y)$ (blue dashed line) is fitted to the values at y_m of $\langle u_y \rangle_x$ (red circles) using the acoustic energy density E_{ac} and half wavelength $\lambda/2$ as fitting parameters. The fit is good and results in $E_{\text{ac}} = (98.0 \pm 1.1)$ J m^{-3} and $\lambda_y/2 = (374.0 \pm 1.5)$ µm, where the latter is close to the channel width $w = 377$ µm.

The results are compared to the particle tracking method described in the latter section and in Fig. 7.6(c) we plot the transverse $y(t)$ component of 16 out of 100 extracted particle tracks, see white lines in Fig. 7.6(a). Each particle track was fitted to Eq. (3.51) for $y(y_0, t)$, and E_{ac} and $\lambda_y/2$ were extracted as the fitting
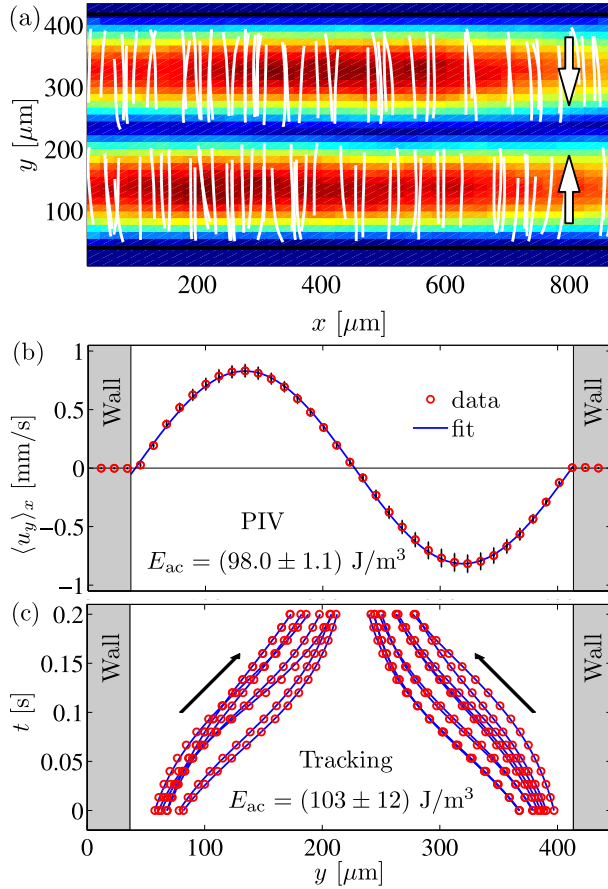
Figure 7.6: (a) Acoustophoretic velocity field $\boldsymbol{u}(x,y)$ (arrow plot) and its magnitude u (color plot from 0 (dark blue) to 900 (dark red)) at the channel center for temperature $T = 25°$, driving frequency $f = 1.968$ MHz, and driving voltage $U_{\text{pp}} = 1.89$ V. Also shown are 100 particle tracks (white) used to extract the acoustic energy density E_{ac} by the tracking method [69]. (b) Plot of the x-averaged y-component $\langle u_y \rangle_x$ (data: red circles; fit: blue line, standard deviations: black lines) of the acoustophoretic velocity field shown in panel (a). (c) Plot of the transverse path $y(t)$ (red circles, only every second data point is shown) and corresponding fit (Eq. (3.51), blue lines) for 16 of the 100 microbead tracks. Adapted from Ref. [36].

parameters leading to the acoustic energy density $E_{\text{ac}} = (103 \pm 12)$ J m^{-3} and the half-wavelength $\lambda_y/2 = (382 \pm 27)$ µm.

The resonance parameters determined independently from the µPIV method and the particle tracking method are in good agreement with relative deviations less than 5 %. We note that the µPIV method allows for improved statistics, and thus in general will lead to better results compared to the particle tracking method. However, both the particle tracking and velocity profile methods require the particles to be reasonably resolved by the microscope. In the next section we challenge this limitation and present a method based on measuring background-illuminated light intensity.

7.1.3 Light-intensity fitting

This section presents a simple, rapid and inexpensive light-intensity-based method for measuring the acoustic energy density E_{ac}. The experimental measurements presented in this section is not carried out using the experimental model system in Section 2.1, but is carried out at Royal University of Technology by PhD student Ida Iranmanesh.

This section is based on work done in collaboration with Professor Martin Wiklund and his PhD student Ida Iranmanesh, Royal University of Technology,
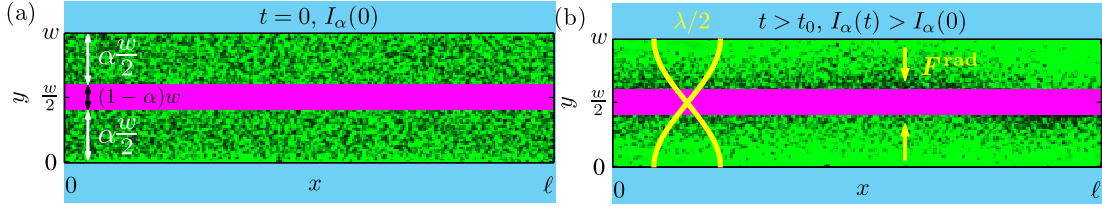
Figure 7.7: Bottom-view of the straight acoustophoresis microchannel (light blue walls) of width w and length ℓ. The microchannel containing a suspension of 5-µm-diameter polyamide microbeads (black/gray dots) is illuminated from top resulting in a green background in the image. The particle motion is only recorded outside a band of relative width $1 - \alpha$ (magenta) along the channel center $y = w/2$, as the particle concentration outside this band remains sufficiently low throughout the entire acoustophoretic focusing process. (a) At time $t = 0$ the microbeads are homogeneously distributed throughout the channel and the light intensity of the image is $I_\alpha(0)$. (b) The microchannel is acoustically actuated in its transverse half-wave resonance (yellow) and the acoustic radiation force (yellow arrows) pushes the suspended particles to the acoustic pressure node at the vertical center plane at $y = w/2$. As the particles gradually leave the interrogation area (green) and enter the excluded band along the center plane, the light intensity of the image increases monotonically, $I_\alpha(t) > I_\alpha(0)$. Adapted from Ref. [72].

and Professor Henrik Bruus, Technical University of Denmark. The work is published in Lab on a Chip and the paper is appended in Chapter C. In the following parts of the paper is reproduced in a slightly modified version to align with the rest of the thesis.

7.1.3.1 Many-particle light-intensity model

We study a glass-silicon-glass chip containing an optically transparent microchannel filled with a particle suspension as described in more detail in Section 7.1.3.3. The channel is illuminated from the top, and the transmitted light is recorded by a CCD camera mounted on a mid-range microscope using a low-numerical-aperture objective (N.A. = 0.25, focal depth ≈ 10 µm). The particles appear as blurred black/gray spots covering about 10 pixel on the resulting images. In this work we only study such a transverse half-wave resonance, and we always have $\Phi > 0$. As a result, the radiation force is directed towards the channel center, and particles, which initially are homogeneously distributed in the microchannel as shown in Fig. 7.7(a), are pushed towards the vertical center plane at $y = w/2$ as shown in Fig. 7.7(b), where ideally they all end up.

We analyze a many-particle suspension of 0.35×10^{14} particles/m^3 (see Section 7.1.3.3), which is dilute enough to minimize both hydrodynamic and acoustic particle-particle interactions as well as the effect of overlapping particles located at different heights in the channel. For our system with the particle diameter $2a = 4.5$ µm and channel height $h = 110$ µm, the threshold particle concentration C^* for particle overlapping is when exactly one particle occupies the cylindrical

volume of base area πa^2 and height h, $C^* = 1/(\pi a^2 h) = 0.6 \times 10^{15}$ m^{-3}. To ensure that the single-particle description is valid in our analysis, we only study the particle motion in the interrogation area of relative width α (green in Figs. 7.7 and 3.4) away from the channel center, while we exclude the region of relative width $1 - \alpha$ (magenta) along the center line, where the particle concentration eventually becomes very large as all the particles end up accumulating there. In this work we found $\alpha = 0.8$ to be a good value and have used it throughout the analysis.

As illustrated in Fig. 7.7, all our images are bottom views of the microchannel (light blue walls). However, as the focal depth ($\simeq 10$ µm) of our microscope is much smaller than the height of the channel (110 µm) all the particles (black/gray dots) in the channel are imaged as shades with relatively uniform but limited resolution. Depending on the presence of a particle, each pixel in a given image of the microchannel has a dimensionless gray-scale pixel intensity ranging from 0 (black) to 255 (white). Summing over all pixels in a given image, we obtain the total pixel intensity I_α. If no particles are present in the interrogation area of relative width α, the light intensity (green) is I_α^{max}. However, at $t = 0$ there are N_0 homogeneously distributed particles present in the interrogation area, Fig. 7.7(a), and these give rise to a relative intensity reduction R ranging from zero to unity, such that the initial intensity can be written as $I_\alpha(0) = (1-R)I_\alpha^{\mathrm{max}}$. When the microchannel is ultrasonically actuated, Fig. 7.7(b), the particles move towards and into the excluded center-region. Each time a particle enters the excluded region, the number $N_\alpha(t)$ of particles left inside the interrogation area decreases by unity, and the light intensity I_α increases correspondingly. This can be expressed as

$$I_\alpha(t) = \left[1 - R\,\frac{N_\alpha(t)}{N_0}\right] I_\alpha^{\mathrm{max}}. \tag{7.2}$$

At time $t = \infty$ there are zero particles left in the interrogation area, $N_\alpha(\infty) = 0$, and $I_\alpha(\infty) = I_\alpha^{\mathrm{max}}$.

The time it takes the ith particle to move from its starting position $y_0^{(i)}$ to the excluded area at $y = \alpha w/2$ is called $\tau_\alpha(y_0^{(i)})$, and at this time its contribution to $N_\alpha(t)$ drops from unity to zero. Mathematically, this is expressed through the Heaviside step function $\Theta[\tau_\alpha(y_0^{(i)}) - t]$, which by definition is unity for $t < \tau_\alpha(y_0^{(i)})$, when the particle is visible in the interrogation area, and zero for $t > \tau_\alpha(y_0^{(i)})$, when the particle is inside the excluded region. We can therefore write

$$N_\alpha(t) = \sum_{i=1}^{N_0} \Theta\left[\tau_\alpha(y_0^{(i)}) - t\right]. \tag{7.3}$$

If the initial number N_0 of particles is sufficiently large, typically around 10^4 as in Fig. 7.7(a), it is a reasonable approximation to replace the discrete sum in Eq. (7.3) by the ensemble average $\langle N_\alpha(t)\rangle$ defined as the average over a homoge-

neous distribution of starting positions,

$$\langle N_\alpha(t)\rangle = \frac{2N0}{\alpha w} \int_0^{\alpha\frac{w}{2}} \mathrm{d}y_0 \, \Theta\Big[\tau_\alpha(y_0) - t\Big], \tag{7.4}$$

where we have used the symmetry of the system to integrate over only half the channel width. Using the dilute-limit expression (3.52), we find that $t < \tau_\alpha(y_0)$ implies that the integrand in Eq. (7.4) is unity in the interval $0 < y_0 < (w/\pi)\arctan\Big[\tan(\frac{\pi}{2}\alpha)\mathrm{e}^{-t/t^*}\Big]$ and zero otherwise. Hence we arrive at

$$\langle N_\alpha(t)\rangle = \frac{2N_0}{\alpha\pi} \arctan\left[\tan\left(\frac{\pi}{2}\alpha\right)\mathrm{e}^{-t/t^*}\right]. \tag{7.5}$$

Taking the ensemble average of the light intensity $I_\alpha(t)$ in Eq. (7.2) results in the normalized light intensity,

$$\frac{\langle I_\alpha(t)\rangle}{I_\alpha^{\max}} = 1 - R\frac{\langle N_\alpha(t)\rangle}{N_0}, \tag{7.6}$$

$$= 1 - \frac{2R}{\alpha\pi} \arctan\left[\tan\left(\frac{\pi}{2}\alpha\right)\mathrm{e}^{-t/t*}\right]. \tag{7.7}$$

This expression is plotted in Fig. 7.8 as function of time t. In panel (a) the energy density E_{ac} is swept for fixed relative width α of the interrogation area, and it is clear that as the acoustic energy density increases, the suspended particles traverse faster to the channel center and the relative intensity reaches its maximum of unity faster. The opposite situation is shown in panel (b), where the relative width α is swept for fixed E_{ac}. The wider an interrogation area, the slower is the increase in intensity.

In a given experiment, the observed intensity $I_\alpha(t)$ is identified with the theoretical ensemble average $\langle I_\alpha\rangle$. From Eq. (7.7) thus follows that $I_\alpha(0) \approx \langle I_\alpha(0)\rangle = (1-R)I_\alpha^{\max}$ and $I_\alpha(\infty) \approx \langle I_\alpha(\infty)\rangle = I_\alpha^{\max}$. Hence, the relative intensity reduction R can be estimated from the intensity measurements as

$$R \approx 1 - \frac{I_\alpha(0)}{I_\alpha(\infty)}. \tag{7.8}$$

Once R is known, the characteristic time t^* can be found as a fitting parameter using Eq. (7.7) to fit measured values $I_\alpha(t)/I_\alpha(\infty)$ versus time t. Then the acoustic energy density can be extracted from Eq. (3.51b) if the material parameters of the microbeads are known.

Finally, the determination of t^* allows for the introduction of the exponentially re-scaled time s given by

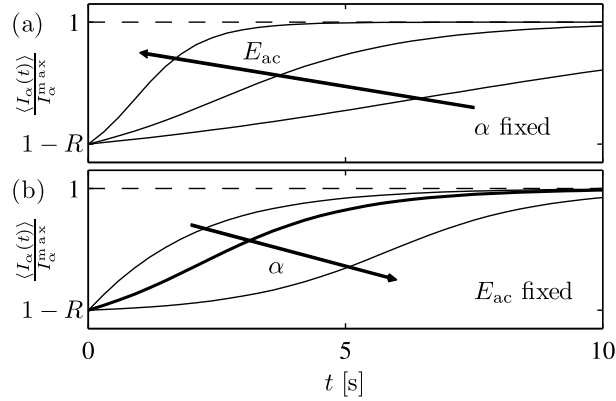$$s = \mathrm{e}^{t/t*}. \tag{7.9}$$

Figure 7.8: Example of the normalized light intensity $\langle I_\alpha(t)\rangle/I_\alpha^{\max}$, Eq. (7.6), as function of time t and using the parameters in the List of Material Parameters. (a) The energy density E_{ac} is swept ($1\,\mathrm{J\,m^{-3}}$, $2.5\,\mathrm{J\,m^{-3}}$, $7\,\mathrm{J\,m^{-3}}$) for fixed relative interrogation-area width $\alpha = 0.8$ of the interrogation area, and it is clear that as the acoustic energy density increases, the suspended particles traverse faster to the channel center and the relative intensity reaches its maximum of unity faster. (b) The relative width α is swept (0.3, 0.8, 0.97) for fixed $E_{\mathrm{ac}} = 2.5\,\mathrm{J\,m^{-3}}$. The wider an interrogation area, the slower is the increase in intensity. Adapted from Ref. [72].

Rearranging Eq. (7.7) leads to the prediction that a plot of all data in the form $\left[1 - I_\alpha/I_\alpha(\infty)\right]/R$ versus re-scaled time s collapses on a universal curve given by

$$\frac{1}{R}\left[1 - \frac{I_\alpha(s)}{I_\alpha(\infty)}\right] = \frac{2}{\pi\alpha}\arctan\left[\frac{1}{s}\tan\left(\alpha\frac{\pi}{2}\right)\right]. \qquad (7.10)$$

It follows from Eq. (7.7) that this particular combination of intensities can be interpreted as the relative average number of particles $n_\alpha(s)$ left in the interrogation area,

$$\frac{1}{R}\left[1 - \frac{I_\alpha(s)}{I_\alpha(\infty)}\right] = \frac{\langle N_\alpha\rangle}{N_0} = n_\alpha(s). \qquad (7.11)$$

7.1.3.2 Intensity method for measuring the acoustic energy density

The presented intensity model can be used to measure the acoustic energy density *in situ*. The basic idea is to measure the total pixel intensity as function of time and then fit the above described model to the data points using the acoustic energy density as a fitting parameter. The method is easily applied; all that is needed is a movie of the acoustophoretic focusing and the following algorithm:

1. Turn the CCD movie into series of image frames.

2. Determine the total pixel intensity $I_\alpha(t)$ of each image frame by summing the individual pixel intensities inside the interrogation area of relative width α.
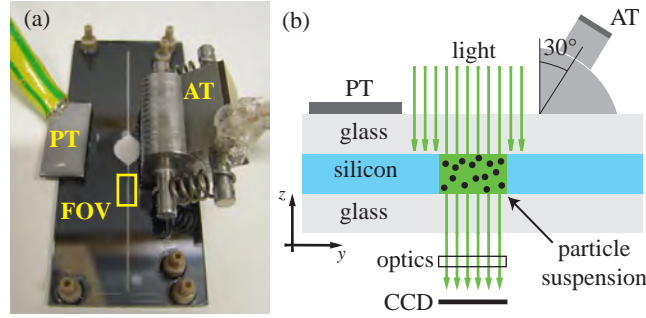
Figure 7.9: (a) Photograph of the acoustophoresis glass-silicon-glass chip mounted with two ultrasonic piezo transducers, a planar transducer (PT) and an angled transducer (AT) fixed at 30°. The chip consists of a top glass layer, an intermediate silicon layer, and a bottom glass layer of thicknesses 0.20 mm, 0.11 mm, and 1.10 mm, respectively. The acoustophoretic motion in the particle suspension is observed in the yellow-square-marked field of view (FOV) of length $\ell = 1.21$ mm containing a microchannel of width $w = 328$ μm and depth $h = 110$ μm. (b) Cross-sectional sketch (not drawn to scale) of the experimental setup. The chip consists of silicon (blue) and glass (light gray) layers and is actuated by either the planar PZT transducer (PT) or the angled PZT transducer (AT) both marked by dark gray. Light (green arrows) passes through the transparent microchannel, which is recorded by a CCD camera (black) via an inverted microscope with a green filter cube (optics). Adapted from Ref. [72].

3. Determine the maximum intensity $I_\alpha^{\max} = I_\alpha(\infty)$ from the last image in the time series.

4. Calculate the normalized intensity $I_\alpha(t)/I_\alpha^{\max}$.

5. Determine the initial relative intensity reduction R using Eq. (7.8).

6. Fit expression Eq. (7.7) to the data $I_\alpha(t)/I_\alpha^{\max}$ using E_{ac} as fitting parameter by Eq. (3.51b).

To obtain the best possible result, the measured acoustophoretic focusing should be long enough in time to reach a near-static bead distribution. Furthermore, α should be chosen as large as possible, but still without resulting in too many particles remaining in the interrogation area of the last image frame. Repeated measurement of the intensity curves enhance the accuracy and enables an estimate of the standard deviation of the measured energy density.

In this work the algorithm was implemented in Matlab. The Matlab script `imgs2energy.m`, we used for extracting E_{ac} via the light-intensity model, can be downloaded from the Electronic Supplementary Information to the published paper on the website of Lab on a Chip [72].

7.1.3.3   Experimental setup

Acoustophoresis microchip. We used a glass-silicon-glass chip (Gesim, Germany) as shown in Fig. 7.9 and described in more detail in Ref. [24]. The thicknesses of the top glass layer, the intermediate silicon layer, and the bottom

glass layer were 0.20 mm, 0.11 mm, and 1.10 mm, respectively. In the silicon layer was etched a cavity connected to inlets and outlets by an microchannel of width $w = 328$ µm and depth $h = 110$ µm. The inlets and outlets were connected to a syringe using Teflon tubing, adapters and valves.

Acoustics driving electronics. The acoustophoresis microchip was acoustically actuated using two different in-house-built transducers, a planar transducer (PT) and an angled transducer (AT), see Fig. 7.9. The planar transducer was mechanically damped by a layer of epoxy, while the angled transducer was glued on a two-part wedge/quarter-cylinder aluminum mounting. The top part was connected through immersion oil to the lower part via two aluminum springs and could thus slide along the cylinder surface from 0° to 90°. This tunability feature of the coupling angle is to be used in a future work; here the angled transducer was fixed at an angle of 30°. Both the planar and angled transducer were built using PZT piezoceramic plates (Pz26, Ferroperm, Denmark) and were attached to the chip using a quick-drying and water soluble adhesive gel ('Tensive', Parker Laboratories, USA). The transducers were driven by a function generator (DS345, Stanford, USA) coupled to a RF amplifier (75A250, Amplifier research, USA). The peak-to-peak voltage was monitored by an oscilloscope (TDS220, Tektronix, USA).

Temperature sensing. To observe a possible drift in resonances caused by varying temperature, the temperature was measured at the top glass layer with a T-type (copper-constant) and Teflon-insulated micro thermocouple with a total tip diameter (sensor and sheath layer) of 0.41 mm (IT-21, Physitemp Instruments, USA). Automatic monitoring of temperature data was done with the accuracy of 0.1°C (Dostmann Electronic GmbH P655-LOG, Germany). Furthermore, the room temperature was logged throughout experimenting and both room- and chip temperatures were stable within 1 °C.

Microbead suspension. The investigated microbead suspension was a 9:1 mixture of Milli-Q water (with 0.01 % Tween20) and a blood-mimicking fluid (EU-DFS-BMF-ver.1 for Flow Doppler Phantoms, Danish Phantom Design, Denmark) containing 5-µm-diameter polyamide microbeads (Orgasol Powders, Arkema, France). Due to its high water content, the suspension acts as pure Milli-Q water containing polyamide microbeads. The material parameters of the suspension are listed in List of Material Parameters. Using a Coulter counter, the polyamide particle concentration was measured to be $C = 3.5 \times 10^{14}$ m^{-3} with a normal distributed particle diameter of $2a = (4.5 \pm 0.7)$ µm. Despite the large size-dispersion, we used the blood-mimicking fluid because it mimicks the size-dispersion of biological cells and is inexpensive.

Imaging. The microchannel was imaged by an inverted microscope (Axiovert 40, Zeiss, Germany) with green filter cube, objective (A-Plan 10x/0.25 Ph1, Zeiss, Germany), and CCD camera (AxioCam HSC, Zeiss, Germany) with frame rates between 30-46 ms. To acquire a set of images from a recorded movie we used AxioVision Rel.4.8 software. The pixel resolution was 634 pixel $\times$ 172 pixel of a channel section of size $\ell \times w = 1209$ µm $\times$ 328 µm. Therefore 1 pixel corresponds to 1.9 µm implying that a 4.5-µm-diameter particle will roughly cover 10 pixel.
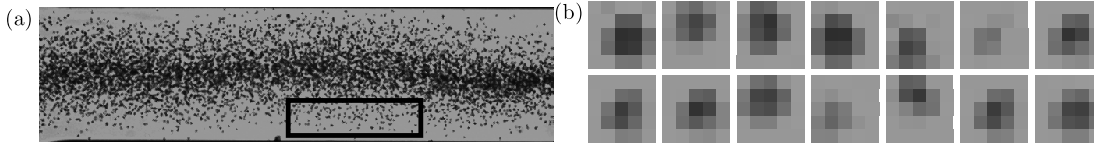
Figure 7.10: (a) Gray-scaled experimental image where the microbeads have traversed acoustophoretically half the way towards the center of the microchannel. Inside the black rectangle all isolated particles are identified and their pixel intensities are analyzed within a 5 pixel × 5 pixel square. (b) 5 pixel × 5 pixel square views of 14 of the 41 isolated microbeads in the black rectangle marked in panel (a). Adapted from Ref. [72].

This is roughly the same as the optical resolution of 1.3 µm of the objective used. Given the above microbead concentration C and a relative interrogation-area width $\alpha = 0.8$, we can estimate the number N_0 of visible microbeads to be $N_0 = \alpha \, C \, \ell wh \approx 1.2 \times 10^4$.

Isolated-particle prediction of the total light-intensity reduction. To verify that optical many-particle effects, such as light scattering and particle shadowing, can be neglected, we predict the total relative intensity reduction R based on the particle concentration C and the intensity reduction of isolated particles. In Fig. 7.10(a) we show a single image frame where the microbeads have traversed acoustophoretically half the way towards the center of the microchannel. The image clearly shows how single particles are less distinguishable as they move closer together near the center plane of the channel. In the image we mark a region (black square) where we investigate 5 pixel × 5 pixel square regions surrounding each of 41 isolated particles. Fig. 7.10(b) shows 14 such squares. On average a 5 pixel × 5 pixel square containing a single particle has a total dimensionless, gray-scale pixel intensity of $I_{\mathrm{p}} = (3.3 \pm 0.2) \times 10^3$. When all the particles have acoustophoretically traversed into the excluded center region, we obtain the maximum total pixel intensity $I_{\alpha}^{\mathrm{max}} \approx 1.3 \times 10^7$ corresponding to an intensity per pixel of 149 implying $I_{\mathrm{ref}} = 3.7 \times 10^3$ for an empty 5 pixel × 5 pixel square. Finally, we predict the relative intensity reduction $R = N_0 \, (I_{\mathrm{ref}} - I_{\mathrm{p}})/I_{\alpha}^{\mathrm{max}} \approx 0.42 \pm 0.16$. Notice, this is an upper estimate for R as it excludes effects such as particle shadowing, which will decrease R.

7.1.3.4 Experimental procedure

Stop-flow particle-focusing experiments. The polyamide microbead suspension were injected into the chip manually using a glass syringe. The flow was stopped and a field of view section (yellow rectangle FOV in Fig. 7.9(a)) in the straight part of the acoustophoresis microchannel was observed. While actuating one of the two transducers close to the transverse half-wave resonance of the microchannel, the acoustophoretic particle motion was recorded with the CCD camera. A movie typically lasted 30 seconds comprising about 600 image frames. The actuation frequency was modulated linearly [110] with a rate of 1 kHz from

2.06 MHz to 2.16 MHz around the center frequency 2.11 MHz.

Energy density determination. We use the intensity method described in Section 7.1.3.2 to extract the acoustic energy density from a given acoustophoretic focus experiment. As the variation Δa in particle radius a is large (about 15 %), we extract E_{ac} for the particle radii a, $a + \Delta a$, and $a - \Delta a$, with $\Delta a = 0.7$ µm.

Scan in PZT voltage. Our experimental study consists of five independent experiment series, where we scanned the PZT voltage U_{pp} of one of the two transducers in the range from 0 to 23 V. For each driving voltage, we performed the above described stop-flow focus experiment. In the two first experiment series, we drove the angled transducer AT, while in the last three series, we drove the planar transducer PT. Each experiment series consisted of typically 16 particle-focusing experiments (16 driving voltages) resulting in a total of 88 acoustophoretic focusing experiments for the experimental study.

7.1.3.5 Results

Validation of the light-intensity method To validate the light-intensity method described in Section 7.1.3.2, we measure the acoustic energy density using the particle tracking method presented in Section 7.1.1 ([69]). In the first experimental series for the planar transducer at $U_{\mathrm{pp}} = 18.9$ V, we use the freeware particle tracking program Tracker 4.61 to track 20 microbeads and using the tracking method, we obtain an acoustic energy density $E_{\mathrm{ac}} = (1.4 \pm 0.5)$ J/m^3. Using the light-intensity method, we obtain the acoustic energy density $E_{\mathrm{ac}} = (1.4 \pm 0.4)$ J/m^3. In conclusion, the obtained acoustic energy density agrees well with that of the previously reported tracking method. For both methods, the presented uncertainty is due to the size dispersion of the particles and wall-enhancement of the drag forces.

The light-intensity method turned out to be a simple, rapid, and robust method compatible with low- or mid-ranged microscopes yielding moderate resolution images of high particle concentrations. In contrast, the tracking method was tedious and micro-PIV was impossible.

Scanning the PZT voltage We use the intensity method described in Section 7.1.3.2 to extract the acoustic energy density from each of the 88 particle-focusing experiments in our experimental study in Section 7.1.3.4. In Fig. 7.11(a) we plot the normalized light-intensity curves $I_\alpha(t)/I_\alpha(\infty)$ for every third (for clarity) of the 88 acoustophoretic focusing experiments of either driving the angled transducer (red points) or driving the planar transducer (blue points). At starting time $t = 0$, it is seen that from Eq. (7.8) the mean of the relative intensity reduction $R = 0.36 \pm 0.07$. This value of the relative intensity reduction is close to, but deviates as expected slightly from, the upper prediction $R = 0.42 \pm 0.16$ in Section 7.1.3.3.

In Fig. 7.11(b) we show the measured acoustic energy densities E_{ac} (red and blue disks) as function of the driving voltage squared U_{pp}^2. The energy density is extracted using the mean particle diameter $2a = 4.5$ µm and is shown for each
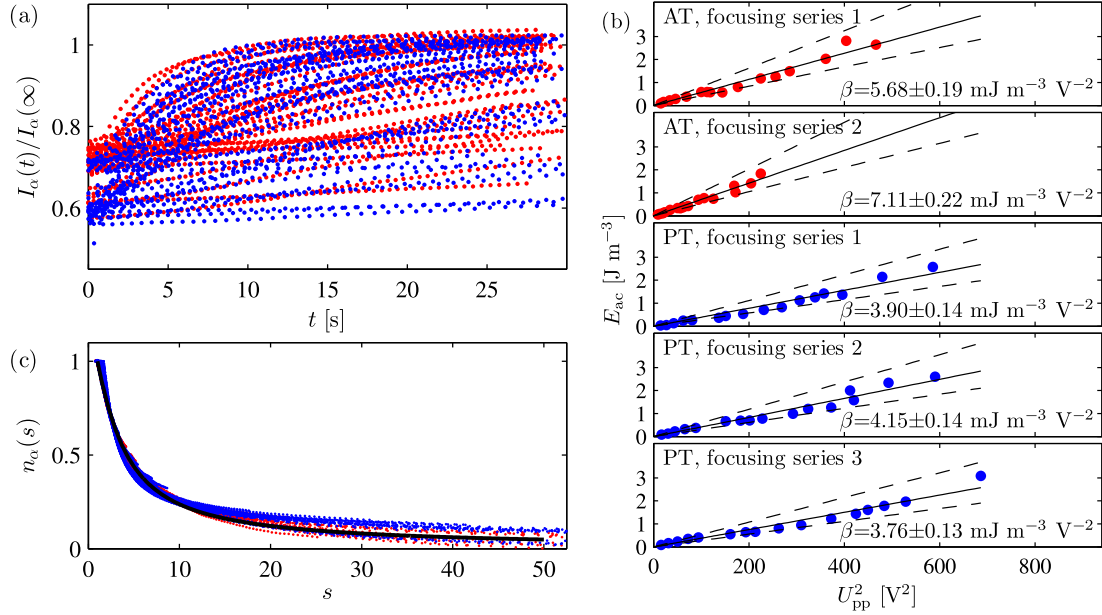
Figure 7.11: Analysis of the five independent experimental series comprising of 88 individual acoustophoretic focusing experiments, where the piezo voltage U_{pp} is scanned from 0 to 23 V. (a) Normalized total intensity curves $I_\alpha(t)/I_\alpha(\infty)$ for every third (for clarity) of the 88 experiments of either driving the angled transducer (red points) or driving the planar transducer (blue points). (b) Fitted acoustic energy densities E_{ac} (red and blue disks) as function of the driving voltage squared U_{pp}^2 for each of the five experimental U_{pp}-scanning series. Within each of the voltage sweep series, a voltage square law $E_{ac} = \beta\, U_{pp}^2$ (black lines) is fitted to the data points. Also shown are two similar fits using the bead radius $a + \Delta a$ (lower dashed line) and $a - \Delta a$ (upper dashed line) with $\Delta a = 0.7$ µm. (c) The data points in panel (a) plotted versus the re-scaled time s, given by Eq. (7.9) and E_{ac} from panel (b), collapse onto the universal curve $n_\alpha(s)$ for the relative average number of particles given in (7.11). Adapted from Ref. [72].

of the five U_{pp}-scanning experimental series. Within each experiment series, we observe that the energies scale with U_{pp}^2 as expected [69], and to the data we fit a straight line $E_{ac} = \beta\, U_{pp}^2$ (black line). Similarly, we plot dashed lines when the energy densities are extracted using particle radius of $a + \Delta a$ and $a - \Delta a$, respectively, with $\Delta a = 0.7$ µm.

Using the fitted energy densities, we find the re-scaled time s given by Eq. (7.9) and plot the intensity data in the form $\left[1 - I_\alpha/I_\alpha(\infty)\right]/R$ versus s. The data points collapse on the universal curve for the relative average number $n_\alpha(s)$ of particles given by Eq. (7.11) thereby providing a consistency check of the underlying single-particle assumption.

7.1.3.6 Discussions on the light-intensity method

The simple and rapid light-intensity method to determine the acoustic energy density in acoustofluidic microsystems is based on a large number of particles, which leads to a reduction of statistical errors. The method is especially useful when analyzing moderate-resolution images of high particle concentration, where tracking- and micro-PIV methods are difficult to apply.

As we have used microbeads with a wide size distribution (about 15 %), our estimates of the acoustic energy densities have similar high relative uncertainties. This is indicated by the dashed lines in Fig. 7.11(b). However, we see from the scatter of the data points around the expected βU_{pp}^2-curve that, for a fixed value of the particle radius, the statistical uncertainty, beyond that due to particle dispersion, is about 4 %. This indicates the potential for high precision measurements using the method on monodisperse particle suspensions.

The method is subject to some uncertainties: (*i*) The particle concentration has to be low enough to maintain single-particle acoustophoresis by avoiding clustering as well as acoustic and hydrodynamic particle-particle interactions (below 10^{15} particles/m^3). It must also be low enough to neglect optical many-particle effects (below 0.6×10^{15} particles/m^3 to avoid shadowing). We checked explicitly in this work that the total intensity reduction obtained from an isolated-particle analysis coincides well with that obtained from the full many-particle images at our density of 0.35×10^{14} particles/m^3. (*ii*) The acoustic wave has to be a 1D planar transverse standing wave to allow for the use of the analytical expressions in the light-intensity model. In some works, such a wave is not intended, for example to achieve particle agglomeration in a point [24, 111], and for those, after excluding the appropriate nodal line regions of more complex shape, the method can only be used to obtain relative figures of merit without the benefit of analytical predictions. In other works, where a 1D planar transverse standing wave is intended, such a wave may still be difficult to achieve as shown in Section 5.3. In the present work we overcame this challenge by using frequency-modulation to average over a large number of resonances all with the transverse wave feature, but with different modal pattern along the axial length of the channel. The choice of excluding the center part in the images containing the focused particles further contributes to minimize the effects of particle-particle interactions or weak axial components in the acoustic field perpendicular to the transverse standing wave used in the model. (*iii*) The focus experiment has to be carried out with acoustophoretic particle velocities large enough to avoid sedimentation and thus avoid influence on the particle motion by the presence of the bottom channel wall. In our work the wall-induced drag enhancement was less than 6 % for the center half of the channel volume, thus the systematic under-estimation of the acoustic energy density is of the same order. If a more accurate estimate of the energy is required, a height-dependent Faxén correction must be included in the calculation of the single-particle tracks [112]. (*iv*) The temperature has to be stable enough to avoid drift in acoustic resonances as shown experimentally in Section 5.4.

In this work the method was applied to a trans-illuminated microchannel. However, in principle, the method can be applied to setups utilizing reflected light in, say, chips where only the lid is transparent. This still needs to be done.

7.1.3.7 Conclusions on the light-intensity method

This section describe a simple and rapid method for *in situ* determination of the acoustic energy density by observing the increase in light intensity as suspended particles undergo acoustophoresis. The method relies on a theoretical model of averaging over many particles each being subject to single-particle acoustic motion, and it has been validated with the single-particle tracking method. We have shown by proper re-scaling that the re-scaled light intensity versus re-scaled time fall on a universal curve predicted by ensemble averaging over acoustophoretic single-particle paths. Compared to other methods, the light-intensity method is especially well suited for images of many particles and of moderate image resolution. We envision it as a main tool in future characterization and optimization of microchips and transducers used for acoustophoresis.

7.1.4 Concluding remarks

This section presented three approaches for determination of the acoustic energy density by means of acoustophoresis. The particle tracking is preferred for low-concentration suspensions of high image resolution, while the intensity method is preferable for data of low resolution.

7.2 Determination of density and compressibility of microparticles using microchannel acoustophoresis

This section proposes a method for determination of density and compressibility of individual particles and cells undergoing microchannel acoustophoresis in an arbitrary acoustic field. The development of the method is still in progress and in this section we simply highlight the essential method principles. Furthermore, the method has been used to carry out preliminary experiments presented on the MicroTAS 2011 conference [107].

7.2.1 Determining the acoustic field from acoustophoresis

We investigate an acoustic resonance actuated in the acoustophoresis microchannel, where the single-particle acoustophoretic velocity $\boldsymbol{u}$ is measured for three particle types denoted "a", "b", and "c", respectively. Combining Eqs. (3.44) and

(3.31), we write the linear system of equations for the particle velocities as

$$
\begin{bmatrix} \dfrac{\boldsymbol{u}^{\mathrm{a}}}{a_{\mathrm{a}}^2} \\[2mm] \dfrac{\boldsymbol{u}^{\mathrm{b}}}{a_{\mathrm{b}}^2} \\[2mm] \dfrac{\boldsymbol{u}^{\mathrm{c}}}{a_{\mathrm{c}}^2} \end{bmatrix} = \begin{bmatrix} f_1^{\mathrm{a}} & f_2^{\mathrm{a}} & \dfrac{1}{a_{\mathrm{a}}^2} \\[2mm] f_1^{\mathrm{b}} & f_2^{\mathrm{b}} & \dfrac{1}{a_{\mathrm{b}}^2} \\[2mm] f_1^{\mathrm{c}} & f_2^{\mathrm{c}} & \dfrac{1}{a_{\mathrm{c}}^2} \end{bmatrix} \begin{bmatrix} -\dfrac{\kappa_0}{9\eta}\boldsymbol{\nabla}\langle p_1^2\rangle \\[2mm] \dfrac{\rho_0}{6\eta}\boldsymbol{\nabla}\langle v_1^2\rangle \\[2mm] \langle\boldsymbol{v}_2\rangle \end{bmatrix},
\tag{7.12}
$$

which on matrix notation can be written as

$$
\mathbf{U}_{\mathrm{abc}} = \mathbf{f}_{\mathrm{abc}}\mathbf{B}.
\tag{7.13}
$$

Here, the velocity matrix $\mathbf{U}_{\mathrm{abc}}$ is purely related to the velocities and sizes of the particles, the field matrix $\mathbf{B}$ solely comprise the acoustic field, radiation and streaming, while the contrast matrix $\mathbf{f}_{\mathrm{abc}}$ connects $\mathbf{U}_{\mathrm{abc}}$ and $\mathbf{B}$. For known material parameters of buffer and particles, the acoustic field matrix $\mathbf{B}$ is determined by taking the inverse of $\mathbf{f}_{\mathrm{abc}}$

$$
\mathbf{B} = \mathbf{f}_{\mathrm{abc}}^{-1}\mathbf{U}_{\mathrm{abc}},
\tag{7.14}
$$

which has a unique solution only if

$$
\frac{1}{a_{\mathrm{a}}^2}(f_1^{\mathrm{b}}f_2^{\mathrm{c}}-f_2^{\mathrm{b}}f_1^{\mathrm{c}}) + \frac{1}{a_{\mathrm{b}}^2}(f_2^{\mathrm{a}}f_1^{\mathrm{c}}-f_1^{\mathrm{a}}f_2^{\mathrm{c}}) + \frac{1}{a_{\mathrm{c}}^2}(f_1^{\mathrm{a}}f_2^{\mathrm{b}}-f_2^{\mathrm{a}}f_1^{\mathrm{b}}) \neq 0.
\tag{7.15}
$$

We note that if all particles have different f-factors, they can be equal-sized, while if only two particles have different f-factors, the remaining particle must be of different size.

7.2.1.1 Large-particle acoustophoresis

We consider the special case of large-particle acoustophoresis, typically 5-µm-diameter particles or larger, where the acoustic radiation force dominates the particle motion [69, 84] resulting in a negligible acoustic streaming velocity $\langle\boldsymbol{v}_2\rangle = \mathbf{0}$. In this case only two different sets of acoustophoretic particle velocities are needed to determine the acoustic field and the linear system of equations of motion in Eq. (7.12) reduces to

$$
\begin{bmatrix} \dfrac{\boldsymbol{u}^{\mathrm{a}}}{a_{\mathrm{a}}^2} \\[2mm] \dfrac{\boldsymbol{u}^{\mathrm{b}}}{a_{\mathrm{b}}^2} \end{bmatrix} = \begin{bmatrix} f_1^{\mathrm{a}} & f_2^{\mathrm{a}} \\[2mm] f_1^{\mathrm{b}} & f_2^{\mathrm{b}} \end{bmatrix} \begin{bmatrix} -\dfrac{\kappa_0}{9\eta}\boldsymbol{\nabla}\langle p_1^2\rangle \\[2mm] \dfrac{\rho_0}{6\eta}\boldsymbol{\nabla}\langle v_1^2\rangle \end{bmatrix},
\tag{7.16}
$$

which as Eq. (7.13) is written on matrix form, $\mathbf{U}_{\mathrm{ab}} = \mathbf{f}_{\mathrm{ab}}\,\mathbf{B}$ form resulting in the acoustic field matrix $\mathbf{B}$ solved by inverting $\mathbf{f}_{\mathrm{ab}}$

$$
\mathbf{B} = \mathbf{f}_{\mathrm{ab}}^{-1}\mathbf{U}_{\mathrm{ab}},
\tag{7.17}
$$

requiring that $f_1^{\mathrm{a}}f_2^{\mathrm{b}} - f_2^{\mathrm{a}}f_1^{\mathrm{b}} \neq 0$.

7.2.2　Determining the density and compressibility of suspended particles using acoustophoresis

We consider a particle suspension of unknown particle type "d" actuated at a known acoustic resonance with field matrix $\mathbf{B}$ obtained from either three or two calibration particles as described in Section 7.2.1. Obtaining the set of acoustophoretic particle velocities $\boldsymbol{u}^{\mathrm{d}}$ of the unknown particle type "d", we can write the equation of motion as

$$\frac{\boldsymbol{u}^{\mathrm{d}}}{a_{\mathrm{d}}^2} = \left[\begin{array}{ccc} f_1^{\mathrm{d}} & f_2^{\mathrm{d}} & \frac{1}{a_{\mathrm{c}}^2} \end{array}\right] \left[\begin{array}{c} -\frac{\kappa_0}{9\eta}\boldsymbol{\nabla}\langle p_1^2\rangle \\[2mm] \frac{\rho_0}{6\eta}\boldsymbol{\nabla}\langle v_1^2\rangle \\[2mm] \langle\boldsymbol{v}_2\rangle \end{array}\right], \tag{7.18}$$

or on matrix notation as

$$\mathbf{U}_{\mathrm{d}} = \left[\begin{array}{ccc} f_1^{\mathrm{d}} & f_2^{\mathrm{d}} & \frac{1}{a_{\mathrm{c}}^2} \end{array}\right]\mathbf{B}, \tag{7.19}$$

which for negligible streaming reduces to

$$\mathbf{U}_{\mathrm{d}} = \left[\begin{array}{cc} f_1^{\mathrm{d}} & f_2^{\mathrm{d}} \end{array}\right]\mathbf{B}. \tag{7.20}$$

Knowing $\mathbf{U}_{\mathrm{d}}$ and $\mathbf{B}$, f_1^{d} and f_2^{d} can be determined as fitting parameters.

7.2.3　Concluding remarks

This section proposes a method for determination of the density and compressibility of single particles undergoing acoustophoresis. The basis for the method is the acquisition of acoustophoretic microparticle velocities, which could be obtained by the µPIV and A-µPTV techniques described in Chapters 5 and 6. The method is still in development and next step is to perform a sensitivity analysis of the scheme to investigate the possible measurement accuracies as function of the uncertainties in velocity measurements and material parameters of the suspending medium and calibration particles.

7.3　High-throughput cell separation using high-voltage temperature-controlled acoustophoresis

In this section we give a brief introduction to a high-throughput temperature-controlled acoustophoresis chip presented in the paper *High-throughput, temperature -controlled microchannel acoustophoresis device made with rapid prototyping* enclosed in Chapter D. The work was carried out in collaboration with at the time PhD student Jonathan D. Adams, Dr. Allen H. J. Yang, and Professor H.

Tom Soh, UC Santa Barbara, CA, USA, and BSc student Christian L. Ebbesen and Professor Henrik, DTU Nanotech, Denmark. All experiments were carried out by Jonathan D. Adams, Dr. Allen H. J. Yang, and Christian L. Ebbesen.

In short, the paper presents a temperature-controlled acoustophoresis device capable of separating particles at volume throughput greater than 1 Liter per hour. The high throughput of the device is obtained by combining the single broad, shallow-channel geometry [16, 21], here of dimension (60 × 17 × 0.83) mm^3, with a temperature control loop similar to that presented in Section 5.1. The temperature control ensures the stability of the temperature-dependent acoustic resonance responsible for the functionality, when operating the device at relatively high ultrasound power levels. The device is only capable of high separation throughput using the temperature control supporting the investigation of the resonance temperature sensitivity in Section 5.4.

CHAPTER 8

Conclusion and outlook

Conclusion

This thesis contributes to the basic understanding of the physics of micropar-
ticle acoustophoresis by comparing quantitative measurements to a theoretical
framework consisting of existing hydrodynamic and acoustic predictions. Fur-
thermore, this framework was employed to develop methods for (*i*) *in situ* de-
termination of the acoustic energy density by means of acoustophoresis, (*ii*) *in
situ* determination of the density and compressibility of microparticles undergo-
ing acoustophoresis, and (*iii*) high-throughput microparticle separation by use of
acoustophoresis.

First, based directly on the governing equations of the theoretical framework
a numerical scheme was presented for studying microparticle acoustophoresis.
For the parameters of an experimental model system the numerical scheme was
used to show the transition in the acoustophoretic particle motion from being
dominated by streaming-induced drag to being dominated by radiation forces as
function of particle size, channel geometry, and suspending medium.

Second, an automated and temperature-controlled platform was developed
for robust measurements of microparticle acoustophoresis. Using this platform,
the in-plane acoustophoretic particle velocities were measured by micro-PIV to
examine the dependency of spatial position, driving voltage and frequency, and
resonator temperature. Further, the micro-PIV measurements were used to study
the acoustic radiation- and streaming-induced particle velocities as function of the
particle size, the actuation frequency, and the suspending medium, showing good
agreement with theoretical predictions.

Third, preliminary 3D measurements were presented of microparticle acousto-
phoresis by combining the automated and temperature-controlled platform with
the Astigmatic micro-PTV method. The 3D measurements clearly showed the
behavior of the radiation- and streaming-induced particle velocities, respectively.

The streaming-induced velocities were compared to existing theoretical predictions showing good agreement with room for improvement.

Fourth, a set of methods were developed for *in situ* determination of the acoustic energy density by means of the motion of microparticles undergoing acoustophoresis. The methods showed good agreement with literature values of the acoustic energy densities in similar acoustic systems as well as good agreement with Q factors estimated by utilizing the methods. Furthermore, a scheme was proposed for *in situ* determination of the density and compressibility of single microparticles by use of acoustophoresis.

Finally, by use of a temperature control loop to ensure stable high-amplitude acoustic resonances, an acoustophoresis microchip was developed capable of continuously separating microparticles at a volume throughput in excess of 1 Liter per hour.

Outlook

This thesis has contributed to the understanding of the physics of microparticle acoustophoresis, in particular by bridging theory and experiment. However, the work has opened for even more future analyses, theoretical as well as experimental.

The simple hydrodynamic pressure wave model adhered to in this thesis has proven to be useful, but it does not describe the complicated spatial behavior of the in-plane acoustophoretic particle velocities as obtained in Section 5.3. Hence, to describe these measurements, it is believed by the author that the elastic waves in the microchip and the precise actuation of the piezoelectric transducer must be taken into account. However, to conduct a successful experimental comparison to such an extended model probably requires better control or knowledge of the thickness and homogeneity of the coupling glue layer between the piezoelectric transducer and the microchip. On the other hand, one can imagine acoustophoresis experiments, where the actuation is done by a point-actuator to limit the influence of the piezo.

As highlighted in Section 4.3, the presented numerical scheme can be extended in many ways, e.g., (*i*) make a full 3D-model taking the elastic properties of the chip surrounding the microchannel into account, (*ii*) include gravitation, (*iii*) include full thermoviscous effects taking into account e.g. the temperature dependency of the viscosity [58], (*iv*) implement wall-enhancement of the drag forces, and (*v*) particle-particle interactions, hydrodynamic as well as acoustic.

Also, the current predictions of the acoustic boundary-driven streaming has proven successful, but as shown from the comparison to the 3D measurements of the acoustophoretic particle velocities, there is room for improvements. Hence, also the work on measuring the 3D aspects of microparticle acoustophoresis is continuing.

The 3D measurements seems to be crucial for future work on the physics of microparticle acoustophoresis. For example, the ability to calibrate the full

three-dimensional behavior of the acoustophoretic particle velocities could be the key for obtaining high-resolution measurements of microparticle densities and compressibilities as outline in the thesis. Furthermore, the ability to map the full 3D behavior of microparticle acoustophoresis in an entire chip system will become a solid base for comparison in order to develop future analytical as well as numerical predictions.

Finally, the numerical, analytical as well as the experimental analyses of the cross-over from radiation- to streaming-dominated acoustophoresis can be applied to develop an experimental device suppresing acoustic streaming enough to be capable of sub-micron particle manipulation by use of the acoustic radiation force. Contrary, the tools could also be used to make a design actually using the acoustic streaming as the active component for sub-micron manipulation. Also, it is the hope that the methods provided for *in situ* determination of the acoustic energy density will be useful in future optimization and design of devices for microparticle acoustophoresis. Furthermore, the method for measuring the density and compressibility of suspended particles by means of acoustophoresis is promising. It is the hope that it holds the key for crucial improvements within acoustic manipulation and separation of cells and bioparticles for which the acoustic parameters are often unknown.

Paper published in Lab on a Chip, January 2010

Lab on a Chip

Micro- & nano- fluidic research for chemistry, physics, biology, & bioengineering
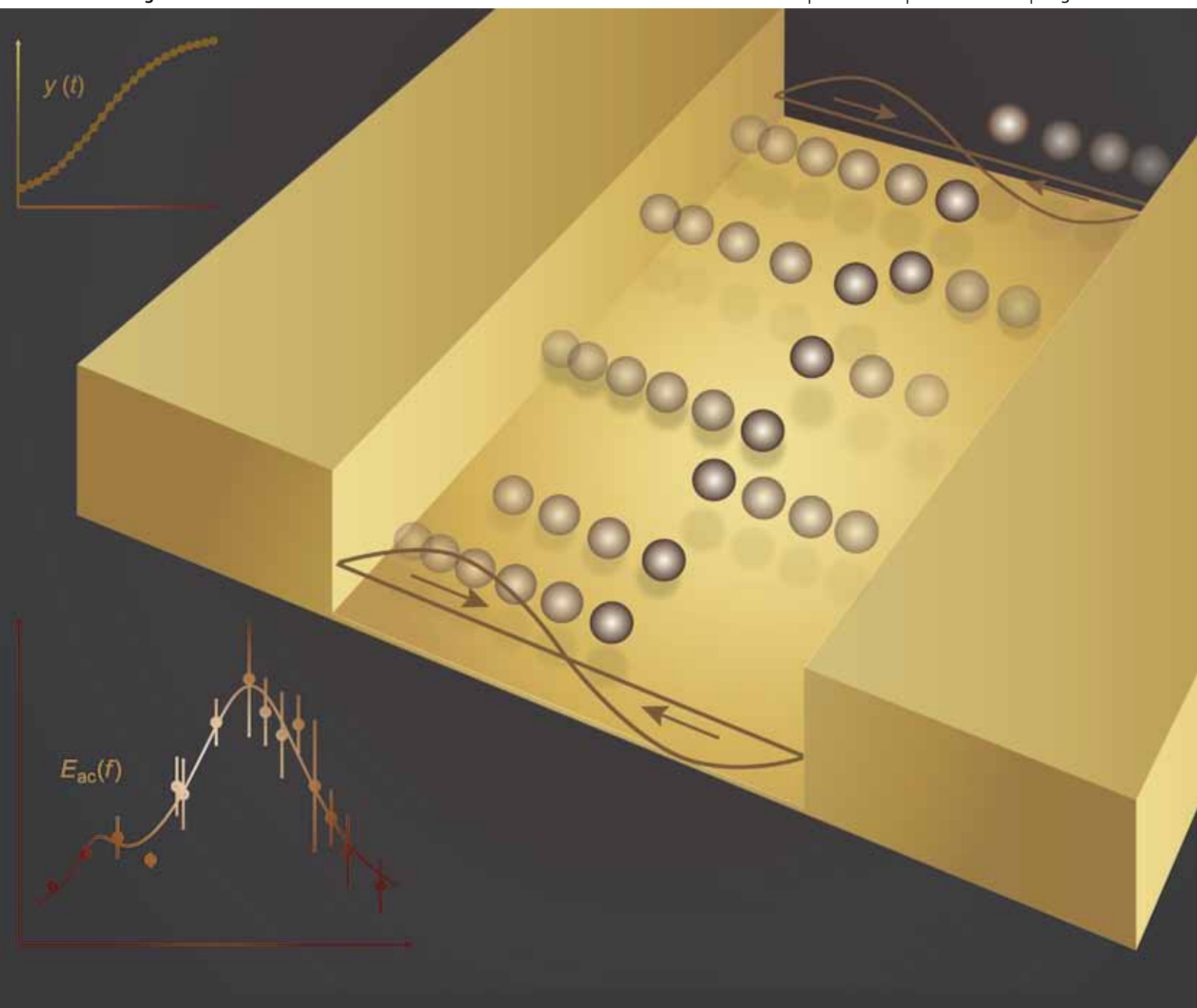
RSC Publishing

Celebrating **10 Years** of publishing
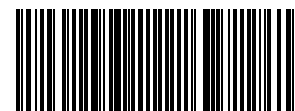
Measuring the local pressure amplitude in microchannel acoustophoresis

Rune Barnkob,[a] Per Augustsson,[b] Thomas Laurell[b] and Henrik Bruus[*a]

A new method is reported on how to measure the local pressure amplitude and the Q factor of ultrasound resonances in microfluidic chips designed for acoustophoresis of particle suspensions. The method relies on tracking individual polystyrene tracer microbeads in straight water-filled silicon/glass microchannels. The system is actuated by a PZT piezo transducer attached beneath the chip and driven by an applied ac voltage near its eigenfrequency of 2 MHz. For a given frequency a number of particle tracks are recorded by a CCD camera and fitted to a theoretical expression for the acoustophoretic motion of the microbeads. From the curve fits we obtain the acoustic energy density, and hence the pressure amplitude as well as the acoustophoretic force. By plotting the obtained energy densities as a function of applied frequency, we obtain Lorentzian line shapes, from which the resonance frequency and the Q factor for each resonance peak are derived. Typical measurements yield acoustic energy densities of the order of 10 J/m^3, pressure amplitudes of 0.2 MPa, and Q factors around 500. The observed half wavelength of the transverse acoustic pressure wave is equal within 2% to the measured width $w = 377$ μm of the channel.

I. Introduction

The studies of acoustic radiation forces on particles have a long history. The analysis of incompressible particles in acoustic fields dates back to the work in 1934 by King,[1] while the forces on compressible particles was calculated in 1955 by Yosioka and Kawasima.[2] Their work was admirably summarized and generalized in 1962 in a short paper by Gorkov.[3] The use of ultrasound standing waves for particle manipulation and separation has received renewed interest in the past decade as represented by the early papers ref. 4–6, which demonstrate this possibility.

The subsequent transition to a microscale format, where the acoustic resonators were tuned to match a half wavelength or a few multiples thereof, has boosted the ability to more precisely control the localization of cells and particles by acoustic forces. In their seminal paper,[7] Hawkes et al. presented a first precision machined half-wavelength resonator for continuous flow focusing of particles, and Nilsson et al. demonstrated early the ability to trap particles in quartz capillaries performing a bead based immuno assay.[8] This was followed by improved fabrication conditions by silicon/glass microfabrication technologies, which opened the route to lab-on-a-chip integration of ultrasonic standing wave technology, where both acoustic trapping and continuous flow separations have emerged as two major application areas in biomedical research as reviewed in ref. 9 and 10.

The method of acoustic particle trapping has subsequently undergone a rapid development, and it is now used in several different microchip configurations.[11–16] Likewise, the development of continuous-flow-based separation and manipulation of particles and cells has progressed rapidly with the advent of precision microfabricated flow-through resonators operating in the laminar flow regime.[17–26] Both the area of acoustic trapping and continuous separation/manipulation show great promise for applications within flow cytometry, and much of the current technological development targets cell biology.

In parallel, intense efforts are made to find physical models which fully describe the resonance modes of the microchips, such that up-front design can be made by numerical simulation. Along this line Benes, Hill, Hawkes and co-workers were early in outlining models for the treatment of the two dimensional layered acoustic resonator.[27–31] Lately, it has proven useful to model resonant microchannel or microcavity lab-on-a-chip systems by the Helmholtz pressure-wave eigenvalue equation for the actual chip geometries. In the 2D-limit, i.e. when the chip thickness is smaller than a half wavelength, the resulting pressure eigenmodes display close resemblance with the experimental conditions.[32,33] However, although these simulations describe the resonance modes, they do not indicate the magnitude of the Q factor or the line width of the modes.

This is also reflected in the key problem of the application of standing ultrasound waves in microfluidic systems, namely the prediction and measurement of the absolute size of the acoustophoretic force and the pressure amplitude acting on suspended particles or cells. Acoustic power sent from the transducer to the microfluidic system suffers losses due to thermal dissipation in the piezo-ceramic transducer, and acoustic radiation losses to the surroundings. These losses often vary from experiment to experiment and are thus difficult to estimate. At the same time there are no reliable methods available that enable the direct measurement of the pressure amplitude inside the microchannel without perturbing the microsystem severely or relying on external electric[34] or gravitational[14] fields. Linking these experimental acoustic parameters to the theoretical modeling is currently not a viable route.

In this paper we present a novel method to measure the acoustic energy density and pressure amplitude acting on suspended

[a]Department of Micro- and Nanotechnology, Technical University of Denmark, DTU Nanotech Building 345 East, DK-2800 Kongens Lyngby, Denmark. E-mail: Henrik.Bruus@nanotech.dtu.dk
[b]Department of Electrical Measurements, Lund University, Box 118, S-221 00 Lund, Sweden

microbeads undergoing acoustophoresis. Also, we experimentally determine the acoustophoretic force on the microbeads and the Q factor of the associated ultrasonic standing wave resonance. The experimental method relies on tracking individual microbeads at a given ultrasound frequency, as they by acoustophoresis traverse the microchannel towards their equilibrium position at the center of the channel. The measured trajectories are fitted to a theoretical prediction derived from the expression for the force[2,3] containing the acoustic energy density as a fitting parameter. By plotting the obtained energy density as a function of applied frequency we can also determine the pressure amplitude, the resonance frequency and the Q factor of the associated ultrasound resonance by fitting the resonance spectra to a sum of Lorentzian response curves.

II.   Background theory

Linear acoustics and acoustic radiation forces are treated in many textbooks. Basic theory is presented in the textbook by Lighthill[35] and theoretical aspects of acoustics in microfluidics, termed acoustofluidics, can be found in the textbook by Bruus.[36] In this work we rely on the formulation of microbead acoustophoresis by Gorkov.[3]

A.   Governing equations and boundary conditions

We consider a silicon/glass chip containing a microchannel filled with an aqueous suspension of particles. A piezo transducer is attached to the chip, such that when applying an ac voltage at MHz frequency, the piezo element vibrates and induces a time-harmonic ultrasound pressure field $p_1 \exp(- i \omega t)$, where $\omega = 2\pi f$ is the angular frequency and f the frequency. Here, we use the complex representation of the harmonic time dependence. In the following the time-harmonic factor is implicitly assumed. Like-wise for the velocity field v_1 of the carrier liquid.

Before the onset of the external ultrasound field the suspension is in a quiescent state at constant uniform pressure and zero velocity. The viscosity of the carrier liquid has a negligible influence on the acoustic radiation forces. Consequently, to a good approximation, the pressure field p_1 and velocity field v_1 inside the chip and the microchannel are governed by simple linear acoustics of inviscid fluids, i.e. the Helmholtz wave equation for the pressure and potential flow for the velocity,

$$\nabla^2 p_1 = -\frac{\omega^2}{c^2} p_1, \tag{1a}$$

$$v_1 = -\frac{i}{\omega\rho} \, \nabla p_1. \tag{1b}$$

Here, c and ρ are the speed of sound and the density of the given material, respectively. Note that in this simple qualitative model we neglect the shear waves in the solids, and in the following c_{si} and c_{py} are taken to be the longitudinal sound velocities representing the elastic behavior in silicon and pyrex glass, respectively, see Table 1.

The time-averaged acoustic energy density E_{ac}^{3D} can be expressed in terms of p_1 as follows,[36]

$$E_{ac}^{3D} = \frac{1}{4\rho_{wa}} \left[\frac{|\nabla p_1|^2}{\omega^2} + \frac{p_1^2}{c_{wa}^2} \right]. \tag{2}$$

Table 1   Physical parameters used in the acoustic model

Speed of sound, water	c_{wa}	1483 m s⁻¹
Speed of sound, silicon	c_{si}	8490 m s⁻¹
Speed of sound, pyrex glass	c_{py}	5647 m s⁻¹
Speed of sound, polystyrene	c_{ps}	1700 m s⁻¹
Density, water	ρ_{wa}	998 kg m⁻³
Density, silicon	ρ_{si}	2331 kg m⁻³
Density, pyrex glass	ρ_{py}	2230 kg m⁻³
Density, polystyrene	ρ_{ps}	1050 kg m⁻³
Sound speed ratio c_{ps}/c_{wa}	β_{ps}	1.15
Density ratio ρ_{ps}/ρ_{wa}	γ_{ps}	1.05
Compressibility factor, polystyrene/water	f_1	0.276
Density factor, polystyrene/water	f_2	0.034
Acoustophoretic coefficient, polystyrene/water	Φ_{ps}	0.328

Henceforth, we only consider time-averaged energy densities.

In this work, at a boundary with surface normal vector n, we employ one of the following three boundary conditions: the hard wall (zero velocity) condition, the soft wall (zero pressure) condition, and the continuity condition for pressure and velocity across interior boundaries,

$$\boldsymbol{n} \cdot \nabla p_1 = 0, \text{ (hard wall)}, \tag{3a}$$

$$p_1 = 0, \text{ (soft wall)}, \tag{3b}$$

$$\frac{\boldsymbol{n} \cdot \nabla p_1^{(a)}}{\rho_a} = \frac{\boldsymbol{n} \cdot \nabla p_1^{(b)}}{\rho_b}, \text{ and } p_1^{(a)} = p_1^{(b)}, \text{ (continuity)}. \tag{3c}$$

Products of these first-order acoustic fields give rise to two second-order effects, which persist even after time averaging: The acoustic radiation force acting on particles in suspension, and the acoustic streaming acting on the carrier liquid itself. As discussed in Section II D, the radiation force is the only second-order effect of importance in this work.

B.   Acoustic resonances

The acoustically soft water inside the channel surrounded by the acoustically hard silicon/glass chip forms an acoustic cavity. This implies that acoustic resonances occur for certain specific frequencies ω_j, $j = 1, 2, 3, \ldots$ An acoustic resonance at frequency ω_j is a state where the average acoustic energy density inside the cavity is several orders of magnitude larger than at other frequencies $\omega \neq \omega_j$. By tuning the applied frequency to one of these resonance frequencies, the acoustic forces become so strong that they, in a reliable way, can be used to manipulate particles suspended in the carrier liquid.

The exact values of the resonance frequencies ω_j depend on the geometry of the acoustic cavity and of the material parameters of the liquid in the cavity as well as the surrounding material. Specifically, the relevant material parameters are the speed of sound c_{wa} and density ρ_{wa} of the water and likewise the speed of sound c_{si} and density ρ_{si} of the silicon chip, see Table 1. In the general case, the resonance frequencies can only be calculated using numerical methods.

For a rectangular channel of length l, width w, and height h, surrounded by an acoustically infinitely hard material, the resonance frequencies may be found analytically. This case approximates our experimental system reasonably well if we disregard the inlet and outlet of the microchannel. Moreover,

since the parameters listed in Table 1 yield an acoustic impedance ratio $(\rho_{si}c_{si})/(\rho_{wa}c_{wa}) = 13.4$ much larger than unity, the silicon surrounding our rectangular water channel can to a good approximation be treated as an infinitely hard material. In that case the normal velocity on all walls is zero, which according to eqn (1b) is equivalent to Neumann boundary conditions $\mathbf{n}\cdot\mathbf{\nabla}p_1 = 0$ for the pressure. It is easily verified that with this boundary condition the pressure p_1 solving eqn (1a) for a rectangular box placed along the coordinate axes with its opposite corners at $(0, 0, 0)$ and (l, w, h) is

$$p_1(x, y, z) = p_a \cos(k_x x) \cos(k_y y) \cos(k_z z) \tag{4}$$

where p_a is the pressure amplitude, and $(k_x, k_y, k_z) = \pi(n_x/l, n_y/w, n_z/h)$ with $n_x, n_y, n_z = 0, 1, 2, \dots$. The corresponding three-index resonance frequencies $f_{n_x,n_y,n_z} = \omega_{n_x,n_y,n_z}/(2\pi)$ are given by

$$f_{n_x,n_y,n_z} = \frac{c_{wa}}{2}\sqrt{\frac{n_x^2}{l^2} + \frac{n_y^2}{w^2} + \frac{n_z^2}{h^2}}, \tag{5}$$
$$\text{with} \quad n_x, n_y, n_z = 0, 1, 2, \dots.$$

For later use we denote the transverse wavelength in the y-direction by λ. The lowest resonance condition in this direction is thus $w = \lambda/2$ or $k_y = \pi/w$. Two examples of resonant standing ultrasound waves are shown in Fig. 1.

C. The acoustic radiation force

Given the pressure field p_1 and velocity field $\mathbf{v}_1$ it is possible to calculate the acoustic radiation force on a particle with volume $V = (4\pi/3)a^3$ and radius a much smaller than the acoustic wavelength λ. Both for biological cells and for microbeads used as tracers we are in this limit. The material parameters, with subscripts "wa" for the water and "p" for the particle, enter as the speed of sound ratio β and the density ratio γ,

$$\beta = \frac{c_p}{c_{wa}}, \qquad \gamma = \frac{\rho_p}{\rho_{wa}} \tag{6}$$

which appear in the compressibility factor f_1 and the density factor f_2 as

$$f_1 = 1 - \frac{1}{\gamma\beta^2}, \qquad f_2 = \frac{2\gamma - 2}{2\gamma + 1}. \tag{7}$$

The general expression for the time-averaged acoustic radiation force $\langle\mathbf{F}_{ac}\rangle$ is a gradient of a potential,[3]

$$\langle\mathbf{F}_{ac}\rangle = -\mathbf{\nabla}U_{ac}, \tag{8}$$

where this acoustic potential U_{ac} is given by

$$U_{ac} = V\left[\frac{f_1}{2\rho_{wa}c_{wa}^2}\langle p_1^2\rangle - \frac{3f_2\rho_{wa}}{4}\langle|\mathbf{v}_1|^2\rangle\right]$$
$$= \frac{V}{4\rho_{wa}c_{wa}^2}\left[2f_1\langle p_1^2\rangle - 3f_2\frac{1}{k^2}\langle|\mathbf{\nabla}p_1|^2\rangle\right]. \tag{9}$$

The latter form is obtained by use of eqn (1b) and $k^2 = k_x^2 + k_y^2 + k_z^2$.

To a good approximation the pressure eigenmodes p_1 are given by simple cosine/sine standing waves in a water channel surrounded by infinitely hard walls. For $h < w, l$, the pressure eigenmode eqn (4) can be approximated by the 2D expression with $k_z = 0$,

$$p_1(x, y, z) = p_a \cos(k_x x) \cos(k_y y), \tag{10a}$$

$$\mathbf{\nabla}p_1(x, y, z) = -k_x p_a \sin(k_x x) \cos(k_y y)\mathbf{e}_x$$
$$-k_y p_a \cos(k_x x) \sin(k_y y)\mathbf{e}_y. \tag{10b}$$

This standing wave can be interpreted as two counter-propagating waves along the direction $\mathbf{k} = k_x\mathbf{e}_x + k_y\mathbf{e}_y$, which forms the angle θ with the x-axis,

$$\cos\theta = \frac{k_x}{k}, \quad \sin\theta = \frac{k_y}{k}, \quad k = \sqrt{k_x^2 + k_y^2}. \tag{11}$$

Inserting this in Gorkov's expression, eqn (9), we arrive at the acoustic potential

$$U_{ac} = U_o[2f_1\cos^2(k_x x)\cos^2(k_y y) - 3f_2\sin^2(k_x x)\cos^2(k_y y)\cos^2\theta -$$
$$3f_2\cos^2(k_x x)\sin^2(k_y y)\sin^2\theta] \tag{12}$$

with an amplitude U_o given by

$$U_o = \frac{p_a^2 V}{8\rho_{wa}c_{wa}^2} = \frac{2\pi}{3}a^3 E_{ac}, \tag{13}$$

where $E_{ac} = p_a^2/(4\rho_{wa}c_{wa}^2)$ is the position-independent acoustic energy density for a 1D standing wave derived from eqn (2). A numerical example of the acoustic potential U_{ac}/U_o for a polystyrene sphere is shown in Fig. 2. Similar plots are found in refs. 37 and 38.

For later use we state the position-dependent acoustic energy density E_{ac}^{2D} for the 2D standing wave given in eqn (10a):

$$E_{ac}^{2D}(x, y) = [\sin^2\theta\cos^2(k_x x) + \cos^2\theta\cos^2(k_y y)] E_{ac}. \tag{14}$$

Fig. 1 Color plot (red positive, blue negative) of the pressure field p_1 at resonance in a water-filled microchannel of length $l = 40$ mm along x, width $w = 377$ μm along y, and height $h = 157$ μm along z, surrounded by an infinitely hard acoustic material, see eqn (4). (a) Resonance $(n_x, n_y, n_z) = (0, 1, 0)$ with $f_{0,1,0} = 1.9668$ MHz, and (b) $(n_x, n_y, n_z) = (3, 1, 0)$ with $f_{3,1,0} = 1.9676$ MHz.
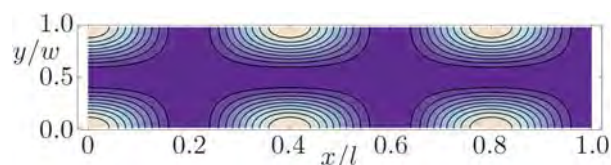

Fig. 2 Contour plot with 10% contour lines from low (dark) to high (light) of the normalized acoustic potential U_{ac}/U_o from eqn (12) for a polystyrene sphere in water given the pressure field p_1 of eqn (10a) with $(k_x, k_y) = (\pi/(2w), \pi/w)$ so that $\theta \approx 63°$. Further parameter values used in the simulation are given in Table 1.

D. Transverse particle path

The path of a microbead moving under acoustophoresis is given by the position vector $(x(t), y(t))$. A particularly simple analytical expression for the transverse part $y(t)$ of this path can be obtained from eqn (8) and (12) in the limit of a long axial wavelength, $k_x \approx 0$, i.e. a 1D transverse wave. Given this, the y-component F_y of the acoustophoretic force becomes

$$F_y = 2k_y U_o \left[\frac{5\gamma - 2}{2\gamma + 1} - \frac{1}{\gamma \beta^2} \right] \sin(2k_y y). \tag{15}$$

We can neglect inertial effects because the flow speed of our 5-μm-microbeads never exceeds 200 μm/s resulting in a Reynolds number less than 0.001. We can also neglect the influence from the Stokes drag due to the acoustic streaming. This was demonstrated experimentally by Hagsäter et al.[32] In a direct comparison of the acoustic forces on microbeads in a microfluidic chamber it was shown that the motion of 1 μm beads was governed entirely by Stokes drag from the acoustic streaming, while the motion of the 5 μm beads was dominated by the acoustic radiation force. Moreover, in this work we never observed any traces of acoustic flow rolls.

To determine the transverse path $y(t)$ we therefore balance the acoustophoretic force F_y with the Stokes drag force due to the viscosity η from the quiescent liquid, and obtain the following differential equation,

$$6\pi\eta a \frac{dy}{dt} = 2k_y U_o \Phi \, \sin(2k_y y) \tag{16}$$

where Φ is the acoustophoretic coefficient,[39]

$$\Phi = \frac{5\gamma - 2}{2\gamma + 1} - \frac{1}{\gamma \beta^2} \tag{17}$$

Separating the variables y and t, and using the fact that $2\int ds/\sin(2s) = \log|\tan(s)|$ leads to an analytical expression for the transverse path

$$y(t) = \frac{1}{k_y} \arctan\left\{ \tan[k_y y(0)] \exp\left[\frac{4\Phi}{9\eta}(k_y a)^2 E_{ac} \, t \right] \right\} \tag{18}$$

where $y(0)$ is the transverse position at time $t = 0$. Such paths have previously been calculated numerically by Townsend et al.[40]

Inverting the above expression, we can also calculate the time t it takes for a particle to move from any initial position $y(0)$ to any final position $y(t)$,

$$t = \frac{9\eta}{4\Phi(k_y a)^2 E_{ac}} \ln\left[\frac{\tan[k_y y(t)]}{\tan[k_y y(0)]} \right] \tag{19}$$

A special case of this expression, namely the time for a particle to reach the nodal line, was derived by Limaye and Coakley.[41]

E. Resonance line shape

It is straightforward to show that the acoustic energy density $E_{ac}(f)$ for a liquid slab between two walls counter-oscillating at frequency f exhibits a Lorentzian line shape near any given resonance frequency f_1,

$$E_{ac}(f) = \frac{E_1}{\left[\frac{2Q_1}{f_1}(f - f_1) \right]^2 + 1}. \tag{20}$$

The maximum of the energy density at resonance is E_1, while the full-width at half-maximum is $\delta f_1 = f_1/Q_1$, where the Q factor Q_1 of the resonance is related to dissipation of the acoustic energy due to viscosity in the bulk liquid and radiation losses from the surfaces of the chip.

III. Chip, setup, and experimental procedure

A. Chip and experimental setup

To study the local acoustic pressure amplitude in acoustophoresis microchannels two microfluidic chips were developed, Fig. 3(a). Each chip consists of a straight channel with one inlet and one outlet fabricated using standard photolithography and anisotropic KOH etching in silicon ⟨100⟩, yielding a rectangular channel cross section. The channel was sealed by an anodically bonded pyrex glass lid, and short pieces of silicone tubing were attached to their respective 1-mm-diameter holes in the glass lid by silicone glue. All dimensions are given in the figure caption. The width W of the chip can be characterized by the ratio α of the number of acoustic wavelengths in silicon and that of water.
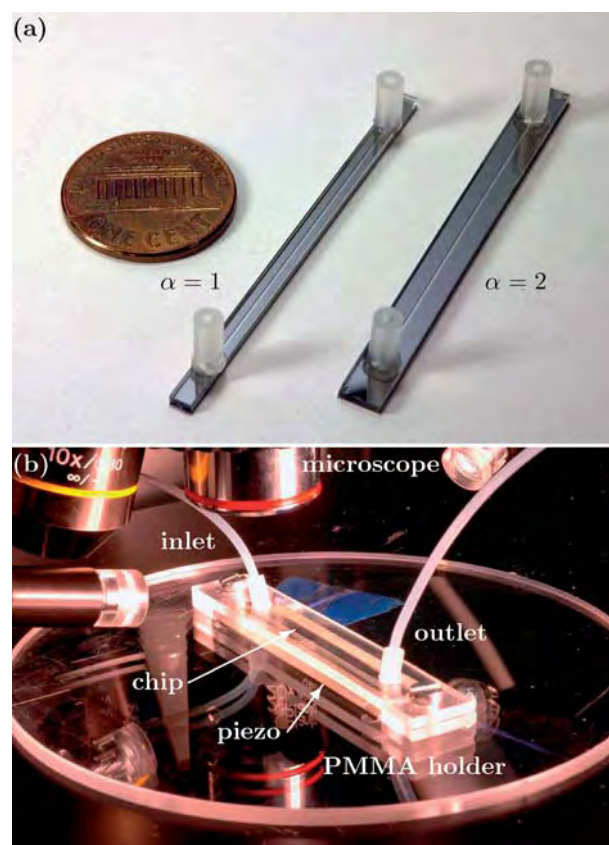

Fig. 3 (a) The silicon/glass chips containing straight channels of length l = 40 mm, width w = 377 μm, and height h = 157 μm. The channels are etched down into the silicon chip of thickness h_{si} = 350 μm, and they are covered by a pyrex glass lid of thickness h_{py} = 1.13 mm. The lengths of the chips are L = 50 mm and the widths are W = 2.52 mm (α = 1) and W = 4.67 mm (α = 2), respectively. (b) A photograph of the experimental setup with the chip and the PZT piezo crystal mounted under the microscope and the CCD camera. The piezo has the dimension 50.0 mm × 12.0 mm × 1.0 mm, and thus the entire chip rests on it.

With the parameters of Table 1 we find $\lambda_{si} = 5.7\lambda_{wa}$ and $\alpha = (W - w)/(5.7w)$. For future experimental purposes we have chosen to fabricate chips with $\alpha = 1$ and $\alpha = 2$.

Fig. 3(b) shows how the chip is mounted on a piezoelectric transducer (piezo) made of hard PZT of the type Pz26 from Ferroperm Piezoceramics A/S. Sufficient acoustic coupling is provided by a thin glycerol layer. The two elements are fixed in a PMMA holder, such that the chip is only in contact with the holder through its inlet/outlet silicone tubing and *via* the piezo, which in turn was mounted so that all contact with the PMMA holder is restricted to its edges.

The piezo is actuated by applying a harmonically oscillating voltage generated from a tone generator, Hewlett Packard 33120A. The voltage is amplified by a T&C Power Conversion Inc. AG Series Amplifier, and the applied peak-to-peak voltage across the piezo transducer is measured by an oscilloscope Tektronix TDS 1002. The channel was monitored through an Olympus BX51WI microscope with an attached CCD camera of the type Infinity 1 from MediaCybernetics.

B. Handling of the microbeads

When carrying out the experiments a liquid suspension of microbeads was injected into the microchannel. The sample liquid consists of Milli-Q water mixed with 0.01% Tween20, a polysorbate surfactant reducing the adhesion of microbeads to the channel walls, and polystyrene microbeads (5.16 ± 0.08) µm from Sigma-Aldrich. The microbead concentrations were in the range from 0.1 g/L to 0.5 g/L. The sample liquid is contained in a 1 mL plastic syringe, in which a small magnet resides. By moving an external magnet, sedimentation of the microbeads inside the syringe is avoided by the stirring, and this reduces the risk of getting an inhomogeneous distribution of microbeads in the microchannel. A syringe pump of the type WPI SP210IWZ was used to purge the microchannel with the sample liquid prior to each run. During all measurements the flow was temporarily stopped.

C. Measuring the Stokes drag force

To investigate the effect of Tween20 in the suspension, repeated recordings were carried out of the sedimentation time of individual microbeads moving from top to bottom of the microchannel. The initial positioning at the lid was achieved by acoustophoresis, which, however, left some microbeads behind, pinned at the channel bottom. We focused the microscope to the microbeads at the lid. These microbeads were then released and followed during their sedimentation by moving the focal plane. The sedimentation was timed from the release until the pinned beads at the bottom appeared in the same focal plane as the sedimenting beads. The sedimentation time for microbeads in Milli-Q water with and without Tween20 (0.01%) was (179 ± 6) s and (182 ± 5) s, respectively. This demonstrates that the influence of the added Tween20 on the density and viscosity is negligible. Moreover, since the theoretical single-microbead sedimentation time calculated from the force balance (neglecting bead–wall interactions) between gravity, buoyancy and Stokes drag is 208 s, our sedimentation measurements also show a fair accuracy in applying the Stokes drag in this confined system.

D. Measuring microbead paths during acoustophoretic focusing

The field of view of the microscope covered the full width $w = 377$ µm of the microchannel, 510 µm along the channel, and it was centered 10 mm downstream from the inlet.

The acoustic energy density was measured by observing the transient acoustophoretic focusing of the microbeads as follows. First, the driving frequency is tuned until observing a strong, resonant, acoustic focusing of the polystyrene microbeads towards the center of the channel. Then the ultrasound field is turned off, and a fresh suspension of microbeads from the syringe pump is injected into the channel. When a homogeneous microbead distribution is observed, the flow is stopped, Fig. 4(a). Finally, the ultrasound is turned back on, and the transient focusing of the microbeads towards the channel center is recorded by the CCD camera, Fig. 4(b). From the frames of the resulting movie we can then determine the transverse paths $y(t)$ of the microbeads, an example of which is shown in Fig. 4(c).
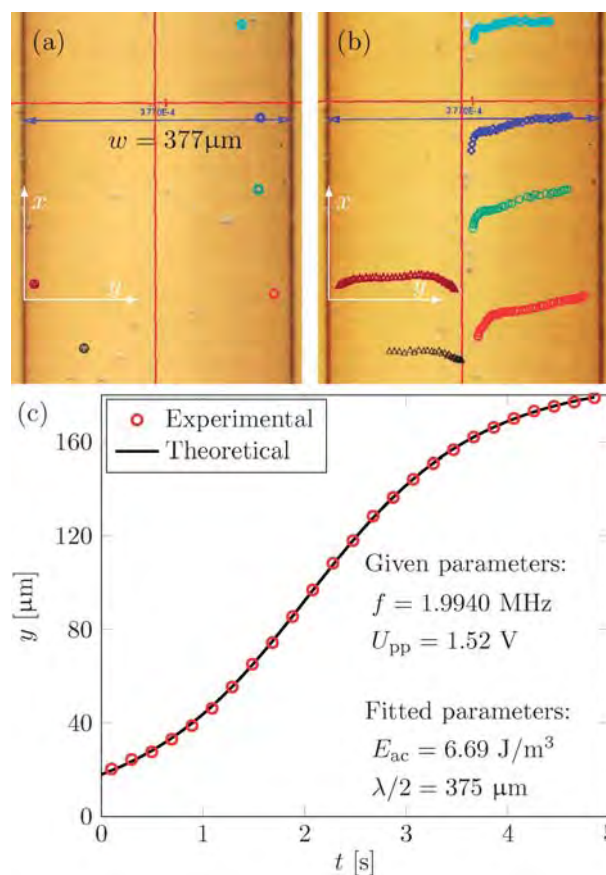

Fig. 4 (a) Starting position (circles) of six microbeads in the channel of the chip with $\alpha = 2$. The channel walls are the two thick vertical lines separated by $w = 377$ µm. (b) Tracking of the paths of the six microbeads. (c) Measurement (circles) for one of the microbeads of its transverse position y from the left wall as a function of time t. The uncertainty in the y-position is 5 µm corresponding to the diameter of the circles. For clarity only every second point is shown, but all points are used in the analysis. The fitted curve (full line) is given by eqn (18) with only two fitting parameters: the acoustic energy density E_{ac} and the half wavelength $\lambda/2$ of the transverse standing pressure wave.

IV. Results

A. Measured acoustic energy density and local pressure amplitude

The transverse path $y(t)$ is extracted from the video recordings by employing the free video analysis tool *Tracker 2.6*.[42] This software enables tracking of a polystyrene microbead by simple manual mouse-clicking on the microbead position y on each movie frame, for which the time t is known. For a general introduction to tracking techniques of microbeads in microfluidics see ref. 43. The length scale in the y-direction is calibrated by the distance between the visible channel walls as shown in Fig. 4(a). The resulting list of (t, y)-coordinates can be extracted for any tracked microbead path, see Fig. 4(b), and plotted as shown in Fig. 4(c) for a driving frequency of $f = 1.9940$ MHz and a driving voltage $U_{pp} = 1.52$ V.

The axial motion $x(t)$ seen in the last part of the paths shown in Fig. 4(b) is due to hydraulic compliance of the system leading to difficulties in keeping the liquid at complete rest.

Using the energy density E_{ac} and the half-wavelength $\lambda/2$ as the only fitting parameters, a curve of the form $y(t)$ given by eqn (18) is fitted to the data points by the least-squares routine lsqcurvefit() in MATLAB. As shown by the full curve in Fig. 4(c), this fitting procedure yields good results: the observed path has the theoretically predicted shape, and we can extract reliable values for the acoustic energy density E_{ac}. In the given case we found $E_{ac} = 6.69$ J/m³, and we also note that the fitted value for $\lambda/2$ is 375 μm, very close to the expected value, namely the width of the channel $w = 377$ μm.

From eqn (13) we find the pressure amplitude in the chip with $\alpha = 2$ to be

$$p_a = 2\sqrt{\rho_{wa} c_{wa}^2 \, E_{ac}} \approx 0.242 \text{ MPa}, \tag{21}$$

which is 10^{-4} times the cohesive energy density 2.6 GPa of water. Equivalently, the density fluctuations are 10^{-4} times ρ_{wa}, and thus the acoustic perturbation theory holds even at resonance.

In our low-voltage experiments we have measured energy densities in the range 0.65–50 J/m³ corresponding to pressure amplitudes in the range 0.08–0.66 MPa. The upper range of these results are consistent with previously reported estimates in the literature for microbead acoustophoresis in microsystems. Using external electric forces, Wiklund *et al.*[34] measured energy densities in the range 65–650 J/m³ corresponding to pressure amplitudes in the range 0.76–2.4 MPa, while Hultström *et al.*[14] used force balance between gravity and acoustophoretic forces to measure energy densities in the range 37–82 J/m³ corresponding to pressure amplitudes in the range 0.57–0.85 MPa

B. Measured energy density *versus* driving voltage

In the following we use the above procedure to extract the acoustic energy density E_{ac} and half the wavelength $\lambda/2$ for 5–15 (typically 8) individual microbeads properly chosen in the field of view for any given setting of the external parameters. When plotting the resulting data as a function of the parameters, each data point is a statistical average of these individual measurements, and the error bars are the associated standard deviations.

First, at the driving frequency $f = 1.9976$ MHz, we study the energy density and the half wavelength as a function of the peak-to-peak value U_{pp} of the driving voltage on the piezo transducer in the range from 0.5 V to 1.9 V.

In Fig. 5(a) we see that the resulting ten data points are well fitted to a power law of the form $E_{ac} \propto (U_{pp})^{2.07}$. This is close to a power of 2, which is expected since the acoustic pressure delivered by the piezo transducer is proportional to the applied voltage, and the acoustic energy density is proportional to the square of the pressure, see eqn (21). We also note that the statistically determined error bars increase with increasing driving voltage and thus with increasing microbead velocity. This is as result of the decreased temporal resolution of the paths given the fixed rate of 16 CCD frames per second and the increased microbead velocity.

Fig. 5(b) shows that for all voltages the average of the other fitting parameter, the half wavelength, is $\bar{\lambda}/2 \pm \Delta\lambda = (380 \pm 3)$ μm, which is very close to the expected value of $w = (377 \pm 5)$ μm, the width of the channel.

C. Measured resonance frequencies and Q factors

By measuring the acoustic energy density E_{ac} as a function of the applied frequency f across the piezo transducer, we have been
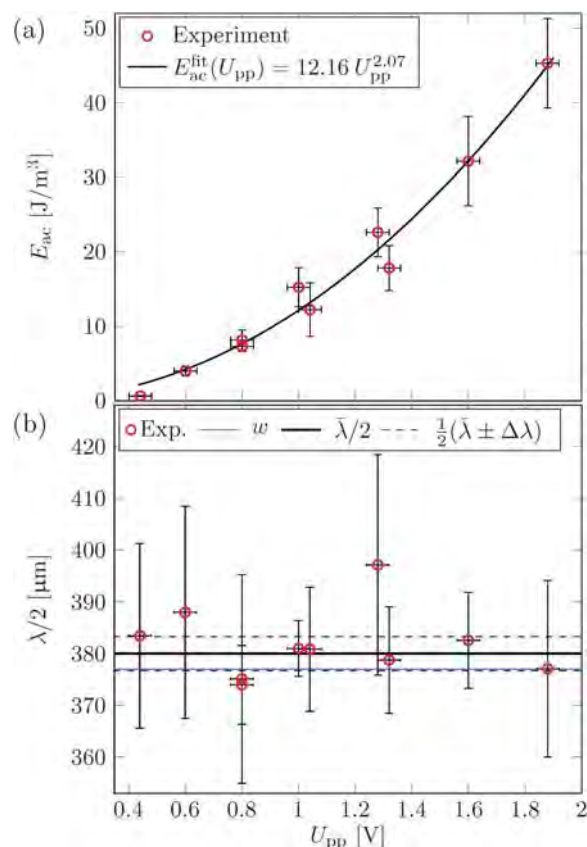

Fig. 5 (a) Measured acoustic energy density E_{ac} *versus* applied peak-to-peak voltage U_{pp} on the piezo transducer (points) for $\alpha = 1$. A power law fit (full line) to the data is close to the expected square law, $E_{ac} \propto (U_{pp})^2$. (b) The measured half wavelength $\lambda/2$ obtained by the path fitting is independent of U_{pp}, and its average value $\bar{\lambda}/2 = 380$ μm (thick black line) differs less than one standard deviation $\Delta\lambda/2 = 3$ μm (dashed lines) from the expected value of $w = 377$ μm (thin blue line).

able to characterize the acoustic resonances in more detail. The following results were obtained on the chip $\alpha = 2$ of width $W = 4.67$ mm, see Fig. 3(a). The driving frequency f was varied from 1.9900 MHz to 2.0100 MHz, while the tone generator and the amplifier were set to fixed values. However, due to the piezo-electric coupling of the transducer, the actual peak-to-peak voltage U_{pp} varied between 1.44 V and 1.60 V as a function of frequency. We used the quadratic dependency of E_{ac} on U_{pp}, as derived in Fig. 5(a), to correct all measured values of E_{ac} to correspond to the same average voltage 1.48 V.

The measured acoustic energy spectrum $E_{ac}(f)$ is shown in Fig. 6. A clear maximum is seen at $f_2 = 2.0021$ MHz while a smaller, less pronounced peak is seen at $f_1 = 1.9927$ MHz. According to eqn (20), a simple acoustic resonance can be described by a Lorentzian line shape, and we therefore fit the measured spectrum by the sum of two Lorentzian line shapes. In this case we thus end up with six fitting parameters, three per peak, the energy density maxima $E_{ac,1}$ and $E_{ac,2}$, the resonance frequencies f_1 and f_2, and the Q factors Q_1 and Q_2. The values of these parameters are listed in the caption of Fig. 6, and from the energy densities we extract as in eqn (21) the pressure amplitudes $p_{a,1} = 0.16$ MPa and $p_{a,2} = 0.37$ MPa for peak 1 and 2 respectively.

The two resonance peaks in Fig. 6 are separated by a spacing $\Delta f_{12} = f_2 - f_1 = 9.4$ kHz, while the line widths of the two peaks are of the same order of magnitude, namely $\delta f_1 = 3.5$ kHz and $\delta f_2 = 9.6$ kHz. These values emphasize, as is also seen directly on the graph, that the individual acoustic resonances are barely resolved.

The origin of the observed two-peak structure is explained qualitatively by the 2D pressure eigenmode simulations shown in Fig. 7. It is seen how axial modes appear and gives rise to close-lying resonances. While our non-shear-wave model does not allow for accurate determination of these resonance frequencies,

Fig. 7 A top view color plot (blue negative, red positive) of the pressure field of three ultrasound resonances calculated in a simplified 2D model. For each resonance is shown the number of n_x of half wavelengths in the axial direction, the resonance frequency f, and the distance Δf in frequency space to the neighboring resonance. The small black rectangles mark the microscope field of view.

it nevertheless provides a reliable order-of-magnitude estimate for the spacing between them, $\Delta f \approx 12$ kHz, close to the observed $\Delta f_{12} = 9.4$ kHz. Furthermore, we speculate that the difference in amplitude between the two peaks shown in Fig. 6 is mainly due to the shift in wave pattern going from one value n_x to the neighboring peak at $n_x + 1$ as illustrated by black rectangles in Fig. 7, representing the microscope field of view. For $n_x = 17$ the pressure amplitude in the field of view is much smaller than that for $n_x = 18$. We note that for $n_x = 17$ the k-related angle θ, see eqn (11), becomes 81°, corresponding to $\sin^2 \theta = 0.98$ and $\cos^2 \theta = 0.02$. According to eqn (14) this fully determines the position dependence of the acoustic energy density. For more details on axial modes see ref. 38.

V. Concluding discussion

We have established a new method to measure *in situ* the energy density, the local pressure amplitude, and the Q factor of ultrasound resonances in microfluidic chips by tracking individual polystyrene microbeads undergoing acoustophoresis in straight water-filled channels in silicon/glass chips. For a given driving frequency and voltage amplitude of the piezo transducer, microbead tracks have been recorded by a CCD camera and fitted to a theoretical curve. From the curve fit we have obtained the acoustic energy density and pressure amplitude. We have shown that, as expected, the acoustic energy density scales with applied piezo voltage to the power 2. Furthermore, by plotting the energy densities as a function of the applied ultrasound frequency, we obtain Lorentzian line shapes, from which we can determine the resonance frequency and the Q factor for each acoustic resonance peak.

In contrast to previous methods, our method to determine the local pressure amplitude in microchannel acoustophoresis has the advantage of relying only on the acoustophoretic effect itself and not on calibration against external forces. Moreover, being based on particle tracking, it provides the means to measure very low pressure levels with high accuracy, here down to 0.08 MPa at $U_{pp} = 0.44$ V. Equipped with high-speed CCD cameras faster than our present 16 frames/s, our method is easily extendable to pressure levels above the 0.66 MPa reported here.

Fig. 6 Measured acoustic energy density E_{ac} *versus* applied frequency f on the piezo transducer (circles) for the $\alpha = 2$ chip for $U_{pp} = 1.48$ V. The data points are fitted by a sum (full line) of two Lorentzian peaks (dashed lines). The values of the fitting parameters for peak 1 are $f_1 = 1.9927$ MHz, $E_{ac,1} = 3.3$ J/m³, and $Q_1 = 577$. For peak 2 they are $f_2 = 2.0021$ MHz, $E_{ac,2} = 15.5$ J/m³, and $Q_2 = 209$. The peak spacing is $\Delta f_{12} = f_2 - f_1 = 9.4$ kHz, while the line widths are $\delta f_1 = 3.5$ kHz and $\delta f_2 = 9.6$ kHz.

The work presented here shows one example of how the new characterization methods may lead to improvements. In Fig. 6 it is shown that the nearest-neighbor resonances are separated by $\Delta f_{12} = 9.4$ kHz, while the line width of the two peaks are of the same order of magnitude, namely $\delta f_1 = 3.5$ kHz and $\delta f_2 = 9.6$ kHz. Thus, for this standard setup, the acoustic resonances are barely resolved due to line widening from loss of acoustic energy from the resonating system. In future work, especially work involving actuation of several frequencies simultaneously or sequentially as in ref. 16 and 44, it is therefore desirable to focus on reducing the acoustic energy loss by a more careful design of the coupling between the chip and the surroundings, in particular regarding the piezo transducer and the fluidic tubing.

In general, our new method paves the way for improved design of lab-on-a-chip systems using acoustophoresis. Once fully automated by computer control of the particle tracking and the subsequent curve fitting, detailed *in situ* characterization of the entire acoustic pressure field in microchannel acoustophoresis will become feasible. Acquisition of such detailed data will be beneficial both for further studies of the fundamental physical nature of acoustophoresis and acoustic streaming, and for improved engineering of chip-based systems.

Acknowledgements

References

1 L. V. King, *Proc. R. Soc. London, Ser. A*, 1934, **147**, 212.
2 K. Yosioka and Y. Kawasima, *Acustica*, 1955, **5**, 167.
3 L. P. Gorkov, *Sov. Phys. Doklady*, 1962, **6**, 773.
4 K. Yasuda, S. Umemura and K. Takeda, *Jpn. J. Appl. Phys.*, 1995, **34**, 2715.
5 H. Gröschl, W. Burger and B. Handl, *Acustica*, 1998, **84**, 815.
6 J. Hawkes and W. T. Coakley, *Enzyme Microb. Technol.*, 1996, **19**, 57.
7 J. Hawkes and W. T. Coakley, *Sens. Actuators, B*, 2001, **75**, 213–222.
8 H. Nilsson, M. Wiklund, T. Johansson, H. M. Hertz and S. Nilsson, *Electrophoresis*, 2001, **22**, 2384.
9 T. Laurell, F. Petersson and A. Nilsson, *Chem. Soc. Rev.*, 2007, **36**, 492.
10 J. Nilsson, M. Evander, B. Hammarström and T. Laurell, *Anal. Chim. Acta*, 2009, **649**, 141–157.
11 T. Lilliehorn, U. Simu, M. Nilsson, M. Almqvist, T. Stepinski, T. Laurell, J. Nilsson and S. Johansson, *Ultrasonics*, 2005, **43**, 293.
12 D. Bazou, L. A. Kutznetsova and W. T. Coakley, *Ultrasound Med. Biol.*, 2005, **31**, 423.
13 M. Evander, L. Johansson, T. Lilliehorn, J. Piskur, M. Lindvall, S. Johansson, M. Almqvist, T. Laurell and J. Nilsson, *Anal. Chem.*, 2007, **79**, 2984.
14 J. Hultström, O. Manneberg, K. Dopf, H. M. Hertz, H. Brismar and M. Wiklund, *Ultrasound Med. Biol.*, 2007, **33**, 145.
15 O. Manneberg, B. Vanherberghen, J. Svennebring, H. M. Hertz, B. Önfelt and M. Wiklund, *Appl. Phys. Lett.*, 2008, **93**, 063901.
16 J. Svennebring, O. Manneberg, P. Skafte-Pedersen, H. Bruus and M. Wiklund, *Biotechnol. Bioeng.*, 2009, **103**, 323.
17 N. R. Harris, M. Hill, S. Beeby, Y. Shen, N. M. White, J. J. Hawkes and W. T. Coakley, *Sens. Actuators, B*, 2003, **95**, 425.
18 M. Bengtsson and T. Laurell, *Anal. Bioanal. Chem.*, 2004, **378**, 1716.
19 J. J. Hawkes, R. W. Barber, D. R. Emerson and W. T. Coakley, *Lab Chip*, 2004, **4**, 446.
20 A. Nilsson, F. Petersson, H. Jonsson and T. Laurell, *Lab Chip*, 2004, **4**, 131.
21 F. Petersson, A. Nilsson, C. Holm, H. Jönsson and T. Laurell, *Analyst*, 2004, **129**, 938.
22 F. Petersson, A. Nilsson, H. Jönsson and T. Laurell, *Anal. Chem.*, 2005, **77**, 1216.
23 F. T. Petersson, L. B. Åberg, A.-M. S. Swärd-Nilsson and T. Laurell, *Anal. Chem.*, 2007, **79**, 5117.
24 J. Persson, P. Augustsson, T. Laurell and M. Ohlin, *FEBS J*, 2008, **275**, 5657.
25 O. Manneberg, S. M. Hagsäter, J. Svennebring, H. M. Hertz, J. P. Kutter, H. Bruus and M. Wiklund, *Ultrasonics*, 2009, **49**, 112.
26 C. Grenvall, P. Augustsson, J. R. Folkenberg and T. Laurell, *Anal. Chem.*, 2009, **81**, 6195.
27 H. Nowotny and E. Benes, *J. Acoust. Soc. Am.*, 1987, **82**, 513.
28 M. Hill and R. J. K. Wood, *Ultrasonics*, 2000, **38**, 662.
29 J. J. Hawkes, W. T. Coakley, M. Gröschl, E. Benes, S. Armstrong and P. J. Tasker, *J. Acoust. Soc. Am.*, 2002, **111**, 1259.
30 M. Hill, Y. Shen and J. J. Hawkes, *Ultrasonics*, 2002, **40**, 385.
31 M. Hill, *J. Acoust. Soc. Am.*, 2003, **114**, 2654.
32 S. M. Hagsäter, T. G. Jensen, H. Bruus and J. P. Kutter, *Lab Chip*, 2007, **7**, 1336.
33 S. M. Hagsäter, A. Lenshof, P. Skafte-Pedersen, J. P. Kutter, T. Laurell and H. Bruus, *Lab Chip*, 2008, **8**, 1178.
34 M. Wiklund, P. Spégel, S. Nilsson and H. M. Hertz, *Ultrasonics*, 2003, **41**, 329.
35 J. Lighthill, *Waves in fluids*, Cambridge University Press, Cambridge, 2005.
36 H. Bruus, *Theoretical Microfluidics*, Oxford University Press, Oxford, 2008.
37 M. Barmatz and P. Collas, *J. Acoust. Soc. Am.*, 1985, **77**, 928.
38 R. Barnkob and H. Bruus, *Proceedings of Meetings on Acoustics*, 2009, **6**, 020001, DOI: 10.1121/1.3186746, 15.
39 W. L. Nyborg, *Ultrasound: Its Applications in Medicine and Biology*, ed. F. J. Fry, Elsevier, New York, 1978, Part 1, pp. 1–76.
40 R. J. Townsend, M. Hill, N. R. Harris and N. M. White, *Ultrasonics*, 2004, **42**, 319.
41 M. S. Limaye and W. T. Coakley, *J. Appl. Microbiol.*, 1998, **84**, 1035.
42 D. Brown. Tracker 2.60, *Free video analysis and modeling tool for physics education. Online open source*: http://www.cabrillo.edu/dbrown/tracker/, April 2009.
43 M. Raffel, C. E. Willert, S. T. Wereley, and J. Kompenhans, *Particle Image Velocimetry, A Practical Guide*, 2nd edn, Springer Verlag, Berlin, 2007.
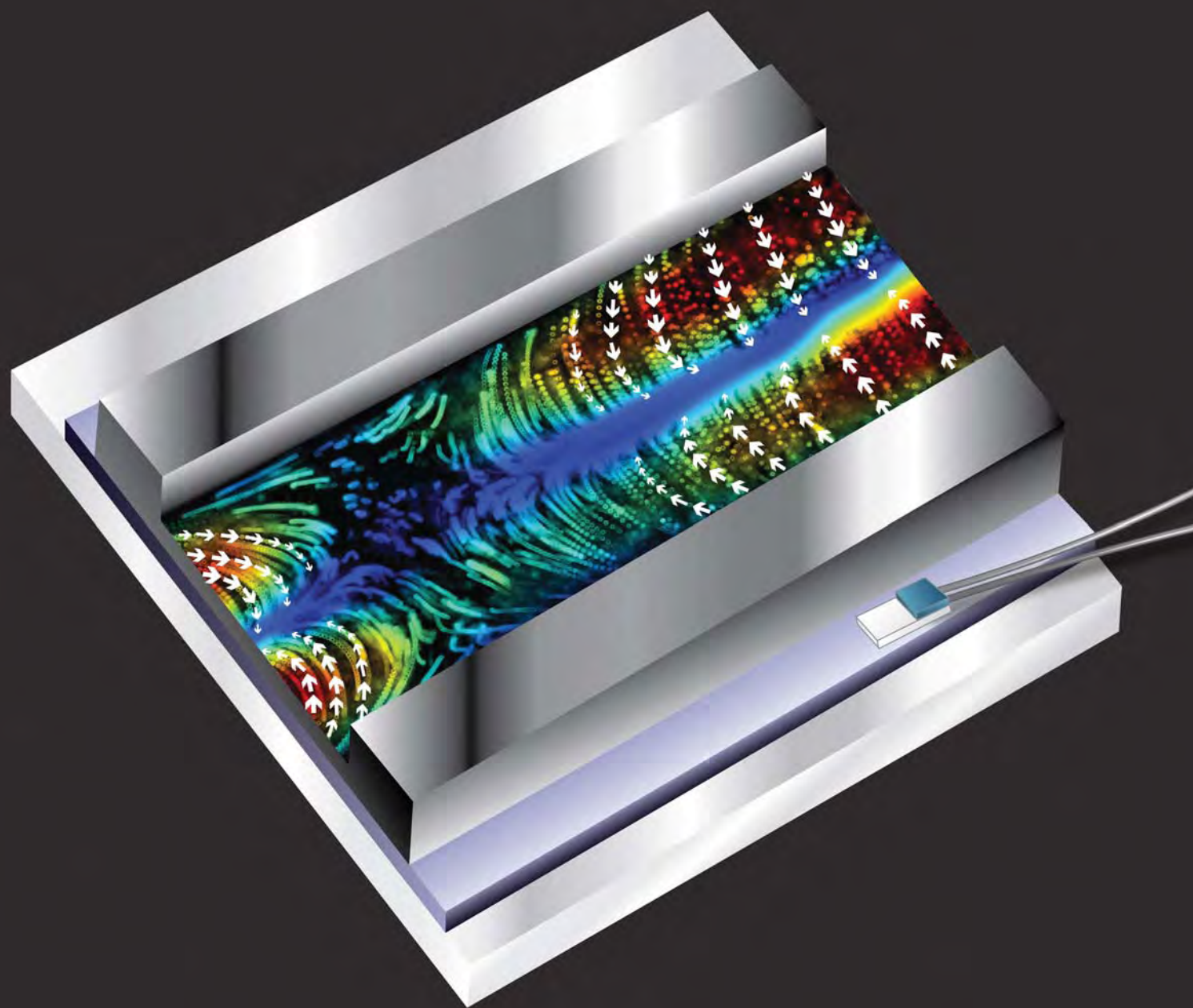44 O. Manneberg, B. Vanherberghen, B. Önfelt and M. Wiklund, *Lab Chip*, 2009, **9**, 833.

Paper published in Lab on a Chip, October 2011

RSCPublishing

PAPER
Laurell *et al.*
Automated and temperature-controlled micro-PIV measurements enabling
long-term-stable microchannel acoustophoresis characterization

Lab on a Chip

PAPER

Automated and temperature-controlled micro-PIV measurements enabling long-term-stable microchannel acoustophoresis characterization

Per Augustsson,†[a] Rune Barnkob,†[b] Steven T. Wereley,[c] Henrik Bruus[b] and Thomas Laurell[ad]

We present a platform for micro particle image velocimetry (μPIV), capable of carrying out full-channel, temperature-controlled, long-term-stable, and automated μPIV-measurement of microchannel acoustophoresis with uncertainties below 5% and a spatial resolution in the order of 20 μm. A method to determine optimal μPIV-settings for obtaining high-quality results of the spatially inhomogeneous acoustophoretic velocity fields of large dynamical range is presented. In particular we study the dependence of the results on the μPIV interrogation window size and the number of repeated experiments. The μPIV-method was further verified by comparing it with our previously published particle tracking method. Using the μPIV platform we present a series of high-resolution measurements of the acoustophoretic velocity field as a function of the driving frequency, the driving voltage, and the resonator temperature. Finally, we establish a direct and consistent connection between the obtained acoustophoretic velocity fields, and continuous flow mode acoustophoresis, commonly used in applications.

I.   Introduction

Microchannel acoustophoresis has received increasing interest within life sciences as an efficient, gentle and label-free method to manipulate cells and microbeads. Since the first microengineered continuous flow acoustophoretic particle filters,[1-4] many applications of microchannel acoustophoresis have emerged, including separation of erythrocytes from lipid particles,[5] bio-affinity purification using functionalized microbeads,[6] raw milk quality control,[7] cell cycle synchronization,[8] acoustic tweezers for cell patterning,[9] and cell sorting using surface acoustic waves.[10] In parallel, the fundamental physics of acoustophoretic micro-devices, acoustofluidics, have been studied, such as particle trajectory analyses,[11,12] whole-chip imaging of acoustic resonances,[13] investigation of separation efficiencies,[14] surface acoustic wave generation of standing waves,[15] multi-mode resonance chips,[16] frequency modulated actuation,[17] on-chip integration with magnetic separators,[18] and measurement of acoustic properties of cells.[19]

A more complete understanding of the fundamental physics remains a core issue in the further development of acoustofluidics in general and acoustophoresis in particular. To achieve this, quantitative, high-resolution, stable, and reproducible measurements of acoustophoretic motion are needed. In a recent paper,[20] we developed a method based on single-particle tracking and curve-fitting to *in situ* determine the local acoustophoretic pressure amplitude and energy density for a specific one-dimensional, transverse acoustic resonance. However, due to a relatively high statistical uncertainty, the method is not appropriate for extending to a more general, two-dimensional, acoustic resonance field.

Hagsäter *et al.* showed that whole-chip micro-particle image velocimetry (μPIV) is a strong tool for analyzing two-dimensional microchannel acoustophoresis.[13] However, the time-consuming process associated with μPIV measurements of time-dependent inhomogeneous particle distributions and the lack of stable devices have hurdled any systematic measurement of the dependence on the system parameters.

In this work we present a μPIV setup capable of automated, quantitative, high resolution, and accurate full-chip measurements of microchannel acoustophoresis. The μPIV analysis is optimized and evaluated, and the method displays conformity with our earlier reported particle tracking algorithm. Moreover, the stability of the platform is investigated, and especially the temperature dependence of the acoustic field is characterized experimentally. The platform is then utilized for assessment of the acoustic field for different driving amplitudes and frequencies, and it is demonstrated that large segments of the acoustophoresis channel can be measured to capture the global features

[a]Department of Measurement Technology and Industrial Electrical Engineering, Lund University, PO-Box 118, S-221 00 Lund, Sweden
[b]Department of Micro- and Nanotechnology, Technical University of Denmark, DTU Nanotech, Building 345 B, DK-2800 Kongens Lyngby, Denmark
[c]School of Mechanical Engineering, Purdue University, West Lafayette, IN, USA
[d]Department of Biomedical Engineering, Dongguk University, Seoul, South Korea
† These authors contributed equally to this work.

of the acoustic resonances. Finally, continuous flow experiments are carried out to establish the strong link between local acoustic field-strength and the overall particle focusing efficiency of the device.

II. Background theory

A. Microchannel acoustophoresis

The background theory for microchannel acoustophoresis, based on the paper by Gorkov[21] and the textbooks by Lighthill,[22] Pierce,[23] and Bruus,[24] is presented in our previous work.[20] Briefly, we consider a silicon/glass chip containing a microchannel filled with an aqueous solution of particles. A piezo transducer is attached to the chip, such that when applying an ac voltage U_{pp} at a MHz frequency f, the piezo element vibrates and induces a time-harmonic ultrasound pressure field $p_1 \exp(-i\omega t)$ and velocity field $v_1 \exp(-i\omega t)$, where we use the complex time-harmonic notation (implicitly assumed in the following), and where $\omega = 2\pi f$ is the angular frequency. As the viscosity of the carrier liquid has a negligible influence on the acoustic radiation forces on the large 5-μm-diameter tracer particles used in this work, the pressure and velocity field inside the microchannel are governed by simple linear acoustics of inviscid fluids, i.e. the Helmholtz wave equation for the pressure and potential flow for the velocity.

The acoustically soft water inside the channel surrounded by the acoustically hard silicon/glass chip forms an acoustic cavity. This implies that acoustic resonances occur for certain specific frequencies ω_j, $j = 1, 2, 3, …$, where the average acoustic energy density inside the cavity is several orders of magnitude larger than at other frequencies $\omega \neq \omega_j$. By tuning the applied frequency to $\omega = \omega_j$, the acoustic forces become so strong that they in a reliable way can be used to manipulate particles suspended in the carrier liquid. The exact values of the resonance frequencies ω_j depend on the geometry of the acoustic cavity and of the material parameters of the liquid in the cavity as well as the surrounding material.

Products of the first-order acoustic fields give rise to two second-order effects, which persist even after time averaging: The acoustic radiation force acting on particles in suspension, and the acoustic streaming acting on the carrier liquid itself. The radiation force is the only second-order effect of importance in this work, cf. ref. 20, and this force is particularly strong at driving frequencies near the resonance frequencies.

Given the pressure field p_1 and velocity field v_1 it is possible to calculate the acoustic radiation force on a spherical particle with volume $V = (4\pi/3)a^3$ and radius a much smaller than the acoustic wavelength λ. Both for biological cells and for microbeads used as tracers we are in this limit. The material parameters, with subscripts "wa" for the water and "p" for the particle, enter as the compressibility ratio $\tilde{\kappa} = \kappa_p/\kappa_{wa}$ in the compressibility factor f_1, and the density ratio $\tilde{\rho} = \rho_p/\rho_{wa}$ in the density factor f_2,

$$f_1 = 1 - \tilde{\kappa}, \quad f_2 = \frac{2\tilde{\rho}-2}{2\tilde{\rho}+1}. \tag{1}$$

The general expression for the time-averaged acoustic radiation force F_{ac} is a gradient of a potential,[21]

$$F_{ac} = -V\nabla\left[f_1\frac{\langle p_1^2\rangle}{2\rho_{wa}c_{wa}^2} - f_2\frac{3}{4}\rho_{wa}\langle v_1^2\rangle\right]. \tag{2}$$

For the special case of a standing transverse wave of wavenumber $k_y = 2\pi/\lambda$, the acoustic pressure amplitude is given by $p_a = 2\sqrt{E_{ac}\rho_{wa}c_{wa}^2}$, where E_{ac} is the acoustic energy density. Defining $\Phi = \frac{1}{3}f_1 + \frac{1}{2}f_2$, the corresponding pressure field p_1, the acoustophoretic force F_y, tracer-particle velocity u_y and transverse path $y(t)$ of the particle are given by[20]

$$p_1 = p_a \cos(k_y y), \tag{3a}$$

$$F_y = 4\pi\Phi a^3 k_y E_{ac}\sin(2k_y y), \tag{3b}$$

$$u_y = \frac{2\Phi}{3\eta}a^2 k_y E_{ac}\sin(2k_y y), \tag{3c}$$

$$y(t) = \frac{1}{k_y}\arctan\left\{\tan\left[k_y y(0)\right]\exp\left[\frac{4\Phi}{3\eta}(k_y a)^2 E_{ac}t\right]\right\}. \tag{3d}$$

To obtain a strong and stable acoustic resonance for a given piezo transducer, the following points must be taken into consideration. The electronic oscillator driving the transducer must have a stable frequency f and peak-to-peak voltage U_{pp}. The acousto-mechanical contact between the transducer and the chip must be stable and acoustically loss-free, preferably by using a hard epoxy glue. The amount of silicon/glass surrounding the microchannel should be minimized to maximize the ratio of acoustic energy inside the microchannel to the acoustic energy in the bulk. The use of soft materials connected to the chip (as e.g. fluidic tubing) must be kept to a minimum to reduce acoustic loses. The temperature of the chip must be kept constant as the temperature dependence of the mechanical properties of the chip (speed of sound, density, Young's modulus, and Poisson's ratio) translate into a temperature dependence of the resonance frequency, and hence of the acoustic energy in the microchannel.

B. μPIV measurements of acoustophoresis

μPIV is a flow measurement technique for obtaining detailed measurements of the velocities of groups of tracer particles
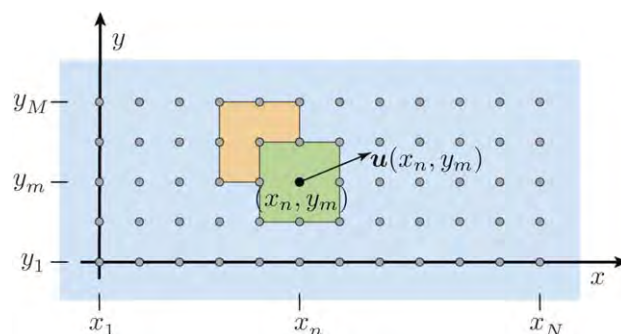

Fig. 1 Sketch of a given image frame (blue rectangle) containing $N \times M$ interrogation windows (green square) of size $S \times S$ pixel centered around the discrete grid points (x_n, y_m), gray circles. Neighboring interrogation windows overlap by 50% (light orange square). The μPIV interrogation window at each grid point results in a 2D velocity vector $u(x_n, y_m)$, black arrow.

(microbeads) in microfluidic systems.[25–29] It is based on digital image frames that, as sketched in Fig. 1, are sub-divided into interrogation windows centered around (x_n, y_m) and containing $S \times S$ pixel (rectangular area can be chosen) at positions $\boldsymbol{r}_{\mathrm{pix}}$ with intensity $I(x_n, y_m, t, \boldsymbol{r}_{\mathrm{pix}})$ at time t. The core of the μPIV technique is the discrete cross-correlation function C formed by the pixel intensities I from two interrogation windows (denoted an image pair), separated by a short time interval Δt,

$$C(x_n, y_m, t, \Delta t, \Delta \boldsymbol{r}) =$$

$$\frac{1}{S^2} \sum_{\boldsymbol{r}_{\mathrm{pix}}}^{S^2} I\left(x_n, y_m, t, \boldsymbol{r}_{\mathrm{pix}} + \Delta \boldsymbol{r}\right) I\left(x_n, y_m, t + \Delta t, \boldsymbol{r}_{\mathrm{pix}}\right). \quad (4)$$

The pixel off-set $\Delta \boldsymbol{r}$ is varied until a maximum value of C is found, $\max_{\Delta \boldsymbol{r}}(C) = C(\Delta \boldsymbol{r}_{\mathrm{max}})$. This pixel displacement is then a measure of the local displacement of the tracer particles, and the corresponding particle velocity is given by $\boldsymbol{u}(x_n, y_m) = \Delta \boldsymbol{r}_{\mathrm{max}}/\Delta t$.

High-quality μPIV analysis with good statistics is achieved by repetitive measurements and subsequent averaging of the correlation function C, a procedure known as correlation average. In this work, all acoustophoretic focusing experiments were repeated between 25 and 100 times. For the procedure to work best, it is imperative to avoid both clustering and depletion of tracer particles.[30] The following procedure was adopted: In a given time-sequence of image frames recorded immediately after the onset of ultrasound, the first frame was discarded to ensure that the acoustic resonance was fully developed; only the second and third frame was analyzed, as the particle distribution rapidly becomes inhomogeneous due to the acoustophoretic force potential. Furthermore, better statistics and sub-pixel resolution was obtained by using an iterative window shifting algorithm based on a smoothed continuum version of the discrete correlation function.[31] Finally, the accuracy of the analysis was refined by use of a central difference interrogation window method and a four-point image correction.[26]

The μPIV analysis was carried out using the software *EDPIV - Evaluation Software for Digital Particle Image Velocimetry* (http://www.edpiv.com). As part of the analysis, the recorded bright-field images were inverted and the background was subtracted. The background was derived by finding the lowest pixel intensity in the whole data set for each pixel position. To ensure convergence of the μPIV algorithm 20 window-shifting iterations was employed. Unless otherwise stated, the interrogation window size $S \times S$ was set to $S = 64$ pixel, and we used a 50% overlap such that the side length in the square grid (x_n, y_m) of Fig. 1 is $S/2 = 32$ pixel. Search radius for the shift-vector $\Delta \boldsymbol{r}$ was set to 20 pixel.

The μPIV results for the acoustophoretic velocity field was validated by particle tracking velocimetry (PTV), see Section IV E. In PTV, a set of tracer particles are identified manually in the first frame and then tracked throughout the subsequent (long) sequence of frames. The tracking is achieved by extraction of a sub-image containing the particle, which is thereafter cross-correlated with a small region in its vicinity in the succeeding frame. Generally, PTV has poor precision, but it is accurate, which can easily be verified by overlaying the acquired tracks with the analyzed frames.

C. Discrete acoustophoretic velocity field

From the μPIV analysis we obtain the acoustophoretic velocity field of the tracer particles

$$\boldsymbol{u} = \boldsymbol{u}(x_n, y_m) = \begin{pmatrix} u_x(x_n, y_m) \\ u_y(x_n, y_m) \end{pmatrix} \quad (5)$$

on the discrete lattice (x_n, y_m) with indices $1 \leq n \leq N$ and $1 \leq m \leq M$, see Fig. 1. The rectangular lattice has the lengths $L_x = x_N$ and $L_y = y_M$ along the x- and y-direction, respectively. For quantitative comparisons of acoustophoretic velocity fields $\boldsymbol{u}$, we use both the local speed $u(x_n, y_m) = |\boldsymbol{u}(x_n, y_m)|$ and the L^2-norm $\|\boldsymbol{u}\|$. The (square of the) latter is defined as

$$\|\boldsymbol{u}\|^2 = \frac{1}{NM} \sum_{n=1}^{N} \sum_{m=1}^{M} \left| \boldsymbol{u}(x_n, y_m) \right|^2. \quad (6)$$

Note that $\|\boldsymbol{u}\|$ can be thought of as an area-average speed, while $\|\boldsymbol{u} - \boldsymbol{u}_0\|^2$ is the variance of $\boldsymbol{u}$ around $\boldsymbol{u}_0$.

III. Chip, setup, and experimental procedure

A. Chip and experimental setup

Acoustophoresis microfluidic chip. A chip was fabricated with similar design as previously examined in ref. 20. Briefly, the chip consists of a straight channel of length $L = 35$ mm, width $w = 377$ μm, and height $h = 157$ μm, KOH-etched in a $\langle 100 \rangle$ silicon wafer of thickness $h_{\mathrm{si}} = 350$ μm. The channel was sealed by an anodically bonded pyrex lid of thickness $h_{\mathrm{py}} = 1.13$ mm. The chip length equals the channel length L and the chip width is $W = 2.52$ mm. To interface the channel, pieces of silicone tubing were glued to the chip inlet and outlet at each end, oriented along the channel axis, see Fig. 2.

Chip assembly. To achieve good long term stability, all parts of the chip assembly were glued together using ethyl-2-cyanoacrylat (ExpressLim, Akzo Nobel Bygglim AB, Sweden). From bottom and up sandwiched together: an aluminum mounting plate also serving as heat sink, a Peltier element (40 mm × 40 mm), an
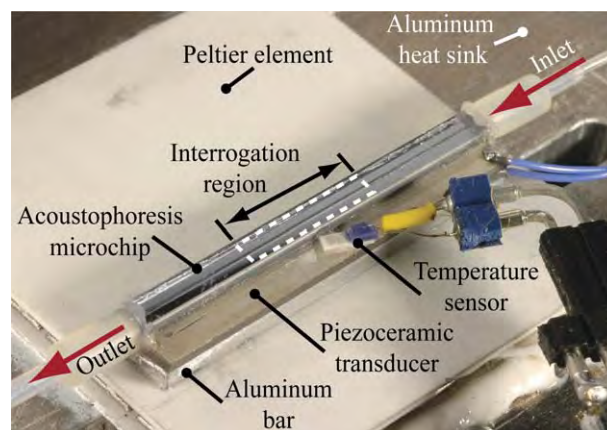

Fig. 2 Photograph of the acoustophoresis microchannel. The chip, piezo transducer (PZT), aluminum bar and Peltier element were sandwiched and glued together on a microscope stage. A Pt100 thermoresistive element was glued onto the PZT for feedback to the temperature control loop.

aluminum bar (35 mm × 5 mm × 1.5 mm), a piezo transducer (PZT) (35 mm × 5 mm × 1 mm, PZT26, Ferroperm Piezoceramics, Denmark), and the acoustophoresis chip, see Fig. 2. A Pt100 thermo-resistive element for temperature measurement was glued onto the PZT alongside the acoustophoresis chip, see Fig. 2.

Acoustics driving electronics. The PZT was driven by a function generator (33120A, Agilent Technologies Inc., Santa Clara, CA, USA) at a frequency f in the 2-MHz-range *via* a power amplifier circuit (LT1210, Linear Technologies Corp., Milpitas, CA, USA) configured with 10 Ω output impedance. The peak-to-peak voltage amplitude U_{pp} over the PZT was recorded with an oscilloscope (TDS 1002, Tektronix UK Ltd., Bracknell, UK). The onset of acoustic actuation was controlled by an external gate signal to the function generator.

Temperature control. Readings from the Pt100 element were recorded and temperature T was regulated using the Peltier element. A PID control loop was implemented on a computer interfaced by a data acquisition card (DAQ) (NI USB-6008, National instruments, Austin, TX, USA) and complementary circuits for generating constant current for 4-wire temperature measurement and for power amplification of the Peltier drive.

External fluidics. A syringe pump (neMESYS, Cetoni GmbH, Korbussen, Germany) and a motorized 2-position 4-way diagonal valve (V101, Upchurch Scientific, Oak Harbor, WA, USA), was interfaced to the computer. When the valve is in its initial position, microbead suspension can be withdrawn from a test tube into a 1-mL syringe (1001 LT, Hamilton Bonaduz AG, Bonaduz, Switzerland), while the inlet and outlet of the microchannel is short circuited, abruptly stopping flow in the channel. Switching the valve will connect the syringe with the chip inlet while the outlet will be open to the test tube. The configuration has two main advantages: microbeads can be reused for several passages through the microchannel, and repeated withdrawal and infusion of sample at high flow rates induces mixing in the test tube, preventing microbeads from sedimenting during long measurement series.

Imaging. A brightfield microscope (DM2500 M, Leica Microsystems CMS GmbH, Wetzlar, Germany) was equipped with a high-speed camera (EoSens mini MC-1370, Mikrotron GmbH, Unterschleissheim, Germany) set to an exposure time of 150 μs and frame rates ranging from 50 to 800 Hz. The image size is 1280 × 640 pixel corresponding to 0.88 mm × 0.44 mm in object plane (*i.e.* 1 pixel ∼ 0.69 μm). The image of a 5-μm-diameter tracer particle is thus ∼ 7 × 7 pixel. The camera is trigged by an external signal that is also the gate signal for the onset of ultrasound. For each trig, the camera records a predetermined number of images that are stored in an on board memory. The memory can store a maximum of 2500 images which has to be accounted for when setting up experimental series of multiple repeats. The frame rate of the camera can be set by the computer software by an external synchronization signal from a GPIB interfaced function generator.

Spatial positioning. To assess the global behavior of the acoustic resonances, image sequences must be captured from multiple positions along the channel. To be able to reliably stitch together the recorded velocity fields, accurate and reproducible positioning of the chip mount is important. Spatial positioning was controlled *via* a motorized *xyz*-stage (MTmot, Märzhäuser Wetzlar GmbH, Wetzlar, Germany). Positions were chosen with a 10% overlap between images. Overlapping areas would thereby be analyzed twice providing a measure of the discrepancy between adjacent fields of view.

Control software. A LabView program was developed, dedicated for controlling the experimental sequence. Its primary functionality is to regulate temperature in a PID-loop and to create a gate signal to the system to actuate ultrasound and trig the camera. A list of settings specifies ultrasound frequency and amplitude, camera frame rate and oscilloscope measurement range. For each onset of ultrasound, voltage over the PZT is recorded and stored *via* the GPIB interfaced oscilloscope. The program also controls the syringe pump and the motorized valve which enables the program to complete a whole sequence of experiments with different settings, each repeated a specified number of times. The experimental setup is sketched in Fig. 3.

B. Experimental procedures

In general, various aspects of acoustophoretic focusing were measured in stop-flow mode using an aqueous suspension of polystyrene microbeads (3 g L^{-1}, diameter $d = (5.16 \pm 0.08)$ μm, Sigma-Aldrich) with the addition of the surfactant Tween20 (0.01%, Sigma-Aldrich). The particle concentration is kept low to diminish particle–particle interactions and ensuring the validity of the single-particle theory presented in Section II A. Prior to each experiment 1 mL of this suspension was loaded into the system, and the *xyz*-stage position and the microscope focal plane were calibrated.

A given experiment was specified in the control software by the following list of settings: ultrasound frequency and amplitude, oscilloscope measurement range, camera frame rate, temperature set point, ultrasound gate time, temperature settling time, and number of repeats. Once initiated, the software automatically executes the timing of events for each individual acoustophoretic focusing experiment throughout the experimental series in the following order, Fig. 3(e):

1. The valve is switched to position I, Fig. 3(c), and 500 μL of bead suspension is withdrawn from the test tube into the syringe.

2. The valve is switched to position II, Fig. 3(d), and 100 μL of bead suspension is injected through the chip at 33 μL s^{-1} into the test tube.

3. The valve is switched back to position I to stop the flow in the microchannel, and the remaining bead suspension is emptied at a flow rate of 100 μL s^{-1} into the test tube to induce mixing.

4. The system is idle for a time of ∼ 10 s to allow for the temperature to stabilize to within ± 0.1 °C of the preset value.

5. A gate signal activates ultrasound for ∼ 100 ms and triggers the camera to capture a predefined number of frames.

6. The PZT voltage amplitude U_{pp} is registered *via* the oscilloscope. It has an uncertainty of 5%.

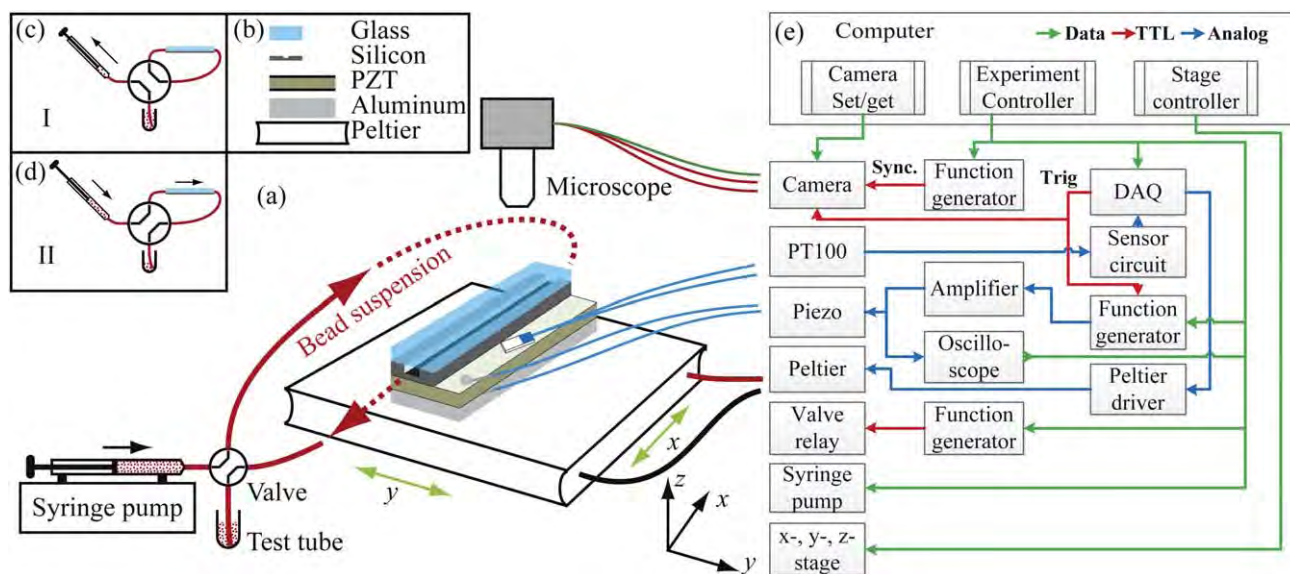The system automatically closes down at the end of a complete experimental series.

Fig. 3 (a) Schematic of the automated, temperature-controlled acoustophoresis µPIV setup. (b) The chip, PZT, aluminum slab, and Peltier element were sandwiched and glued together, resting on the microscope stage. (c) The valve in position *I* stops the flow in the chip, and the particle suspension can be transferred between syringe and test tube. (d) The valve in position *II* allows for injecting the particle suspension into the channel and redirecting it back into the test tube for reuse. (e) Diagram of the software and hardware configuration controlling the temperature and experimental timing sequence, positioning of the channel, and the camera setup.

The above procedure was employed to carry out the following eight types of experiments reported in this work:

1. The global spatial structure of the three resonance modes at $f = 1.940$ MHz, 1.951 MHz, and 1.968 MHz in a 12 mm long section of the microchannel at $T = 25\,^\circ$C, see Section IV A.

2. Optimization of µPIV settings: image-pair time-shift and standard deviation of velocities, see Section IV B.

3. Optimization of µPIV settings: window size S in the range 16 to 128 pixel, and image pair number n_{tot}^{pair} in the range 1 to 100, see Section IV C.

4. The scaling of the acoustophoretic velocity with the PZT-voltage U_{pp} to the power 2, see Section IV D.

5. Comparison of µPIV with PTV, see Section IV E.

6. Temperature stability toggling between $T = 20\,^\circ$C and $25\,^\circ$C for the fixed frequency $f = 1.963$ MHz and driving voltage $U_{pp} = 1.8$ V, see Section V A.

7. Temperature sensitivity during frequency scans from $f = 1.931$ MHz to 1.980 MHz in steps of 1 kHz at $T = 23\,^\circ$C, $25\,^\circ$C, and $27\,^\circ$C for $U_{pp} = 2.0$ V, see Section V B.

8. The focusing efficiency in continuous-flow mode correlated with the resonance modes measured by µPIV in stop-flow mode, see Section VI.

IV. Evaluation of the µPIV analysis

The results section begins with an evaluation of the µPIV analysis and a description of how appropriate settings of the µPIV parameters were chosen. The spatial inhomogeneity of the resonant modes results in inhomogeneous acoustophoretic velocity fields with a large dynamic range, which hurdles the accuracy of the µPIV analysis. To obtain good results, µPIV-parameters were optimized by analyzing the standard deviation of the velocity fields.

A. Global spatial structure of the resonance modes

The capability of the automated µPIV system is illustrated in Fig. 4. Here, the result of high-resolution measurements of the global spatial structure of the acoustic resonance modes ($f = 1.940$ MHz, 1.951 MHz, and 1.968 MHz determined as described in Section V B) is shown for a 12-mm-long section at the center of the 35-mm-long microchannel, Fig. 4(a). The color plots in Fig. 4 (b) show the speed u/u_{max} of the acoustophoretic velocity fields for the 5-µm-diameter polystyrene tracer particles normalized by the maximum speed u_{max}. For each frequency a total of 15 adjacent image frames were stitched together with an overlap of 10%, and the acoustophoretic focus experiment was repeated 25 times for each position of the image frame. For all measurements the temperature was kept constant at 25 °C.

To accommodate for the high dynamic range in the acoustophoretic velocity of the tracer particles, the cameras frame rate was set to either 400 Hz or 800 Hz. To achieve the same microbead displacement for each of the three frequencies as described in Section IV B, the driving voltage was set to $U_{pp} = 2.00$ V at $f = 1.940$ MHz, 1.25 V at 1.951 MHz, and 0.75 V at 1.968 MHz. The interrogation window size was $S = 64$ pixel leading to a grid size of 32 pixel and thus a grid resolution of 22 µm.

In Fig. 4(c) more details in the spatial structure of the resonances are made visible by color plots of $\log(u/u_{max})$. This is particularly evident for $f = 1.968$ MHz, where four local maxima become visible.

B. Image-pair time-shift and standard deviation

The uncertainty in terms of standard deviation in the velocity fields obtained by µPIV was minimized by optimizing three parameters: the displacement of the tracer particles between the
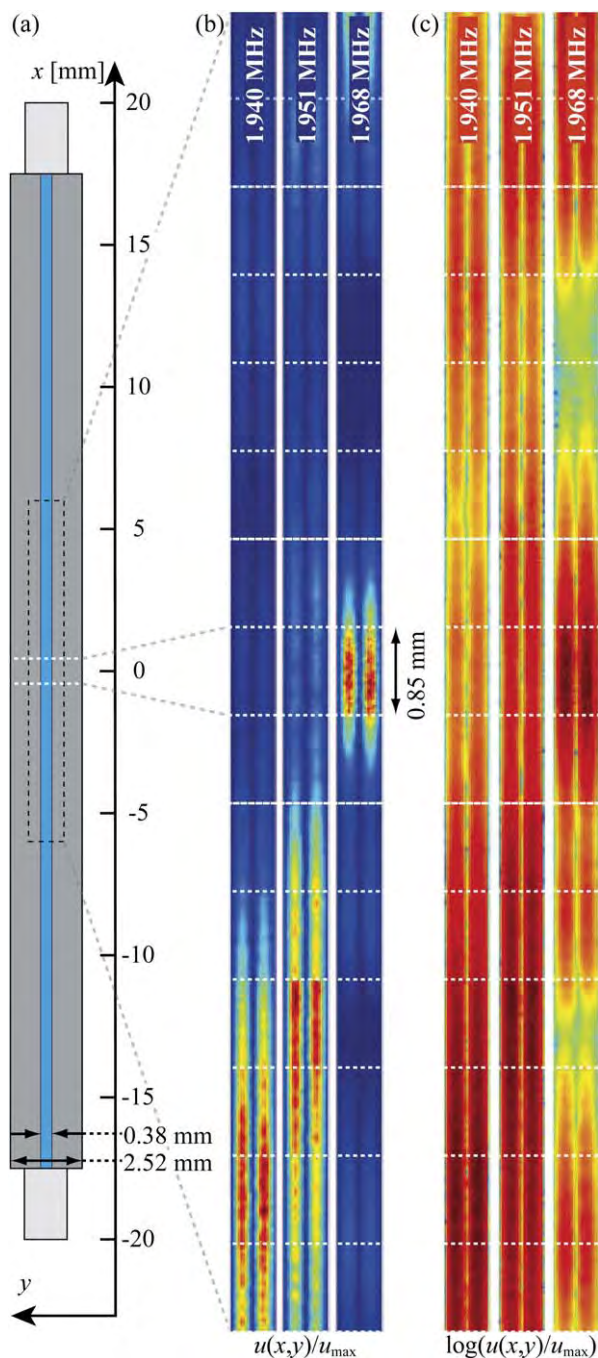
two images in an image pair, the number of repeated measurements, and the size S of the interrogation window.

In μPIV the best results are obtained if the maximum displacement of the tracer particles within an image pair is about one to a few times the diameter of the particles. To verify this, the image frame was positioned in the channel center as indicated in Fig. 4(a), with $T = 25\,°C$, $f = 1.968$ MHz, and $U_{pp} = 2.95$ V. Then 100 repeats of the acoustophoretic focusing were recorded, capturing 10 time frames per repeat at a frame rate of 800 Hz. From the data, nine different μPIV image pairs can be constructed by pairing frame 1 with frame $1 + n$ (for $n = 1, 2, …, 9$), and this leads to the nine possible time shifts $\Delta t = n \times 1.25$ ms, see eqn (4).

The maximum acoustophoretic velocity in this experiment was measured to be 1 mm s^{-1} corresponding to a maximum particle displacement of $n \times 1.8$ pixel for the nine different image-pair time shifts. In Fig. 5(a) we plot the normalized area-average acoustophoretic speed $\|u\|$ as a function of this maximum pixel displacement. A distinct maximum is seen around 7 pixel corresponding to the tracer-particle diameter of 5 μm. In all of the μPIV analysis the PZT voltage U_{pp} was therefore set to achieve this displacement as accurate as possible.

The image-pair time-shift is only one of many parameters of the μPIV analysis we need to optimize. In practice, the determination the acoustophoretic velocity field is a trade-off between the desired velocity accuracy and the time it takes to carry out the experiment and μPIV analysis. For a given microbead concentration, a certain velocity accuracy requires a minimum number of uncorrelated image pairs n_{tot}^{pair} and a maximum interrogation window size $S \times S$. If the interrogation window size is too large, the resolution of the velocity field is too low to resolve the dynamics, but the smaller the window gets, the more experimental repetitions n_{tot}^{pair} are needed to ensure a proper bead coverage and thus sufficient statistics in

Fig. 4 Global spatial structure of three acoustic resonance modes. (a) Schematic of the chip indicating the 12-mm-long section investigated. The white lines represent the channel-center single-image frame used in Secs. IV and V. (b) Color plot from 0 (dark blue) to 1 (dark red) of the normalized acoustophoretic speed $u(x, y)/u_{max}$ measured by μPIV at $T = 25\,°C$ for the three resonance frequencies $f = 1.940$ MHz, 1.951 MHz, and 1.968 MHz. For other experimental parameters see Section IV.A. The data consist of 25 repetitions in 15 stitched image frames per frequency (white lines), and the acquisition took 3 days. (c) Color plot of the natural logarithm of $u(x, y)/u_{max}$ from panel (b).
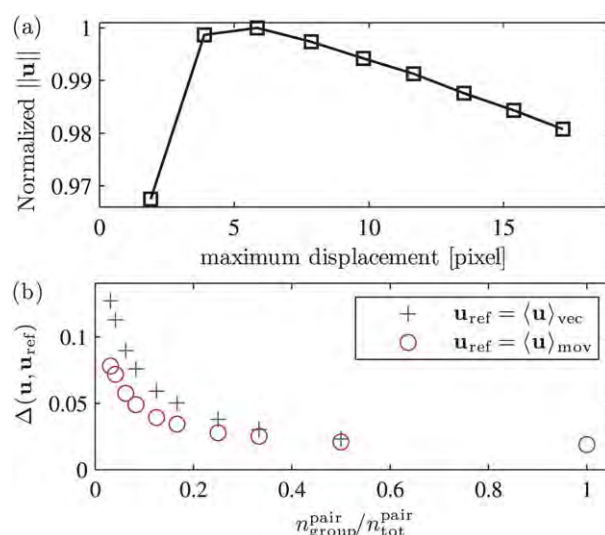

Fig. 5 (a) Area-average acoustophoretic speed $\|u\|$ *versus* maximum particle displacement within the channel-center single-image frame using $n_{tot}^{pair} = 100$ and $S = 32$ pixel. (b) The relative standard deviation $\Delta(u, u_{ref})$ of the acoustophoretic velocity field u with $u_{max} = 0.8$ mm s^{-1} determined by μPIV as function of the amount $n_{group}^{pair}/n_{tot}^{pair}$ of correlation averaging for integer division of $n_{tot}^{pair} = 96$. For u_{ref} is used either the vector average $\langle u \rangle_{vec}$ (blue +) or the moving average $\langle u \rangle_{mov}$ (red ○), see eqn (7).

the μPIV analysis. Therefore, it is important to carry out a parametric study of the μPIV analysis settings and number of experimental repetitions for a certain set of experimental parameters, such as microbead concentration, camera frame rate, and microbead velocities.

One way to estimate the standard deviation on an acoustophoretic velocity field determined by μPIV is to repeat a given image-pair measurement n_{tot}^{pair} times, and then sub-divide this series into N_{group} groups each containing n_{group}^{pair} image pairs ($n_{group}^{pair} = N_{group} \times n_{group}^{pair}$). For each group a μPIV analysis involving averaging over the n_{group}^{pair} cross-correlation functions is performed resulting in N_{group} velocity fields u_i. The vector average $\langle u \rangle_{vec} = \sum_{i=1}^{N_{group}} u_i / N_{group}$ is calculated, and the relative standard deviation $\Delta(u, u_{ref})$ of u around the reference field $u_{ref} = \langle u \rangle_{vec}$ can be estimated from the variance $\|u - u_{ref}\|^2$, see eqn (9), and the maximum speed u_{max} of u, as

$$\Delta(u, u_{ref}) = \sqrt{\frac{1}{N_{group}} \sum_{i=1}^{N_{group}} \frac{\|u_i - u_{ref}\|^2}{u_{max}^2}}. \quad (7)$$

In Fig. 5(b) is shown the result of this vector-average estimate (blue +) of the relative standard deviation $\Delta(u, \langle u \rangle_{vec})$ versus for $n_{tot}^{pair} = 96$. In the limit where the sub-groups contains a single image pair ($n_{tot}^{pair} = 1$) each of which leads to a μPIV velocity field by a single cross-correlation function eqn (7), the method corresponds to pure vector averaging of the resulting $N_{group} = n_{tot}^{pair} = 96$ velocity vector fields. In the opposite limit ($n_{group}^{pair} = n_{tot}^{pair}$), the average of the correlation functions of all 96 image pairs is used to calculate a single μPIV velocity field ($N_{group} = 1$), and the method corresponds to pure correlation function averaging. For intermediate values $1/96 < n_{group}^{pair}/n_{tot}^{pair} < 1$, the method is a combination of vector averaging and correlation averaging. In Fig. 5(b) it is seen that for the given 96 image pairs, $\Delta(u, \langle u \rangle_{vec})$ decreases monotonically from 12% for $n_{group}^{pair}/n_{tot}^{pair} = 0.01$ to below 3% for $n_{group}^{pair}/n_{tot}^{pair} = 0.5$ supporting the fact[27] that correlation average yields better precision in μPIV than vector average. Although viable, the vector-averaging method is a time-consuming way (24 h to obtain the results for $\Delta(u, \langle u \rangle_{vec})$) to obtain the standard deviation as it requires additional μPIV analysis and additional number of experimental repeats. A more efficient way is to use the 3-by-3-point moving-average method, where $\Delta(u, u_{ref})$ is calculated using for each point (x_n, y_m) in the grid the nearest-neighbor average $u_{ref}(x_n, y_m) = \langle u \rangle_{mov}(x_n, y_m)$ of the velocity u_i of the 3×3 points having (x_n, y_m) in the center. It is seen in Fig. 5(b) that the moving-average estimate $\Delta(u, \langle u \rangle_{mov})$ (red ○) agrees well with the vector-average method, settling around 2% for $n_{group}^{pair}/n_{tot}^{pair} = 1$. No additional effort is needed when using the moving-average method and thus it is used in the rest of the paper to evaluate the standard deviation $\Delta(u, u_{ref})$.

Another test of the accuracy of the μPIV measurements is to measure the velocity in the case of no acoustical drive, i.e. for $U_{pp} = 0$. The obtained area-averaged speed is $\|u\| = 7.3 \ \mu m \ s^{-1}$, which primarily stems from the x-component, indicative of a small drift even though the flow is stopped. Thus, the velocity magnitude cannot be expected to be determined more accurately than this. For resonant modes typically $\|u\| \approx 500 \ \mu m \ s^{-1}$, thus the accuracy cannot be better than $\sim 2\%$.

In conclusion, using the μPIV settings described above, our automated system is routinely capable of obtaining acoustophoretic velocity fields with a spatial resolution of about 20 μm with an uncertainty of $\sim 5\%$. Higher resolution and lower uncertainty can be obtained by going beyond 100 repeats per focus experiment.

C. Window size and number of image pairs

The next step is to investigate how the quality of the μPIV results depends on the number n_{tot}^{pair} of uncorrelated image pairs (number of repeats) and the pixel size S of the quadratic $S \times S$ interrogation window. Other more detailed studies of additional μPIV parameters such as the search radius, number of window shifting iterations, and various central-difference schemes are not treated here.

In Fig. 6(a) is shown plots of the relative standard deviation $\Delta(u, u_{ref})$ of the velocity field u as a function of n_{tot}^{pair} and S using the moving-average method $u_{ref} = \langle u \rangle_{mov}$ with $n_{group}^{pair} = n_{tot}^{pair}$ and $N_{group} = 1$. As the number of uncorrelated image pairs n_{tot}^{pair} increases, $\Delta(u, \langle u \rangle_{mov})$ decreases. The high uncertainty $\sim 10\%$ for $S = 128$ pixel is also visible in the line and color plots of the speed u in panel (b) and (c), respectively. The effect of the low tracer particle concentration used, is reflected in the observation that the lowest standard deviation is obtained for $S = 32$ pixel. For the smallest interrogation window size $S = 16$ pixel the number of tracer particles per window is so low that the statistical fluctuations increase noticeably, compare 16 pixel and 32 pixel in panel (c). The relative standard deviation for $S = 32$ pixel drops below 3% already for $n_{tot}^{pair} = 20$. This tendency is supported by the plot of $\Delta(u, u_{ref})$ using the velocity field u_{32}^{100} obtained for $S = 32$ pixel and $n_{tot}^{pair} = 100$ as u_{ref} for all four values of S. This plot also shows that to obtain an uncertainty below 5% it is thus sufficient to use $n_{tot}^{pair} = 20$ and $S = 64$, so this we use in our application example in Section VI leading to a spatial resolution of 20 μm.

In Fig. 6(b) are shown two line plots of the speed $u(x_0, y)$ along the transverse y-direction at $x_0 = 223 \ \mu m$ and $x_0 = 713 \ \mu m$ with $n_{tot}^{pair} = 100$ for the same data as in panel (a). Except for the most coarse-grained resolution ($S = 128$ pixel), the other three window sizes $S = 64$ pixel, 32 pixel, and 16 pixel agree well. However, close to the wall both $S = 128$ pixel and 64 pixel differs from $S = 32$ pixel and 16 pixel, because the large window sizes results in a significant overlap of windows with the channel walls, which results in an erroneous contribution of non-zero velocities outside the channel.

In Fig. 6(c) are shown plots of the acoustophoretic velocity field u (arrows) and speed u (colors) corresponding to the data in Fig. 6(b) using $n_{tot}^{pair} = 100$ and $S = 128, 64, 32,$ and 16 pixel. The resolution clearly increases as S decreases, but simultaneously the noise increases because the number of tracer particles in each interrogation window decrease. In the color plots are marked the two x-coordinates, $x_0 = 223 \ \mu m$ and $x_0 = 713 \ \mu m$ corresponding to the two line plots in Fig. 6(b).

As observed, a lower standard deviation $\Delta(u, u_{ref})$ can be obtained by increasing n_{tot}^{pair}. However, the cost is an increased time t^* for data acquisition and analysis: $t^* = (\tilde{t}_{exp} + \tilde{t}_{img} + \tilde{t}_{PIV})n_{tot}^{pair}$, where $\tilde{t}_{exp}$ is the measurement time per image pair, $\tilde{t}_{img}$ the image analysis time per image pair, and $\tilde{t}_{PIV}$ the time for the total μPIV analysis per image pair. Rough estimates of the times per image
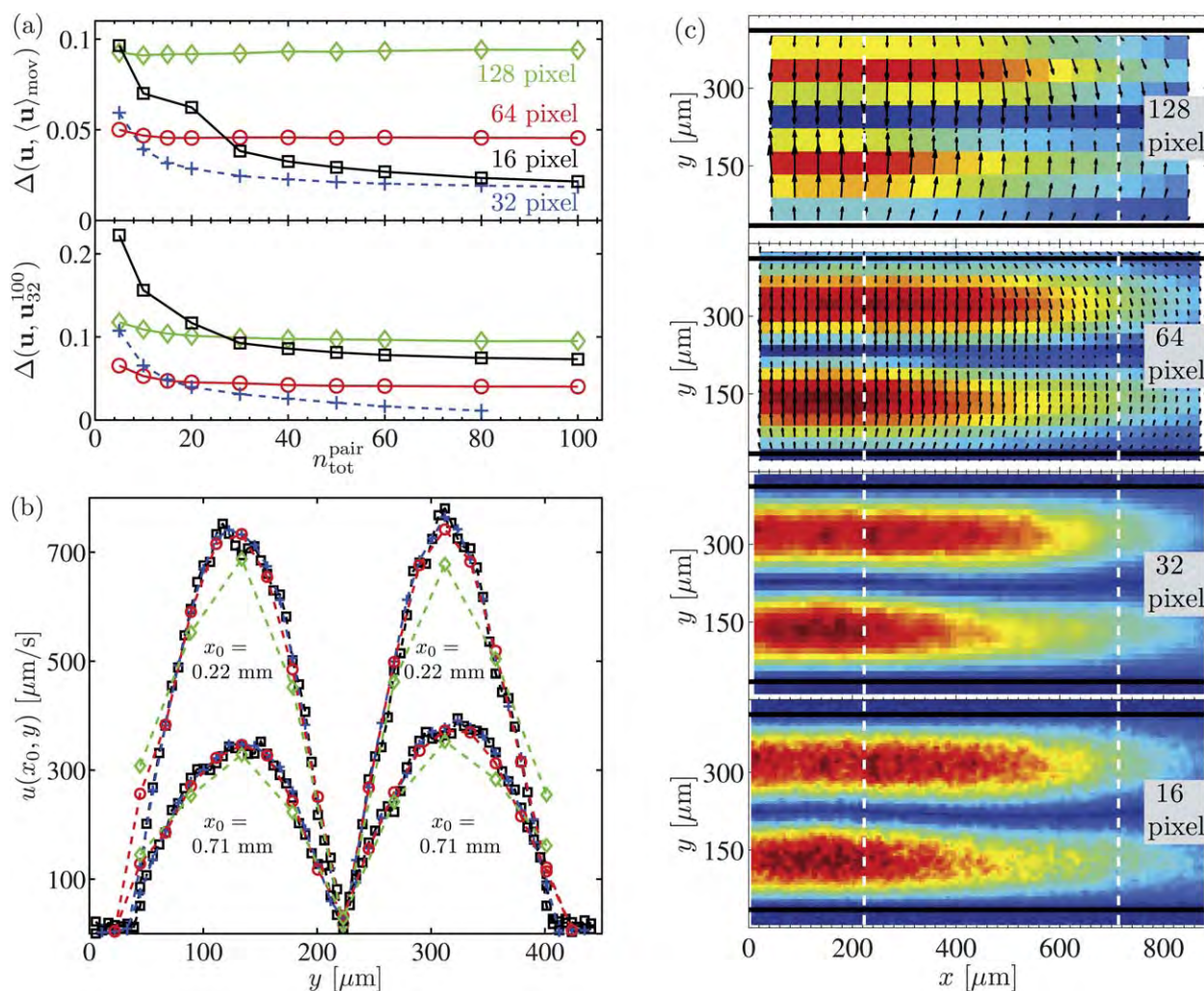
Fig. 6 The μPIV acoustophoretic velocity fields ($T = 25\,°C$, $f = 1.968$ MHz, $U_{pp} = 1.89$ V) in the channel-center single-image frame of Fig. 4 *versus* the number n_{tot}^{pair} of uncorrelated image pairs and of the interrogation window size S. (a) The relative deviation $\Delta(\boldsymbol{u}, \boldsymbol{u}_{ref})$ of the velocity u relative to the reference velocity fields $\langle\boldsymbol{u}\rangle_{mov}$ (moving average field) and u_{32}^{100} ($S = 32$ pixel and $n_{tot}^{pair} = 100$) as a function of n_{tot}^{pair} (from 1 to 100) and S [128 pixel (green $\diamondsuit$), 64 pixel (red $\bigcirc$), 32 pixel (blue +), and 16 pixel (black $\square$)]. (b) Two line plots of the speed $u(x_0, y)$ along the transverse y-direction at $x_0 = 223$ μm and $x_0 = 713$ μm with $n_{tot}^{pair} = 100$ for the same data as the previous panel. (c) Acoustophoretic velocity fields (arrow plots) and speed fields (color plots, from 0 μm s^{-1} (dark blue) to 800 μm s^{-1} (dark red)) for the same data as the previous panel. From top to bottom panel the window size is $S = 128$ pixel, 64 pixel, 32 pixel, and 16 pixel. The white dashed lines indicate the two line plots in panel (b).

pair are $\tilde{t}_{exp} \sim 30$ s, $\tilde{t}_{img} \sim 20$ s, and $\tilde{t}_{PIV} \sim 60$ s, which for $n_{tot}^{pair} = 20$ results in a total time $t^* \sim 30$ min to run one set of parameters.

D.   Frame rate and voltage dependence

The PZT driving voltage U_{pp} appears in the acoustic responses as $p_a \propto U_{pp}$ and $u_y \propto U_{pp}^2$. The latter is clear from eqn (3c) and the fact that $E_{ac} \propto p_a^2$. Therefore, U_{pp} has a decisive influence of which frame rate to choose for the μPIV analysis. The dependence of the acoustophoretic velocity u on U_{pp} was evaluated for the three frequencies $f = 1.940$ MHz, 1.951 MHz, and 1.968 MHz, each identified as a local maximum of u in the recorded frequency spectrum at $T = 25\,°C$. The maximum allowed driving voltage U_{pp}^{max} was limited by the maximum camera frame rate of 800 Hz at the chosen image size. For each frequency, U_{pp}^{max} was adjusted to obtain the optimal tracer particle displacement shown in Fig. 5(a), and then the

acoustophoretic velocity field was acquired for seven driving voltages ranging from zero to U_{pp}^{max}.

From the analyses of the three resonance frequencies it was verified that the acoustophoretic velocity scales by U_{pp} to the power of 2. For each frequency, the measured data points $\|\boldsymbol{u}\|$ were fitted to a power law $(U_{pp})^\alpha$ resulting in $\alpha = 1.7$, 2.1 and 2.0, respectively (data not shown). Fitting instead the measured maximum speed u_{max} yielded the same behavior with a distribution of the power ranging from 1.87 to 2.09. These results agree well with the findings in ref. [20].

E.   Comparing μPIV with particle tracking

The μPIV analysis of the acoustophoretic velocity field was validated further by comparing estimates of the one-dimensional acoustic energy density E_{ac} obtained by the μPIV method developed in this work to our previously reported particle tracking method developed in ref. 20. This comparison is carried

out for the resonance mode at $f = 1.968$ MHz at $T = 25\,°C$, which is nearly a straight 1D resonance within the channel-center single-image frame of Fig. 4.

By μPIV analysis with $n_{tot}^{pair} = 100$ we obtained the acousto-phoretic velocity field $\boldsymbol{u}(x, y)$, the magnitude of which is shown as the color plot in Fig. 7(a). As it is a nearly perfect 1D transverse standing wave, it is meaningful to calculate the x-direction-average $\langle u_y \rangle_x$ of the y-component u_y of $\boldsymbol{u}(x, y)$,

$$\langle u_y \rangle_x = \frac{1}{N} \sum_{n=1}^{N} u_y(x_n, y_m), \tag{8}$$

which is a function of the transverse grid coordinate y_m. In Fig. 7 (b), the analytical expression (4) for $u_y(y)$ (blue dashed line) is fitted to the values at y_m of $\langle u_y \rangle_x$ (red circles) using the acoustic energy density E_{ac} and half wavelength $\lambda/2$ as fitting parameters. The fit is good and results in $E_{ac} = (98.0 \pm 1.1)$ J m^{-3} and $\lambda_y/2 = (374.0 \pm 1.5)$ μm, where the latter is close to the channel width $w = 377$ μm.
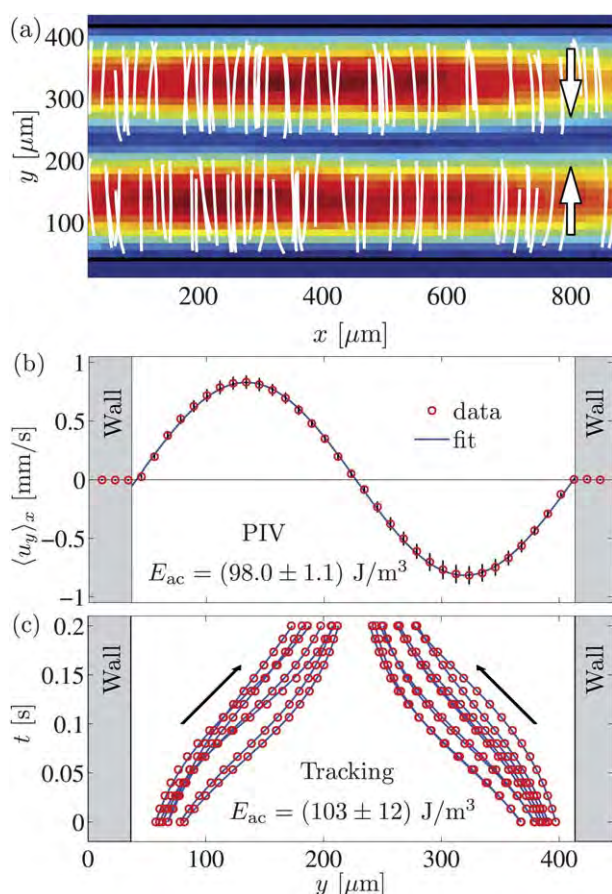
Fig. 7 (a) Acoustophoretic velocity field $\boldsymbol{u}(x, y)$ (arrow plot) and its magnitude (color plot from 0 μm s^{-1} (dark blue) to 900 μm s^{-1} (dark red)) at the channel center for temperature $T = 25\,°C$, driving frequency $f = 1.968$ MHz, and driving voltage $U_{pp} = 1.89$ V. Also shown are 100 particle tracks (white) used to extract the acoustic energy density E_{ac} by the tracking method.[20] (b) Plot of the x-averaged y-component $\langle u_y \rangle_x$ (data: red circles; fit: blue line, standard deviations: black lines) of the acoustophoretic velocity field shown in panel (a). (c) Plot of the trans-verse path $y(t)$ (red circles, only every second data point is shown) and corresponding fit (eqn (5), blue lines) for 16 of the 100 microbead tracks.

To perform particle tracking, 10 additional focus experiments with the same settings as above were carried out. From these, the transverse $y(t)$ component of 100 particle tracks were extracted, see white lines in Fig. 7(a). Using our previously developed method ref. 20, each particle track was fitted to eqn (5) for $y(t)$, and E_{ac} and $\lambda_y/2$ were extracted as the fitting parameters leading to the acoustic energy density $E_{ac} = (103 \pm 12)$ J m^{-3} and the half-wavelength $\lambda_y/2 = (382 \pm 27)$ μm. In Fig. 7(c) are shown 16 of the 100 tracks including the fitting curves.

The resonance parameters determined independently from the μPIV method and the particle tracking method are in good agreement with relative deviations less than 5%. We note that our new μPIV method allows for improved and faster statistics, and thus in general will lead to better results compared to the particle tracking method.

V. Stability and reproducibility of μPIV with temperature control

In the following we characterize the temperature control described in Section III A by performing stability and repro-ducibility tests *versus* frequency. In all the μPIV analyses we use $S = 64$ pixel and $n_{tot}^{pair} = 20$ repeats.

A. Fixed frequency

In order to obtain reliable data, the setup has to be state-dependent and reproducible without hysteresis effects. In Fig. 8 is shown a short-term temperature stability test, where the resonator temperature is toggled between 20 °C (panels (a) and (c)) and 25 °C (panels (b) and (d)) for the fixed frequency $f = 1.963$ MHz and driving voltage $U_{pp} = 1.8$ V. The time between the experiments of same temperature is approximately two hours. The acoustophoretic velocity field $\boldsymbol{u}$ is indeed seen to be reliably state dependent on the resonator temperature with an relative error $\|\boldsymbol{u}_2 - \boldsymbol{u}_1\|/\|\boldsymbol{u}_1\| \approx 7\%$ between two measurements at the same temperature performed two hours apart.

B. Frequency scan

The temperature and frequency dependence of the acousto-phoretic velocity was studied within the channel-center single-image frame for actuation frequencies in the range from 1.930 kHz to 1.980 kHz in steps of 1 kHz. The frequency spec-trum was scanned at three constant temperatures $T = 23\,°C$, $25\,°C$, and $27\,°C$, and the spectrum at $25\,°C$ was re-evaluated two days later to validate the reproducibility of the system, see Fig. 9.

As described in Section 4.4, for each setting of f and T we tune the transducer voltage U_{pp} to a value leading to the optimum pixel displacement in the μPIV analysis shown in Fig. 5(a). In Fig. 9(a) we plot the measured values of U_{pp} *versus* frequency f for the three selected temperatures. Together with the U_{pp}-square scaling of the acoustophoretic velocity, we can use this curve to calibrate for the different voltage amplitudes at the different measurements. This calibration has been performed in Fig. 9(b), where we plot the normalized area-average speed $\left(\frac{1V}{U_{pp}}\right)^2 \|\boldsymbol{u}\|$, such that all values correspond to $U_{pp} = 1$ V and the maximum value in the plot is unity (for $T = 27\,°C$ and $f = 1.967$ MHz). The
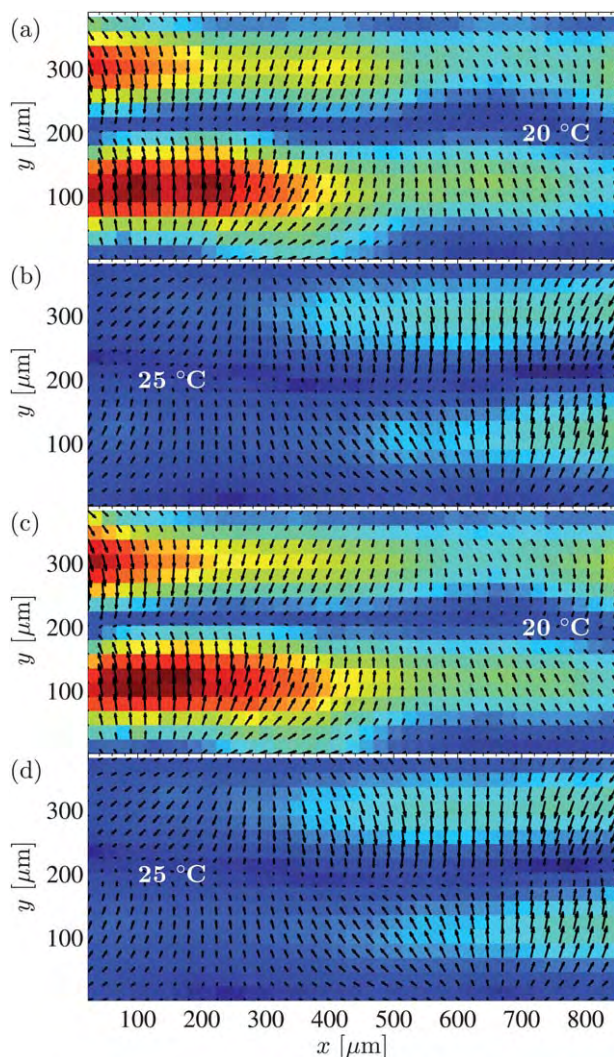
Fig. 8 Temperature stability of the experimental setup at $f = 1.963$ MHz and $U_{pp} = 1.8$ V illustrated by the acoustophoretic velocity field $\boldsymbol{u}(x_n, y_m)$ (arrows) and its magnitude $u(x_n, y_m)$ [color plot from 0 µm s^{-1} (dark blue) to 250 µm s^{-1} (dark red)] in four consecutive measurements at the channel-center single-image frame at temperature (a) $T = 20$ °C, (b) 25 °C, (c) 20 °C, and (d) 25 °C. The average relative error $\|\boldsymbol{u}_2 - \boldsymbol{u}_1\|/\|\boldsymbol{u}_1\| \approx 7\%$ between two measurements at the same temperature performed one hour apart.

recording time of each spectrum is ~ 6 h, but in spite of this long time interval, the moving-average standard deviation $\Delta(\boldsymbol{u}, \langle\boldsymbol{u}\rangle_{mov})$ is only of the order of 5% (the size of the point symbols) in agreement with Fig. 5(b). Moreover, the relative difference between the day-1 and the day-3 spectrum at 25 °C is also only about 5%.

In the frequency dependence of $\|\boldsymbol{u}\|$, we observe three peaks at the frequencies $f = 1.940$ MHz, 1.951 MHz, and 1.968 MHz. Measuring the shift in Lorentzian peaks fitted to the data points, the temperature sensitivity $\Delta f/\Delta T$ of the resonance frequency of the 1.940-MHz-peak is found to be ≈ 1.25 kHz °C^{-1}, for the 1.951-MHz-peak ≈ 1.0 kHz °C^{-1}, and for the 1.968-MHz-peak ≈ 0.0 kHz °C^{-1}. These temperature-induced shifts of the resonance frequencies depend on the spatial distribution of the resonance mode in the full 3D structure of the system and the temperature coefficients of the system materials, and they are therefore difficult
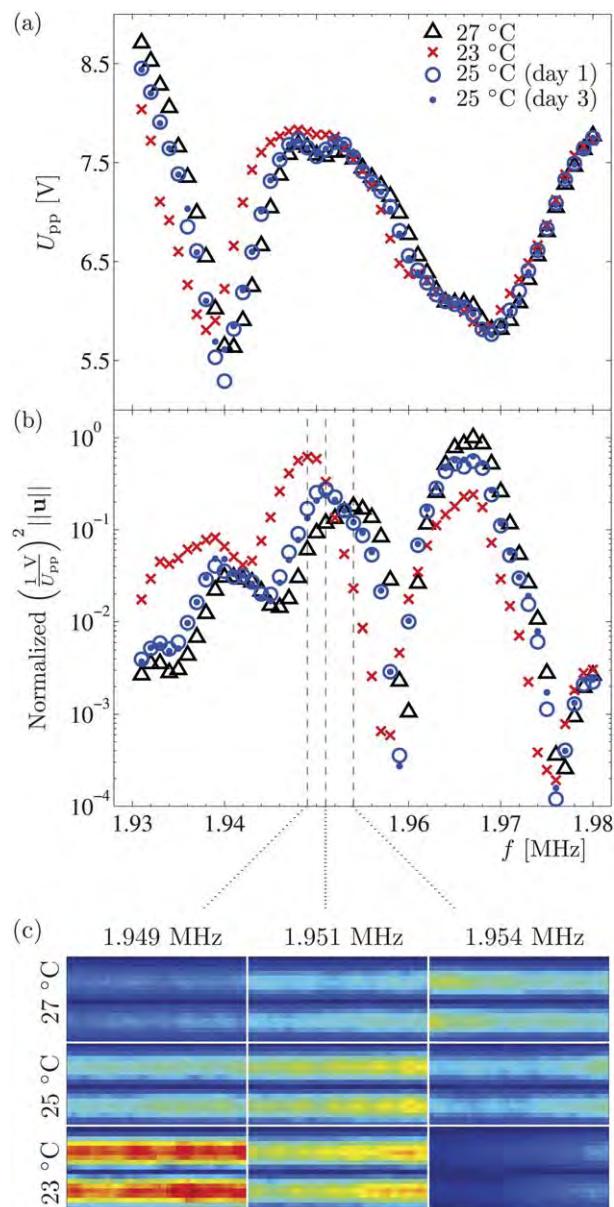

Fig. 9 Frequency dependence in the channel-center single-image frame. (a) The measured value of the transducer voltage U_{pp} *versus* frequency f used to maintain the particular maximum microbead velocity which leads to the optimal maximum pixel displacement in the µPIV analysis, see Fig. 5(a), at temperatures $T = 23$ °C (red ×), 25 °C (blue ○ for day 1, blue ● for day 3), and 27 °C (black △). (b) Semi-logarithmic plot of the area-averaged acoustophoretic speed $\left(\frac{1V}{U_{pp}}\right)^2 \|\boldsymbol{u}\|$ *versus* f normalized to unity at $f = 1.967$ MHz and $T = 27$ °C. All data points are calibrated to correspond to $U_{pp} = 1$ V by use of panel (a) and the $(U_{pp})^2$-dependence. (c) Color plot of the velocity magnitude (dark blue 0 mm s^{-1}, dark red 0.12 mm s^{-1}) normalized to $U_{pp} = 1$ V as in the previous panel for 3×3 temperature and frequency values near the 1.951-MHz resonance.

to determine, even using numerical simulation. However, the measured sensitivities are the right order of magnitude given the following estimates: If we assume that the entire mode is confined in the water, then from $f(T) = c_{wa}(T)/(2w)$ and the table values of $c_{wa}(T)$ we find $\Delta f/\Delta T \approx 3.5$ kHz °C^{-1}, while the sensitivity for

pyrex given $f(T) = c_{py}(T)/(2W)$ is $\Delta f/\Delta T \approx 0.1$ kHz °C^{-1} (for longitudinal waves).

C. Global spatial scan

After fixing the µPIV parameters using the above local analysis of the center-channel single-image frame, we now return to the global spatial scan of Fig. 4 for the three resonance frequencies $f = 1.940$ MHz, 1.951 MHz, and 1.968 MHz. A single frame is 0.85 mm long and thus only covers about 2.5% of the 35 mm long microchannel, whereas the 15 consecutive of Fig. 4(b) cover a length of 12 mm or about 34% of the microchannel.

It is striking that in this highly symmetric and very simple rectangular geometry with a horizontal inlet and outlet, we have succeeded in generating resonances, which in the 2D top-view appear as acoustophoretic velocity fields $\boldsymbol{u}$ with a mirror symmetry around the centerline in the transverse y-direction resulting in a nearly perfect straight line pressure nodal-line with $\boldsymbol{u} = \boldsymbol{0}$. However, equally clear are the strong variations along the channel axis (x-direction) in the measured $\boldsymbol{u}$-field. Despite the near-perfect geometry, the present data does not exhibit the sinusoidal axial pressure distribution in the resonance predicted by the idealized hard-wall model discussed in ref. 20. The reasons for this may be sought in the walls not being infinitely hard, the asymmetry due to the acoustical differences between the bottom silicon and top pyrex layer, the presence of inlet/outlet tubing, as well as imprecise mounting of the chip, the PZT, and the Peltier element.

To allow for quantitative comparisons between the three resonance modes, we do two things. First, we abandon the normalization used in Fig. 4(b), and instead use the absolute but voltage-calibrated, acoustophoretic velocities $\left(\frac{1\text{V}}{U_{pp}}\right)^2 \boldsymbol{u}$; and second, given the regular behavior in the transverse direction, we introduce the y-direction-average $\langle u \rangle_y$ of the speed $u(x_n, y_m)$,

$$\langle u \rangle_y = \frac{1}{M} \sum_{m=1}^{M} u(x_n, y_m), \tag{9}$$

which is a function of axial coordinate x_n.

In Fig. 10 we plot the voltage-corrected speed $\left(\frac{1\text{V}}{U_{pp}}\right)^2 \langle u \rangle_y$ versus axial position x for each of the three resonance frequencies at $T = 25$ °C. It is clear that globally the 1.940-MHz-mode (blue) leads to the highest acoustophoretic velocity, followed by 1.968 MHz (red), and 1.951 MHz (black) being lowest. Counting local maxima, the 1.940-MHz-mode (blue) has two peaks (at −4.8 mm and 3.6 mm), the 1.951-MHz-mode (black) three (at −2.8 mm, 0.8 mm and 4.6 mm), and the 1.968-MHz-mode (red) four (at −5.2 mm, −2.2 mm, 0 mm, and > 6 mm).

The global strengths of the resonance modes, expressed as the voltage corrected average transverse particle speed, can be characterized by the average $\sum(f) = \left(\frac{1\text{V}}{U_{pp}}\right)^2 \int_\Omega \langle u(f) \rangle_y \mathrm{d}x/(12 \text{ mm})$, where Ω is the interval −6 mm < x < 6 mm. For the three modes we obtain $\Sigma(1.940 \text{ MHz}) = 51$ µm s^{-1}, $\Sigma(1.951 \text{ MHz}) = 29$ µm s^{-1}, and $\Sigma(1.968 \text{ MHz}) = 22$ µm s^{-1}.
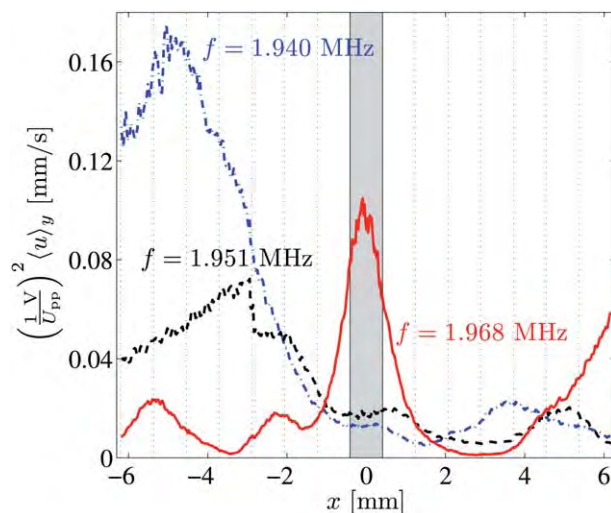

Fig. 10 The y-direction-average $\langle u \rangle_y$ of eqn (9) plotted as function of the axial position x along the 12-mm channel section shown in Fig. 4 for the three resonance frequencies $f = 1.940$ kHz (dash-dotted blue line), 1.951 kHz (dashed black line), and 1.968 kHz (solid red line) at $T = 25$ °C. The borders between the 15 neighboring image frames are marked by vertical dashed black lines (white dashed lines in Fig. 4(a and b)). The channel-center single-image frame is colored light gray. The discontinuity at the fourth border ($x = -2.8$ mm) is due to a glitch we could not compensate for when switching frame rates.

If we restrict ourselves to observe the image frame in the center of the channel (gray box), we now find that the 1.940-MHz-mode (blue) is the weakest. Moreover, if we in this single frame let the frequency increase from 1.940 MHz to 1.968 MHz, we see how the magnitude of the subsequent resonances increases. This is the spatial structure of the resonances corresponding to the frequency spectra in Fig. 9(b), where the normalized area-average speed increases from 0.05, via 0.3 to 0.6 for the three respective frequencies. This observation confirms our conjecture in ref. 20 about the dependence of the locally determined energy density on the spatial structure of the resonance modes.

VI. Application example: focusing efficiency during flow

While the stop-flow mode with time-gated ultrasound actuation at zero flow rate is well suited for characterization of our setup, it is the continuous-flow mode with continuous ultrasound actuation at non-zero flow rate that most often is used in applications. In the following we therefore study the connection between these modes of operation.

The flow focusing efficiency can be characterized by the magnitude of the PZT actuation voltage U_{pp} needed to exactly focus the tracer particles transversely near the outlet of the channel. At this condition the axial transit time equals the transverse focus time, and this special time we denote τ. At the given flow rate of the experiment, $Q = 0.1$ mL min$^{-1} = 1.67 \times 10^{-9}$ m^3 s^{-1}, we obtain $\tau = wLh/Q = 1.24$ s from the channel volume and flow rate. If the special focus condition is obtained by the voltage U_{pp}, a theoretical measure of the focus efficiency

can be defined as the voltage-corrected, transverse, average acoustophoretic velocity

$$\langle u_y \rangle = \left(\frac{1\text{V}}{U_{\text{pp}}}\right)^2 \frac{w}{2} \frac{1}{\tau} = \left(\frac{1\text{V}}{U_{\text{pp}}}\right)^2 0.15 \frac{\text{mm}}{\text{s}}. \quad (10)$$

In Fig. 11(a) the measured voltage U_{pp} required to focus particles to a predefined region 5 mm before the outlet is plotted *versus* frequency f at the two temperatures $T = 23\,°\text{C}$ (red points) and $25\,°\text{C}$ (blue points). Based on these data and the definition in eqn (10), we plot in Fig. 11(b) the focus efficiency $\langle u_y \rangle$ *versus* f for the same two temperatures. In agreement with the global stop-flow measurements in Fig. 10, the continuous flow measurements also reveal resonance peaks at the three frequencies $f = 1.940$ MHz, 1.951 MHz, and 1.968 MHz. The values of the focus efficiency at the three resonance frequencies are 105 μm s^{-1}, 32 μm s^{-1}, and 47 μm s^{-1}, respectively. These continuous-flow values are in the same order of magnitude as the respective stop-flow resonance strengths $\Sigma(f) = 51$ μm s^{-1}, 29 μm s^{-1}, and 22 μm s^{-1} obtained in Section V C, but about a factor of 2 larger, as the latter was obtained for one third of the channel length.

Finally, we note that the globally measured shift in resonance frequencies in Fig. 11(b) due to temperature is approximately 2 kHz °C^{-1} which is in agreement with the local velocity measurements of Fig. 9. Notably, the peak at $f = 1.968$ MHz is not significantly shifted in any of the experiments. We have thus established a direct and consistent connection between the stop-flow mode and continuous-flow mode acoustophoretic measurements.

VII. Discussion

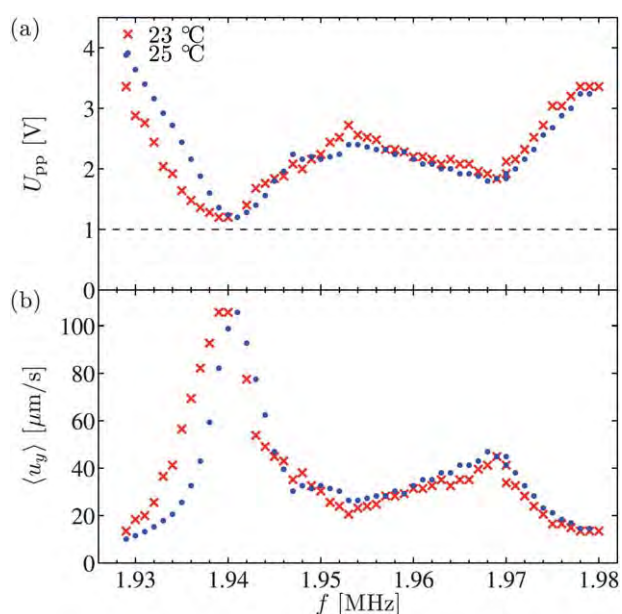We have presented an automated and temperature-controlled experimental platform for characterization of microchannel

Fig. 11 (a) The measured voltage U_{pp} required to focus particles to a predefined region 5 mm before the outlet of the microchannel ($x = 30$ mm), at an average axial speed $\langle u_x \rangle \approx 0.03$ m s^{-1}. (b) The focus efficiency $\langle u_y \rangle$ obtained by combining eqn (10) with the data for U_{pp} in panel (a).

acoustophoresis by μPIV. The platform was operated in stop-flow mode.

The high mechanical, thermal, and electronic stability of the platform and the good reproducibility of the measurements provided acoustophoretic velocity data with a spatial resolution of about 20 μm and a relative uncertainty of the velocity measurements of about 5%. The good experimental statistics was enabled by the system automation allowing individual experiments to be repeated 20 to 100 times. The standard deviation of the obtained data can be further reduced, but in practise this is balanced against the time it takes to acquire and analyze the data.

We have demonstrated both short-term stability of the order of 1 h (the time it takes to measure a single frame at a given frequency and temperature), and long-term stability over several days (the time it takes to make multi-frame scans over large sections of the microchannel).

The net total active μPIV experimental time reported in this paper was ∼ 60 h corresponding to approximately 7000 gated ultrasound onsets. Furthermore, automated data transfer, image processing, and μPIV-evaluation of the more than 7000 acquired image pairs was carried out in the subsequent data analysis.

We have further shown that temperature control is the key feature to obtain stable and reproducible resonant ultrasound modes in an acoustophoresis microchannel. For minute temperature changes (∼2 °C), the acoustic resonance peaks are shifted by ∼ 1 kHz/°C. However, a temperature change of 5 °C can lead to a complete change from one resonance mode into another.

In an attempt to capture the global features of some resonant modes it was found that the transverse velocity field varied greatly along the channel. This is indicative of the acoustic resonance having similarities with a box potential. The particle velocity dynamics (> 10-fold) of the system was found to be experimentally very challenging as the quality of the μPIV-analysis benefit from moderate frame-to-frame motion of tracer particles. An iterative scheme was employed, adjusting either camera frame rate or ultrasound intensity to fit the expected velocity magnitude at a certain position.

The large spatial variation in velocity magnitude calls for some concern regarding the strategy that we employed for the frequency spectra data, where a single field of view was evaluated for a range of frequencies. An alternative approach, rather than measuring the resonance peaks in the frequency domain, would be to measure the spatial shifts of the resonant modes. Conversely, spatial shifts of resonances caused by temperature and frequency shifts could give rise to apparent translation of resonance peaks in the frequency domain, which under strict temperature control should be feasible.

The development of our automated μPIV platform has enabled the establishment of a direct and consistent connection between the stop-flow mode and continuous-flow mode acoustophoretic measurements. As the latter essentially is a area-average of the acoustophoretic velocity, the most direct comparisons were conducted on the global stop-flow measurements.

With this work we have advanced acoustophoretic characterization methods considerably since our automated μPIV method leads to more accurate and rapid determination of the local

acoustic energy density. We have in the present work been able to confirm the conjecture in our former work on how the locally determined energy density depends on the spatial structure of the resonance modes.

The complexity of the acoustic resonance patterns in this type of resonator requires further studies of the frequency, temperature, and spatial domain. This vast parameter space calls not only for automation, but also, predictive models are needed to better understand acoustophoresis. In this work we have pinpointed some of the minimum requirements on an experimental approach for detailed measurements and analysis of microchannel acoustophoresis.

VIII. Conclusions

Long-term, reproducible, and quantitative assessment of acoustic standing wave forces in microchannels has to a very limited degree been reported in the literature. This paper outlines an effort to standardize the characterization of microchannels intended for acoustophoresis, and an optimized μPIV setup and its use as a powerful analytical tool to high resolution characterization of the acoustophoretic properties of microchannels is reported.

The obtained high accuracy μPIV data allows for in-depth analysis of the influence of systemic parameters on the acoustophoresis performance such as temperature and we propose a normalized measure to describe acoustophoresis channels in terms of its ability to focus particles in continuous flow. The importance of analyzing system response to the actuation frequency in relation to the employed PZT voltage is highlighted, and most importantly we demonstrate the strong dependence of the obtained microchannel resonances with respect to temperature, which calls for a strict temperature control in all acoustophoresis systems of analytical grade.

Based on these developments we now anticipate the use of this system as a standard tool to normalize the performance of different microchannels as well as to decouple other forces acting on particles/cells in the primary acoustic standing wave field. Most importantly, the μPIV system will enable the measurement of fundamental acoustophysical properties such as acoustophoretic mobility of different particle and cell species in various buffer systems. We will continue to build on the interplay between experiment and theoretical predictions such that we can broaden the understanding of the critical system parameters in acoustofluidics and hence facilitate an engineering-based computational approach to acoustophoresis system design.

Acknowledgements

References

1 J. Hawkes, D. Barrow, J. Cefai and W. Coakley, *Ultrasonics*, 1998, **36**, 901–903.
2 J. J. Hawkes and W. T. Coakley, *Sens. Actuators, B*, 2001, **75**, 213–222.
3 N. R. Harris, M. Hill, S. Beeby, Y. Shen, N. M. White, J. J. Hawkes and W. T. Coakley, *Sens. Actuators, B*, 2003, **95**, 425–434.
4 A. Nilsson, F. Petersson, H. Jönsson and T. Laurell, *Lab Chip*, 2004, **4**, 131–5.
5 F. Petersson, A. Nilsson, C. Holm, H. Jönsson and T. Laurell, *Analyst*, 2004, **129**, 938–43.
6 P. Augustsson, J. Persson, S. Ekström, M. Ohlin and T. Laurell, *Lab Chip*, 2009, **9**, 810–818.
7 C. Grenvall, P. Augustsson, J. R. Folkenberg and T. Laurell, *Anal. Chem.*, 2009, **81**, 6195–6200.
8 P. Thevoz, J. D. Adams, H. Shea, H. Bruus and H. T. Soh, *Anal. Chem.*, 2010, **82**, 3094–3098.
9 J. Shi, D. Ahmed, X. Mao, S.-C. S. Lin, A. Lawit and T. J. Huang, *Lab Chip*, 2009, **9**, 2890–2895.
10 T. Franke, S. Braunmueller, L. Schmid, A. Wixforth and D. A. Weitz, *Lab Chip*, 2010, **10**, 789–794.
11 G. T. Haar and S. Wyard, *Ultrasound Med. Biol.*, 1978, **4**, 111–123.
12 R. J. Townsend, M. Hill, N. R. Harris and N. M. White, *Ultrasonics*, 2004, **42**, 319–324.
13 S. M. Hagsäter, T. G. Jensen, H. Bruus and J. P. Kutter, *Lab Chip*, 2007, **7**, 1336–1344.
14 S. M. Hagsäter, A. Lenshof, P. Skafte-Pedersen, J. P. Kutter, T. Laurell and H. Bruus, *Lab Chip*, 2008, **8**, 1178–1184.
15 J. Shi, H. Huang, Z. Stratton, Y. Huang and T. J. Huang, *Lab Chip*, 2009, **9**, 3354–3359.
16 O. Manneberg, J. Svennebring, H. M. Hertz and M. Wiklund, *J. Micromech. Microeng.*, 2008, **18**, 095025.
17 O. Manneberg, B. Vanherberghen, B. Onfelt and M. Wiklund, *Lab Chip*, 2009, **9**, 833–837.
18 J. D. Adams, P. Thevoz, H. Bruus and H. T. Soh, *Appl. Phys. Lett.*, 2009, **95**, 254103–1.
19 P. Augustsson, R. Barnkob, C. Grenvall, T. Deierborg, P. Brundin, H. Bruus and T. Laurell, *Proc. 14th MicroTAS*, 3–7 October 2010, Groningen, The Netherlands, 2010, pp. 1337–39.
20 R. Barnkob, P. Augustsson, T. Laurell and H. Bruus, *Lab Chip*, 2010, **10**, 563–570.
21 L. P. Gorkov, *Soviet Physics - Doklady*, 1962, **6**, 773–775.
22 J. Lighthill, *Waves in Fluids*, Cambridge University Press, 2002.
23 A. D. Pierce, *Acoustics*, Acoustical Society of America, Woodbury, 1991.
24 H. Bruus, *Theoretical Microfluidics*, Oxford University Press, Oxford, 2008.
25 J. Santiago, S. Wereley, C. Meinhart, D. Beebe and R. Adrian, *Exp. Fluids*, 1998, **25**, 316–319.
26 R. Adrian, *Exp. Fluids*, 2005, **39**, 159–169.
27 M. Raffel, C. E. Willert, S. T. Wereley and J. Kompenhans, *Particle Image Velocimetry*, Springer, 2007.
28 R. Lindken, M. Rossi, S. Grosse and J. Westerweel, *Lab Chip*, 2009, **9**, 2551–2567.
29 S. T. Wereley and C. D. Meinhart, *Annu. Rev. Fluid Mech.*, 2010, **42**, 557–576.
30 C. Meinhart, S. Wereley and J. Santiago, *J. Fluids Eng.*, 2000, **122**, 285–289.
31 R. Adrian, *Appl. Opt.*, 1986, **25**, 3855–3858.

Paper published in Lab on a Chip, March 2012

PAPER

Measuring acoustic energy density in microchannel acoustophoresis using a simple and rapid light-intensity method†

Rune Barnkob,*[a] Ida Iranmanesh,[b] Martin Wiklund[b] and Henrik Bruus[a]

We present a simple and rapid method for measuring the acoustic energy density in microchannel acoustophoresis based on light-intensity measurements of a suspension of particles. The method relies on the assumption that each particle in the suspension undergoes single-particle acoustophoresis. It is validated by the single-particle tracking method, and we show by proper re-scaling that the re-scaled light intensity plotted *versus* re-scaled time falls on a universal curve. The method allows for analysis of moderate-resolution images in the concentration range encountered in typical experiments, and it is an attractive alternative to particle tracking and particle image velocimetry for quantifying acoustophoretic performance in microchannels.

I. Introduction

Acoustofluidics and ultrasound handling of particle suspensions is a research field in rapid growth both concerning physical characterization and optimization of the devices as well as biological applications.[1,2] When designing a microchip for microchannel acoustophoresis, the acoustic energy density inside the microchannel is an important parameter. For example, the energy density scales the acoustic radiation forces acting on suspended particles or cells and can therefore be used as a figure of merit of the acoustophoretic performance. However, it is neither straightforward to theoretically predict, nor experimentally determine the energy density in the microchannel. The acoustic power sent from the transducer to the microchannel is subject to losses from thermal dissipation and acoustic radiation, making it difficult to predict the acoustic energies inside the microchannel from a given input power of the actuating transducer. Moreover, it is difficult to model the exact actuated acoustic resonance and therefore difficult to predict the distribution of energy between the microchannel and the surrounding microchip.

Existing techniques for measuring the acoustic energy density (or acoustic pressure amplitude) mostly rely on external electric[3] or gravitational[4,5] forces. However, based on the acoustophoretic alignment of particles advected along a microchannel, Wiklund *et al.*[6] estimated the acoustic pressure amplitude using the advection length and advection time needed to align the particles, and Barnkob *et al.*[7] measured the acoustic energy

density relying solely on the acoustophoretic motion of the particles. The latter method based on single-particle tracking is particularly suited for low particle concentrations and provides an important step in measuring compressibilities of individual cells using acoustophoresis.[8–10] Later, Augustsson *et al.*[11] used acoustophoretic velocity fields measured by micro-particle-image velocimetry (micro-PIV) to determine the energy density as function of position across an entire microscope field of view with a relative uncertainty of less than 2%. Although these methods each have their individual strengths, there exists none for simple and rapid determination of the acoustic energy density.

In this work we present a simple, rapid and inexpensive light-intensity-based method for measuring the acoustic energy density E_{ac} in microchannel acoustophoresis with the primary motive to characterize the performance of an acoustophoresis microchip. The measured light intensity originates from trans-illumination light microscopy operated at moderate resolution. The theoretical foundation and an experimental realization of the method are described, and the method is validated by comparing the measured E_{ac} with that obtained by the single-particle tracking method.[7] Furthermore, the new method yields the expected scaling of E_{ac} with the applied piezo transducer voltage to the power 2. Also, it is shown theoretically that by proper re-scaling, the re-scaled intensity plotted *versus* re-scaled time should fall on a universal curve. This universality is successfully tested experimentally. We end by discussing the limitations of the method.

II. Single-particle theory

We study a glass–silicon–glass chip containing an optically transparent microchannel filled with a particle suspension, as described in more detail in Section V. The channel is illuminated from the top, and the transmitted light is recorded by a CCD

[a]*Department of Micro- and Nanotechnology, Technical University of Denmark DTU Nanotech Building 345 East, DK-2800, Kongens Lyngby, Denmark. E-mail: barnkob@alumni.dtu.dk*
[b]*Department of Applied Physics, Royal Institute of Technology, AlbaNova University Center, SE-106 91, Stockholm, Sweden*
† Electronic supplementary information (ESI) available. See DOI: 10.1039/c2lc40120g/

camera mounted on a mid-range microscope using a low-numerical-aperture objective (N.A. = 0.25, focal depth ≈ 10 μm). The particles appear as blurred black/gray spots covering about 10 pixels on the resulting images. The microchip is ultrasonically actuated by attaching a piezo transducer to the chip and driving it with a voltage U_{pp} at MHz frequencies. The ultrasound actuation induces a time-harmonic pressure field $p_1 \exp(-i\omega t)$ and oscillation velocity field $\boldsymbol{v}_1 \exp(-i\omega t)$, where we use the complex time-harmonic notation and where ω is the angular frequency. The viscosity of the suspension is negligible for the acoustic waves in this work, and the pressure and velocity fields in the microchannel are governed by the linear acoustic Helmholtz wave equation of inviscid fluids. By proper tuning of the applied frequency to a resonance frequency of the system, the acoustic fields become so strong that they can be used for manipulation of the particles suspended in the liquid.

The particle solutions are dilute enough that the particle–particle interactions are negligible (less than 10^{15} particles/m^3 to avoid hydrodynamic particle–particle interaction effects[12]), and thus only single-particle physics is relevant. This comprises the acoustic radiation force acting on suspended particles, due to particle-wave scattering, and viscous drag from acoustic streaming of the carrier liquid. Both these effects are time-averaged second-order effects arising from products of the first-order fields. This work is restricted to large 5-μm-diameter particles for which the acoustic radiation force dominates and the acoustic streaming is negligible.[7,13]

A. Microchannel single-particle acoustophoresis

Consider a single spherical particle of radius a, density ρ_p, and compressibility κ_p suspended in a liquid of density ρ_0 and compressibility κ_0. In terms of the acoustic pressure p_1 and the oscillation velocity v_1 at the position of the particle, and given that a is much smaller than the acoustic wavelength λ, the time-averaged acoustic radiation force $\boldsymbol{F}^{\mathrm{rad}}$ on the particle neglecting viscosity is[14,15]

$$\boldsymbol{F}^{\mathrm{rad}} = -V \left[\frac{f_1}{2} \kappa_0 \nabla \langle p_1^2 \rangle - \frac{3 f_2}{4} \rho_0 \nabla \langle v_1^2 \rangle \right], \qquad (1)$$

where $f_1 = 1 - \tilde{\kappa}$ and $f_2 = (2\tilde{\rho} - 2)/(2\tilde{\rho} + 1)$ in terms of the compressibility ratio $\tilde{\kappa} = \kappa_p / \kappa_0$ and the density ratio $\tilde{\rho} = \rho_p / \rho_0$. For a transverse acoustic wave $p = p_a \cos(ky)$ of wavenumber $k = 2\pi/\lambda = \pi/w$, such that the wavelength is twice the channel width, $\lambda = 2w$, the above expression reduces to the y component[16]

$$F^{\mathrm{rad}} = 4\pi^2 \Phi \frac{a^3}{w} E_{\mathrm{ac}} \sin\left(2\frac{\pi}{w}y\right), \qquad (2)$$

where E_{ac} is the time-averaged acoustic energy density and $\Phi = f_1/3 + f_2/2$ is the acoustic contrast factor.

In this work we only study such a transverse half-wave resonance, and we always have $\Phi > 0$. As a result, the radiation force is directed towards the channel center, and particles, which initially are homogeneously distributed in the microchannel as shown in Fig. 1(a), are pushed towards the vertical center plane at $y = w/2$ as shown in Fig. 1(b), where ideally they all end up.
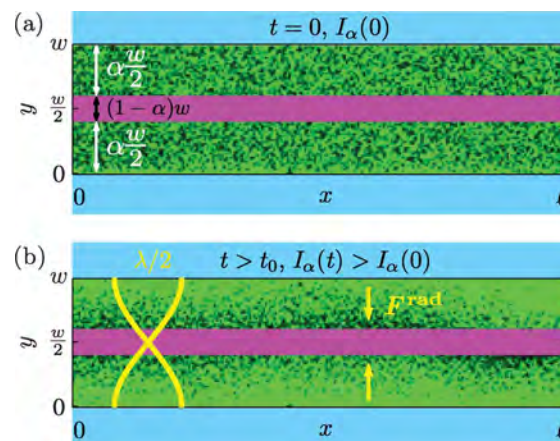

Fig. 1 Bottom-view of the straight acoustophoresis microchannel (light blue walls) of width w and length ℓ. The microchannel containing a suspension of 5-μm-diameter polyamide microbeads (black/gray dots) is illuminated from the top, resulting in a green background in the image. The particle motion is only recorded outside a band of relative width $1 - \alpha$ (magenta) along the channel center $y = w/2$, as the particle concentration outside this band remains sufficiently low throughout the entire acoustophoretic focusing process. (a) At time $t = 0$ the microbeads are homogeneously distributed throughout the channel and the light intensity of the image is $I_\alpha(0)$. (b) The microchannel is acoustically actuated in its transverse half-wave resonance (yellow) and the acoustic radiation force (yellow arrows) pushes the suspended particles to the acoustic pressure node at the vertical center plane at $y = w/2$. As the particles gradually leave the interrogation area (green) and enter the excluded band along the center plane, the light intensity of the image increases monotonically, $I_\alpha(t) > I_\alpha(0)$.

B. Transverse acoustophoretic single-particle path

Given the transverse half-wave resonance, an analytical expression for the transverse path $y(y_0, t)$ of a particle starting at y_0 at time $t = 0$ can be derived by balancing F^{rad} with the viscous Stokes drag[7,17]

$$y(y_0, t) = \frac{w}{\pi} \arctan\left[\tan\left(\pi \frac{y_0}{w}\right) \exp\left(\frac{t}{t^*}\right)\right], \qquad (3a)$$

$$t^* = \frac{3\eta}{4\Phi(\pi a/w)^2} \frac{1}{E_{\mathrm{ac}}}, \qquad (3b)$$

where η is the viscosity of the carrier liquid, and where we have introduced the characteristic time scale t^*, which is inversely proportional to the acoustic energy density E_{ac}. Here, using a channel of height $h = 110$ μm and particles with diameter $2a = 4.5$ μm, the wall-induced drag enhancement has been neglected, because for particles at half the height in the channel the classic Faxén enhancement factor[18,19] is $1/[1 - 1.004(2a/h)] = 1.043$, while at a quarter of the height it is $1/[1 - 0.6526(4a/h)] = 1.056$, both deviating less than 6% from unity. However, for more shallow channels the wall-induced drag enhancement may be significant.[20] In ref. 7 E_{ac} was determined as a fitting parameter by fitting eqn (3a) to the measured paths obtained by single-particle tracking. In Fig. 2 the transverse particle path $y(y_0, t)$ is plotted as a function of normalized time t/t^* for three different starting positions y_0, keeping all other parameters fixed.

Inverting eqn (3a), we obtain as in ref. 7 and 21 the time t it takes a particle to move from any initial position $0 < y_0 < w/2$ to
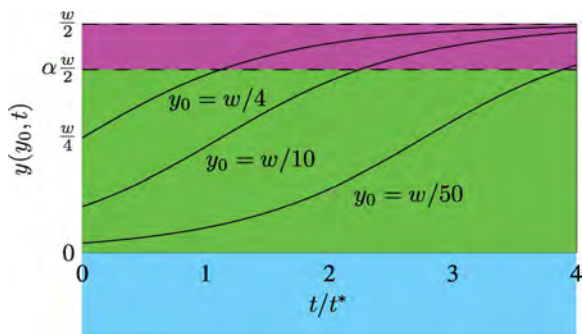
Fig. 2 Transverse particle path $y(y_0, t)$, eqn (3a), as function of normalized time t/t^*, eqn (3b). For given fixed parameters, the particle paths (black lines) are plotted for three different starting positions y_0. The channel is divided into two regions: the interrogation area of relative width α (green), and the excluded center band of relative width $1 - \alpha$ (magenta).

any final position y at $y_0 < y < w/2$,

$$t(y_0, y) = t^* \ln\left[\frac{\tan\left(\pi\frac{y}{w}\right)}{\tan\left(\pi\frac{y_0}{w}\right)}\right]. \quad (4)$$

III. Many-particle light-intensity model

We analyze a many-particle suspension of 0.35×10^{15} particles/m^3 (see Section VA), which is dilute enough to minimize both hydrodynamic and acoustic particle–particle interactions as well as the effect of overlapping particles located at different heights in the channel. For our system with the particle diameter $2a = 4.5$ μm and channel height $h = 110$ μm, the threshold particle concentration C^* for particle overlapping is when exactly one particle occupies the cylindrical volume of base area πa^2 and height h, $C^* = 1/(\pi a^2 h) = 0.6 \times 10^{15}$ m^{-3}, which is half of the threshold value mentioned above for particle–particle interactions. Consequently, we assume that each particle undergoes single-particle acoustophoresis as described in the previous section. To ensure that this single-particle description is valid in our analysis, we only study the particle motion in the interrogation area of relative width α (green in Fig. 1 and 2) away from the channel center, while we exclude the region of relative width $1 - \alpha$ (magenta) along the center line, where the particle concentration eventually becomes very large as all the particles end up accumulating there. In this work we found $\alpha = 0.8$ to be a good value and have used it throughout the analysis.

As illustrated in Fig. 1, all our images are bottom views of the microchannel (light blue walls). Depending on the presence of a particle, each pixel in a given image of the microchannel has a dimensionless gray-scale pixel intensity ranging from 0 (black) to 255 (white). Summing over all pixels in a given image, we obtain the total pixel intensity I_α. If no particles are present in the interrogation area of relative width α, the light intensity (green) is $I_\alpha^{\max}$. However, at $t = 0$ there are N_0 homogeneously distributed particles present in the interrogation area, Fig. 1 (a), and these give rise to a relative intensity reduction R ranging from zero to unity, such that the initial intensity can be written as $I_\alpha(0) = (1 - R)I_\alpha^{\max}$. When the microchannel is ultrasonically actuated, Fig. 1

(b), the particles move towards and into the excluded center-region. Each time a particle enters the excluded region, the number $N_\alpha(t)$ of particles left inside the interrogation area decreases by unity, and the light intensity I_α increases correspondingly. This can be expressed as

$$I_\alpha(t) = \left[1 - R\frac{N_\alpha(t)}{N_0}\right]I_\alpha^{\max}. \quad (5)$$

At time $t = \infty$ there are zero particles left in the interrogation area, $N_\alpha(\infty) = 0$, and $I_\alpha(\infty) = I_\alpha^{\max}$.

The time it takes the ith particle to move from its starting position $y_0^{(i)}$ to the excluded area at $y = \alpha w/2$ is called $\tau_\alpha(y_0^{(i)})$, and at this time its contribution to $N_\alpha(t)$ drops from unity to zero. Mathematically, this is expressed through the Heaviside step function $\Theta[\tau_\alpha(y_0^{(i)}) - t]$, which by definition is unity for $t < \tau_\alpha(y_0^{(i)})$, when the particle is visible in the interrogation area, and zero for $t > \tau_\alpha(y_0^{(i)})$, when the particle is inside the excluded region. We can therefore write

$$N_\alpha(t) = \sum_{i=1}^{N_0} \Theta[\tau_\alpha(y_0^{(i)}) - t]. \quad (6)$$

If the initial number N_0 of particles is sufficiently large, typically around 10^4 as in Fig. 1 (a), it is a reasonable approximation to replace the discrete sum in eqn (6) by the ensemble average $\langle N_\alpha(t)\rangle$ defined as the average over a homogeneous distribution of starting positions,

$$\langle N_\alpha(t)\rangle = \frac{2N_0}{\alpha w}\int_0^{\alpha\frac{w}{2}} dy_0\, \Theta[\tau_\alpha(y_0) - t], \quad (7)$$

where we have used the symmetry of the system to integrate over only half the channel width. Using the dilute-limit expression (4), we find that $t < \tau_\alpha(y_0)$ implies that the integrand in eqn (7) is unity in the interval $0 < y_0 < (w/\pi)\arctan[\tan(\pi\alpha/2)e^{-t/t^*}]$ and zero otherwise. Hence we arrive at

$$\langle N_\alpha(t)\rangle = \frac{2N_0}{\alpha\pi}\arctan\left[\tan\left(\frac{\pi}{2}\alpha\right)e^{-t/t^*}\right]. \quad (8)$$

Taking the ensemble average of the light intensity $I_\alpha(t)$ in eqn (5) results in the normalized light intensity,

$$\frac{\langle I_\alpha(t)\rangle}{I_\alpha^{\max}} = 1 - R\frac{\langle N_\alpha(t)\rangle}{N_0}, \quad (9a)$$

$$= 1 - \frac{2R}{\alpha\pi}\arctan\left[\tan\left(\frac{\pi}{2}\alpha\right)e^{-t/t^*}\right]. \quad (9b)$$

This expression is plotted in Fig. 3 as function of time t. In panel (a) the energy density E_{ac} is swept for fixed relative width α of the interrogation area, and it is clear that as the acoustic energy density increases, the suspended particles traverse faster to the channel center and the relative intensity reaches its maximum of unity faster. The opposite situation is shown in panel (b), where the relative width α is swept for fixed E_{ac}. The wider an interrogation area, the slower is the increase in intensity.
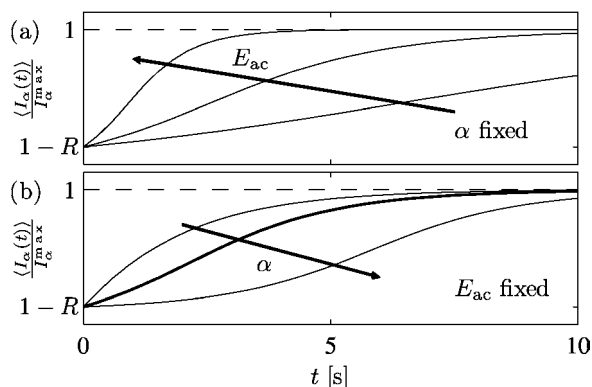
Fig. 3 Example of the normalized light intensity $\langle I_\alpha(t)\rangle/I_\alpha^{max}$, eqn (9a), as function of time t and using the parameters in Table 1. (a) The energy density E_{ac} is swept (1 J/m³, 2.5 J/m³, 7 J/m³) for fixed relative interrogation-area width $\alpha = 0.8$ of the interrogation area, and it is clear that as the acoustic energy density increases, the suspended particles traverse faster to the channel center and the relative intensity reaches is maximum of unity faster. (b) The relative width α is swept (0.3, 0.8, 0.97) for fixed $E_{ac} = 2.5$ J/m³. The wider an interrogation area, the slower is the increase in intensity.

In a given experiment, the observed intensity $I_\alpha(t)$ is identified with the theoretical ensemble average $\langle I_\alpha \rangle$. From eqn (9b) it follows that $I_\alpha(0) \approx \langle I_\alpha(0)\rangle = (1-R)I_\alpha^{max}$ and $I_\alpha(\infty) \approx \langle I_\alpha(\infty)\rangle = I_\alpha^{max}$. Hence, the relative intensity reduction R can be estimated from the intensity measurements as

$$R \approx 1 - \frac{I_\alpha(0)}{I_\alpha(\infty)}. \tag{10}$$

Once R is known, the characteristic time t^* can be found as a fitting parameter using eqn (3) to fit measured values $I_\alpha(t)/I_\alpha(\infty)$ versus time t. Then the acoustic energy density can be extracted from eqn (3b) if the material parameters of the microbeads are known.

Finally, the determination of t^* allows for the introduction of the exponentially re-scaled time s given by

$$s = e^{t/t^*}. \tag{11}$$

Rearranging eqn (9b) leads to the prediction that a plot of all data in the form $[1 - I_\alpha/I_\alpha(\infty)]/R$ versus re-scaled time s collapses on a universal curve given by

$$\frac{1}{R}\left[1 - \frac{I_\alpha(s)}{I_\alpha(\infty)}\right] = \frac{2}{\pi\alpha}\arctan\left[\frac{1}{s}\tan\left(\alpha\frac{\pi}{2}\right)\right]. \tag{12}$$

It follows from eqn (9a) that this particular combination of intensities can be interpreted as the relative average number of particles $n_\alpha(s)$ left in the interrogation area,

$$\frac{1}{R}\left[1 - \frac{I_\alpha(s)}{I_\alpha(\infty)}\right] = \frac{\langle N_\alpha\rangle}{N_0} = n_\alpha(s). \tag{13}$$

IV. Intensity method for measuring the acoustic energy density

The presented intensity model can be used to measure the acoustic energy density in situ. The basic idea is to measure the total pixel intensity as function of time and then fit the model described above to the data points using the acoustic energy density as a fitting parameter. The method is easily applied; all that is needed is a movie of the acoustophoretic focusing and the following algorithm:

1. Turn the CCD movie into a series of image frames.
2. Determine the total pixel intensity $I_\alpha(t)$ of each image frame by summing the individual pixel intensities inside the interrogation area of relative width α.
3. Determine the maximum intensity $I_\alpha^{max} = I_\alpha(\infty)$ from the last image in the time series.
4. Calculate the normalized intensity $I_\alpha(t)/I_\alpha^{max}$.
5. Determine the initial relative intensity reduction R using eqn (10).
6. Fit expression eqn (9b) to the data $I_\alpha(t)/I_\alpha^{max}$ using E_{ac} as fitting parameter by eqn (3b).

To obtain the best possible result, the measured acoustophoretic focusing should last long enough to reach a near-static bead distribution. Furthermore, α should be chosen as large as possible, but still without resulting in too many particles remaining in the interrogation area of the last image frame. Repeated measurement of the intensity curves enhances the accuracy and enables an estimate of the standard deviation of the measured energy density.

In this work the algorithm was implemented in Matlab. The Matlab script imgs2energy.m, we used for extracting E_{ac} via the light-intensity model, can be downloaded from the ESI.†

V. Chip, setup, and experimental procedure

A. Chip and experimental setup

Acoustophoresis microchip. We used a glass–silicon–glass chip (Gesim, Germany) as shown in Fig. 4 and described in more detail in ref. 22. The thicknesses of the top glass layer, the intermediate silicon layer, and the bottom glass layer were 0.20 mm, 0.11 mm, and 1.10 mm, respectively. In the silicon layer was etched a cavity connected to inlets and outlets by an microchannel of width $w = 328$ μm and depth $h = 110$ μm. The inlets and outlets were connected to a syringe using Teflon tubing, adapters and valves.

Acoustics driving electronics. The acoustophoresis microchip was acoustically actuated using two different in-house-built transducers, a planar transducer (PT) and an angled transducer (AT), see Fig. 4. The planar transducer was mechanically damped by a layer of epoxy, while the angled transducer was glued on a two-part wedge/quarter-cylinder aluminum mounting. The top part was connected through immersion oil to the lower part via two aluminum springs and could thus slide along the cylinder surface from 0° to 90°. This tunability feature of the coupling angle is to be used in a future work; here the angled transducer was fixed at an angle of 30°. Both the planar and angled transducer were built using PZT piezoceramic plates (Pz26, Ferroperm, Denmark) and were attached to the chip using a quick-drying and water-soluble adhesive gel ('Tensive', Parker Laboratories, USA). The transducers were driven by a function generator (DS345, Stanford, USA) coupled to an RF amplifier (75A250, Amplifier research, USA). The peak-to-peak voltage was monitored by an oscilloscope (TDS220, Tektronix, USA).
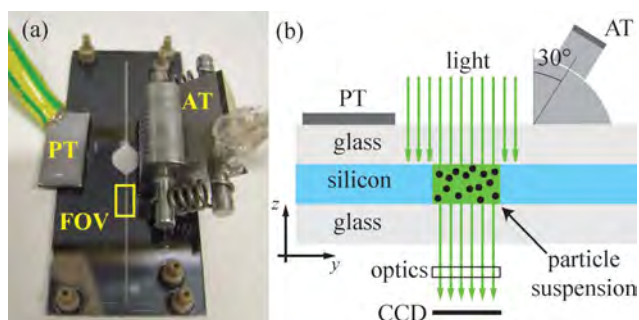
Fig. 4 (a) Photograph of the acoustophoresis glass–silicon–glass chip mounted with two ultrasonic piezo transducers, a planar transducer (PT) and an angled transducer (AT) fixed at 30°. The chip consists of a top glass layer, an intermediate silicon layer, and a bottom glass layer of thicknesses 0.20 mm, 0.11 mm, and 1.10 mm, respectively. The acoustophoretic motion in the particle suspension is observed in the yellow-square-marked field of view (FOV) of length $\ell = 1.21$ mm containing a microchannel of width $w = 328$ μm and depth $h = 110$ μm. (b) Cross-sectional sketch (not drawn to scale) of the experimental setup. The chip consists of silicon (blue) and glass (light gray) layers and is actuated by either the planar PZT transducer (PT) or the angled PZT transducer (AT) both marked by dark gray. Light (green arrows) passes through the transparent microchannel, which is recorded by a CCD camera (black) *via* an inverted microscope with a green filter cube (optics).

Temperature sensing. To observe a possible drift in resonances caused by varying temperature, the temperature was measured at the top glass layer with a T-type (copper-constant) and Teflon-insulated micro thermocouple with a total tip diameter (sensor and sheath layer) of 0.41 mm (IT-21, Physitemp Instruments, USA). Automatic monitoring of temperature data was done with the accuracy of 0.1 °C (Dostmann Electronic GmbH P655-LOG, Germany). Furthermore, the room temperature was logged throughout experimenting and both room- and chip temperatures were stable within 1 °C.

Microbead suspension. The investigated microbead suspension was a 9 : 1 mixture of Milli-Q water (with 0.01% Tween20) and a blood-mimicking fluid (EU-DFS-BMF-ver.1 for Flow Doppler Phantoms, Danish Phantom Design, Denmark) containing 5-μm-diameter polyamide microbeads (Orgasol Powders, Arkema, France). Due to its high water content, the suspension acts as pure Milli-Q water containing polyamide microbeads. The material parameters of the suspension are listed in Table 1. Using a Coulter counter, the polyamide particle concentration was measured to be $C = 3.5 \times 10^{14}$ m^{-3} with a normal distributed particle diameter of $2a = (4.5 \pm 0.7)$ μm. Despite the large size-dispersion, we used the blood-mimicking fluid because it mimics the size-dispersion of biological cells and is inexpensive.

Imaging. The microchannel was imaged by an inverted microscope (Axiovert 40, Zeiss, Germany) with green filter cube, objective (A-Plan $10 \times /0.25$ Ph1, Zeiss, Germany), and CCD camera (AxioCam HSC, Zeiss, Germany) with frame rates between 30–46 ms. To acquire a set of images from a recorded movie we used AxioVision Rel.4.8 software. The pixel resolution was 634 pixel $\times$ 172 pixel of a channel section of size $\ell \times w =$

1209 μm $\times$ 328 μm. Therefore 1 pixel corresponds to 1.9 μm implying that a 4.5 μm diameter particle will roughly cover 10 pixels. This is roughly the same as the optical resolution of 1.3 μm of the objective used. Given the above microbead concentration C and a relative interrogation-area width $\alpha = 0.8$, we can estimate the number N_0 of visible microbeads to be $N_0 = \alpha C \ell w h \approx 1.2 \times 10^4$.

Isolated-particle prediction of the total light-intensity reduction. To verify that optical many-particle effects, such as light scattering and particle shadowing, can be neglected, we predict the total relative intensity reduction R based on the particle concentration C and the intensity reduction of isolated particles. In Fig. 5 (a) we show a single image frame where the microbeads have traversed acoustophoretically half way towards the center of the microchannel. The image clearly shows how single particles are less distinguishable as they move closer together near the center plane of the channel. In the image we mark a region (black square) where we investigate 5 pixel $\times$ 5 pixel square regions surrounding each of 41 isolated particles. Fig. 5 (b) shows 14 such squares. On average a 5 pixel $\times$ 5 pixel square containing a single particle has a total dimensionless, gray-scale pixel intensity of $I_P = (3.3 \pm 0.2) \times 10^3$. When all the particles
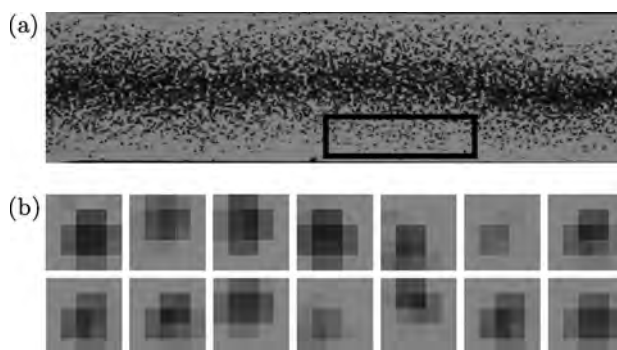

Fig. 5 (a) Gray-scaled experimental image where the microbeads have traversed acoustophoretically half the way towards the center of the microchannel. Inside the black rectangle all isolated particles are identified and their pixel intensities are analyzed within a 5 pixel $\times$ 5 pixel square. (b) 5 pixel $\times$ 5 pixel square views of 14 of the 41 isolated microbeads in the black rectangle marked in panel (a).

by acoustophoresis have traversed into the excluded center region, we obtain the maximum total pixel intensity $I_\alpha^{max} \approx 1.3 \times 10^7$ corresponding to an intensity per pixel of 149 and implying $I_{ref} = 3.7 \times 10^3$ for an empty 5 pixel × 5 pixel square. Finally, we predict the relative intensity reduction $R = N_0 (I_{ref} - I_p)/I_\alpha^{max} \approx 0.42 \pm 0.16$. Notice, this is an upper estimate for R as it excludes effects such as particle shadowing, which will decrease R.

B. Experimental procedure

Stop-flow particle-focusing experiments. The polyamide microbead suspension was injected into the chip manually using a glass syringe. The flow was stopped and a field of view section (yellow rectangle FOV in Fig. 4 (a)) in the straight part of the acoustophoresis microchannel was observed. While actuating one of the two transducers close to the transverse half-wave resonance of the microchannel, the acoustophoretic particle motion was recorded with the CCD camera. A movie typically lasted 30 s comprising about 600 image frames. The actuation frequency was modulated linearly[23] with a rate of 1 kHz from 2.06 MHz to 2.16 MHz around the center frequency 2.11 MHz.

Energy density determination. We use the intensity method described in Section IV to extract the acoustic energy density from a given acoustophoretic focus experiment. As the variation Δa in particle radius a is large (about 15%), we extract E_{ac} for the particle radii a, $a + \Delta a$, and $a - \Delta a$, with $\Delta a = 0.7$ μm.

Scan in PZT voltage. Our experimental study consists of five independent experiment series, where we scanned the PZT voltage U_{pp} of one of the two transducers in the range from 0 to 23 V. For each driving voltage, we performed the above described stop-flow focus experiment. In the two first experiment series, we drove the angled transducer AT, while in the last three series, we drove the planar transducer PT. Each experiment series consisted of typically 16 particle-focusing experiments (16 driving voltages) resulting in a total of 88 acoustophoretic focusing experiments for the experimental study.

VI. Results

A. Validation of the light-intensity method

To validate the light-intensity method described in Section IV, we measure the acoustic energy density using the particle tracking method.[7] In the first experimental series for the planar transducer at $U_{pp} = 18.9$ V, we use the freeware particle tracking program Tracker 4.61 to track 20 microbeads and using the tracking method, we obtain an acoustic energy density $E_{ac} = (1.45 \pm 0.5)$ J m^{-3}. Using the light-intensity method, we obtain the acoustic energy density $E_{ac} = (1.4 \pm 0.4)$ J m^{-3}. In conclusion, the obtained acoustic energy density agrees well with that of the previously reported tracking method. For both methods, the presented uncertainty is due to the size dispersion of the particles.

The light-intensity method turned out to be a simple, rapid, and robust method compatible with low- or mid-ranged microscopes yielding moderate resolution images of high particle concentrations. In contrast, the tracking method was tedious and micro-PIV was impossible.

B. Scanning the PZT voltage

We use the intensity method described in Section IV to extract the acoustic energy density from each of the 88 particle-focusing experiments in our experimental study in Section IV. In Fig. 6 (a) we plot the normalized light-intensity curves $I_\alpha(t)/I_\alpha(\infty)$ for every third (for clarity) of the 88 acoustophoretic focusing experiments of either driving the angled transducer (red points) or driving the planar transducer (blue points). At starting time $t = 0$, it is seen from eqn (10) that the mean of the relative intensity reduction $R = 0.36 \pm 0.07$. This value of the relative intensity reduction is close to, but deviates as expected slightly from, the upper prediction $R = 0.42 \pm 0.16$ in Section V A.

In Fig. 6 (b) we show the measured acoustic energy densities E_{ac} (red and blue disks) as function of the driving voltage squared U_{pp}^2. The energy density is extracted using the mean particle diameter $2a = 4.5$ μm and is shown for each of the five U_{pp}-scanning experimental series. Within each experiment series, we observe that the energies scale with U_{pp}^2 as expected[7], and to the data we fit a straight line $E_{ac} = \beta U_{pp}^2$ (black line). Similarly, we plot dashed lines when the energy densities are extracted using particle radius of $a + \Delta a$ and $a - \Delta a$, respectively, with $\Delta a = 0.7$ μm.

Using the fitted energy densities, we find the re-scaled time s given by eqn (11) and subsequently plot the intensity data in the form $[1 - I_\alpha/I_\alpha(\infty)]/R$ versus s. The data points collapse on the universal curve for the relative average number $n_\alpha(s)$ of particles given by eqn (13) thereby providing a consistency check of the underlying single-particle assumption.

VII. Discussion

The simple and rapid light-intensity method to determine the acoustic energy density in acoustofluidic microsystems is based on a large number of particles, which leads to a reduction of statistical errors. The method is especially useful when analyzing moderate-resolution images of high particle concentration, where tracking- and micro-PIV methods are difficult to apply.

As we have used microbeads with a wide size distribution (about 15%), our estimates of the acoustic energy densities have similar high relative uncertainties. This is indicated by the dashed lines in Fig. 6 (b). However, we see from the scatter of the data points around the expected βU_{pp}^2-curve that, for a fixed value of the particle radius, the statistical uncertainty, beyond that due to particle dispersion, is about 4%. This indicates the potential for high precision measurements using the method on monodisperse particle suspensions.

The method is subject to some uncertainties: (*i*) The particle concentration has to be low enough to maintain single-particle acoustophoresis by avoiding clustering as well as acoustic and hydrodynamic particle–particle interactions (below 10^{15} particles/m^3). It must also be low enough to neglect optical many-particle effects (below 0.6×10^{15} particles/m^3 to avoid shadowing). We checked explicitly in this work that the total intensity reduction obtained from an isolated-particle analysis coincides well with that obtained from the full many-particle images at our density of 0.35 ± 10^{15} particles/m^3. (*ii*) The acoustic wave has to be a 1D planar transverse standing wave to allow for the use of the analytical expressions in the light-intensity model. In some works, such a wave is not intended, for
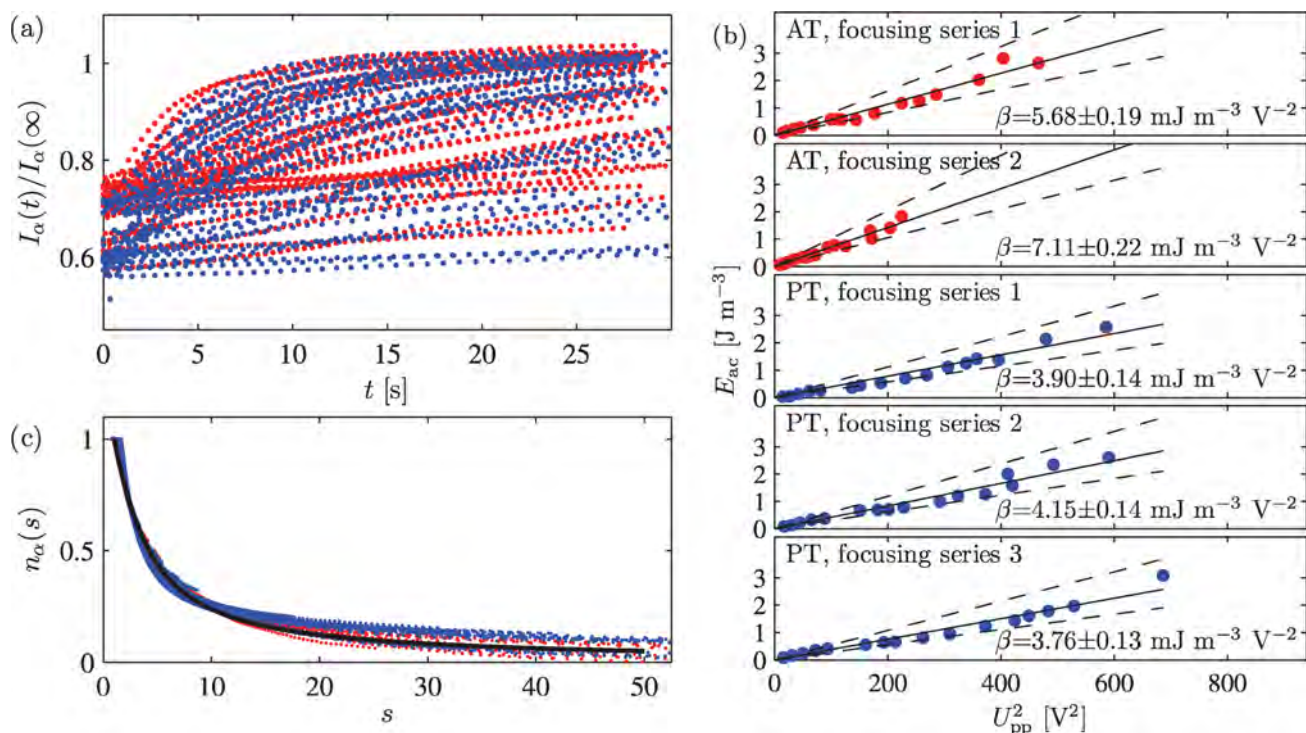
Fig. 6 Analysis of the five independent experimental series comprising of 88 individual acoustophoretic focusing experiments, where the piezo voltage U_{pp} is scanned from 0 to 23 V. (a) Normalized total intensity curves $I_\alpha(t)/I_\alpha(\infty)$ for every third (for clarity) of the 88 experiments of either driving the angled transducer (red points) or driving the planar transducer (blue points). (b) Fitted acoustic energy densities E_{ac} (red and blue disks) as function of the driving voltage squared U_{pp}^2 for each of the five experimental U_{pp}-scanning series. Within each of the voltage sweep series, a voltage square law $E_{ac} = \beta U_{pp}^2$ (black lines) is fitted to the data points. Also shown are two similar fits using the bead radius $a + \Delta a$ (lower dashed line) and $a - \Delta a$ (upper dashed line) with $\Delta a = 0.7$ μm. (c) The data points in panel (a) plotted *versus* the re-scaled time s, given by eqn (11) and E_{ac} from panel (b), collapse onto the universal curve $n_\alpha(s)$ for the relative average number of particles given in eqn (13).

example to achieve particle agglomeration in a point,[22,24] and for those, after excluding the appropriate nodal line regions of more complex shape, the method can only be used to obtain relative figures of merit without the benefit of analytical predictions. In other works, where a 1D planar transverse standing wave is intended, such a wave may still be difficult to achieve, as shown in recent work by Augustsson *et al.*[11] In the present work we overcame this challenge by using frequency-modulation to average over a large number of resonances all with the transverse wave feature, but with different modal patterns along the axial length of the channel. The choice of excluding the center part in the images containing the focused particles further contributes to minimize the effects of particle–particle interactions or weak axial components in the acoustic field perpendicular to the transverse standing wave used in the model. (*iii*) The focus experiment has to be carried out with acoustophoretic particle velocities large enough to avoid sedimentation and thus avoid influence on the particle motion by the presence of the bottom channel wall. In our work, the wall-induced drag enhancement was less than 6% for the center half of the channel volume, thus the systematic under-estimation of the acoustic energy density is of the same order. If a more accurate estimate of the energy is required, a height-dependent Faxén correction must be included in the calculation of the single-particle tracks.[20] (*iv*) The temperature has to be stable enough to avoid drift in acoustic resonances.[11]

In this work the method was applied to a trans-illuminated microchannel. However, in principle, the method can be applied to setups utilizing reflected light in, say, chips where only the lid is transparent.

VIII Conclusions

This paper describes a simple and rapid method for *in situ* determination of the acoustic energy density by observing the increase in light intensity as suspended particles undergo acoustophoresis. The method relies on a theoretical model of averaging over many particles each being subject to single-particle acoustic motion, and it has been validated with the single-particle tracking method. We have shown by proper re-scaling that the re-scaled light intensity *versus* re-scaled time fall on a universal curve predicted by ensemble averaging over acoustophoretic single-particle paths. Compared to other methods, the light-intensity method is especially well suited for images of many particles and of moderate image resolution. We envision it as a main tool in future characterization and optimization of microchips and transducers used for acoustophoresis. Moreover, it has the potential for use in biological applications, such as measurements of the acoustic contrast factor of an ensemble of cells. This would enable a simple and fast method for measuring the stiffness of *e.g.* blood cells, which is a parameter of clinical significance in a wide range of medical conditions.[25]

Note added after first publication

This article replaces the version published on 20th April 2012, which contained errors in eqn (4).

References

1 J. Friend and L. Y. Yeo, *Rev. Mod. Phys.*, 2011, **83**, 647.
2 H. Bruus, J. Dual, J. Hawkes, M. Hill, T. Laurell, J. Nilsson, S. Radel, S. Sadhal and M. Wiklund, *Lab Chip*, 2011, **11**, 3579.
3 M. Wiklund, P. Spégel, S. Nilsson and H. M. Hertz, *Ultrasonics*, 2003, **41**, 329.
4 S. P. Martin, R. J. Towsend, L. A. Kuznetsova, K. A. J. Borthwick, M. Hill, M. B. McDonnell and W. T. Coakley, *Biosens. Bioelectron.*, 2005, **21**, 758.
5 J. Hultström, O. Manneberg, K. Dopf, H. M. Hertz, H. Brismar and M. Wiklund, *Ultrasound Med. Biol.*, 2007, **33**, 145.
6 M. Wiklund, C. Günther, R. Lemor, M. Jäger, G. Fuhr and H. M. Hertz, *Lab Chip*, 2006, **6**, 1537.
7 R. Barnkob, P. Augustsson, T. Laurell and H. Bruus, *Lab Chip*, 2010, **10**, 563.
8 P. Augustsson, R. Barnkob, C. Grenvall, T. Deierborg, P. Brundin, H. Bruus and T. Laurell, in Proc. 14th MicroTAS, 3–7 October 2010, Groningen, The Netherlands, edited by S. Verporte, H. Andersson, J. Emneus, and N. Pamme (CBMS, 2010) pp. 1337–39.
9 R. Barnkob, P. Augustsson, C. Magnusson, H. Lilja, T. Laurell and H. Bruus, in Proc. 15th MicroTAS, 2–6 October 2011, Seattle (WA), USA, edited by J. Landers, A. Herr, D. Juncker, N. Pamme, and J. Bienvenue (CBMS, 2011) pp. 127–129.
10 D. Hartono, Y. Liu, P. L. Tan, X. Y. S. Then, L.-Y. L. Yung and K.-M. Lim, *Lab Chip*, 2011, **11**, 4072.
11 P. Augustsson, R. Barnkob, S. T. Wereley, H. Bruus and T. Laurell, *Lab Chip*, 2011, **11**, 4152.
12 C. Mikkelsen and H. Bruus, *Lab Chip*, 2005, **5**, 1293.
13 S. M. Hagsäter, T. G. Jensen, H. Bruus and J. P. Kutter, *Lab Chip*, 2007, **7**, 1336.
14 L. P. Gorkov, *Soviet Physics-Doklady*, 1962, **6**, 773.
15 M. Settnes and H. Bruus, *Phys. Rev. E*, 2012, **85**, 016327.
16 K. Yosioka and Y. Kawasima, *Acustica*, 1955, **5**, 167.
17 M. Kumar, D. Feke and J. Belovich, *Biotechnol. Bioeng.*, 2005, **89**, 129.
18 H. Faxén, *Ann. Phys.*, 1922, **68**, 89.
19 J. Happel and H. Brenner, *Low Reynolds number hydrodynamics with special applications to particulate media* (Martinus Nijhoff Publishers, The Hague) 1983.
20 M. Koklu, A. C. Sabuncu and A. Beskok, *J. Colloid Interface Sci.*, 2010, **351**, 407.
21 M. S. Limaye and W. T. Coakley, *J. Appl. Microbiol.*, 1998, **84**, 1035.
22 J. Svennebring, O. Manneberg, P. Skafte-Pedersen, H. Bruus and M. Wiklund, *Biotechnol. Bioeng.*, 2009, **103**, 323.
23 O. Manneberg, B. Vanherberghen, B. Onfelt and M. Wiklund, *Lab Chip*, 2009, **9**, 833.
24 D. Bazou, L. A. Kuznetsova and W. T. Coakley, *Ultrasound Med. Biol.*, 2005, **31**, 423.
25 F. C. Mokken, M. Kedaria, C. P. Henny, M. R. Hardeman and A. W. Gelb, *Ann. Hematol.*, 1992, **64**, 113.

Paper published in J Micromech Microeng, June 2012

High-throughput, temperature-controlled microchannel acoustophoresis device made with rapid prototyping

Jonathan D Adams[1,4]**, Christian L Ebbesen**[2,4]**, Rune Barnkob**[2]**,
Allen H J Yang**[3]**, H Tom Soh**[3] **and Henrik Bruus**[2]

[1] Department of Physics, University of California, Santa Barbara, CA 93106, USA
[2] Department of Micro- and Nanotechnology, Technical University of Denmark, DTU Nanotech Building
345 East, DK-2800 Kongens Lyngby, Denmark
[3] Department of Mechanical Engineering, University of California, Santa Barbara, CA 93106, USA

E-mail: tsoh@engr.ucsb.edu and Henrik.Bruus@nanotech.dtu.dk

Abstract

We report a temperature-controlled microfluidic acoustophoresis device capable of separating particles and transferring blood cells from undiluted whole human blood at a volume throughput greater than 1 L h^{-1}. The device is fabricated from glass substrates and polymer sheets in microscope-slide format using low-cost, rapid-prototyping techniques. This high-throughput acoustophoresis chip (HTAC) utilizes a temperature-stabilized, standing ultrasonic wave, which imposes differential acoustic radiation forces that can separate particles according to size, density and compressibility. The device proved capable of separating a mixture of 10- and 2-μm-diameter polystyrene beads with a sorting efficiency of 0.8 at a flow rate of 1 L h^{-1}. As a first step toward biological applications, the HTAC was also tested in processing whole human blood and proved capable of transferring blood cells from undiluted whole human blood with an efficiency of 0.95 at 1 L h^{-1} and 0.82 at 2 L h^{-1}.

(Some figures may appear in colour only in the online journal)

1. Introduction

Systems for the separation and purification of particles and cells from complex mixtures have become essential tools in many areas of biological research and medicine. Microfluidics technology offers the potential for many high-performance cell-sorting applications because it allows precise manipulation of the separation forces that govern purity, recovery and throughput [1, 2]. A number of different force fields have been successfully utilized within microchannels including inertia [3], electrokinetics [4], dielectrophoretics [5], magnetophoretics [6], as well as mechanical contact forces [7].

Recently, as reviewed in [8, 9], there has been growing interest in on-chip microchannel acoustophoresis for biological applications, which allows gentle and label-free separation based on the size, density and compressibility

of particles. Examples are acoustophoretic cell separation devices [10–12], cell trapping [13–15], plasmapheresis [16], forensic analysis [17], food analysis [18], cell sorting using surface acoustic waves [19], cell synchronization [20], cell differentiation [21] and cell compressibility studies [22]. At the same time, substantial advancements in understanding the fundamental physics of biochip acoustophoresis have been achieved through full-chip imaging of acoustic resonances [23], particle handling by surface acoustic waves [24–28], multi-resonance chips [29], advanced frequency control [30, 31], on-chip integration with magnetic separators [32], acoustics-assisted microgrippers [33], acoustic programming [34], band-pass filters [35], *in situ* force calibration [36] and automated micro-PIV systems [37].

However, regardless of the separation mechanism, volume throughput limitations represent a major Achilles heel for microfluidics-based cell sorting devices. These typically exhibit volume flow rates below 0.06 L h^{-1} (= 1 mL min^{-1})

<hr />

[4] These authors contributed equally to this work.

[19, 38, 39], and this limitation has restricted the use of microfluidics technology to low-volume applications. The availability of devices capable of high volume throughput separation would open new avenues in cell-based therapies [40], environmental monitoring [41] and food-borne pathogen detection [42]. The following three papers have reported above-the-norm sample flow rates Q of about 0.3 L h^{-1} for microchannel-based acoustophoretic particle separation or transfer devices: (i) $Q = 0.3$ L h^{-1} for the $(100 \times 60 \times 12)$ mm^3 plexiglass/stainless steel device containing a single $(70 \times 48 \times 3)$ mm^3 broad, shallow channel with transfer ratios of 0.85–0.95 and 0.0–0.1 for a 340-μm-diameter and 200-μm-diameter polystyrene particle suspensions, respectively, [43] (20 times larger than cells); (ii) $Q = 0.2$ L h^{-1} for the $(70 \times 15 \times 5)$ mm^3 quartz glass/stainless steel device containing a single $(50 \times 10 \times 0.25)$ mm^3 broad, shallow channel with transfer ratio of 0.7 for 5-μm-diameter yeast cells [12] (the transfer ratio dropped to 0.3 for $Q = 1$ L h^{-1}); and (iii) $Q = 0.24$ L h^{-1} for the $(55 \times 20 \times 1.5)$ mm^3 Si/glass device containing eight $(40 \times 0.38 \times 0.16)$ mm^3 narrow, shallow channels coupled in parallel with separation coefficients of 0.7–0.9 for suspensions of blood cells (BCs) and lipid particles [44]. We note that in none of these works temperature control has been applied, which, as we shall discuss below, limits a further increase of the throughput.

As a step toward addressing the compelling need for large volume separation capability in biomedical applications, we report here the high-throughput acoustophoresis chip (HTAC). The high throughput of the HTAC is obtained by combining the single broad, shallow-channel geometry [12, 43], here of dimension $(60 \times 17 \times 0.83)$ mm^3, with thermally controlled acoustofluidics [37]. The latter ensures the stability of the temperature-dependent ultrasound resonance responsible for the functionality, when operating the HTAC at relatively high ultrasound power levels. The HTAC is fabricated using a low-cost, rapid prototyping microscope-slide format of overall size $(75 \times 25 \times 4.5)$ mm^3, convenient for biotech applications, and with externally adjustable tubing for controlling the ratio of the sample and buffer flow rates. The HTAC has successfully been tested to separate polystyrene microbeads and to transfer BCs from undiluted whole human blood. We have achieved microchannel separation and transfer results comparable to those reported in the literature, but for flow rates nearly an order of magnitude higher than the previously highest reported flow rates and about two orders of magnitudes higher than the typical flow rates reported in the field.

2. Device design

2.1. HTAC device architecture

The design of the HTAC device builds on the broad, shallow-channel geometry [12, 43] and is fabricated with a low-cost, multi-layer, rapid prototyping process. The device is designed with five functional layers (bottom slide, bottom gasket, divider, top gasket, and top slide), wherein the height of the bottom gasket is half that of the top gasket to place the divider at approximately one-third of the channel height
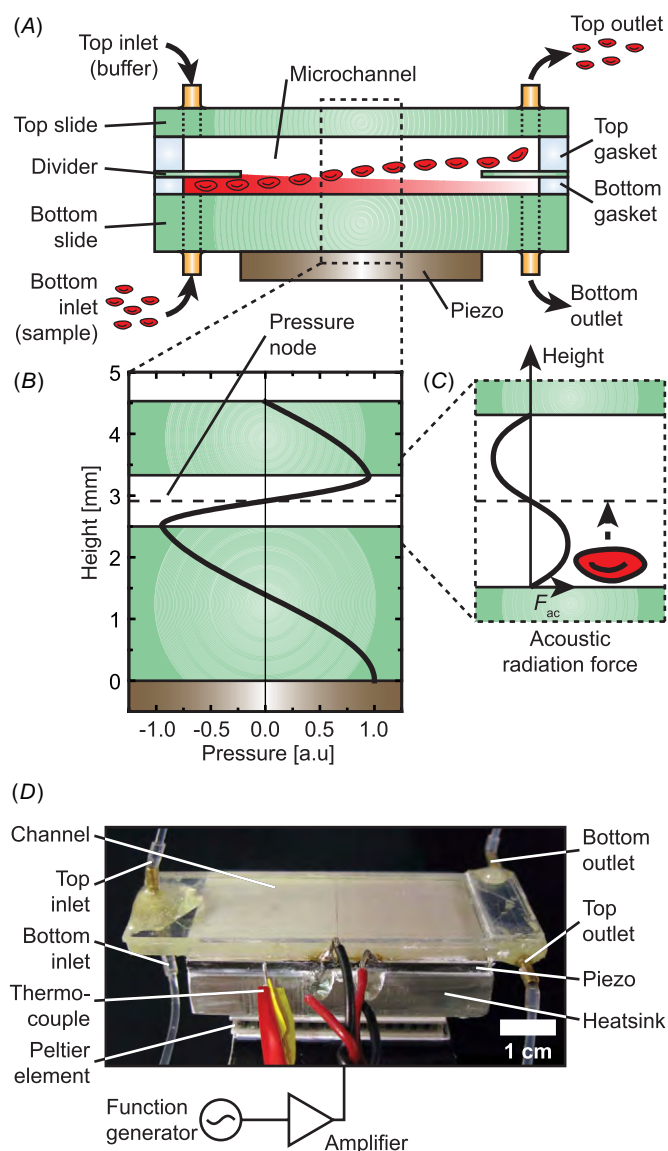

Figure 1. (A) Design schematic of the HTAC showing the microchannel formed by the bottom gasket, divider and top gasket sandwiched between the bottom and top slides. The sample suspension and buffer are injected through the bottom inlet and top inlet, respectively. (B) The device is designed to support a standing half-wave in the applied ultrasound pressure field across the height of the microchannel, with its nodal plane at half the channel height, i.e. above the flow divider at one-third the channel height. (C) The acoustophoretic force F_{ac} (sinusoidal black line) driving particles toward the nodal plane. (D) Photograph of the HTAC placed on top of the piezo transducer mounted on a Peltier element and an aluminum-block heat sink fitted with a thermocouple for thermal control.

(figure 1(A)). The details of the device fabrication and dimensions are provided in section 3.1. The sample (a polystyrene particle suspension or whole blood) and the buffer are pumped into the horizontally placed device through the bottom and top inlets, respectively, and by keeping the Reynolds number below 100, these two streams are fully laminar under the operating conditions. By adjusting the ratio of the two flow rates and relying on gravity-induced sedimentation, we ensure that no particles are transferred

between the two streams without acoustic actuation, such that the sample and buffer elute through the bottom and top outlets, respectively.

A piezo transducer is attached to the bottom slide and driven with a function generator through a custom-built amplifier to generate standing ultrasound waves of frequency f within the device. Importantly, the HTAC structure is designed such that the vertical component of the standing wave has a half-wave in the bottom slide, a half-wave in the microchannel and a quarter wave in the top slide (figure 1(*B*)). In this configuration, the particles experience an acoustic radiation force directed toward the horizontal nodal plane located at one-half the microchannel height—above the divider, which is situated at one-third the channel height. In this way, the strength of the acoustic field, and the magnitude of the flow rates can be adjusted to control the selective transfer of particles from the lower stream to the upper stream.

2.2. HTAC acoustic theory and design

The acoustic radiation force F_{ac} generated by the vertical standing waves of wavelength λ_o in the microchannel and acting on a particle with radius a has the sinusoidal form [45] (figure 1(*C*)):

$$F_{ac} = 4\pi a^3 k_o E_o \left[\frac{\rho_p + \frac{2}{3}(\rho_p - \rho_o)}{2\rho_p + \rho_o} - \frac{1}{3}\frac{\kappa_p}{\kappa_o} \right] \sin(2k_o z),$$
(1)

where k_o is $2\pi/\lambda_o$, z is the vertical coordinate, E_o is the energy density, ρ is density and κ is compressibility with subscripts 'p' and 'o' respectively denoting the particle and the suspension medium. Since F_{ac} depends on the particle volume, larger particles will move faster due to the radius-squared dependence on the velocity $u = F_{ac}/(6\pi\eta a)$ from balancing F_{ac} with the Stokes drag from the liquid with viscosity η. Because the particle radii in this work are larger than $1\ \mu$m, the η-dependence of F_{ac} can be neglected [46].

To determine the optimal dimensions of the device components, we modeled the acoustic field in the HTAC by approximating the geometry as a parallel-plate triple layer structure (bottom slide, water-filled microchannel, top slide) placed on a piezo transducer and by considering only the dependence of the pressure field p of the vertical z coordinate. We only treat longitudinal elastic waves in the top and bottom slides, and since the viscous damping factor $\eta f\pi/(\rho_o c_o^2)$ is minute ($\approx 10^{-6}$), we neglect the viscosity of water. In this simplified 1D model, the pressure p satisfies the Helmholtz wave equation $p''(z) = -[2\pi f/c(z)]^2 p(z)$, where $c(z)$ is the speed of sound in the slides or in the liquid at position z. The boundary conditions are $p' = 0$ at the lower surface of the bottom slide facing the piezo transducer, continuity of pressure and oscillation velocity at the slide/liquid interfaces, and $p = 0$ at the top slide facing the air.

Using the material properties listed in table 1, our simulation shows that at a fixed temperature of 25 °C the desired optimal resonance pattern (figure 1(*B*)) is achieved at an operating frequency of $f = 938$ kHz for a pyrex bottom-slide thickness of 2.50 mm, a pyrex top-slide thickness of 1.25 mm and a channel height of 0.83 mm.

Table 1. Acoustic parameters used for modeling [47, 48].

Parameter	Symbol	T (°C)	Value
Density, water	ρ_o	5–50	998 kg m^{-3}
Speed of sound, water	c_o	5	1424 m s^{-1}
		25	1497 m s^{-1}
		50	1541 m s^{-1}
Density, pyrex	ρ	5–50	2230 kg m^{-3}
Longitudinal speed of sound, pyrex	c	25	5661 m s^{-1}
Young's modulus, pyrex	Y	5	62.4 GPa
		25	62.6 GPa
		50	62.8 GPa
Poisson's ratio, pyrex	σ	5	0.2179
		25	0.2200
		50	0.2226

2.3. HTAC thermal theory and design

During the operation of the HTAC, the power consumption of the piezo transducer was a maximum of 10 W, which resulted in device heating. We therefore analyzed the sensitivity of the acoustic resonance to changes in temperature using numerical modeling, performing a 2D analysis in the vertical plane (neglecting effects of the finite width) of the triple layer pyrex/water/pyrex structure. All simulations were performed using Comsol Multiphysics (COSMOL, www.comsol.com), and convergence tests were performed showing that more than 500 000 degrees of freedom were needed to ensure a mesh-independent result. Given the approximation of the device geometry, the numerical uncertainty of the results is estimated to be 5%.

First, we calculated the temperature profile in the HTAC. We found that the sample and buffer injected at room temperature act as cooling water preventing the top slide from being heated, resulting in a roughly linear temperature change from T_{pz}, the temperature of the piezo transducer, at the bottom of the bottom slide to room temperature at the top of the microchannel. Using this temperature profile, we then calculated the thermal sensitivity of the acoustic resonances in terms of the acoustic energy density E_o in the water from a standard acoustic model [49]: the equations of motion for the elastic displacement field u of the pyrex slides coupled with the Helmholtz wave equation for the pressure p of the water in the microchannel,

$$\nabla^2 \boldsymbol{u} + \frac{\nabla(\nabla \cdot \boldsymbol{u})}{1 - 2\sigma} = -\frac{2(1+\sigma)\rho}{Y}[(1+\mathrm{i}\gamma)\omega]^2 \boldsymbol{u}, \quad (2)$$

$$\nabla^2 p = -\frac{1}{c_o^2}[(1+\mathrm{i}\gamma)\omega]^2 p. \quad (3)$$

Here, c_o is the speed of sound of water, while Y, σ and ρ is Young's modulus, Poisson's ratio and density of the pyrex, respectively. The temperature dependence of these parameters are listed in table 1. To model the dissipation of acoustic energy due to radiation as well as friction in the bulk and in the boundary layers, we have followed [36, 50] and multiplied the angular frequency by the complex-valued damping factor $(1+\mathrm{i}\gamma)$ with $\gamma = 10^{-3}$. This corresponds

to experimentally obtained Q values [36] of the acoustic resonances, $Q = 1/(2\gamma) \approx 500$.

The resulting energy density $E_o(f)$ at a given temperature T_{pz} exhibited a Lorentzian resonance peak [36] with center frequency $f_o(T_{pz})$ and a full peak width at half-maximum Δf_{FW}. At $T_{pz} = 25\,°C$, we determined a center frequency of $f_o = 938\,kHz$ (in agreement with our previous 1D model) and a peak width $\Delta f_{FW} = 4\,kHz$. Importantly, we found that the thermal sensitivity of the resonance mode was $[f_o(T_{pz} + \Delta T) - f_o(T_{pz})]/\Delta T \sim 0.4\,kHz\,°C^{-1}$ corresponding to a displacement of f_o by a full peak width Δf_{FW} per $10\,°C$. We further calculated that such a shift in f leads to a reduction in E_o by about a factor of 20. This numerical estimate, combined with equation (1) and experimental observations, led us to conclude that active temperature control is critical for maintaining device functionality; without active temperature control, heating of the device from the piezo transducer would shift the acoustic resonance thereby significantly decreasing the acoustic energy and result in poor separation efficiency. Thus, we incorporated an active Peltier cooling element with an aluminum heat sink fitted with a thermocouple, so that the interface between the piezo transducer and the bottom slide was maintained at $25\,°C$ (figure 1(*D*)).

3. Device fabrication, setup and experimental procedures

3.1. Device fabrication

Our device consists of a single broad and shallow microchannel ($60\,mm \times 17\,mm \times 0.83\,mm$) equipped with two inlet/outlet pairs and fabricated from PDMS gaskets, cut from $250\,\mu m$ thick PDMS sheets using a plotting cutter (Graphtec America Inc., www.graphtecamerica.com), plasma bonded between standard $25\,mm \times 75\,mm$ glass microscope slides of thickness $1.25\,mm$ (Fisher Scientific, www.fishersci.com). Two bottom slides are bonded together using 5-minute-epoxy glue. Together with the single-thickness top slide, they act as acoustic reflectors. The central flow divider is milled from a $150\,\mu m$ thick borofloat glass wafer (Mark Optics, www.markoptics.com) using a CNC mill (Flashcut CNC, www.flashcutcnc.com), and etched in 49% HF to a final thickness of $70\,\mu m$. To avoid working with the toxic HF etchant, one could instead use a glass slide with a thickness as close as possible to $70\,\mu m$ and cope with the reduced amplitude of the standing ultrasound wave resulting from the less-than-perfect height ratios. Borosilicate glass wafers only $100\,\mu m$ thick are now commercially available from SCHOTT North America Inc. Alternatively, one could use a thin polymer sheet with sufficiently high stiffness to reduce the generation of acoustic streaming (leading to unwanted mixing of the flow streams) from vibrations of its edges. Two $27\,mm \times 27\,mm$ piezoelectric transducers (Ferroperm Piezoceramics, www.ferroperm-piezo.com), fully covering the separation channel, are attached on the underside of the device using superglue and induce a strong acoustic resonance in the microchannel when powered by a sinusoidal voltage at $899\,kHz$ and an amplitude of up to $55\,V$ (all

voltages in this paper are peak-to-peak values), using a custom-built amplifier based on bridged LT1210 op-amps (Linear Technology, www.linear.com).

3.2. Experimental setup

The device is mounted in a stable fluidic setup with $500\text{-}\mu m$-diameter teflon tubing (Upchurch Scientific, www.idex-hs.com/Upchurch-Scientific.aspx). The hydraulic resistance (length) of the outlet tubing is matched to ensure a correct sample: buffer flow ratio of 1:2, which for the whole human blood was achieved by adjusting the length of the outer tubing with the acoustics on. Two and six parallel-coupled syringe pumps (Harvard Apparatus, www.harvardapparatus.com) inject sample and buffer solutions into the system, respectively, achieving a maximum flow rate of $2\,L\,h^{-1}$ sample and $6\,L\,h^{-1}$ buffer. The temperature of the bottom surface of the device is measured using a chromel/alumel thermocouple (Omega Engineering Inc., www.omega.com). The device is mounted in thermal compound on an aluminum heat sink and cooled by a Peltier element with a power consumption of typically $2\,W$. To reduce separation degradation from acoustic streaming near the flow divider [51], we sweep the frequency linearly in $1\,ms$ periods from $10\,kHz$ below to $10\,kHz$ above the center frequency [30], corresponding to about twice the peak width Δf_{FW}.

3.3. Fluorescent polystyrene bead sample

$2\text{-}\mu m$-diameter red fluorescent and $10\text{-}\mu m$-diameter green fluorescent beads were purchased from Microgenics (www.microgenics.com). A degassed solution consisting of DI water with surfactant (0.01% v/v Tween-20) added to reduce nonspecific adhesion of beads was used as a buffer (unless indicated, all reagents were obtained from Sigma). Sample solutions were prepared by suspending the beads at a total concentration of 10^6 beads/mL in the buffer solution. Following separation, outlet samples that were collected in microcentrifuge tubes were directly analyzed via flow cytometry (Accuri Cytometers) to quantitate separation performance.

3.4. Whole human blood sample

Whole human blood purchased from Bioreclamation (www.bioreclamation.com) was used in the HTAC within five days of receipt. It was injected into the device alongside a buffer of degassed standard concentration phosphate buffered saline ($1 \times PBS$, Fisher Scientific). Collected outlet samples were diluted 100-fold in $1 \times PBS$ before being analyzed by flow cytometry for fractionation performance. To characterize the state of the BCs we analyzed resting platelets in the blood sample on the day of receipt and then quantified platelet activation post-HTAC processing within five days of receipt using the procedure described in the appendix.
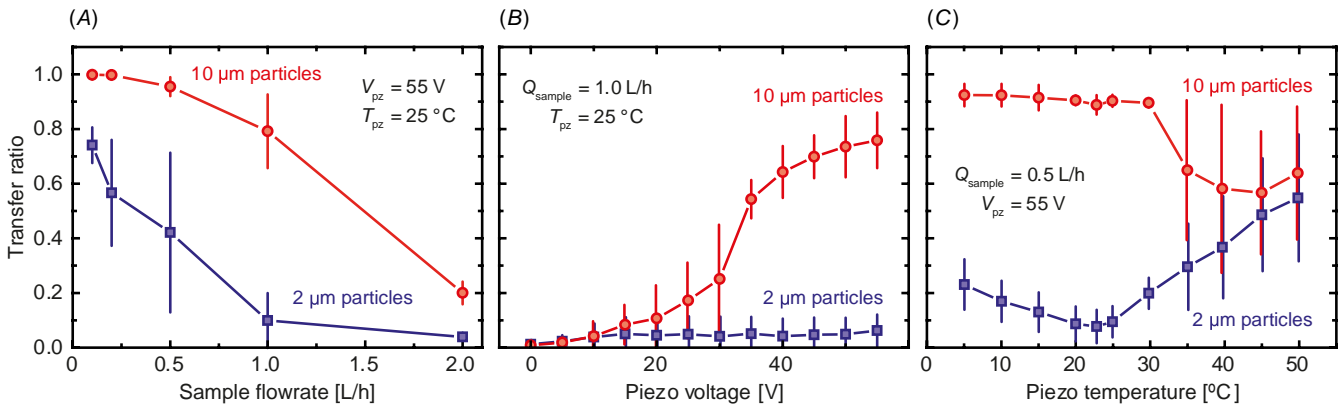
Figure 2. Transfer ratio (fraction of beads transferred from the bottom inlet to the top outlet) of 2- and 10-μm-diameter polystyrene beads at the resonance frequency of 899 kHz. Error bars are standard deviations obtained from experiments performed in triplicate. (*A*) Transfer ratio as a function of the sample flow rate at 25 °C and a piezo voltage of 55 V. Maximum difference in the transfer ratio was observed at 1 L h^{-1}. (*B*) Transfer ratio as a function of the piezo voltage at a temperature of 25 °C and the sample flow rate of 1.0 L h^{-1}. The difference in transfer ratios increases monotonically. (*C*) Transfer ratio as a function of piezo temperature shows optimal operation between 20 and 25 °C. Above 45 °C, the transfer ratio approaches 0.66 corresponding to equal particle density in both outlets (total mixing) and reflecting the 2:1 outlet flow rate ratio between the buffer and the sample.

4. Results

4.1. Bead separation performance

Using the suspension of fluorescent polystyrene beads (section 3.3), we characterized the purity and throughput of the HTAC. The sample and buffer were injected by syringe pumps into the device at a flow ratio of 1:3, and the outlet tubing lengths were adjusted to maintain a top:bottom outlet flow ratio of 1:2. The HTAC was operated at the experimentally determined resonance at $f = 899$ kHz, which was only 4% lower than the theoretically predicted $f_o = 938$ kHz. We used this frequency throughout the experiments. Eluents from outlets were collected in microcentrifuge tubes and were measured with flow cytometry. We define the transfer ratio for a given type of particle as the number of particles in the top outlet relative to the total number of particles in both the top and bottom outlets.

We first measured the dependence of the transfer ratio on the flow rate, keeping the piezo temperature constant at 25 °C and the applied voltage constant at 55 V (figure 2(*A*)). At low flow rates (below 0.5 L h^{-1}) we observe that both particle types have sufficient transit time to get transferred from the lower inlet to the upper outlet (both transfer ratios are above 0.5). Conversely, at the high flow rate (2.0 L h^{-1}) the transfer ratios of both particle types were below 0.2. A successful separation (a large difference in transfer ratios) was observed at a sample flow rate of 1.0 L h^{-1}, where the transfer ratios are 0.8 and 0.1 for the 10- and 2-μm-diameter microbeads, respectively.

We note that the transfer ratio can be adjusted by the piezo voltage V_{pz} because it controls E_o. At the sample flow rate of 1.0 L h^{-1} and at the piezo temperature of 25 °C, we observe that the difference in transfer ratios increases monotonically as a function of the piezo voltage and saturates near 55 V where the transfer ratios are 0.8 and 0.1 for the 10- and 2-μm-diameter microbeads, respectively (figure 2(*B*)).

Finally, in figure 2(*C*), we demonstrate the importance of piezo temperature control by plotting the transfer ratio

as a function of temperature at a constant sample flow rate of 0.5 L h^{-1}, and at a constant piezo voltage of 55 V. We observe a maximal difference in the transfer ratio at 25 °C. For some biological experiments it would be desirable to have an optimal transfer ratio at a temperature of 4 or 37 °C. For such applications, the HTAC operation can be readily adjusted by tuning the temperature settings and the driving frequency.

The data in the three panels were taken on different days. All data points acquired under the same settings agree within the error bars, except the 2-μm-diameter bead at $Q_{sample} = 0.5$ L h^{-1} and $T_{pz} = 25$ °C. For this point the error bars in panel (*A*) and (*C*) barely overlap.

4.2. Blood cell transfer performance

As a step toward biotech applications, we used the HTAC to transfer BCs from the whole human blood sample (section 3.4) into the buffer in a continuous flow manner (figure 3(*A*)). The idea was to test whether the HTAC could handle the high viscosity and high cell concentration of such a realistic sample, a difficult issue often bypassed in on-chip handling of blood by using diluted samples [9]. We also wanted to test, if suspended cells would be damaged by the large shear forces due to the high flow rate. Due to the large difference in viscosity between whole blood and 1×PBS buffer, we adjusted the relative lengths of the outlet tubing sections to retain a top:bottom outlet flow ratio of 1:2. As a negative control, the HTAC was operated without activating the piezo transducer. We found a transfer ratio of BCs to be negligible (figure 3(*B*) blue line). Next, we operated the HTAC at a piezo voltage of 55 V and a piezo temperature of 25 °C, and measured the BC transfer ratio as a function of the flow rate from 0.1 to 2 L h^{-1} (figure 3(*B*) red line).

Remarkably, we found the transfer ratio of BCs in whole blood to be 0.95 for sample flow rates up to 1 L h^{-1}, which decreased slightly to 0.82 at 2 L h^{-1}. We note, that at this latter sample flow rate, the buffer flow rate is about 6 L h^{-1}, and our device thus carries a total flow rate of 8 L h^{-1}. Interestingly, the
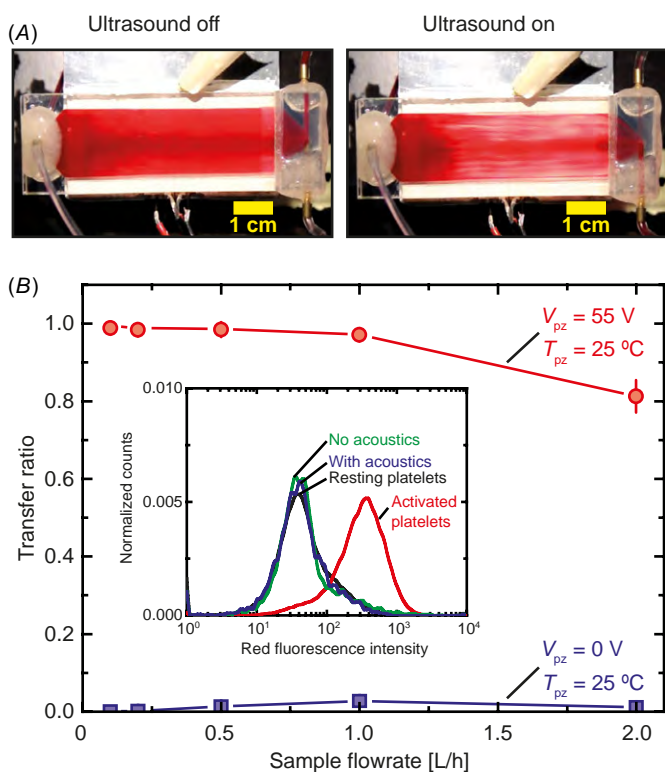
Figure 3. Separation of whole blood samples. (*A*) During operation at a sample flow rate of 0.5 L h^{-1} and a buffer flow rate of 1.5 L h^{-1}, whole blood is injected into the lower half of the device. From there, by the acoustic radiation force from the piezo-induced ultrasound standing wave, the BCs are lifted up into the upper half of the device, forming clearly visible red stripes due to transverse components of the standing ultrasound wave, and leave through the top outlet. (*B*) Measured acoustophoretic transfer of BCs from the undiluted whole blood in the bottom inlet to the buffer top outlet as a function of the flow rate at 25 °C with acoustics ($V_{pz} = 55V$, top curve) and without ($V_{pz} = 0V$, bottom curve). The inset shows red fluorescence for platelets stained with red fluorescent anti-CD62-PE. Activation is not induced by passage through the device either without (green) or with (blue) the presence of the ultrasound field as compared to resting platelets (black) and pro-thrombin-activated platelets (red).

transfer ratio of BCs was higher than that of 10-μm-diameter polystyrene particles at sample flow rates above 1 L h^{-1}. We speculate that this could be due to many-particle effects, as the concentration of red BCs is approaching a magnitude beyond which a previous model study has shown that hydrodynamic many-particle interaction can cause enhanced transfer of particles [52].

To investigate whether the HTAC device damaged the cells or affected their viability, we measured the activation of platelets in whole blood as described in the appendix. To do so, the expression level of CD62 was measured with flow cytometry by labeling the platelets with CD62-PE antibody (figure 3(*B*) inset). The counts obtained in each bin for each curve were normalized by the total counts for that curve. Prothrombin-activated platelets show highest level of CD62 expression (isolated red curve on the right). In comparison, platelets processed without (green) and with (blue) acoustic actuation (at piezo voltage of 55 V and temperature of 25 °C) show negligible differences in CD 62 expression compared to resting platelets (black). Since platelet activation is known to

be highly sensitive to mechanical forces, we extrapolate that the HTAC has minimal effect on the other blood cells.

5. Conclusion

In this work, we have described the HTAC, a temperature controlled, microfluidic acoustophoresis device capable of continuously separating microparticles and transferring BCs from undiluted whole human blood into a buffer at a volume throughput in excess of 1 L h^{-1}, one to two orders of magnitude higher than previous approaches. Importantly, we have shown that despite the high flow rate, our label-free separation method is gentle on the cells, and does not activate platelets when whole blood is processed through the device. From experiments and numerical simulations, we have discovered that active temperature control is critical for sustained device function. Without active control, the heat from the piezo transducer, driven at the high voltage necessary for achieving high throughput, causes significant shifts in the acoustic resonance frequency, rendering the device inoperative.

Central to the design of HTAC are the laminar, low aspect-ratio, co-flowing sample and buffer streams in the device kept at a fixed temperature. The cross-sectional geometry of the channel featuring a shallow height (830 μm) enables precise formation of ultrasound standing waves that vertically transport the target cells, while a large perpendicular width (17 mm) enables high-volume flow rates. Importantly, miniaturization in our device design not only ensures laminar flow but it also allows efficient generation of acoustophoretic forces by ultrasound: (i) the sub-millimeter vertical dimension of the HTAC supports a half-wavelength standing wave resonance in the channel, (ii) the acoustophoretic force scales inversely proportional with the acoustic wavelength (see equation (1)) and (iii) at ultrasound frequencies the formation of air bubbles is minimized, which is important for sustained, reproducible operation of the device.

Given the high flow rate of 1 L h^{-1}, the obtained transfer ratios of 0.8:0.1 for the 10:2-μm-diameter bead suspension are comparable to or better than those obtained in the three previous high flow-rate studies [12, 43, 44] performed at much lower flow rates 0.2–0.3 L h^{-1} as quoted in the introduction. The separation sensitivity can be improved by a serial connection of two or more HTACs or by including an acoustic pre-focusing step just after the inlet inside a single HTAC. Such a pre-focusing step increases the control of the particle motion, as it would place all incoming particles at the same vertical position in the parabolic flow profile of the channel and thus ensure they all have more equal velocities before they reach the region where the transfer to the buffer stream sets in.

The capability of the HTAC to function with the viscous, undiluted, whole blood at high sample flow rates is notable. The measured transfer ratio 0.95 of BCs from undiluted whole blood at the high sample flow rate of 1 L h^{-1} in the HTAC is on par with most blood handling microdevices running with flow rates lower than 0.06 L h^{-1}. The majority of the latter works (quoted in the introduction) were even done with diluted samples, which are easier to handle. One prominent

example of a chip handling undiluted whole blood is the plasmapheresis chip developed in 2009 by Lenshof *et al* and applied for prostate-specific antigen microarray diagnostics [16]. In that work, undiluted whole blood was injected at the low flow rate of 1 mL h^{-1} and BCs were transferred out of this sample stream by acoustophoresis leaving high-quality plasma for diagnostics. Clearly, the HTAC offers an appealing starting point for the development of a plasmapheresis chip with a 1000-fold increase in the sample flow rate.

Although it is beyond the scope of this work, we envision that the device architecture shown here can be further developed to achieve fractionation of different cell types (i.e. thrombocytes, erythrocytes and leukocytes) with higher purities, target cell recoveries at higher volume throughput. Toward this end, we believe that further insights into the effects of acoustic streaming (e.g. on sub-micron particles) as well as particle–particle interactions within high-density samples may hold the key toward higher separation performance.

Acknowledgments

Appendix. Platelet activation analysis

To prepare platelet samples for activation analysis, the whole blood (section 3.4) was centrifuged at $75 \times g$ for 20 min. For resting platelets, the platelet-rich plasma was extracted and Prostaglandin E1 (PGE$_1$) was added to a final concentration of 10 μM. A fraction of the sample was mixed with an equal volume of 2% v/v formaldehyde and incubated for 10 min to fix the resting platelets. The other fraction of the sample was diluted ten-fold in $1 \times$ PBS and injected into the HTAC device alongside a buffer of $1 \times$ PBS. For the 'acoustics on' sample, the device was run at a frequency as described in section 3.2 and an amplitude of 55 V. The device output was collected in microcentrifuge tubes. Samples were then fixed by mixing with an equal volume of 2% v/v formaldehyde and incubating for 10 min. To prepare activated platelets, the platelet-rich plasma was removed and washed in 30% human albumin at $75 \times g$ and resuspended in $1 \times$ PBS with 2 mM EDTA. Pro-thrombin (Haematologic Technologies) was added to the cell suspension at a final concentration of 5 μM and the mixture was incubated at room temperature for 10 min to activate the platelets. We then added an equal volume of 2% formaldehyde and the suspension, and incubated the mixture for 30 min at room temperature to fix the platelets. The cells were then washed twice in $1 \times$ PBS solution. We fluorescently labeled the various platelet samples by adding 20 μL of anti-CD62-PE (BD Pharmigen) per 100 μL platelet suspension, and incubated the mixtures in the dark for 30 min at room temperature. We washed the suspensions twice at $75 \times g$ and added 500 μL of the PBS solution to complete the final suspensions. All samples were then analyzed by flow cytometry for activation level.

References

[1] Adams J D and Soh H T 2009 *J. Assoc. Lab. Autom.* **14** 331
[2] Lenshof A and Laurell T 2010 *Chem. Soc. Rev.* **39** 1203
[3] Mach A J and Di Carlo D 2010 *Biotechnol. Bioeng.* **107** 302
[4] Jacobson S, Hergenroder R, Koutny L and Ramsey J 1994 *Anal. Chem.* **66** 1114
[5] Gascoyne P R C, Noshari J, Anderson T J and Becker F F 2009 *Electrophoresis* **30** 1388
[6] Gijs M A M 2004 *Microfluidics Nanofluidics* **1** 22
[7] Huang L, Cox E, Austin R and Sturm J 2004 *Science* **304** 987
[8] Friend J and Yeo L Y 2011 *Rev. Mod. Phys.* **83** 647
[9] Bruus H, Dual J, Hawkes J, Hill M, Laurell T, Nilsson J, Radel S, Sadhal S and Wiklund M 2011 *Lab Chip* **11** 3579
[10] Petersson F, Nilsson A, Holm C, Jönsson H and Laurell T 2004 *Analyst* **129** 938
[11] Petersson F, Nilsson A, Holm C, Jönsson H and Laurell T 2005 *Lab Chip* **5** 20
[12] Hawkes J J, Barber R W, Emerson D R and Coakley W T 2004 *Lab Chip* **4** 446
[13] Hultström J, Manneberg O, Dopf K, Hertz H M, Brismar H and Wiklund M 2007 *Ultrasound Med. Biol.* **33** 145
[14] Evander M, Johansson L, Lilliehorn T, Piskur J, Lindvall M, Johansson S, Almqvist M, Laurell T and Nilsson J 2007 *Anal. Chem.* **79** 2984
[15] Svennebring J, Manneberg O, Skafte-Pedersen P, Bruus H and Wiklund M 2009 *Biotechnol. Bioeng.* **103** 323
[16] Lenshof A, Ahmad-Tajudin A, Jaras K, Sward-Nilsson A M, Aberg L, Marko-Varga G, Malm J, Lilja H and Laurell T 2009 *Anal. Chem.* **81** 6030
[17] Norris J V, Evander M, Horsman-Hall K M, Nilsson J, Laurell T and Landers J P 2009 *Anal. Chem.* **81** 6089
[18] Grenvall C, Augustsson P, Folkenberg J R and Laurell T 2009 *Anal. Chem.* **81** 6195
[19] Franke T, Braunmueller S, Schmid L, Wixforth A and Weitz D A 2010 *Lab Chip* **10** 789
[20] Thevoz P, Adams J D, Shea H, Bruus H and Soh H T 2010 *Anal. Chem.* **82** 3094
[21] Augustsson P, Barnkob R, Grenvall C, Deierborg T, Brundin P, Bruus H and Laurell T 2010 *Proc. 14th MicroTAS (Groningen, The Netherlands, 3–7 Oct. 2010)* ed S Verporte, H Andersson, J Emneus and N Pamme pp 1337–39 (CBMS) http://www.rsc.org/binaries/LOC/2010/PDFs/Papers/456_0474.pdf
[22] Hartono D, Liu Y, Tan P L, Then X Y S, Yung L Y L and Lim K M 2011 *Lab Chip* **11** 4072
[23] Hagsäter S M, Jensen T G, Bruus H and Kutter J P 2007 *Lab Chip* **7** 1336
[24] Shi J, Mao X, Ahmed D, Colletti A and Huang T J 2008 *Lab Chip* **8** 221
[25] Shi J, Huang H, Stratton Z, Huang Y and Huang T J 2009 *Lab Chip* **9** 3354
[26] Tan M K, Tjeung R, Ervin H, Yeo L Y and Friend J 2009 *Appl. Phys. Lett.* **95** 134101
[27] Tan M K, Yeo L Y and Friend J R 2010 *Appl. Phys. Lett.* **97** 234106
[28] Shi J, Yazdi S, Lin S C S, Ding X, Chiang I K, Sharp K and Huang T J 2011 *Lab Chip* **11** 2319
[29] Manneberg O, Hagsäter S M, Svennebring J, Hertz H M, Kutter J P, Bruus H and Wiklund M 2009 *Ultrasonics* **49** 112
[30] Manneberg O, Vanherberghen B, Onfelt B and Wiklund M 2009 *Lab Chip* **9** 833
[31] Glynne-Jones P, Boltryk R J, Harris N R, Cranny A W J and Hill M 2010 *Ultrasoncis* **50** 68
[32] Adams J D, Thevoz P, Bruus H and Soh H T 2009 *Appl. Phys. Lett.* **95** 254103
[33] Oberti S, Moeller D, Neild A, Dual J, Beyeler F, Nelson B J and Gutmann S 2010 *Ultrasonics* **50** 247

[34] Ratier C and Hoyos M 2010 *Anal. Chem.* **82** 1318
[35] Adams J D and Soh H T 2010 *Appl. Phys. Lett.* **97** 064103
[36] Barnkob R, Augustsson P, Laurell T and Bruus H 2010 *Lab Chip* **10** 563
[37] Augustsson P, Barnkob R, Wereley S T, Bruus H and Laurell T 2011 *Lab Chip* **11** 4152
[38] Nilsson J, Evander M, Hammarström B and Laurell T 2009 *Anal. Chim. Acta* **649** 141
[39] Gossett D R, Weaver W M, Mach A J, Hur S C, Tse H T K, Lee W, Amini H and Di Carlo D 2010 *Anal. Bioanal. Chem.* **397** 3249
[40] Mancardi G and Saccardi R 2008 *Lancet Neurol.* **7** 626
[41] Lemarchand K, Masson L and Brousseau R 2004 *Crit. Rev. Microbiol.* **30** 145
[42] Neethirajan S, Kobayashi I, Nakajima M, Wu D, Nandagopal S and Lin F 2011 *Lab Chip* **11** 1574
[43] Johnson D and Feke D 1995 *Separations Technol.* **5** 251
[44] Jönsson H, Holm C, Nilsson A, Petersson F, Johnsson P and Laurell T 2004 *Ann. Thorac. Surg.* **78** 1572
[45] Yosioka K and Kawasima Y 1955 *Acustica* **5** 167
[46] Settnes M and Bruus H 2012 *Phys. Rev.* E **85** 016327
[47] CRCnetBASE Product 2012 *CRC Handbook of Chemistry and Physics* 92nd edn (London: Taylor and Francis)
[48] Spinner S 1956 *J. Am. Ceram. Soc.* **39** 113
[49] Dual J and Schwarz T 2012 *Lab Chip* **12** 244
[50] Groschl M 1998 *Acustica* **84** 432
[51] Hagsäter S M, Lenshof A, Skafte-Pedersen P, Kutter J P, Laurell T and Bruus H 2008 *Lab Chip* **8** 1178
[52] Mikkelsen C and Bruus H 2005 *Lab Chip* **5** 1293

Paper published in Lab on a Chip, July 2012

A numerical study of microparticle acoustophoresis driven by acoustic radiation forces and streaming-induced drag forces

Peter Barkholt Muller,[a] Rune Barnkob,[b] Mads Jakob Herring Jensen[c] and Henrik Bruus*[a]

We present a numerical study of the transient acoustophoretic motion of microparticles suspended in a liquid-filled microchannel and driven by the acoustic forces arising from an imposed standing ultrasound wave: the acoustic radiation force from the scattering of sound waves on the particles and the Stokes drag force from the induced acoustic streaming flow. These forces are calculated numerically in two steps. First, the thermoacoustic equations are solved to first order in the imposed ultrasound field taking into account the micrometer-thin but crucial thermoviscous boundary layer near the rigid walls. Second, the products of the resulting first-order fields are used as source terms in the time-averaged second-order equations, from which the net acoustic forces acting on the particles are determined. The resulting acoustophoretic particle velocities are quantified for experimentally relevant parameters using a numerical particle-tracking scheme. The model shows the transition in the acoustophoretic particle motion from being dominated by streaming-induced drag to being dominated by radiation forces as a function of particle size, channel geometry, and material properties.

I Introduction

In the past decade there has been a markedly increasing interest in applying ultrasound acoustofluidics as a tool for purely mechanical and label-free manipulation of particle and cell suspensions in MEMS and biologically oriented lab-on-a-chip systems. Recent extended reviews of acoustofluidics can be found in *Review of Modern Physics*[1] and the tutorial series in *Lab on a Chip*[2] which, among other topics, treats the application of ultrasound bulk[3] and surface[4] acoustic waves as well as acoustic forces on particles from acoustic radiation[5] and from streaming-induced drag.[6]

When a standing ultrasound wave is established in a microchannel containing a microparticle suspension, the particles are subject to two acoustic forces: the acoustic radiation force from the scattering of sound waves on the particles, and the Stokes drag force from the induced acoustic streaming flow. The resulting motion of a given particle is termed acoustophoresis, migration by sound. Experimental work on acoustophoresis has mainly dealt with the radiation force, primarily because this force dominates over the streaming-induced drag force for the studied aqueous suspensions of polymer particles or biological cells with diameters larger than 2 μm. Detailed measurements of

the acoustophoretic motion of large 5 μm diameter polystyrene particles in water[7,8] have shown good agreement with the theoretical predictions[9,10] for the radiation force on compressible particles with a radius a much smaller than the acoustic wavelength λ and neglecting the viscosity of the suspending fluid.

However, as the particle diameter $2a$ is reduced below 2 μm, viscous effects are expected to become significant, because this length corresponds to a few times the viscous penetration depth or boundary-layer thickness δ. Analytical expressions for the viscous corrections to the radiation force valid in the experimentally relevant limit of long wavelength λ, characterized by $a \ll \lambda$ and $\delta \ll \lambda$, have been given recently,[11] but have not yet been tested experimentally. In addition to these modifications of the radiation force, the acoustic streaming flow induced by viscous stresses in the boundary layers near rigid walls, and depending critically on the detailed geometry and boundary conditions, also significantly influences the acoustophoretic particle motion as the size of the particle or the confining microchannel is reduced.[12,13] The cross-over from radiation-dominated to streaming-dominated motion has been observed in experiments,[14,15] and a scaling analysis of the critical particle diameter for this cross-over has been provided in the literature[16] and will be restated in Section IV D.

Although acoustic streaming is a well-known phenomenon in acoustics, it is pointed out in a recent review[6] that streaming is often misunderstood outside the relatively small circles of acoustics experts due to the many forms in which it may arise in, *e.g.*, acoustofluidic microsystems. Not only is acoustic streaming difficult to predict quantitatively due to its sensitivity

[a]*Department of Physics, Technical University of Denmark, DTU Physics Building 309, DK-2800 Kongens Lyngby, Denmark.*
E-mail: bruus@fysik.dtu.dk
[b]*Department of Micro- and Nanotechnology, Technical University of Denmark, DTU Nanotech Building 345 East, DK-2800 Kongens Lyngby, Denmark*
[c]*COMSOL A/S, Diplomvej 373, DK-2800 Kongens Lyngby, Denmark*

to the detailed geometry and boundary conditions, but part of the more conceptual difficulties with acoustic streaming in acoustfluidics may be related to the lack of theoretical analysis in the experimental relevant limit where the microchannel height h is equal to one or a few times half the acoustic wavelength λ, i.e. $h \simeq \lambda$. The classical Rayleigh–Schlichting boundary-layer theory for acoustic streaming,[17–20] see Fig. 1, is valid in the limit of thin boundary layers in medium-sized channels, $\delta \ll h \ll \lambda$, and a later extension[13] is valid in the limit of thin boundary layers in shallow channels, $\delta \simeq h \ll \lambda$. Moreover, in contrast to rectangular channel cross sections of experimental relevance, the classical analysis of the parallel-plate channel and recent numerical studies of it[21] do not include the effects of the vertical side walls. One exception is the special case of gases in shallow, low-aspect-ratio channels studied by Aktas and Farouk.[22]

The push within contemporary acoustofluidics for handling smaller particles like bacteria, viruses, and large biomolecules, and for doing so with better accuracy, emphasizes the urgency of performing a numerical analysis of microparticle acoustophoresis including acoustic radiation forces, streaming flows, and boundary layers. Based directly on the governing equations, we provide such an analysis in this paper for a simple, yet experimentally relevant microsystem. In Section II we present the governing thermoacoustic equations to first and second order in the external ultrasound actuation. In Section III we describe the model system, the numerical implementation of it, as well as mesh-convergence analysis. In Section IV this is followed by the results for first-order fields, time-averaged second-order fields, and microparticle acoustophoresis as function of particle size and material properties. We end with a concluding discussion in Section V.

II Governing equations

The governing perturbation equations for the thermoacoustic fields are well-known textbook material.[23–25] The full acoustic
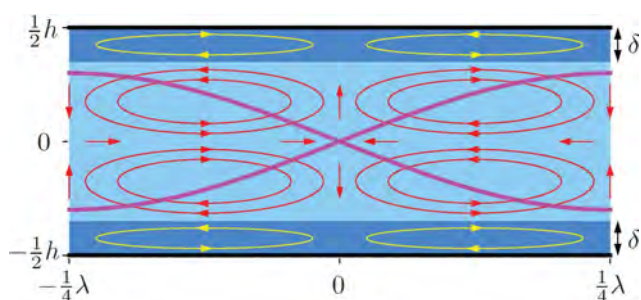
Fig. 1 A sketch of the classical Rayleigh-Schlichting streaming pattern in a liquid-filled gap of height h between two infinite, parallel rigid walls (black lines). The bulk liquid (light blue) supports a horizontal standing sinusoidal pressure wave (magenta line) of wavelength λ in the horizontal direction parallel to the walls. In the viscous boundary layers (dark blue) of sub-micrometer thickness δ, large shear stresses appear, which generate the boundary-layer (Schlichting) streaming rolls (yellow). These then drive the bulk (Rayleigh) streaming rolls (red). The streaming pattern is periodic in the horizontal direction with periodicity $\lambda/2$, and thus only the top and bottom walls are subject to the no-slip boundary condition.

problem in a fluid, which before the presence of any acoustic wave is quiescent with constant temperature T_0, density ρ_0, and pressure p_0, is described by the four scalar fields pressure p, temperature T, density ρ, and entropy s per mass unit as well as the velocity vector field v. Changes in ρ and s are given by the two thermodynamic relations

$$d\rho = \gamma \kappa \rho \, dp - \alpha \rho \, dT, \tag{1a}$$

$$ds = \frac{C_p}{T} \, dT - \frac{\alpha}{\rho} dp, \tag{1b}$$

which, besides the specific heat capacity C_p at constant pressure, also contain the specific heat capacity ratio γ, the isentropic compressibility κ, and the isobaric thermal expansion coefficient α given by

$$\gamma = \frac{C_p}{C_V}, \tag{2a}$$

$$\kappa = \frac{1}{\rho} \left(\frac{\partial \rho}{\partial p} \right)_s, \tag{2b}$$

$$\alpha = -\frac{1}{\rho} \left(\frac{\partial \rho}{\partial T} \right)_p. \tag{2c}$$

Eqn (1) can be used to eliminate ρ and s, so that we only need to deal with the acoustic perturbations in temperature T, pressure p, and velocity v. Taking first and second order (subscript 1 and 2, respectively) into account, we write the perturbation series

$$T = T_0 + T_1 + T_2, \tag{3a}$$

$$p = p_0 + p_1 + p_2, \tag{3b}$$

$$v = v_1 + v_2. \tag{3c}$$

We model the external ultrasound actuation through boundary conditions on the first-order velocity v_1 while keeping the temperature constant,

$$T = T_0, \text{ on all walls}, \tag{4a}$$

$$v = 0, \text{ on all walls}, \tag{4b}$$

$$n \cdot v_1 = v_{bc}(y,z) e^{-i\omega t}, \text{ added to actuated walls}. \tag{4c}$$

Here n is the outward pointing surface normal vector, and ω is the angular frequency characterizing the harmonic time dependence.

A First-order equations

To first order in the amplitude of the imposed ultrasound field, the thermodynamic heat transfer equation for T_1, the kinematic continuity equation expressed in terms of p_1, and the dynamic Navier–Stokes equation for v_1, become

$$\partial_t T_1 = D_{th} \nabla^2 T_1 + \frac{\alpha T_0}{\rho_0 C_p} \partial_t p_1, \tag{5a}$$

$$\partial_t p_1 = \frac{1}{\gamma\kappa}\left[\alpha\partial_t T_1 - \nabla\cdot\boldsymbol{v}_1\right], \tag{5b}$$

$$\rho_0\partial_t\boldsymbol{v}_1 = -\nabla p_1 + \eta\nabla^2\boldsymbol{v}_1 + \beta\eta\nabla(\nabla\cdot\boldsymbol{v}_1). \tag{5c}$$

Here, D_{th} is the thermal diffusivity, η is the dynamic viscosity, and β is the viscosity ratio, which has the value 1/3 for simple liquids.[23] A further simplification can be obtained when assuming that all first-order fields have a harmonic time dependence $e^{-i\omega t}$ inherited from the imposed ultrasound field (eqn (4c)), because then p_1 is eliminated by inserting eqn (5b) with $\partial_t p_1 = -i\omega p_1$ into eqn (5a) and (c). After using the thermodynamic identity[26] $T_0\alpha^2/(\rho_0 C_p\kappa) = \gamma - 1$, we arrive at

$$i\omega T_1 + \gamma D_{th}\nabla^2 T_1 = \frac{\gamma-1}{\alpha}\nabla\cdot\boldsymbol{v}_1, \tag{6a}$$

$$i\omega\boldsymbol{v}_1 + \nu\nabla^2\boldsymbol{v}_1 + \nu\left[\beta + i\frac{1}{\gamma\rho_0\kappa\nu\omega}\right]\nabla(\nabla\cdot\boldsymbol{v}_1) = \frac{\alpha}{\gamma\rho_0\kappa}\nabla T_1, \tag{6b}$$

where $\nu = \eta/\rho_0$. From eqn (6) arise the thermal and the viscous penetration depth δ_{th} and δ, respectively (values for ultrasound waves at 2 MHz in water at 25 °C),

$$\delta_{th} = \sqrt{\frac{2D_{th}}{\omega}} = 0.15\ \mu m, \quad\text{and}\quad \delta = \sqrt{\frac{2\nu}{\omega}} = 0.38\ \mu m. \tag{7}$$

These are the length scales over which the thermoacoustic fields change from their bulk values to the boundary conditions of the rigid walls stated in eqn (4).

B Second-order, time-averaged equations

For water and most other liquids, the thermal effects in the above first-order equations are minute because of the smallness of the pre-factor $\gamma - 1 \approx 10^{-2}$ and $\delta_{th}/\delta \approx 0.3$. To simplify the following treatment, we therefore neglect the coupling in the second-order equations between the temperature field T_2 and the mechanical variables $\boldsymbol{v}_2$ and p_2. Furthermore, the values of η and β are kept fixed at the ones given at $T = T_0$. The second-order continuity equation and Navier–Stokes equation are

$$\partial_t\rho_2 = -\rho_0\nabla\cdot\boldsymbol{v}_2 - \nabla\cdot(\rho_1\boldsymbol{v}_1), \tag{8a}$$

$$\rho_0\partial_t\boldsymbol{v}_2 = -\nabla p_2 + \eta\nabla^2\boldsymbol{v}_2 + \beta\eta\nabla(\nabla\cdot\boldsymbol{v}_2) \\ - \rho_1\partial_t\boldsymbol{v}_1 - \rho_0(\boldsymbol{v}_1\cdot\nabla)\boldsymbol{v}_1, \tag{8b}$$

and consequently, thermal effects enter solely through the temperature-dependent first-order fields ρ_1 and $\boldsymbol{v}_1$.

In a typical experiment on microparticle acoustophoresis, the microsecond timescale of the ultrasound oscillations is not resolved. It therefore suffices to treat only the time-averaged equations. The time average over a full oscillation period, denoted by the angled brackets $\langle...\rangle$, of the second-order continuity equation and Navier–Stokes equation becomes[27]

$$\rho_0\nabla\cdot\langle\boldsymbol{v}_2\rangle = -\nabla\cdot\langle\rho_1\boldsymbol{v}_1\rangle, \tag{9a}$$

$$\eta\nabla^2\langle\boldsymbol{v}_2\rangle + \beta\eta\nabla(\nabla\cdot\langle\boldsymbol{v}_2\rangle) - \langle\nabla p_2\rangle \\ = \langle\rho_1\partial_t\boldsymbol{v}_1\rangle + \rho_0\langle(\boldsymbol{v}_1\cdot\nabla)\boldsymbol{v}_1\rangle. \tag{9b}$$

It is seen that products of first-order fields act as source terms (at the right-hand sides) for the second-order fields (at the left-hand sides). We note that for complex-valued fields $A(t)$ and $B(t)$ with harmonic time-dependence $e^{-i\omega t}$, the time average is given by the real-part rule $\langle A(t)B(t)\rangle = \frac{1}{2}Re[A(0)^* B(0)]$, where the asterisk represents complex conjugation.

The second-order problem was solved in the case of the infinite parallel-plate channel by Rayleigh,[17,20] see Fig. 1. Assuming a first-order bulk velocity field with only the horizontal y-component v_{1y} being non-zero and of the form $v_{1y} = U_1\cos(2\pi y/\lambda)e^{-i\omega t}$, the resulting y-component $\langle v_{2y}^{bnd}\rangle$ of $\langle\boldsymbol{v}_2\rangle$ just outside the boundary layers (in our notation at $z \approx \pm[h/2 - 3\delta]$), becomes

$$\langle v_{2y}^{bnd}\rangle = \frac{3}{8}\frac{U_1^2}{c_0}\sin\left(4\pi\frac{y}{\lambda}\right), \tag{10}$$

Relative to the first-order bulk velocity v_{1y}, the second-order field $\langle v_{2y}^{bnd}\rangle$ is phase shifted by $\pi/2$, period doubled in space, and smaller by a factor of U_1/c_0, where c_0 is the speed of sound of the liquid.

C Time-averaged acoustic forces on a single suspended microparticle

Once the first- and second-order acoustic fields have been calculated, it is possible to determine the time-averaged acoustic forces on a single suspended particle. These are the acoustic radiation force $\boldsymbol{F}^{rad}$ due to the scattering of acoustic waves on the particle and the Stokes drag force $\boldsymbol{F}^{drag}$ from the acoustic streaming.

The time-average acoustic radiation force $\boldsymbol{F}^{rad}$ on a single small spherical particle of radius a, density ρ_p, and compressibility κ_p in a viscous fluid is given by[11]

$$\boldsymbol{F}^{rad} = -\pi a^3\left[\frac{2\kappa_0}{3}Re[f_1^* p_1^*\nabla p_1] - \rho_0 Re[f_2^*\boldsymbol{v}_1^*\cdot\nabla\boldsymbol{v}_1]\right], \tag{11}$$

where $\kappa_0 = 1/(\rho_0 c_0^2)$ is the compressibility of the fluid, and where the pre-factors f_1 and f_2 are given by

$$f_1(\tilde{\kappa}) = 1 - \tilde{\kappa}, \qquad\text{with } \tilde{\kappa} = \frac{\kappa_p}{\kappa_0}, \tag{12a}$$

$$f_2(\tilde{\rho},\tilde{\delta}) = \frac{2\left[1-\Gamma(\tilde{\delta})\right](\tilde{\rho}-1)}{2\tilde{\rho}+1-3\Gamma(\tilde{\delta})}, \quad\text{with } \tilde{\rho} = \frac{\rho_p}{\rho_0}, \tag{12b}$$

$$\Gamma(\tilde{\delta}) = -\frac{3}{2}\left[1+i\left(1+\tilde{\delta}\right)\right]\tilde{\delta}, \quad\text{with } \tilde{\delta} = \frac{\delta}{a}, \tag{12c}$$

For the special case of the horizontal pressure half-wave resonance, $p_1 = p_a\sin(qy)$, with channel width w and wavenumber $q = \pi/w$, the acoustic energy density is $E_{ac} = \frac{1}{4}\kappa_0 p_a^2 = \frac{1}{4}\rho_0 U_1^2$. The expression for the radiation force then simplifies to

$$F_{1D}^{rad} = 4\pi\Phi(\tilde{\kappa},\tilde{\rho},\tilde{\delta})a^3 qE_{ac}\sin(2qy), \quad (13a)$$

$$\Phi\left(\tilde{\kappa},\tilde{\rho},\tilde{\delta}\right) = \frac{1}{3}f_1(\tilde{\kappa}) + \frac{1}{2}\,\mathrm{Re}\left[f_2\left(\tilde{\rho},\tilde{\delta}\right)\right], \quad (13b)$$

where Φ is the so-called acoustic contrast factor.

The time-averaged Stokes drag force $\boldsymbol{F}^{drag}$ on a spherical particle of radius a moving with velocity $\boldsymbol{u}$ in a fluid having the streaming velocity $\langle\boldsymbol{v}_2\rangle$ is given by the usual expression

$$\boldsymbol{F}^{drag} = 6\pi\eta a(\langle\boldsymbol{v}_2\rangle - \boldsymbol{u}), \quad (14)$$

valid for particles sufficiently far from the channel walls.[28]

III Numerical model

In the following we present the idealized numerical model, and how we implement and solve the governing equations for this model using the finite element software COMSOL Multiphysics 4.2a, see ref. 29.

A Model system and computational domain

Given the detailed measurements of the acoustophoretic motion and the successful comparison with theoretical predictions presented in ref. 7 and 8, it is natural to use an idealization of their straight microchannel of length 35 mm and rectangular cross section as a model system in our numerical study. We neglect the chip structure and simply represent the silicon–glass chip as hard-wall boundary conditions. We further neglect any axial dynamics in the long straight channel, and thus restrict our analysis to the rectangular cross section Ω of width $w = 0.38$ mm and height $h = 0.16$ mm in the vertical yz-plane, see Fig. 2. Finally, we represent the ultrasonic piezo transducer by the velocity boundary condition eqn (4). The particle suspensions are modeled as being mono-disperse and containing non-interacting, spherical polystyrene particles with diameters of 0.5, 1.0, 2.0, 3.0, or 5.0 μm, respectively.

The model system has a horizontal half-wave resonance across the width w given by the frequency $f = \omega/(2\pi) = c_0/(2w)$, equal to 1.97 MHz for water. To excite this resonance, we let all external acoustic excitations have a harmonic time dependence of frequency $f = 1.97$ MHz. All relevant material parameters are listed in Table 1 .

B Particle tracing model

In order to study the acoustophoretic motion of N particles suspended in the microchannel, we apply the COMSOL Particle Tracing Module, which closely mimics experimental particle
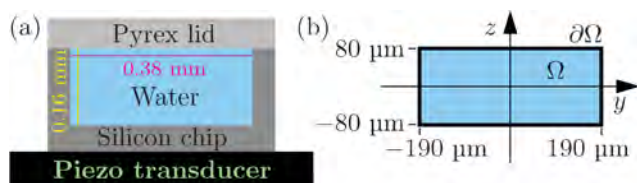

Fig. 2 (a) End-view sketch of the acoustophoresis microchip with a fluidic channel of width $w = 0.38$ mm and height $h = 0.16$ mm used in experiments.[7,8] It consists of a silicon chip (dark gray), a pyrex lid (light gray), water (blue), and a piezo transducer (black). (b) The corresponding two-dimensional computational domain Ω (blue) surrounded by rigid walls $\partial\Omega$ (black) implemented in our numerical model.

Table 1 Model parameters. The parameters are given at temperature $T = 25°$ and taken from the COMSOL Material Library unless explicit stated otherwise.

Polystyrene			
Density[30]	ρ_{ps}	1050	kg m^{-3}
Speed of sound[31] (at 20 °C)	c_{ps}	2350	m s^{-1}
Poisson's ratio[32]	σ_{ps}	0.35	
Compressibility[a]	κ_{ps}	249	TPa^{-1}

Water			
Density	ρ_0	998	kg m^{-3}
Speed of sound	c_0	1495	m s^{-1}
Compressibility[b]	κ_0	448	TPa^{-1}
Viscosity	η	0.893	mPa s
Visc. boundary layer, 1.97 MHz	δ	0.38	μm
Thermal conductivity	k_{th}	0.603	W m^{-1} K^{-1}
Specific heat capacity	C_p	4183	Jkg^{-1}K^{-1}
Specific heat capacity ratio[c]	γ	1.014	
Thermal diffusivity[d]	D_{th}	1.43×10^{-7}	m^2 s^{-1}
Thermal expansion coeff.[e]	α	2.97×10^{-4}	K^{-1}

50% glycerol-in-water mixture			
Density[34]	ρ_0	1129	kg m^{-3}
Speed of sound[35]	c_0	1725	m s^{-1}
Compressibility[b]	κ_0	298	TPa^{-1}
Viscosity[34]	η	5.00	mPa s
Visc. boundary layer, 2.27 MHz	δ	0.79	μm
Thermal cond.[36] (at 20 °C)	k_{th}	0.416	W m^{-1} K^{-1}
Specific heat cap.[37] (at 1.7 °C)	C_p	3360	J kg^{-1} K^{-1}
Specific heat capacity ratio[c]	γ	1.043	
Thermal diffusivity[d]	D_{th}	1.10×10^{-7}	m^2 s^{-1}
Thermal expansion coeff.[e]	α	4.03×10^{-4}	K^{-1}

[a] Calculated as $\kappa_{ps} = \dfrac{3(1-\sigma_{ps})}{1+\sigma_{ps}}\dfrac{1}{(\rho_{ps}c_{ps}^2)}$ from ref. 33.
[b] Calculated as $\kappa_0 = 1/(\rho_0 c_0^2)$ from eqn (2b).
[c] Calculated from $T_0\alpha^2/(\rho_0 C_p\kappa) = \gamma - 1$.
[d] Calculated as $D_{th} = k_{th}/(\rho_0 C_p)$.
[e] Calculated from eqn (2c).

tracing and velocimetry.[7,8] This module provides a Lagrangian description of the motion of the particles, each of which is treated as a point particle governed by Newton's law of motion, and thus involving one ordinary differential equation (ODE) for each spatial direction. Consequently, in total $2N$ ODEs are solved for the particle suspension. The input are the particle masses m_j and all forces $F_i(\boldsymbol{r}_j)$ acting on each particle at position $\boldsymbol{r}_j$. The ODE for the jth particle with velocity $\boldsymbol{v}_j = d\boldsymbol{r}_j/dt$ is

$$m_j\frac{d\boldsymbol{v}_j}{dt} = \sum_i \boldsymbol{F}_i(\boldsymbol{r}_j). \quad (15)$$

Neglecting gravitational effects, the forces acting on a particle in our model are the radiation force $\boldsymbol{F}^{rad}$, eqn (11) , and the Stokes drag force $\boldsymbol{F}^{drag}$, eqn (14). These forces are calculated numerically as described in the following sub-section.

C Numerical procedure

We have used the following sequential procedure to solve the problem numerically in COMSOL:

(*i*) The first-order acoustic fields of eqn (5), subject to the boundary conditions of eqn (4), are calculated using the predefined Thermoacoustic Physics Interface.

(ii) The time-averaged second-order flow $\langle \mathbf{v}_2 \rangle$ is calculated by implementing eqn (9) in the Laminar Flow Physics Interface, modified to include the addition of the time-averaged first-order products from step (i) on the right-hand sides: the right-hand side of eqn (9a) is included as a mass source term by adding a so-called weak contribution to the governing equations, $-\frac{1}{2}\int_\Omega [\partial_x Re(\rho_1 v_{1x}^*) + \partial_y Re(\rho_1 v_{1y}^*)]\tilde{p}_2 \, dV$ ($\tilde{p}_2$ being the pressure test function), while the right-hand side of eqn (9b) is added straightforwardly as a body force term. Furthermore, the fourth-order non-linear term $\rho_0(\langle \mathbf{v}_2 \rangle \cdot \nabla)\langle \mathbf{v}_2 \rangle$ is kept in the laminar flow equations in COMSOL to enhance numerical stability.

(iii) The acoustic radiation forces are determined using eqn (11) with the first-order fields of step (i).

(iv) Finally, the time-dependent motion of the particles is determined using the COMSOL Particle Tracing Module only taking into account the radiation force of step (iii) and the drag force of eqn (14).

The solution strategy was carried out on a computational mesh large enough for all dependent variables to reach convergence, while taking special care to properly resolve the acoustic boundary layer with an adequate computational mesh, see Section III E. This fine mesh was used when determining the first-order fields and the time-averaged second-order fields. In the subsequent simulation of the time-dependent particle motion, the flow field and radiation forces were interpolated to a coarser mesh to speed up the transient solving procedure substantially.

D Computer hardware requirements

The computation was performed on a DELL Precision 7500 workstation running Windows 7 (64-bit) equipped with 48 GB RAM (1333 MHz) and two hexa-core Intel Xeon X5650 processors of clock frequency 2.66 GHz and 12 MB cache.

When calculating the first-order acoustic fields in step (i), we used the mesh found by the mesh-convergence analysis described in the following subsection, and this resulted in about 3×10^6 degrees of freedom, a calculation time of 4.5 min, and a peak RAM usage of 64% or 31 GB. The calculation of the second-order acoustic fields in step (ii) required around 5×10^5 degrees of freedom and took 2 min, while having a peak RAM usage of 19% or 9 GB. The computation time for steps (iii) and (iv) was less than 15 s for calculation of 144 particle trajectories of 100 time steps and solved on a coarser mesh resulting in about 9×10^4 degrees of freedom.

E Mesh convergence

The computational mesh is generated from a maximum element size length d_{mesh} at the domain boundaries $\partial\Omega$ and a maximum element size in the bulk of the domain Ω given by $10d_{mesh}$. For illustrative purposes, the computational mesh shown in Fig. 3(a) is a coarse mesh with 1204 elements and $d_{mesh} = 20\delta$, or $\delta/d_{mesh} = 0.05$, where δ is the boundary layer thickness defined in eqn (7). In order to verify the correctness of the solution, a mesh-convergence analysis is required. The solutions are compared for decreasing mesh element size d_{mesh} to determine the point at which the solution becomes independent of any further decrease of d_{mesh}. We define a relative convergence parameter $C(g)$ for a solution g with respect to a reference solution g_{ref} taken to be the

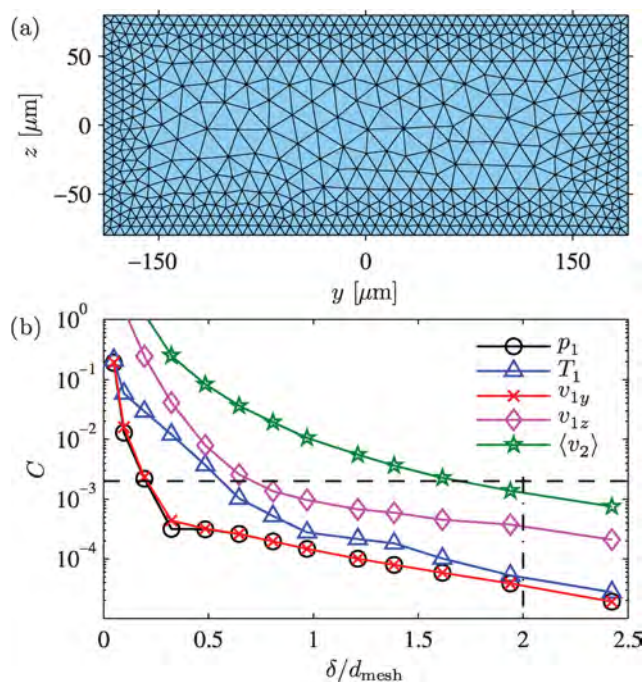**Fig. 3** (a) The computational mesh for a maximum element size of $d_{mesh} = 20\delta$ at the boundaries, resulting in a coarse mesh with only 1204 triangular elements. (b) Semi-logarithmic plot of the relative convergence parameter C, eqn (16), for the physical fields as the size of the mesh elements is decreased. The dashed line indicates a threshold of $C = 0.002$, chosen as a trade off between accuracy and computational time. For the second-order velocity field to get below this convergence threshold, a maximum element size of $d_{mesh} = 0.5\delta$ or $\delta/d_{mesh} = 2.0$ is needed at the boundaries of the domain (dash-dotted line).

solution for the smallest value of d_{mesh},

$$C(g) = \sqrt{\frac{\int (g - g_{ref})^2 \, dy \, dz}{\int (g_{ref})^2 \, dy \, dz}}. \quad (16)$$

For g_{ref} we have chosen $d_{mesh} = 0.3\delta$ or $\delta/d_{mesh} = 3.3$, which resulted in 2.6×10^5 triangular mesh elements.

The exponential convergence of both first- and second-order fields for $d_{mesh} < \delta$ shows up as straight lines in the semi-logarithmic plots of Fig. 3(b). The time-averaged second-order velocity field $\langle \mathbf{v}_2 \rangle$ converges considerably slower than the first-order fields, as it depends on the gradients of the first-order fields, and thus demands better resolution. In order to obtain a relative convergence of the second-order velocity field below 0.002 (dashed line), a maximum element size of $d_{mesh} = 0.5\delta$ or $\delta/d_{mesh} = 2.0$ is needed at the boundaries. This mesh size, which results in 1.2×10^5 triangular elements, is used for the results presented in this paper.

IV Results

The following results are aimed at showing the insensitivity of the horizontal half-wave resonance to the specific form of the ultrasound actuation, at characterizing the first- and second-order acoustic fields, and at investigating the dependence of the acoustophoretic microparticle motion on system geometry and material parameters.

A Actuation

The ultrasound actuation is modeled using the velocity boundary condition in eqn (4c) at the frequency 1.97 MHz to excite the horizontal half-wave resonance in our model system Fig. 2(b). Using the following three actuation modes for the velocity boundary condition v_{bc} in eqn (4c),

$$v_{bc}^A(\pm w/2, z) = \pm v_{bc,0}^A, \tag{17a}$$

$$v_{bc}^B(y, -h/2) = v_{bc,0}^B \sin\left(2\pi \frac{y}{w}\right), \tag{17b}$$

$$v_{bc}^C(y, -h/2) = v_{bc,0}^C \left(\frac{1}{2} - \frac{y}{w}\right)\left(\frac{1}{2} + \frac{y}{w}\right)^2, \tag{17c}$$

we show the expected result that this resonance is indeed excited regardless of the detailed spatial dependence of v_{bc} as long as the oscillation frequency equals the resonance frequency.

For all three actuation modes, the amplitude of the velocity boundary conditions is chosen in such a way that the line integral of the absolute value $|v_{bc}|$ of the velocity along the perimeter $\partial\Omega$ of the domain Ω is given in terms of the angular frequency ω and a characteristic value d_0 of the displacement of an actuated boundary,

$$\oint_{\partial\Omega} |v_{bc}^X|\, d\ell = 2h\omega d_0, \quad X = A, B, C. \tag{18}$$

In particular, the normalization constant $2h$ is chosen so that $v_{bc,0}^A = \omega d_0$, with $d_0 = 0.1$ nm, a typical value of displacements,[38] which results in resonance amplitudes in the range of those measured in typical experiments.[7,39–41]

The first-order pressure fields resulting from the three different actuation modes are shown in Fig. 4. It is seen that all of the actuation modes excite the horizontal half-wave 1.97-MHz resonance. Although the velocity boundary conditions have been normalized, the amplitude of the resonance is different for each of the three actuation modes, i.e. each actuation mode couples to the resonance mode with its own strength. In the studies presented in the rest of this paper, we have used the velocity boundary condition eqn (17a), shown in Fig. 4(a), due to its simplicity and strong coupling to the resonance mode.

B First-order fields

We now turn to a study of the first-order fields resulting from the velocity boundary condition eqn (17a) and Fig. 4(a). In Fig. 5, color plots of the pressure p_1, temperature T_1, horizontal velocity
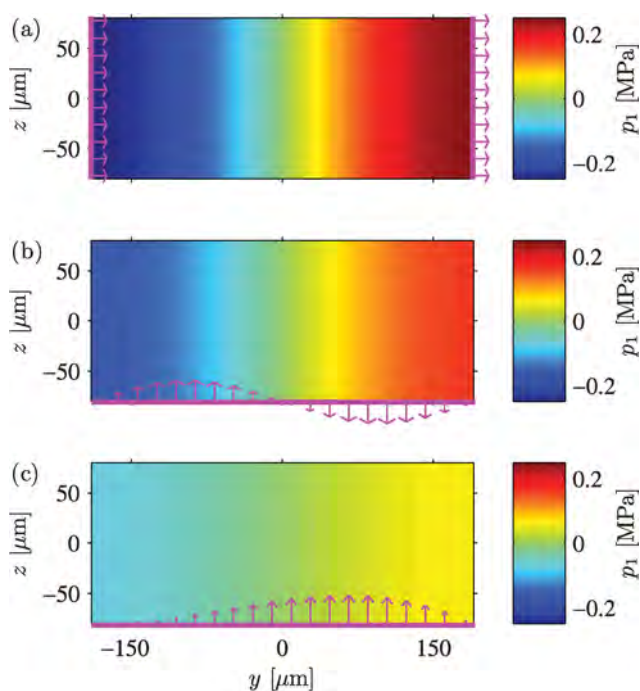

Fig. 4 Three different actuation modes v_{bc} (magenta arrows) of the water-filled cavity. Color plot of the first-order pressure field p_1 resulting from the actuation, eqn (17). In all cases the actuation frequency is 1.97 MHz, corresponding to the lowest resonance frequency of the cavity, and it is seen that all three actuation modes excite the horizontal half-wave resonance. The pressure amplitude of the resonance mode is (a) 0.24 MPa with side-wall actuation, (b) 0.16 MPa with anti-symmetric bottom-wall actuation, and (c) 0.06 MPa with non-symmetric bottom-wall actuation.
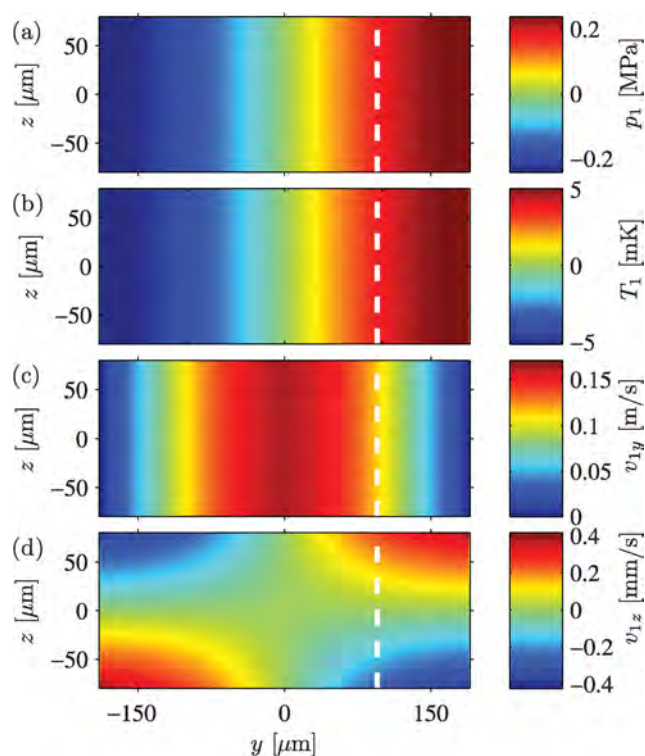

Fig. 5 Color plots of the amplitudes of the oscillating first-order fields in the water-filled channel at the horizontal standing half-wave 1.97-MHz resonance excited by velocity boundary condition eqn (17a): (a) pressure p_1, identical to panel (a) in Fig. 4, (b) temperature T_1, (c) horizontal velocity v_{1y}, and (d) vertical velocity v_{1z}. The horizontal velocity is much larger than the vertical velocity, arising because of the interaction of the acoustic resonance with the bottom and top walls. The sub-micrometer thin viscous boundary cannot be seen on the 100-μm scale of the plot. The dashed white lines indicate the domain for the line plots in Fig. 6.
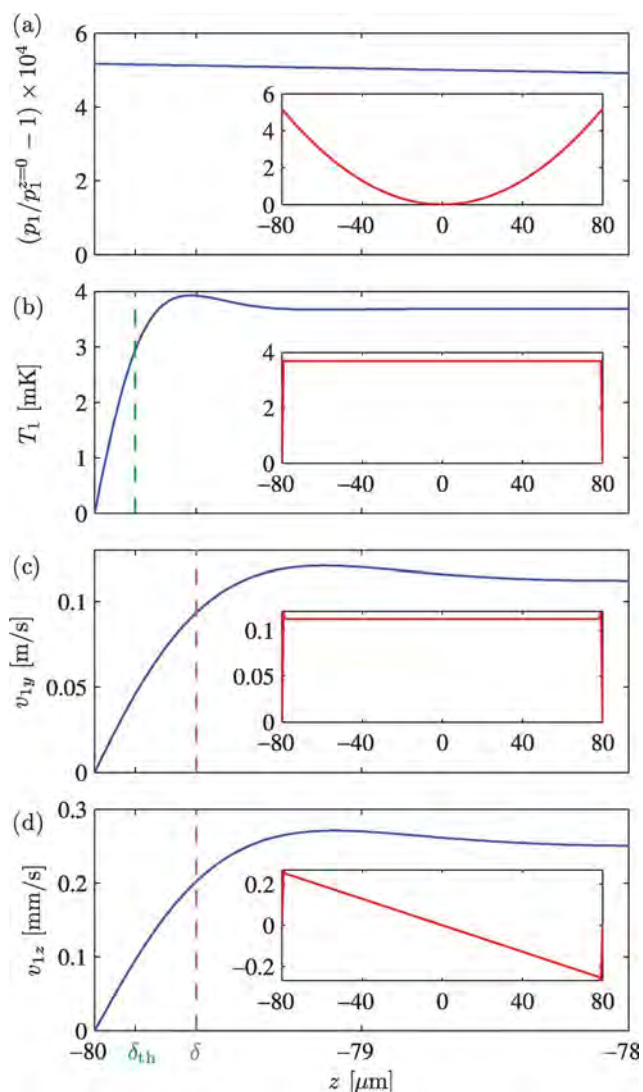
Fig. 6 Line plots, along the dashed white lines at $y = w/4$ shown in Fig. 5, of the amplitudes of the oscillating first-order fields: (a) relative pressure change $p_1/p_1^{z=0} - 1$, (b) temperature T_1, (c) horizontal velocity v_{1y}, and (d) vertical velocity v_{1z}. The main plots (blue curves) show the field amplitudes close to the bottom wall, while the insets (red curves) show the field amplitudes along the entire height of the channel. The characteristic length scales of the thermal and viscous boundary layers, δ_{th} and δ, are indicated by the green and magenta dashed lines, respectively. T_1, v_{1y}, and v_{1z} all show marked variations on the length scale of the boundary layer, while p_1 and v_{1z} only show variations across the full height of the domain.

v_{1y}, and vertical velocity v_{1z} are shown. The amplitudes and structures of p_1, T_1, and v_{1y} relate to the acoustic resonance, while v_{1z} arises due to the viscous interaction of the horizontal half-wave resonance in the bulk with the bottom and top walls. Consequently, the magnitude of v_{1z} is insignificant compared to the magnitude of v_{1y}. The amplitudes of p_1 and T_1 have the same spatial structure, shifted horizontally by $\lambda/4$ with respect to the spatial structure of v_{1y}.

In Fig. 6 the amplitudes of the first-order fields are plotted along the dashed white lines at $y = w/4$ shown in Fig. 5. In Fig. 6(a) we have plotted the relative pressure change, $p_1/p_1^{z=0} - 1$,

with respect to the pressure amplitude at the center $(y,z) = (w/4,0)$. This relative change is in the order of 10^{-4}, implying that p_1 is nearly independent of z. In particular, p_1 shows no marked variation on the length scale of the boundary layer thickness δ as opposed to the velocity v_{1y} and temperature T_1 of Fig. 6(b)–(c). To fulfill the boundary conditions in eqn (4), the latter two decrease from their bulk values to zero at the wall over a few times δ_{th} and δ, respectively, which defines the thicknesses of the thermal and viscous boundary layers, respectively (dashed lines in Fig. 6). Further, also v_{1z} increases from zero at the wall, but then it exhibits a slow linear decrease outside the boundary layer, Fig. 6(d). T_1, v_{1y}, and v_{1z} all overshoot slightly before settling at their respective bulk values, an effect similar to that observed in the classical problem of a planar wall executing in-plane oscillations.[20] While T_1 and v_{1y} show no variations in the height of the channel outside the boundary layers, p_1 and v_{1z} do so, with p_1 being symmetric (nearly parabolic) and v_{1z} being anti-symmetric (nearly linear). These variations of p_1 and v_{1z} result from the viscous interaction between the horizontal acoustic resonance and the bottom and top wall, bounding the acoustic resonance fields.
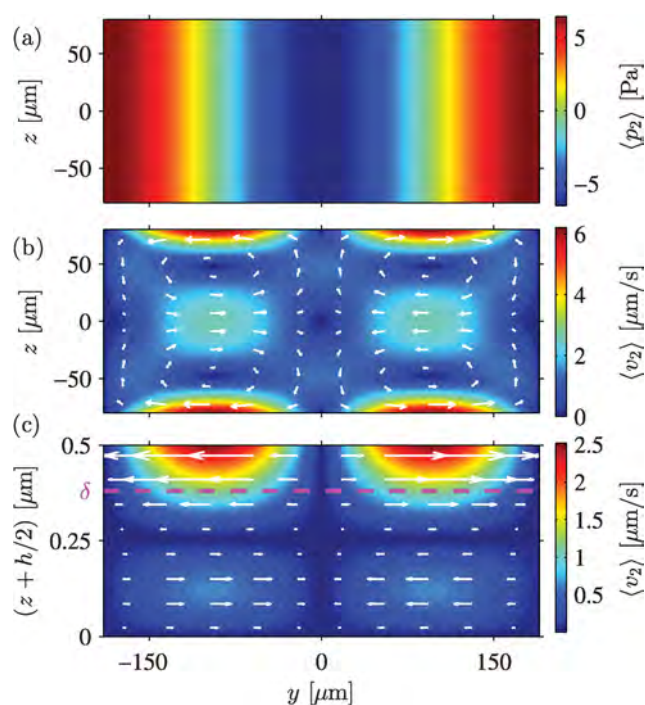

Fig. 7 Time-averaged second-order fields in the water-filled channel excited in the horizontal half-wave 1.97-MHz resonance by the side-wall actuation shown in Fig. 4(a) and driven by the first-order fields plotted in Fig. 5. (a) Color plot of the time-averaged second-order pressure $\langle p_2 \rangle$ with a magnitude approximately 2.5×10^{-5} times smaller than the amplitude of the oscillating first-order pressure p_1 in Fig. 5(a). (b) Vector plot (white arrows) of the time-averaged second-order streaming velocity $\langle \mathbf{v}_2 \rangle$ and color plot of its magnitude $\langle v_2 \rangle$. Four bulk (Rayleigh) streaming rolls are clearly seen having the maximum speed near the top and bottom walls. (c) Zoom-in on the 0.4-μm-thick boundary layer near the bottom wall exhibiting the two boundary (Schlichting) streaming rolls that drive the bulk (Rayleigh) streaming rolls.

C Second-order fields and acoustic streaming

As described by eqn (9) the non-linear interactions of the first-order fields give rise to time-averaged second-order fields, resulting in a static pressure field and a steady velocity field as shown in Fig. 7. The time-averaged second-order fields exhibit a spatial oscillation in the horizontal y-direction of wave length $\lambda/2$. This is reminiscent of the spatial period doubling for the classical infinite parallel-plate system of Fig. 1.

The magnitude of the time-averaged second-order pressure $\langle p_2 \rangle$ in Fig. 7(a) is approximately 2.5×10^{-5} times smaller than the amplitude of the oscillating first-order pressure in Fig. 5(a). The time-averaged velocity field $\langle v_2 \rangle$ in Fig. 7(b) contains four bulk (Rayleigh) streaming rolls. The streaming velocity is maximum close to the top and bottom wall and has two local maxima on the horizontal center axis $z = 0$, where opposite pairs of bulk rolls meet. The solution in Fig. 7(b) is similar to Rayleigh's analytical solution[17,20] sketched in Fig. 1, but it deviates on the following two points: (*i*) as we consider a rectangular geometry and not parallel plates, the velocity is forced to be zero at the side walls, which slightly slows down the rotational flow of the streaming rolls, and (*ii*) as we are not in the limit $h \ll \lambda$, the strength of the streaming rolls decreases slightly before meeting in the center of the channel, which results in a lower magnitude of the streaming velocity in the horizontal center plane than predicted by Rayleigh.

Fig. 7(c) shows a zoom-in on the 0.4-μm-thick viscous boundary layer close to the bottom wall containing two boundary (Schlicting) streaming rolls. These boundary rolls are very elongated in the horizontal direction; the z-axis in Fig. 7(c) is stretched nearly a factor 10^3 relative to the y-axis. It is important to mention that the boundary streaming rolls are generated by the non-linear interactions of the first-order fields inside the boundary layer, whereas the bulk streaming rolls are driven by the boundary streaming rolls and not by the non-linear interaction of the first-order fields in the bulk. The time-averaged second-order velocity $\langle v_2 \rangle$ is zero at the bottom wall, thus fulfilling the boundary conditions eqn (4b), while the maximum of its horizontal component $v_{2y}^{\text{bnd}} = 6.42$ μm s^{-1} is reached at a distance of approximately 3δ from the wall. The maximum bulk amplitude $U_1 = 0.162$ m s^{-1} of the horizontal first-order velocity component, v_{1y} shown in Fig. 5(c), is reached at the channel center $y = 0$. From this we calculate the characteristic velocity ratio $\Psi = c_0 v_{2y}^{\text{bnd}}/U_1^2 = 0.367$, which deviates less than 3% from the value $\Psi = 3/8 = 0.375$ of the parallel-plate model eqn (10).

D Particle tracing simulations

In most experimental microfluidic flow visualization techniques, tracer particles are employed.[42] To mimic this and to ease comparison with experiment, we have performed particle tracing simulations using the technique described in Section III B. In all simulations, we have studied the motion of 144 polystyrene microparticles suspended in water and distributed evenly at the initial time $t = 0$ as shown in Fig. 8(a).

In Fig. 8(b)–(f), the particle trajectories after 10 s of acoustophoretic motion of the 144 microparticles are shown. Within each panel, all particles have the same diameter $2a$, but the particle size is progressively enlarged from one panel to the next: (b) $2a = 0.5$ μm, (c) 1 μm, (d) 2 μm, (e) 3 μm, and (f) 5 μm.

For the smallest particles, panels (b) and (c), the drag force from the acoustic streaming dominates the particle motion, and the characteristic streaming flow rolls are clearly visualized. For the larger particles, panels (e) and (f), the acoustic radiation force dominates the particle motion, and the particle velocity $\boldsymbol{u}$ is nearly horizontal with the sinusoidal spatial dependence given by $u_y(y) = F_{1D}^{\text{rad}}(y)/(6\pi\eta a)$ found from eqn (13a). This results in a focusing motion of the particles towards the vertical pressure nodal plane at $y = 0$. Panels (d) and (e) show an intermediate regime where drag and radiation forces are of the same order of magnitude.

At the nodal plane $y = 0$ the radiation forces are zero, and consequently for times t larger than 10 s all particles in panel (f) that have reached $y = 0$ end up at $(y,z) = (0, \pm h/2)$ due to the weak but non-zero streaming-induced drag forces.

The cross-over from one acoustophoretic behavior to the other as a function of particle size, with a critical particle diameter of 2 μm found in Fig. 8(d), is in agreement with the following scaling argument:[16] If we assume a force balance between the radiation force and the drag force from acoustic streaming, $\boldsymbol{F}^{\text{rad}} = -\boldsymbol{F}^{\text{drag}}$, keeping a given particle fixed ($\boldsymbol{u} = \boldsymbol{0}$), and if we estimate the magnitude of the streaming velocity to be given by eqn (10) as $\langle v_2 \rangle = \Psi U_1^2/c_0$, where Ψ is a geometry-dependent factor of order unity, then eqn (13) and (14) lead to

$$\pi a_c^3 q \rho_0 U_1^2 \Phi \approx 6\pi\eta a_c \Psi \frac{U_1^2}{c_0}, \qquad (19)$$

where a_c is the critical particle radius. Thus, as found in eqn (16), the critical particle diameter $2a_c$ becomes

$$2a_c = \sqrt{12\frac{\Psi}{\Phi}}\,\delta \approx 2.0 \text{ μm}. \qquad (20)$$

The value is calculated using $\Psi = 0.375$, valid for a planar wall (eqn (10)), and $\Phi = 0.165$, obtained for polystyrene particles with diameters between 0.5 μm and 5 μm in water obtained from eqn (13b) using the parameter values from Table 1. The relation eqn (20) for the critical cross-over particle diameter is important for designing experiments relying on specific acoustophoretic behaviors as function of particle size. Channel geometry enters through the factor Ψ, particle and liquid material parameters through Φ, and liquid parameters and frequency through the boundary layer thickness δ.

E Streaming for an increased aspect ratio

As an example of how geometry affects the acoustophoretic motion of polystyrene microparticles, we study here the consequences of increasing the aspect ratio of the channel cross-section from $h/w = 0.42$ to 2 keeping all other parameters fixed. As illustrated in Fig. 9(a), the streaming velocity field is only significant close to the top and bottom of the channel for the large aspect ratio $h/w = 2$. This happens because given enough vertical space, the vertical extension Δ of the streaming roll is identical to the horizontal one, which is $\Delta = \lambda/4$. For the horizontal half-wave resonance in a channel of aspect ratio $h/w = 2$ we have $\lambda = 2w = h$, which implies $\Delta = h/4$, and we therefore expect a streaming-free region with a vertical extent of $h - 2(h/4) = h/2$ around the center of the channel, which indeed is seen in Fig. 9(a).
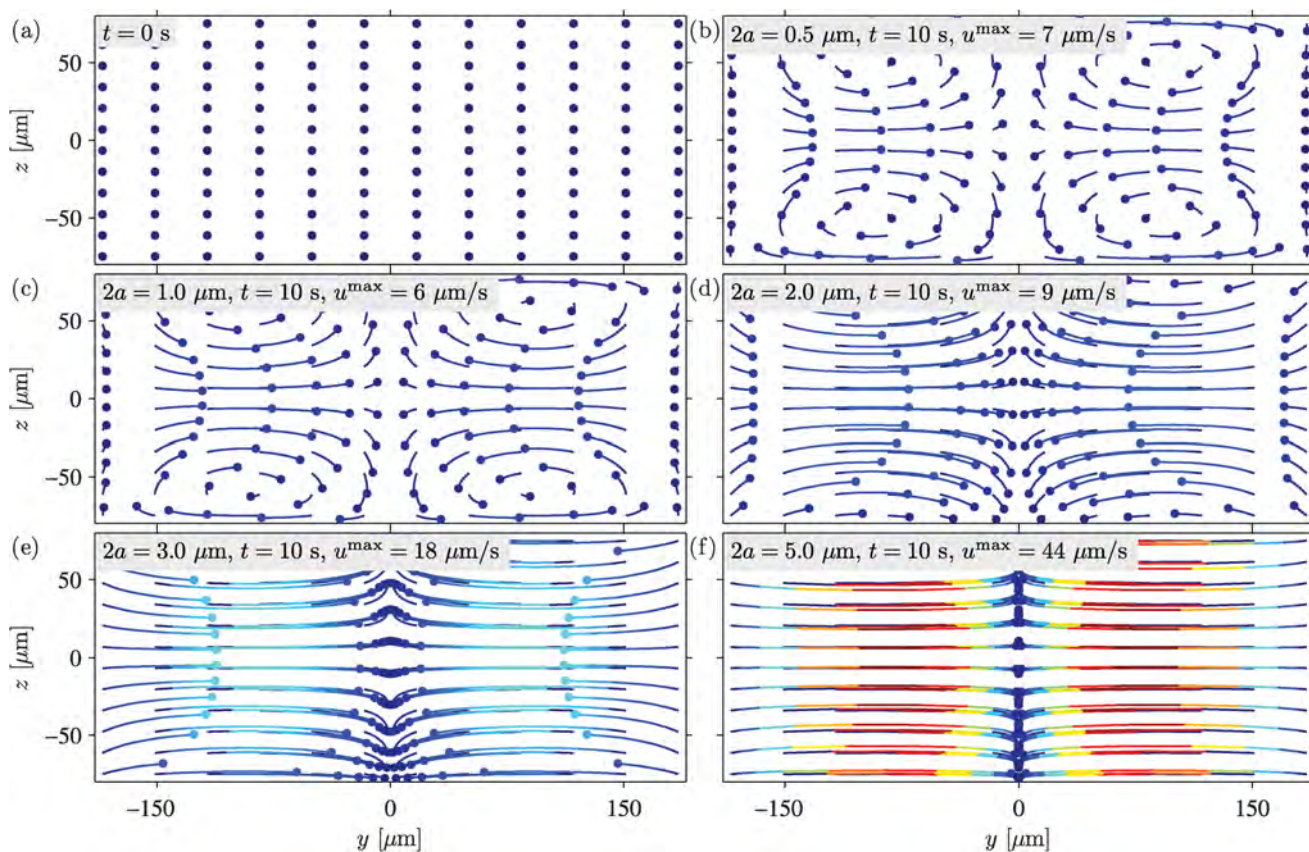
Fig. 8 (a) The starting positions (dots) of 144 evenly distributed particles at $t = 0$ s in the computational domain at the onset of the horizontal half-wave 1.97-MHz resonance shown in Fig. 5 and 7. The following five panels show the trajectories (colored lines) and positions (dots) that the particles have reached by acoustophoresis at $t = 10$ s for five different particle diameters: (b) 0.5 μm, (c) 1 μm, (d) 2 μm, (e) 3 μm, and (f) 5 μm. The colors indicate the instantaneous particle velocity u ranging from 0 μm s^{-1} (dark blue) to 44 μm s^{-1} (dark red). The lengths of the trajectories indicate the distance covered by the particles in 10 s. Streaming-induced drag dominates the motion of the smallest particles, which consequently are being advected along the acoustic streaming rolls of Fig. 7(b). In contrast, the acoustic radiation force dominates the motion of the larger particles, which therefore are forced to the vertical nodal plane at $y = 0$ of the first-order pressure p_1 shown in Fig. 5(a).

As a consequence, the acoustophoretic motion of particles in the center region is controlled by the radiation force. This is illustrated in Fig. 9(b), where trajectories of small 1-μm-diameter particles are shown. For $-h/4 < z < h/4$ their motion is similar to the radiation-force dominated motion of the larger 5-μm-diameter particles moving in the shallow channel with $h/w = 0.42$ as shown in Fig. 8(f). Near the top and bottom walls, the 1 μm diameter particles exhibit the usual small-particle streaming-induced motion.

Clearly, geometry can be used to obtain more control of the acoustophoretic motion of suspended particles in microchannels.

F Streaming in a high-viscosity buffer

According to eqn (20), the critical particle diameter for cross-over between radiation-dominated and streaming-dominated acoustophoretic motion is proportional to the boundary layer thickness $\delta = \sqrt{2\eta/(\rho_0\omega)}$. Obviously, viscosity can also be used to control acoustophoresis. We therefore studied the effects of replacing water ($\eta = 1$ mPa s) with glycerol mixtures, in particular the 50% glycerol-in-water mixture ($\eta = 5$ mPa s), for which the relevant material parameters are listed in Table 1.

First, to ensure comparable conditions, we wanted to excite the horizontal half-wave resonance in the glycerol-in-water

system. As the speed of sound of the glycerol mixture is 15% larger than that of water, we found the resonance frequency to be $f = c_0/(2w) = 2.27$ MHz. This frequency was used in the velocity boundary condition eqn (17a) to calculate the results shown in Fig. 10 for the first-order pressure field, the time-averaged second-order streaming velocity field, and particle trajectories for 5-μm-diameter polystyrene particles.

The glycerol-in-water and the water system are actuated with the same boundary velocity given in eqn (18), but the difference in viscosity of the two liquids leads to different acoustic responses. The amplitude of the induced first-order resonance pressure is reduced by a factor of 2.6 from 0.243 MPa in the low-viscosity water of Fig. 5(a) to 0.094 MPa in the high-viscosity glycerol mixture of Fig. 10(a). Likewise, the induced streaming velocity $\langle v_{2y}^{bnd} \rangle$ near the boundary is reduced by a factor of 15 from 6.42 μm s^{-1} in water, Fig. 7(b), to 0.43 μm s^{-1} in glycerol-in-water, Fig. 10(b). In contrast, given the validity of Rayleigh's streaming theory, the velocity ratio $\Psi = c_0\langle v_{2y}^{bnd} \rangle/U_1^2$ should be independent of viscosity. For the glycerol-in-water mixture it is 0.336 deviating 8% from the value in water, see Section IV C, and 10% from the Rayleigh value 3/8 of eqn (10). The significant difference in the numerically determined values of Ψ for water and glycerol-in-water points to the inadequacy of the Rayleigh
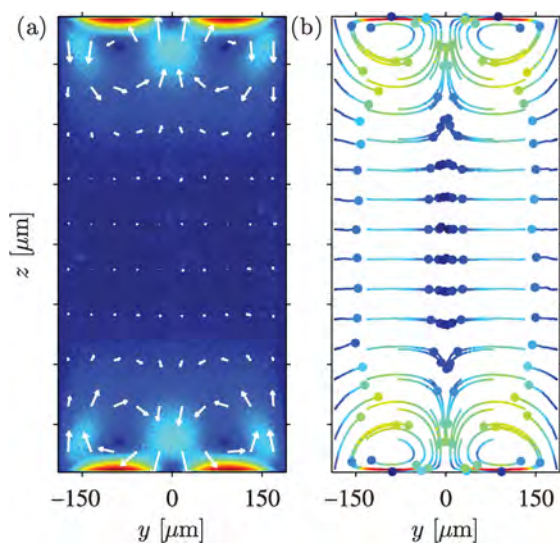
Fig. 9 Acoustophoresis in a high-aspect-ratio channel. The setup is identical to Fig. 4(a) except that for the fixed width $w = 0.38$ mm the channel height h has been increased from 0.16 mm (aspect ratio $h/w = 0.42$) to 0.76 mm (aspect ratio $h/w = 2$). (a) Vector plot (white arrows), similar to Fig. 7(b), of the time-averaged second-order streaming velocity $\langle v_2 \rangle$ and color plot [from 0 μm s^{-1} (dark blue) to 4.2 μm s^{-1} (dark red)] of its magnitude. (b) Particle tracing plot for 1-μm-diameter polystyrene particles corresponding to Fig. 8(c) but for time $t = 100$ s, aspect ratio $h/w = 2$, and velocity ranging from 0 μm s^{-1} (dark blue) to 3.3 μm s^{-1} (dark red). In this high aspect-ratio geometry the acoustic streaming flow rolls are located near the top and bottom walls leaving the center region nearly streaming free.

theory in a rectangular channel. This is perhaps not a surprise, as this theory is derived for an infinite parallel-plate channel.

In Fig. 10(c) is shown that the viscous boundary-layer thickness in the glycerol-in-water mixture at 2.27 MHz is $\delta = 0.79$ μm, a factor 2.1 larger than the value $\delta = 0.38$ μm in water at 1.97 MHz shown in Fig. 7(c). As the two resonance frequencies only differ by 10%, the change in the boundary-layer thickness is mainly due to the viscosity ratio, $\sqrt{5 \text{ mPa s}}/\sqrt{1 \text{ mPa s}} \approx 2.2$.

Finally, from eqn (10) using $\Psi = 3/8$ and $\Phi = 0.031$, we calculated the critical particle diameter to be $2a_c = 9.5$ μm for the cross-over from radiation-dominated to streaming-dominated acoustophoretic motion in the glycerol-in-water system. This value explains why the particle trajectories for the 5-μm-diameter polystyrene particles in Fig. 10(d) appear to be much more influenced by the acoustic streaming rolls, compared to the same-sized particles in water, Fig. 8(f). Instead, Fig. 10(d) resembles more the motion of the 1-μm-diameter particles in water, Fig. 8(c). This resemblance can be quantified by the ratio a/a_c: for 5-μm-diameter particles in the glycerol-in-water mixture it is 0.52, while for 1-μm-diameter particles in pure water it is 0.50, only 4% lower. Note that because of the reduction in streaming velocity by the above-mentioned factor of 15, we have chosen to follow the particles in the glycerol-in-water mixture for 150 s and in water only for 10 s.

V Concluding discussion

The finite element method was successfully used to model the acoustophoretic motion of microparticles inside a microchannel
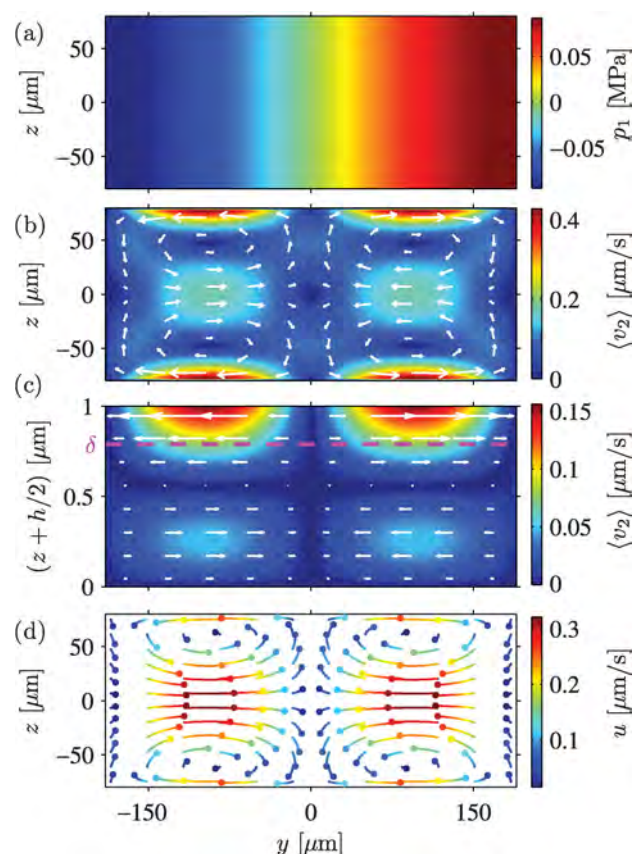

Fig. 10 Acoustophoresis in a 50% glycerol-in-water mixture. The setup is identical to Fig. 4(a) except that the resonance frequency is increased to $f = c_0/(2w) = 2.27$ MHz. (a) Color plot of the pressure p_1 showing the horizontal half-wave resonance. (b) Vector plot (white arrows) of the time-averaged second-order streaming velocity $\langle v_2 \rangle$ and color plot of its magnitude corresponding to Fig. 7(b). (c) Zoom-in on the 0.4-μm-thick boundary layer near the bottom wall corresponding to Fig. 7(c). (d) Particle tracing plot for 5-μm-diameter polystyrene particles corresponding to Fig. 8(f) but for 150 s. Contrary to the water-filled channel in Fig. 8(f), the motion of the 5-μm-particles in the more viscous glycerol-in-water mixture are dominated by the streaming-induced drag, whereby the particle trajectories end up looking more like those of the smaller 1-μm-diameter particles Fig. 8(c).

subject to a transverse horizontal half-wave ultrasound resonance. The motion is due to the combined effect of Stokes drag from the time-averaged second-order streaming flow and the acoustic radiation forces. To achieve this, the first-order acoustic field of a standing wave was determined inside a microchannel cavity by solving the linearized compressional Navier–Stokes equation, the continuity equation, and the heat equation, while resolving the boundary layers near rigid walls. The first-order field was then used to determine the streaming flow and the acoustic radiation forces, and from this the time-dependent trajectories of an ensemble of non-interacting microparticles was calculated.

A main result is the characterization of the cross over from streaming-dominated to radiation-dominated acoustophoretic microparticle motion as a function of particle diameter, geometry, and viscosity. Using a water-filled shallow microchannel as the base example, we demonstrated how to get rid of streaming effects in the center region of a microchannel by

increasing the height-to-width ratio. In contrast, by replacing water by a 50% glycerol-in-water mixture, we demonstrated how to enhance the streaming effects. The former study may form a good starting point for designing streaming-free devices for handling of sub-micrometer particles, such as small cells, bacteria, and viruses, and thus supporting concurrent experimental efforts to suppress streaming, e.g., through averaging over alternating actuation frequencies.[43] The latter study is pointing in the direction of developing devices with improved mixing capabilities by enhancing streaming.[44,45] We have thus shown that our simulation tool has a great potential for enabling improved design of acoustofluidic devices.

An important next step is to obtain a direct experimental verification of our numerical simulation. As the relative uncertainty of measured acoustophoretic particle velocities in current experimental acoustofluidics is 5% or better,[8] it is within reach to obtain such an experimental verification. A problem is of course that the streaming fields calculated in this work are in the vertical plane, which is perpendicular to the usual horizontal viewing plane, and thus specialized 3-dimensional visualization techniques are required such as stereoscopic micro particle–image velocimetry[42,46] or astigmatism particle tracking velocimetry.[47] But even if such 3D-methods are complex to carry out, it would be worth the effort given the great use of having a well-verified numerical model of acoustophoretic particle motion.

Given a successful experimental verification, it would clearly be valuable to extend the numerical model. One obvious step, which is not conceptually difficult, but which would require significant computational resources, would be to make a full 3D-model taking the elastic properties of the chip surrounding the microchannel into account. The relevance of such an extension lies in the sensitivity of the acoustic streaming on the boundary conditions. Only a full acousto-elastic theory would supply realistic and accurate boundary conditions. Another class of obvious model extensions deals with the modeling of the particle suspension. A trivial extension would be to include gravity and buoyancy, but more importantly and much more difficult would be the inclusion of particle–particle and particle–wall interactions that are neglected in the present work. These many-particle effects include, e.g., the generation of streaming flow in the boundary layer of each particle[48] and not just the boundary layer of the wall. After such an extension, our model could be used together with high-precision experiments as a new and better research tool to study and clarify the many yet unsolved problems with particle–particle and particle–wall interactions in acoustofluidics.

The above-mentioned applications all demonstrate that our numerical model is both timely and has a huge potential within device design and studies of basic physical aspects of acoustophoresis.

Acknowledgements

References

1 J. Friend and L. Y. Yeo, *Rev. Mod. Phys.*, 2011, **83**, 647–704.
2 H. Bruus, J. Dual, J. Hawkes, M. Hill, T. Laurell, J. Nilsson, S. Radel, S. Sadhal and M. Wiklund, *Lab Chip*, 2011, **11**, 3579–3580.
3 A. Lenshof, C. Magnusson and T. Laurell, *Lab Chip*, 2012, **12**, 1210–1223.
4 M. Gedge and M. Hill, *Lab Chip*, 2012, **12**, 2998–3007.
5 H. Bruus, *Lab Chip*, 2012, **12**, 1014–1021.
6 M. Wiklund, R. Green and M. Ohlin, *Lab Chip*, 2012, **12**, 2438–2451.
7 R. Barnkob, P. Augustsson, T. Laurell and H. Bruus, *Lab Chip*, 2010, **10**, 563–570.
8 P. Augustsson, R. Barnkob, S. T. Wereley, H. Bruus and T. Laurell, *Lab Chip*, 2011, **11**, 4152–4164.
9 K. Yosioka and Y. Kawasima, *Acustica*, 1955, **5**, 167–173.
10 L. P. Gorkov, *Soviet Physics – Doklady*, 1962, **6**, 773–775.
11 M. Settnes and H. Bruus, *Phys. Rev. E*, 2012, **85**, 016327.
12 K. Frampton, S. Martin and K. Minor, *Appl. Acoust.*, 2003, **64**, 681–692.
13 M. Hamilton, Y. Ilinskii and E. Zabolotskaya, *J. Acoust. Soc. Am.*, 2003, **113**, 153–160.
14 J. F. Spengler, W. T. Coakley and K. T. Christensen, *AIChE J.*, 2003, **49**, 2773–2782.
15 S. M. Hagsäter, T. G. Jensen, H. Bruus and J. P. Kutter, *Lab Chip*, 2007, **7**, 1336–1344.
16 H. Bruus, *Lab Chip*, 2012, **12**, 1578–1586.
17 L. Rayleigh, *Philos. Trans. R. Soc. London*, 1884, **175**, 1–21.
18 H. Schlichting, *Physik Z*, 1932, **33**, 327–335.
19 J. Lighthill, *J. Sound Vib.*, 1978, **61**, 391–418.
20 L. D. Landau and E. M. Lifshitz, *Fluid Mechanics*, Pergamon Press, Oxford, 2nd edn, 1993, **vol. 6**, Course of Theoretical Physics.
21 H. Lei, D. Henry and H. BenHadid, *Appl. Acoust.*, 2011, **72**, 754–759.
22 M. K. Aktas and B. Farouk, *J. Acoust. Soc. Am.*, 2004, **116**, 2822–2831.
23 P. M. Morse and K. U. Ingard, *Theoretical Acoustics*, Princeton University Press, Princeton NJ, 1986.
24 A. D. Pierce, *Acoustics*, Acoustical Society of America, Woodbury, 1991.
25 D. T. Blackstock, *Physical acoustics*, John Wiley and Sons, Hoboken NJ, 2000.
26 L. D. Landau and E. M. Lifshitz, *Statistical physics, Part 1*, Butterworth-Heinemann, Oxford, 3rd edn, 1980, **vol. 5**.
27 W. L. Nyborg, *J. Acoust. Soc. Am.*, 1953, **25**, 68–75.
28 M. Koklu, A. C. Sabuncu and A. Beskok, *J. Colloid Interface Sci.*, 2010, **351**, 407–414.
29 COMSOL Multiphysics 4.2a, www.comsol.com, 2012.
30 CRCnetBASE Product, *CRC Handbook of Chemistry and Physics*, Taylor and Francis Group, www.hbcpnetbase.com/, 92nd edn, 2012.
31 L. Bergmann, *Der Ultraschall und seine Anwendung in Wissenschaft und Technik*, S. Hirzel Verlag, Stuttgart, 6th edn, 1954.
32 P. H. Mott, J. R. Dorgan and C. M. Roland, *J. Sound Vib.*, 2008, **312**, 572–575.
33 L. D. Landau and E. M. Lifshitz, *Theory of Elasticity. Course of Theoretical Physics*, Pergamon Press, Oxford, 3rd edn, 1986, **vol. 7**.
34 N.-S. Cheng, *Ind. Eng. Chem. Res.*, 2008, **47**, 3285–3288.
35 F. Fergusson, E. Guptill and A. MacDonald, *J. Acoust. Soc. Am.*, 1954, **26**, 67–69.
36 O. Bates, *Ind. Eng. Chem.*, 1936, **28**, 494–498.
37 F. Gucker and G. Marsh, *Ind. Eng. Chem.*, 1948, **40**, 908–915.
38 J. Dual and T. Schwarz, *Lab Chip*, 2012, **12**, 244–252.
39 M. Wiklund, P. Spégel, S. Nilsson and H. M. Hertz, *Ultrasonics*, 2003, **41**, 329–333.
40 J. Hultström, O. Manneberg, K. Dopf, H. M. Hertz, H. Brismar and M. Wiklund, *Ultrasound Med. Biol.*, 2007, **33**, 145–151.
41 R. Barnkob, I. Iranmanesh, M. Wiklund and H. Bruus, *Lab Chip*, 2012, **12**, 2337–2344.
42 M. Raffel, C. E. Willert, S. T. Wereley and J. Kompenhans, *Particle Image Velocimetry*, Springer, New York, 2007.
43 M. Ohlin, A. Christakou, T. Frisk, B. Önfelt and M. Wiklund, Proc. 15th MicroTAS, 2 - 6 October 2011, Seattle (WA), USA, 2011, pp. 1612–1614.
44 K. Sritharan, C. Strobl, M. Schneider, A. Wixforth and Z. Guttenberg, *Appl. Phys. Lett.*, 2006, **88**, 054102.
45 T. Frommelt, M. Kostur, M. Wenzel-Schaefer, P. Talkner, P. Haenggi and A. Wixforth, *Phys. Rev. Lett.*, 2008, **100**, 034502.
46 R. Lindken, M. Rossi, S. Grosse and J. Westerweel, *Lab Chip*, 2009, **9**, 2551–2567.
47 C. Cierpka, M. Rossi, R. Segura and C. J. Kaehler, *Meas. Sci. Technol.*, 2011, **22**, 015401.
48 S. Sadhal, *Lab Chip*, 2012, **12**, 2600–2611.

Paper published in Phys Rev E, November 2012

Acoustic radiation- and streaming-induced microparticle velocities determined by microparticle image velocimetry in an ultrasound symmetry plane

Rune Barnkob,[1,*] Per Augustsson,[2] Thomas Laurell,[2,3] and Henrik Bruus[4]

[1]*Department of Micro- and Nanotechnology, Technical University of Denmark, DTU Nanotech Building 345 East,*
DK-2800 Kongens Lyngby, Denmark
[2]*Department of Measurement Technology and Industrial Electrical Engineering, Division of Nanobiotechnology, Lund University,*
Box 118, S-221 00 Lund, Sweden
[3]*Department of Biomedical Engineering, Dongguk University, Seoul, South Korea*
[4]*Department of Physics, Technical University of Denmark, DTU Physics Building 309, DK-2800 Kongens Lyngby, Denmark*
(Received 31 August 2012; published 13 November 2012)

We present microparticle image velocimetry measurements of suspended microparticles of diameters from 0.6 to 10 μm undergoing acoustophoresis in an ultrasound symmetry plane in a microchannel. The motion of the smallest particles is dominated by the Stokes drag from the induced acoustic streaming flow, while the motion of the largest particles is dominated by the acoustic radiation force. For all particle sizes we predict theoretically how much of the particle velocity is due to radiation and streaming, respectively. These predictions include corrections for particle-wall interactions and ultrasonic thermoviscous effects and match our measurements within the experimental uncertainty. Finally, we predict theoretically and confirm experimentally that the ratio between the acoustic radiation- and streaming-induced particle velocities is proportional to the actuation frequency, the acoustic contrast factor, and the square of the particle size, while it is inversely proportional to the kinematic viscosity.

I. INTRODUCTION

Acoustofluidics, i.e., ultrasound handling of fluids and particle suspensions, recently reviewed in Refs. [1,2], is a field in rapid growth for its use in biological applications such as separation and manipulation of cells and bioparticles. Microchannel acoustophoresis has largely been limited to manipulation of micrometer-sized particles such as yeast [3], blood cells [4], cancer cells [5–7], natural killer cells [8], and affinity ligand complexed microbeads [9], for which the acoustic radiation force dominates. Precise acoustic control of submicrometer particles (e.g., small bacteria, vira, and large biomolecules) remains a challenge due to induction of acoustic streaming of the suspending fluid. Nevertheless, acoustic streaming has been used to enhance the convective transport of substrate in a microenzyme reactor for improved efficiency [10], while acoustic manipulation of submicrometer particles has been achieved in a few specific cases including enhanced biosensor readout of bacteria [11] and bacterial spores [12] and trapping of *E. coli* bacteria [13].

When a standing ultrasound wave is imposed in a microchannel containing an aqueous suspension of particles, two forces of acoustic origin act on the particles: the Stokes drag force from the induced acoustic streaming and the acoustic radiation force from sound wave scattering on the particles. To date, the experimental work on acoustophoresis has primarily dealt with cases where the acoustic radiation force dominates the motion, typically for particles of diameters larger than 2 μm. Quantitative experiments of 5-μm-diam polymer particles in water [14–16] have shown good agreement with the classical theoretical predictions [17,18] of the acoustic radiation force acting on a microparticle of radius

_____

*Corresponding author: barnkob@alumni.dtu.dk

a much smaller than the acoustic wavelength λ, where the viscosity of the suspending fluid is neglected. However, as the particle diameter decreases below 2 μm, a few times the acoustic boundary-layer thickness, the particle motion is typically strongly influenced by the Stokes drag force from the induced acoustic streaming flow, which has been reported by several groups [19–21], and the radiation force is modified due to the acoustic boundary layer [22].

As pointed out in a recent review [19], the acoustic streaming is difficult to fully characterize due to its many driving mechanisms and forms. In acoustofluidic systems, the streaming is primarily boundary driven, arising at rigid walls from the large viscous stresses inside the submicrometer-thin acoustic boundary layer of width δ. The boundary-driven acoustic streaming was treated theoretically by Rayleigh [23] for an isothermal fluid in an infinite parallel-plate channel with a standing wave parallel to the plates of wavelength λ much larger than the plate distance h, where h is large compared to δ, i.e., $\lambda \gg h \gg \delta$. However, in many applications of acoustofluidic systems the channels provide enhanced confinement, the acoustic wavelength is comparable to the channel height, and the liquid cannot be treated as being isothermal. Rayleigh's prediction is often cited, but the literature is lacking a quantitative validation of its accuracy when applied to acoustofludic systems. This lack of quantitative tests is most likely due to the fact that boundary-driven acoustic streaming is very sensitive to geometry and boundary conditions, making it difficult to achieve sufficient experimental control. However, quantitative comparisons between theory and experiment of acoustic streaming are crucial for the advancement of the acoustofluidics research field. Understanding and controlling the ratio of radiation- and streaming-induced acoustophoretic velocities may be the key for future realization of ultrasound manipulation of submicrometer particles.
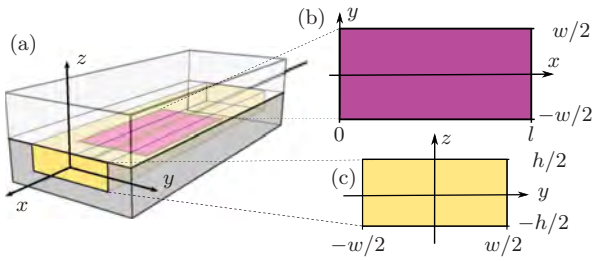
FIG. 1. (Color online) (a) Sketch of the silicon and glass microchip used in our experiments (see also Ref. [14]). It contains a straight rectangular water-filled microchannel of length $L = 35$ mm, width $w = 377$ μm, and height $h = 157$ μm. (b) The horizontal ultrasound symmetry plane of length $l = 892$ μm and width w in the xy plane at the center of the channel. (c) The vertical channel cross section. The micro-PIV volume around the ultrasound symmetry plane is given as $|z| < 7$ and 47 μm for the 0.6- and 10-μm particles, respectively (see Sec. III C).

Recently, we presented a temperature-controlled microparticle image velocimetry (micro-PIV) setup for accurate measurements of the acoustophoretic microparticle motion in a plane [14]. Here we use the same system and the ability to establish a well-controlled transverse resonance for quantitative studies of how much the radiation- and streaming-induced velocities, respectively, contribute to the total acoustophoretic velocity. More specifically, as illustrated in Fig. 1, we study the microparticle motion in the ultrasound symmetry plane [Fig. 1(b)] of a straight rectangular microchannel of width $w = 377$ μm and height $h = 157$ μm. We determine the velocities for particles of diameter $2a$ ranging from 0.6 to 10 μm, and based on this we examine the validity of Rayleigh's theoretical streaming prediction. We also derive theoretically and validate experimentally an expression for the microparticle velocity as a function of particle size, ultrasound frequency, and mechanical properties of the suspending medium.

II. THEORY OF SINGLE-PARTICLE ACOUSTOPHORESIS

In this work we study a silicon-glass chip containing a rectangular microchannel sketched in Fig. 1 and described further in Sec. III. The microchannel contains a particle suspension and the chip is ultrasonically actuated by attaching a piezo transducer to the chip and driving it with the

voltage U_{pp} at the angular frequency $\omega = 2\pi f$, where f is a frequency in the low-MHz range. By proper tuning of the applied frequency, the actuation induces a resonant time-harmonic ultrasonic pressure field $p_1(\mathbf{r}) \exp(-i\omega t)$ and velocity field $\mathbf{v}_1(\mathbf{r}) \exp(-i\omega t)$, here expressed in the complex time-harmonic notation. In this work we study only the case of a one-dimensional (1D) transverse pressure resonance of amplitude p_a and wave number $k = 2\pi/\lambda = n\pi/w$, with integer n,

$$p_1(\mathbf{r}) = p_a \cos\left[n\pi\left(\frac{y}{w} + \frac{1}{2}\right)\right], \quad n = 1,2,3,\ldots. \quad (1)$$

The case of $\lambda/2 = w$ or $k = \pi/w$ is shown in Fig. 2(a).

The particle suspensions are dilute enough that the particle-particle interactions are negligible and thus only single-particle effects are relevant. These comprise the acoustic radiation force due to particle-wave scattering and the viscous Stokes drag force from the acoustic streaming flow. Both effects are time-averaged second-order effects arising from products of the first-order fields. The drag force from the acoustic streaming flow dominates the motion of small particles, while the motion of larger particles is dominated by the acoustic radiation force. This is clearly illustrated in recent numerical simulations by Muller *et al.* [24], which are reproduced in Fig. 2: The streaming flow advects small particles in a vortex pattern [Fig. 2(b)] and radiation force pushes larger particles to the pressure nodal plane at $y = 0$ [Fig. 2(c)].

A. Acoustic radiation force

We consider a spherical particle of radius a, density ρ_p, and compressibility κ_p suspended in a liquid of density ρ_0, compressibility κ_0, viscosity η, and momentum diffusivity $\nu = \eta/\rho_0$. Recently, Settnes and Bruus [22] gave an analytical expression for the viscosity-dependent time-averaged radiation force $\mathbf{F}^{rad}$ in the experimentally relevant limit of the wavelength λ being much larger than both the particle radius a and the thickness $\delta = \sqrt{2\nu/\omega}$ of the acoustic boundary layer, without any restrictions on the ratio $\tilde{\delta} = \delta/a$. For the case of a 1D transverse pressure resonance [Eq. (1)], the viscosity-dependent acoustic radiation force on a particle located at (y,z) reduces to the z-independent expression

$$F^{rad}(y,z) = n4\pi^2 \Phi(\tilde{\kappa}, \tilde{\rho}, \tilde{\delta}) \frac{a^3 E_{ac}}{w} \sin\left(n2\pi\frac{y}{w} + n\pi\right), \quad (2)$$
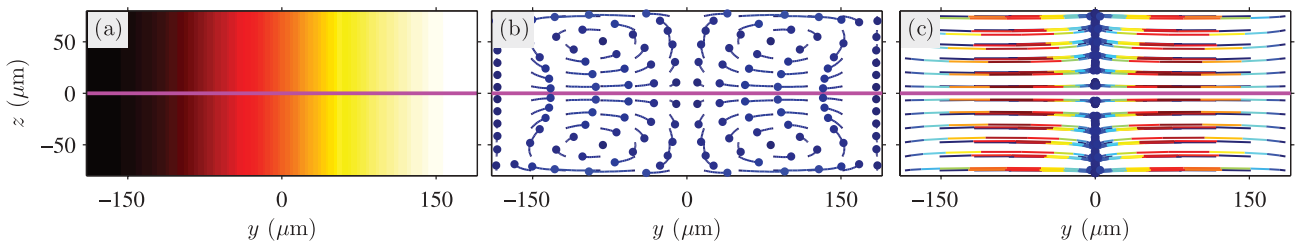

FIG. 2. (Color online) Numerical simulation of microparticle acoustophoresis in the vertical microchannel cross section of Fig. 1(c) adapted from Ref. [24]. The thick horizontal line represents the ultrasound symmetry plane of Fig. 1(b). (a) Color plot of the transverse standing ultrasound pressure wave p_1 of Eq. (1) with $n = 1$ ranging from $-p_a$ (black) to p_a (white). (b) Trajectories (thin lines) of small 0.5-μm-diam particles (dots) dominated by the Stokes drag force from the boundary-induced streaming. (c) Trajectories (thin colored lines) of large 5.0-μm-diam particles (dots) dominated by the acoustic radiation force.

where $E_{ac} = \frac{1}{4}\kappa_0 p_a^2$ is the time-averaged acoustic energy density and the acoustic contrast factor Φ is given in terms of the material parameters as

$$\Phi(\tilde{\kappa}, \tilde{\rho}, \tilde{\delta}) = \frac{1}{3}f_1(\tilde{\kappa}) + \frac{1}{2}\text{Re}[f_2(\tilde{\rho}, \tilde{\delta})], \qquad (3a)$$

$$f_1(\tilde{\kappa}) = 1 - \tilde{\kappa}, \quad \tilde{\kappa} = \frac{\kappa_p}{\kappa_0}, \qquad (3b)$$

$$f_2(\tilde{\rho}, \tilde{\delta}) = \frac{2[1 - \Gamma(\tilde{\delta})](\tilde{\rho} - 1)}{2\tilde{\rho} + 1 - 3\Gamma(\tilde{\delta})}, \quad \tilde{\rho} = \frac{\rho_p}{\rho_0}, \qquad (3c)$$

$$\Gamma(\tilde{\delta}) = -\frac{3}{2}[1 + i(1 + \tilde{\delta})]\tilde{\delta}, \quad \tilde{\delta} = \frac{\delta}{a}. \qquad (3d)$$

We note that for all the microparticle suspensions studied in this work including the viscous 0.75:0.25 water:glycerol mixture, the viscous corrections to Φ are negligible as we find $|\Phi(\tilde{\kappa}, \tilde{\rho}, \tilde{\delta})/\Phi(\tilde{\kappa}, \tilde{\rho}, 0) - 1| < 0.4\%$.

If $\boldsymbol{F}^{rad}$ is the only force acting on a suspended particle, the terminal speed of the particle is ideally given by the Stokes drag as $\boldsymbol{u}^{rad} = \boldsymbol{F}^{rad}/6\pi\eta a$. Using Eq. (2) for the transverse resonance, $\boldsymbol{u}^{rad}$ only has a horizontal component u_y^{rad}, which can be written in the form

$$u_y^{rad} = u_0 \frac{a^2}{a_0^2} \sin\left(n2\pi\frac{y}{w} + n\pi\right), \qquad (4)$$

where the characteristic velocity amplitude u_0 and particle radius a_0 are given by

$$u_0 = \frac{4E_{ac}}{\rho_0 c_0} = \frac{4E_{ac}}{Z_0} = 27 \ \mu\text{m s}^{-1}, \qquad (5a)$$

$$a_0 = \sqrt{\frac{6\nu}{\Phi}\frac{1}{\omega}} = \delta\sqrt{\frac{3}{\Phi}} = 1.6 \ \mu\text{m}. \qquad (5b)$$

Here Z_0 is the characteristic acoustic impedance and the numerical values are calculated for polystyrene particles suspended in water using parameter values listed in Sec. III with $f = 2$ MHz and $E_{ac} = 10$ J m^{-3} as in Refs. [15,16].

B. Boundary-driven acoustic streaming

In 1884 Lord Rayleigh [23] published his now classical analysis of the boundary-driven acoustic streaming velocity field $\boldsymbol{U}$ in an infinite parallel-plate channel induced by a first-order bulk velocity field having only a horizontal y component given by $v_1 = v_a \sin[n\pi(y/w + 1/2)]$. This corresponds to the first-order pressure of Eq. (1) illustrated in Fig. 2(a). For an isothermal fluid in the case of $\lambda \gg h \gg \delta$, Rayleigh found the components $U_y(y,z)$ and $U_z(y,z)$ of $\boldsymbol{U}$ outside the acoustic boundary to be

$$U_y = \frac{3}{16}\frac{v_a^2}{c_0}\sin\left(n2\pi\frac{y}{w} + n\pi\right)\left[1 - 3\frac{(2z)^2}{h^2}\right], \qquad (6a)$$

$$U_z = \frac{3}{16}\frac{v_a^2}{c_0}\frac{n\pi h}{w}\cos\left(n2\pi\frac{y}{w} + n\pi\right)\left[\frac{(2z)^3}{h^3} - \frac{2z}{h}\right], \qquad (6b)$$

$$v_a = \frac{p_a}{\rho_0 c_0} = 2\sqrt{\frac{E_{ac}}{\rho_0}}. \qquad (6c)$$

A plot of $\boldsymbol{U}$ driven by the 1D transverse standing half-wave resonance is shown in Fig. 3. We expect this analytical expression to deviate from our measurements because the
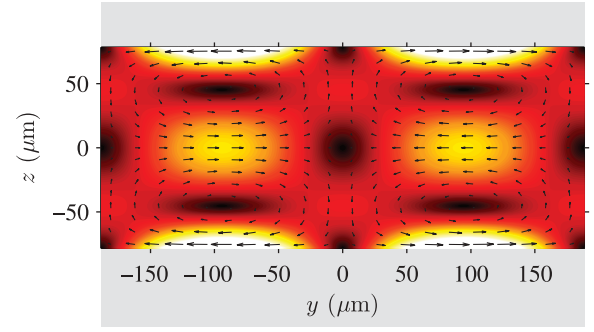

FIG. 3. (Color online) Vector plot (black arrows) of the acoustic streaming $\boldsymbol{U}$ and color plot of its magnitude U from zero (black) to maximum (white) given by Rayleigh's analytical expression [Eqs. (12)] and valid for a shallow isothermal liquid slab ($\lambda \gg h$) between two parallel plates (gray) of distance h driven by a standing ultrasound pressure wave $p_1 = p_a\cos[n\pi(y/w + 1/2)]$ for $n = 1$ and $w = 377 \ \mu\text{m}$.

actual channel does have sidewalls, it is not isothermal, and instead of $\lambda \gg h$ we have $\lambda = 4.8h$ for $\lambda = 2w$ and $\lambda = 2.4h$ for $\lambda = w$.

At the ultrasound symmetry plane $z = 0$, $\boldsymbol{U}$ only has a horizontal component, which we denote u_y^{str}. In analogy with Eq. (4) this can be written as

$$u_y^{str} = u_0 s_p^0 \sin\left(n2\pi\frac{y}{w} + n\pi\right), \quad s_p^0 = \frac{3}{16} \approx 0.188, \qquad (7)$$

where the subscript and superscript in the streaming coefficient s_p^0 refer respectively to the parallel-plate geometry and the isothermal liquid in Rayleigh's analysis.

To estimate the effect on u_y^{str} of the sidewalls and the large height $h \approx \lambda$ in the rectangular channel of Fig. 1(c), we use the numerical scheme developed by Muller et al. [24] for calculating the acoustic streaming based directly on the hydrodynamic equations and resolving the acoustic boundary layers, but without taking thermoviscous effects fully into account. The result shown in Fig. 4 reveals that u_y^{str} is suppressed by a factor of 0.82 in the rectangular geometry relative to the parallel-plate geometry and that it approaches zero faster near the sidewalls at $y = \pm w/2$. The approximate
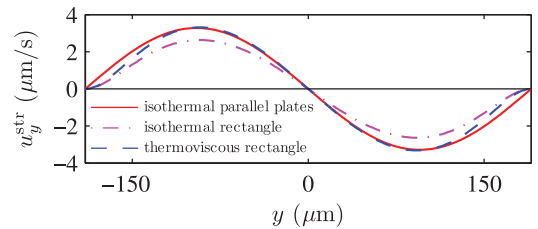

FIG. 4. (Color online) Numerical simulation of the horizontal component u_y^{str} of the streaming velocity in the ultrasound symmetry plane at $z = 0$. In this plane the vertical component is zero $u_z^{str} = 0$. Three cases are shown: the isothermal parallel-plate channel [Eq. (7)], the isothermal rectangular channel [Eq. (8)], and the thermoviscous rectangular channel [Eq. (10)].

result is

$$u_y^{\text{str}} \approx u_0 s_r^0 \sin\left(n2\pi\frac{y}{w} + n\pi\right), \quad s_r^0 \approx 0.154, \quad (8)$$

where the subscript and superscript in the streaming coefficient s_r^0 refer respectively to the rectangular geometry and the isothermal liquid.

We estimate the thermoviscous effect on u_y^{str}, in particular the temperature dependence of viscosity, using the analytical result by Rednikov and Sadhal for the parallel-plate geometry [25]. They found a streaming factor s_p^T enhanced relative to s_p^0,

$$s_p^T = \left(1 + \frac{2}{3}B_T\right)s_p^0 \approx 1.26 s_p^0, \quad (9a)$$

$$B_T = (\gamma - 1)\left[1 - \frac{(\partial_T \eta)_p}{\eta\alpha}\right]\frac{\sqrt{\nu D_{\text{th}}}}{\nu + D_{\text{th}}}, \quad (9b)$$

where α is the thermal expansion coefficient, D_{th} is the thermal diffusivity, γ is the specific heat ratio, and the value is calculated for water at $T = 25\,^\circ\text{C}$.

Combining the reduction factor 0.82 from the rectangular geometry with the enhancement factor 1.26 from thermoviscous effects leads to $s_r^T \approx 1.03 s_p^0$ or

$$u_y^{\text{str}} \approx u_0 s_r^T \sin\left(n2\pi\frac{y}{w} + n\pi\right), \quad s_r^T \approx 0.194, \quad (10)$$

where the subscript and superscript in the streaming coefficient s_r^T refer respectively to the rectangular geometry and a thermoviscous liquid (see Fig. 4).

C. Acoustophoretic particle velocity

A single particle undergoing acoustophoresis is directly acted upon by the acoustic radiation force $\boldsymbol{F}^{\text{rad}}$, while the acoustic streaming of velocity $\boldsymbol{U}$ contributes with a force on the particle through the viscous Stokes drag from the suspending liquid. Given a maximum acoustophoretic velocity $u^{\text{p}} \approx 1$ mm/s for the largest particles of $a = 5\,\mu\text{m}$, the liquid Reynolds number becomes $\rho_0 a^2 u^{\text{p}}/\eta \approx 5 \times 10^{-3}$ and the particle inertia relative to the viscous drag is $[(4/3)\pi a^3 \rho_{\text{p}}(u^{\text{p}}/\tau)]/6\pi\eta a u^{\text{p}} < 6 \times 10^{-3}$ using the observed time scale $\tau > 1$ ms for acceleration of the particles. Consequently, inertial effects can be neglected.

The equation of motion for a spherical particle of velocity $\boldsymbol{u}^{\text{p}}$ then becomes

$$\boldsymbol{u}^{\text{p}} = \frac{\boldsymbol{F}^{\text{rad}}}{6\pi\eta a} + \boldsymbol{U}. \quad (11)$$

As we have seen above, there are no vertical velocity components in the ultrasound symmetry plane at $z = 0$, and combining Eqs. (4) and (10) we obtain the horizontal particle velocity component u_y^{p} of amplitude u_{a},

$$u_y^{\text{p}} = u_y^{\text{rad}} + u_y^{\text{str}} = u_{\text{a}}\sin\left(n2\pi\frac{y}{w} + n\pi\right), \quad (12a)$$

$$u_{\text{a}} = u_0\frac{a^2}{a_0^2} + u_0 s, \quad (12b)$$

where we have dropped the subscripts and superscripts of the streaming coefficient s. The ratio of the radiation- and streaming-induced velocity amplitudes becomes

$$\frac{u_y^{\text{rad}}}{u_y^{\text{str}}} = \frac{1}{s}\frac{a^2}{a_0^2} = \frac{1}{6s}\frac{\Phi}{\nu}\omega a^2, \quad (13)$$

which scales linearly with the angular frequency ω and the square a^2 of the particle radius, but inversely with the streaming coefficient s and the momentum diffusivity ν/Φ rescaled by the acoustic contrast factor.

In Fig. 5 we show contour plots of the ratio $u_y^{\text{rad}}/u_y^{\text{str}}$ for polystyrene particles in water at $25\,^\circ\text{C}$ as function of the particle diameter $2a$ and the ultrasound frequency f [Fig. 5(a)] and
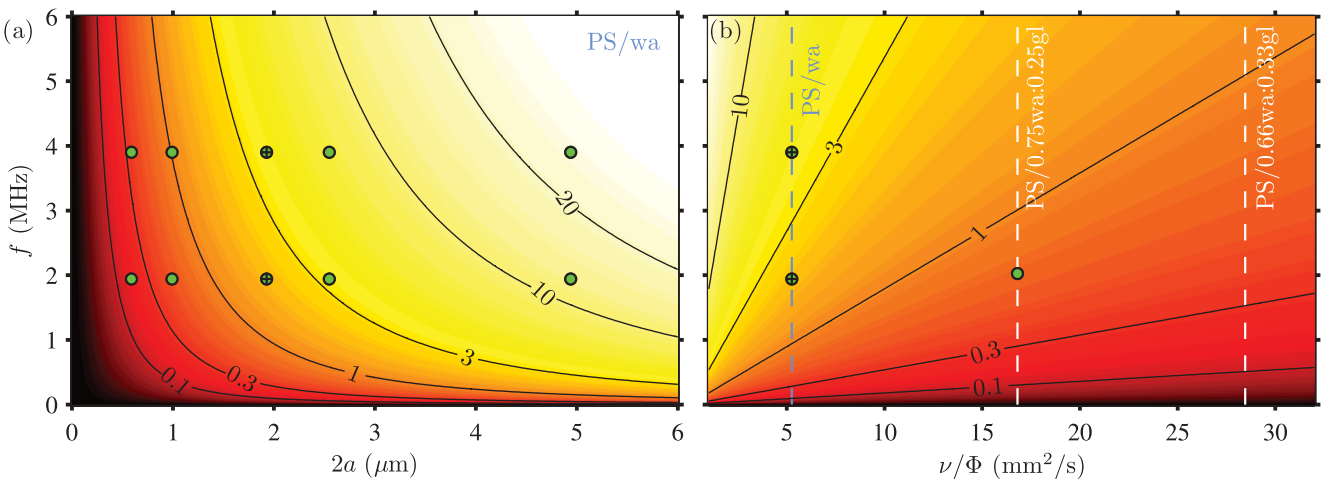

FIG. 5. (Color online) Theoretical prediction of the ratio $u_y^{\text{rad}}/u_y^{\text{str}}$ [Eq. (13)] of radiation- and streaming-induced velocities in the ultrasound symmetry plane of the microchannel [Fig. 1(b) and thick line in Fig. 2] at $25\,^\circ\text{C}$. (a) Contour plot of $u_y^{\text{rad}}/u_y^{\text{str}}$ as a function of particle diameter $2a$ and ultrasound frequency f for a suspension of polystyrene particles (PS) in pure water. (b) Contour plot of $u_y^{\text{rad}}/u_y^{\text{str}}$ as a function of f and the rescaled momentum diffusivity ν/Φ for fixed particle diameter $2a = 2\,\mu\text{m}$. The dots indicate the cases studied experimentally in Secs. III and IV. Suspensions of polystyrene particles in three different liquids are indicated by dashed lines: pure water (dark) as well as 0.75:0.25 and 0.67:0.33 mixtures of water:glycerol (white).

as function of f and the rescaled momentum diffusivity ν/Φ for fixed particle diameter $2a = 2$ μm [Fig. 5(b)]. The solid dots indicate the experiments described in Secs. III and IV.

We define the critical particle diameter $2a_c$ for crossover from radiation-dominated to streaming-dominated acoustophoresis as the particle diameter for which $u_y^{\rm rad}(a_c) = u_y^{\rm str}(a_c)$. This results in

$$2a_c = 2a_0\sqrt{s} = \sqrt{\frac{24\nu}{\omega}\frac{s}{\Phi}} \approx 1.4 \ \mu\text{m}, \qquad (14)$$

where the numerical value is calculated for polystyrene particles in water ($\Phi = 0.17$) at $f = 2$ MHz using $s = s_r^T$. For $a = a_c$ the ratio of the velocity amplitudes $u_y^{\rm rad}/u_y^{\rm str}$ is unity and consequently the unity contour line in Fig. 5(a) represents $2a_c$ as a function of ultrasound frequency f.

D. Wall corrections to single-particle drag

The submillimeter width and height of the rectangular microchannel enhance the hydrodynamic drag on the microparticles. This problem was treated by Faxén for a sphere moving parallel to a planar wall or in between a pair of parallel planar walls [26]. Later, Brenner studied motion perpendicular to a planar wall [27]. (See also the thorough review by Happel and Brenner [28].) The enhancement of the Stokes drag is characterized by a dimensionless correction factor $\chi(a)$ modifying Eqs. (12),

$$u_y^{\rm p} = \left[\frac{1}{\chi(a)}\frac{a^2}{a_0^2} + s\right]u_0 \sin\left(n2\pi\frac{y}{w} + n\pi\right). \qquad (15)$$

No general analytical form exists for χ, so we list the result for three specific cases. For a particle moving parallel to the surface in the symmetry plane $z = 0$ in the gap of height h between two parallel planar walls, χ is

$$\chi_{z=0}^{\rm paral} \approx [1 - 1.004(2a/h) + 0.418(2a/h)^3]^{-1} \approx 1.070, \qquad (16)$$

while for motion in the planes at $z = \pm h/4$ it is

$$\chi_{z=\pm h/4}^{\rm paral} \approx [1 - 1.305(2a/h) + 1.18(2a/h)^3]^{-1} \approx 1.092. \qquad (17)$$

Here the numerical values refer to a particle with diameter $2a = 10$ μm moving in a gap of height $h = 157$ μm. Similarly, for particle motion perpendicular to a single planar wall, the correction factor is

$$\chi^{\rm perp} = \frac{4}{3}\sinh(\alpha)\sum_{j=1}^{\infty}\frac{j(j+1)}{(2j-1)(2j+3)}$$

$$\times\left[\frac{2\sinh[(2j+1)\alpha] + (2j+1)\sinh(2\alpha)}{4\sinh^2\left[(j+\frac{1}{2})\alpha\right] - (2j+1)^2\sinh^2(\alpha)} - 1\right]$$

$$\approx 1.065, \qquad (18)$$

where $\alpha = \cosh^{-1}(\Delta y/a)$ and Δy is the distance from the center of the particle to the wall. The numerical value refers to a 10-μm particle located at $\Delta y = w/4$. The values of the wall correction factor χ for all the particle sizes used in this work are summarized in Table I.

TABLE I. Wall correction factor χ to the single-particle drag for the particle sizes used in the experiment.

$2a$ (μm)	$\chi_{z=0}^{\rm paral}$	$\chi_{z=\pm h/4}^{\rm paral}$	$\chi_{\Delta y=w/4}^{\rm perp}$
0.6	1.004	1.005	1.004
1.0	1.006	1.008	1.006
1.9	1.012	1.016	1.011
2.6	1.017	1.022	1.016
4.9	1.032	1.042	1.030
10.2	1.070	1.092	1.065

III. EXPERIMENTAL PROCEDURE

Experiments were carried out to test the validity of the theoretical predictions for the acoustophoretic particle velocity [Eq. (15)] in the horizontal ultrasound symmetry plane and for the ratio of the corresponding radiation and streaming-induced velocities [see Eq. (13) and Fig. 5]. We use the experimental technique and micro-PIV system as presented in Sec. III (Figs. 2 and 3) in Ref. [14]. The setup is automated and temperature controlled. This enables stable and reproducible generation of acoustic resonances as a function of temperature and frequency. It also enables repeated measurements that lead to good statistics in the micro-PIV analyses. The resulting acoustophoretic particle velocities are thus of high precision and accuracy.

Using the chip sketched in Fig. 1, a total of 22 sets of repeated velocity measurement cycles were carried out on polystyrene particles of different diameters undergoing acoustophoresis in different suspending liquids and at different ultrasound frequencies. In the beginning of each measurement cycle, a particle suspension was infused in the channel while flushing out any previous suspensions. Subsequently, the flow was stopped and a time lapse microscope image sequence was recorded at the onset of the ultrasound. The cycle was then repeated.

A. Microparticle suspensions

Two types of microparticle suspensions were examined: polystyrene particles suspended in Milli-Q water and polystyrene particles suspended in a 0.75:0.25 mixture of Milli-Q water and glycerol. Added to each of the two suspending liquids was 0.01% wt./vol Triton-X surfactant to avoid particle adhesion. The material parameters of the suspensions are listed in Table II. Note that the rescaled momentum diffusivity ν/Φ of the glycerol suspension is 3 times larger than that for the Milli-Q water suspension.

We analyzed 12 particle suspensions by adding particles of 6 different diameters $2a$ from 0.6 to 10 μm to the two liquids. The particle diameters were measured by a Coulter Counter (Multisizer 3, Beckman Coulter Inc., Fullerton, CA, USA) and fitting their distributions to Gaussian distributions (see Ref. [35]). The resulting diameters are listed in Table III.

The concentration C of the particles was calculated based on the concentrations provided by the manufacturer and varies in this work from 10^{10} m^{-3} for the largest particles in the 0.75:0.25 mixture of water and glycerol to 10^{15} m^{-3} for the smallest particles in the pure water solution. The

TABLE II. Material parameters at $T = 25\,°C$. For parameters involving both fluid and solid properties, the solid is always taken to be polystyrene.

Polystyrene		
density[a]	ρ_p	$1050\ \mathrm{kg\,m^{-3}}$
speed of sound[b] (at $20\,°C$)	c_p	$2350\ \mathrm{m\,s^{-1}}$
Poisson's ratio[c]	σ_p	0.35
compressibility[d]	κ_p	$249\ \mathrm{T\,Pa^{-1}}$
Water		
density[a]	ρ_0	$997\ \mathrm{kg\,m^{-3}}$
speed of sound[a]	c_0	$1497\ \mathrm{m\,s^{-1}}$
viscosity[a]	η	$0.890\ \mathrm{mPa\,s}$
viscous boundary layer, 1.940 MHz	δ	$0.38\ \mu\mathrm{m}$
viscous boundary layer, 3.900 MHz	δ	$0.27\ \mu\mathrm{m}$
compressibility[e]	κ_0	$448\ \mathrm{T\,Pa^{-1}}$
compressibility factor	f_1	0.444
density factor	f_2	0.034
contrast factor	Φ	0.17
rescaled momentum diffusivity	ν/Φ	$5.25\ \mathrm{mm^2s^{-1}}$
0.75:0.25 mixture of water and glycerol		
density[f]	ρ_0	$1063\ \mathrm{kg\,m^{-3}}$
speed of sound[g]	c_0	$1611\ \mathrm{m\,s^{-1}}$
viscosity[f]	η	$1.787\ \mathrm{mPa\,s}$
viscous boundary layer, 2.027 MHz	δ	$0.51\ \mu\mathrm{m}$
compressibility[e]	κ_0	$363\ \mathrm{T\,Pa^{-1}}$
compressibility factor	f_1	0.313
density factor	f_2	-0.008
contrast factor	Φ	0.10
rescaled momentum diffusivity	ν/Φ	$16.8\ \mathrm{mm^2\,s^{-1}}$

[a]Reference [29].
[b]Reference [30].
[c]Reference [31].
[d]Calculated as $\kappa_p = \frac{3(1-\sigma_p)}{1+\sigma_p}\frac{1}{\rho_p c_p^2}$ from Ref. [32].
[e]Calculated as $\kappa_0 = 1/\rho_0 c_0^2$.
[f]Reference [33].
[g]Reference [34].

concentrations correspond to mean interparticle distances $C^{-1/3}$ ranging from 4 particle diameters for the largest 10-μm particle in water to 173 particle diameters for the smallest 0.6-μm particle in the 0.75:0.25 mixture of water and glycerol. For this size and concentration range Batchelor's correction factor of $1 - [1.83 \times (4\pi/3)a^3 C]$ for the hydrodynamic effects can be used [36], resulting in negligible quantitative

TABLE III. Nominal and measured diameters of the polystyrene particles used in the experiment.

Nominal diameter	Measured diameter $2a$
591 nm	$(0.59 \pm 0.03)\ \mu\mathrm{m}$[a]
992 nm	$(0.99 \pm 0.05)\ \mu\mathrm{m}$[a]
2.0 μm	$(1.91 \pm 0.07)\ \mu\mathrm{m}$[b]
3.0 μm	$(2.57 \pm 0.07)\ \mu\mathrm{m}$[b]
5 μm	$(5.11 \pm 0.16)\ \mu\mathrm{m}$[b]
10 μm	$(10.16 \pm 0.20)\ \mu\mathrm{m}$[b]

[a]Value from manufacturer and assumed 5% standard deviation.
[b]Measured by the Coulter counter.

changes less than 0.02%. Mikkelsen and Bruus [37] have reported that the hydrodynamic effects result in qualitative changes for interparticle distances below 2 particle diameters. Thus we can apply the single-particle theory presented in Sec. II.

B. Measurement series

We measured the acoustophoretic velocities of polystyrene microparticles in the following four series of experiments, the second being a repeat of the first.

MQ0: Milli-Q water, $f = 1.940$ MHz, $\lambda = 2w$, and $2a = 1.0, 1.9, 2.6$, and $5.1\ \mu$m.

MQ1: Milli-Q water, $f = 1.940$ MHz, $\lambda = 2w$, and $2a = 0.6, 1.0, 1.9, 2.6, 5.1$, and $10.2\ \mu$m.

MQ2: Milli-Q water, $f = 3.900$ MHz $\lambda = w$, and $2a = 0.6, 1.0, 1.9, 2.6, 5.1$, and $10.2\ \mu$m.

Gl1: 0.75:0.25 Milli-Q water:glycerol, $f = 2.027$ MHz $\lambda = 2w$, and $2a = 0.6, 1.0, 1.9, 2.6, 5.1$, and $10.2\ \mu$m.

Given the different particle diameters, we thus have the above-mentioned 22 sets of acoustophoretic particle-velocity measurements, each consisting of 50–250 measurement cycles. All experiments were carried out at a fixed temperature of $25\,°C$ and the applied piezo voltage U_{pp}^*. The camera frame rate was chosen such that the particles would move at least a particle diameter between two consecutive images. The measurement field of view was 1280×640 pixels corresponding to $892 \times 446\ \mu\mathrm{m}^2$. The imaging parameters were an optical wavelength of 520 nm for which the microscope objective is most sensitive, a numerical aperture of 0.4, and a magnification of 20. See more details in Ref. [35].

C. Micro-PIV analysis

The micro-PIV analyses were carried out using the software EDPIV—Evaluation Software for Digital Particle Image Velocimetry, including the image procedure, the averaging in correlation space, and the window shifting described in detail in Ref. [14]. For the MQ1, MQ2, and Gl1 series, the interrogation window size was 32×32 pixels with a 50% overlap resulting in a 79×39 square grid with 16 pixels between each grid point. For the MQ0 series, the interrogation window size was 64×64 pixels with a 50% overlap resulting in a 39×19 square grid with 32 pixels between each grid point.

In micro-PIV all particles in the volume are illuminated and the thickness of the measurement plane is therefore related to the focal depth of the microscope objective. This thickness, called the depth of correlation (DOC), is defined as twice the distance from the measurement plane to the nearest plane for which the particles are sufficiently defocused such that it no longer contributes significantly to the cross-correlation analysis [38]. The first analytical expression for the DOC was derived by Olsen and Adrian [39] and later improved by Rossi *et al.* [40]. Using the latter, we found that the DOC ranges from 14 to $94\ \mu\mathrm{m} \approx h/2$ for the smallest and the largest particles, respectively. Consequently, in the vertical direction all observed particles reside within the middle half of the channel.

IV. RESULTS

The core of our results is the 22 discrete acoustophoretic particle-velocity fields obtained by micro-PIV analysis of the 22 sets of acoustic focusing experiments and shown in Ref. [35]. As in Ref. [14], the measured microparticle velocities u^p are thus represented on a discrete $x_n \times y_m$ micro-PIV grid

$$u^p = u^p(x_n, y_m) = \begin{bmatrix} u_x^p(x_n, y_m) \\ u_y^p(x_n, y_m) \end{bmatrix}. \quad (19)$$

All measured velocities presented in the following are normalized to their values at $U_{pp} = 1$ V using the voltage-squared law [15]

$$u^p = \left(\frac{1\,\mathrm{V}}{U_{pp}^*}\right)^2 u^{p*}, \quad (20)$$

where the asterisk denotes the actual measured values. As a result, the extracted velocity amplitudes and acoustic energy densities are normalized as well,

$$u_a = \left(\frac{1\,\mathrm{V}}{U_{pp}^*}\right)^2 u_a^*, \quad (21a)$$

$$E_{ac} = \left(\frac{1\,\mathrm{V}}{U_{pp}^*}\right)^2 E_{ac}^*. \quad (21b)$$

The actual peak-to-peak values of the applied voltage U_{pp}^* for all four experimental series are given in Ref. [35].

A. Excitation of a 1D transverse standing wave

In Figs. 6 and 7 we verify experimentally that the acoustophoretic particle velocity is of the predicted sinusoidal form given in Eqs. (12) and resulting from a 1D transverse standing wave. For the actual applied voltage of $U_{pp}^* = 7.94$ V the maximum velocity was measured to be $1.77\,\mathrm{mm\,s}^{-1}$, which by Eq. (20) is normalized to the maximum velocity $u_{max}^{p*} = 28\,\mu\mathrm{m\,s}^{-1}$ seen in Fig. 6.

A detailed analysis of the measured velocity field reveals three main points: (i) The average of the ratio of the axial to the transverse velocity component is practically zero $\langle |u_x^p/u_y^p| \rangle <$ 5%, (ii) the maximum particle velocity along any line with
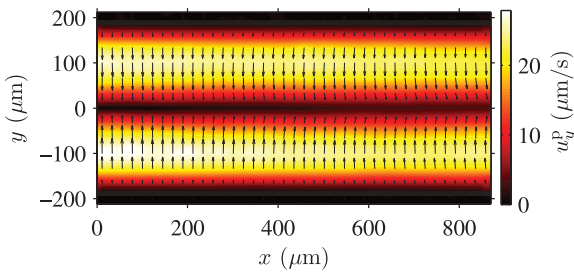

FIG. 6. (Color online) Experimental micro-PIV measurement of acoustophoresis in the horizontal ultrasound symmetry plane of 1-μm-diam polystyrene particles suspended in water and driven at the piezo frequency $f = 1.940$ MHz corresponding to $\lambda/2 = w$, temperature 25 °C, and voltage $U_{pp}^* = 7.94$ V. The arrows represent the measured velocity vectors u^p and the grayscale (colorscale) their magnitude u^p normalized to U_{pp}^* [see Eq. (20)].
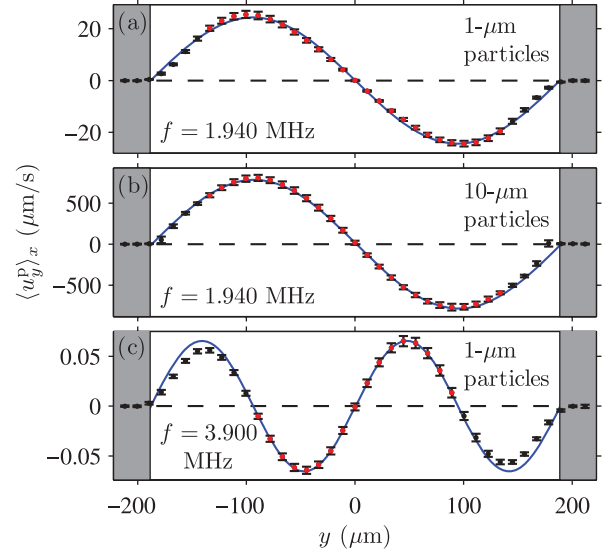

FIG. 7. (Color online) Measured average $\langle u_y^p \rangle_x$ (dark and light points) and its standard deviation $\sigma(\langle u_y^p \rangle_x)$ (error bars) of the transverse velocity u_y^p of polystyrene particles in water. The sinusoidal prediction [Eqs. (12)] for u^p (solid line) is fitted to data points $\langle u_y^p \rangle_x$ away from the sidewalls (light points). (a) Streaming-dominated acoustophoresis for $2a = 1\,\mu$m driven at $f = 1.940$ MHz ($\lambda/2 = w$, same data as in Fig. 6). (b) Radiation-dominated acoustophoresis for $2a = 10\,\mu$m at $f = 1.940$ MHz ($\lambda/2 = w$). (c) Streaming-dominated acoustophoresis for $2a = 1\,\mu$m at $f = 3.900$ MHz ($\lambda = w$).

a given axial grid point coordinate x_m varies less than 6% as a function of x_m, and (iii) the axial average $\langle u_y^p \rangle_x$ of the transverse velocity component u_y^p is well fitted within small error bars ($< 1\%$) by Eqs. (12).

B. Measuring the velocity amplitude

In Fig. 7(a) we plot the axial average $\langle u_y^p \rangle_x$ of the transverse velocity component u_y^p (dark and light points) and its standard deviation $\sigma(\langle u_y^p \rangle_x)$ (error bars) for the velocity field shown in Fig. 6 at the standing-half-wave resonance frequency $f = 1.940$ MHz for the 1-μm-diam streaming-dominated particles (series MQ1). The measured velocities away from the sidewalls (light points) are fitted well by the predicted sinusoidal velocity profile $u_a \sin(n2\pi y/w + n\pi)$ (solid line) [Eqs. (12)] for fixed wavelength $\lambda = 2w$ and using u_a as the only fitting parameter. Velocities close to the sidewalls (black points) are discarded due to their interaction with the sidewalls. As seen numerically in Fig. 4, the no-slip boundary condition on the sidewalls of the rectangular geometry suppresses the streaming velocity near the sidewalls relative to sinusoidal velocity profile of the parallel-plate geometry.

As shown in Fig. 7(b), the theoretical prediction also fits well the measured velocities away from the sidewalls for the large radiation-dominated 10-μm-diam particles (series MQ1, $\lambda/2 = w$). Likewise, as seen in Fig. 7(c), a good fit is also obtained for the 1-μm-diam particles away from the sidewalls at the standing-full-wave frequency $f = 3.900$ MHz (series MQ2, $\lambda = w$). Given this strong support for the presence of standing transverse waves, we use this standing-wave

fitting procedure to determine the velocity amplitude u_a in the following analysis of the acoustophoretic particle velocity.

In spite of the normalization to the same driving voltage of 1 V, the velocity amplitude of the half-wave resonance in Fig. 7(a) is 400 times larger than that of the full-wave resonance in Fig. 7(c). This is due to the different coupling of the piezo transducer to the specific spatial wave structure of each resonance mode and the different dissipation or Q values of these modes.

C. Velocity as a function of particle diameter

To analyze in detail the transverse velocity amplitude u_a in all four series MQ0, MQ1, MQ2, and Gl1, we return to the wall-enhanced drag coefficient χ of Sec. II D. In general, χ depends in a nonlinear way on the motion and position of the particle relative to the rigid walls. However, in Sec. III C we established that the majority of the observed particles reside in the middle half of the channel, and in our standing-wave fitting procedure for u_a in Sec. IV B we discarded particles close to the sidewalls. Consequently, given this and the values of χ in Table I, it is a good approximation to assume that all involved particles have the same wall correction factor, namely, the symmetry-plane parallel-motion factor

$$\chi \approx \chi_{z=0}^{\text{paral}}. \tag{22}$$

As the drag correction only enters on the radiation-induced term in Eq. (15), we introduce a wall-drag-corrected particle size $a_{\text{wd}} = (\chi_{z=0}^{\text{paral}})^{-1/2} a$.

To determine the acoustic energy density E_{ac} and the streaming coefficient s we plot in Fig. 8, for each of the four experiment series, u_a/u_0 versus the particle diameter $2a$ (colored symbols) and wall-drag-corrected particle diameter $2a_{\text{wd}}$ (gray symbols). The characteristic velocity amplitude u_0 is determined in each series by fitting the wall-drag-corrected data points to Eqs. (12) using E_{ac} and s as fitting parameters. In all four experiment series, a clear a^2 dependence is seen. Notice further that the velocities follow almost the same distribution around the fitted line in all series. This we suspect may be due to systematic errors, e.g., that the 5-μm-diam particles are slightly underestimated (see the Coulter data in Ref. [35]). The resulting fitting parameters E_{ac} and s are listed in Table IV(a). The energy densities normalized to $U_{\text{pp}} = 1$ V [see Eq. (21b)] vary with more than a factor of 700 due to a large difference in the strength of the excited resonances. According to the predictions in Sec. II, the streaming coefficient s should be constant, but experimentally it varies from 0.18 to 0.26. However, taking the fitting uncertainties into account in a weighted average leads to $\langle s \rangle_w = 0.192 \pm 0.010$, which is close to $s_r^T \approx 0.194$ of Eq. (10).

Another approach for extracting E_{ac} and s is to assume that the smallest particles $2a = 0.6$ μm are influenced only by the streaming-induced drag. If so, the velocity of the largest $2a = 10$ μm particle has a streaming component of less than 6% (see the measured ratios $u_a^{0.6\,\mu\text{m}}/u_a^{10\,\mu\text{m}}$ in Table V). Therefore, we further assume that the 10-μm-diam particles are influenced solely by the radiation force, and from $u_a^{\text{rad}} = u_0 (a/a_0)^2$ we
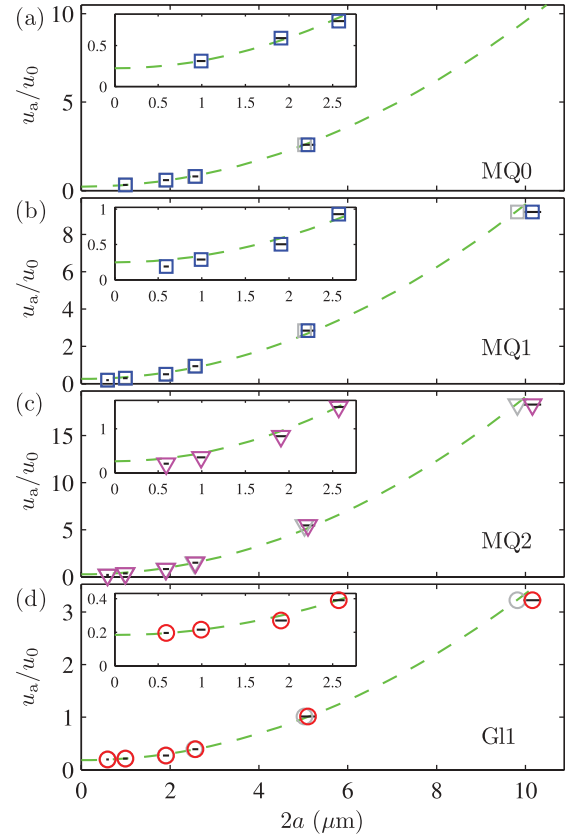

FIG. 8. (Color online) Measured and normalized acoustophoretic velocity amplitudes u_a/u_0 as functions of particle diameter $2a$ (dark colored symbols) and wall-drag-corrected particle diameter $2a_{\text{wd}}$ (light gray symbols) for the four experiment series (a) MQ0, (b) MQ1, (c) MQ2, and (d) Gl1 described in Sec. III B. The characteristic velocity amplitude u_0 is determined from fitting Eqs. to the gray points in each series using E_{ac} and s as fitting parameters resulting in the values listed in Table IV(a) (green dashed lines). The standard deviation of u_a/u_0 is less than the symbol size and the standard deviations on the particle diameters are indicated as black lines.

determine the acoustic energy density as

$$E_{\text{ac}} = \frac{3}{2} \frac{\eta c_0}{\Phi \omega} \frac{u_a^{10\,\mu\text{m}}}{a_{\text{wd}}^2}. \tag{23}$$

Knowing the acoustic energy density, we use Eq. (7) to calculate the streaming coefficient s from $u_a^{\text{str}} = u_0 s$ as

$$s = \frac{\rho_0 c_0}{4 E_{\text{ac}}} u_a^{0.6\,\mu\text{m}}. \tag{24}$$

Assuming that the largest error is due to the dispersion in particle size, we obtain the results listed in Table IV(b). The acoustic energy densities are close to the ones extracted from the fits in Fig. 8 and the geometric streaming coefficient varies from 0.180 to 0.203 with an weighted average of $\langle s \rangle_w = 0.191 \pm 0.005$. Note that using Eqs. (23) and (24), we only need to consider the dispersion of the 10-μm-diam particles, which results in a more reliable estimate of s.

We use the acoustic energy densities in Table IV(b) together with the material parameters in Table II to calculate u_0 and a_0 [Eqs. (5)] for each of the experiment series MQ1, MQ2, and

TABLE IV. Measured acoustic energy densities E_{ac} normalized to $U_{\text{pp}} = 1$ V and streaming coefficient s.

(a) Unweighted fit to all points (see Fig. 8)		
Suspension Frequency (MHz)	E_{ac} (J m^{-3})	s
MQ0 1.940	52.306 ± 0.918	0.222 ± 0.025
MQ1 1.940	31.807 ± 0.569	0.247 ± 0.071
MQ2 3.900	0.070 ± 0.001	0.262 ± 0.125
Gl1 2.027	2.420 ± 0.020	0.184 ± 0.012
(b) Based on particles with $2a = 0.6$ and 10 μm		
Suspension Frequency (MHz)	E_{ac} (J m^{-3})[a]	s[b]
MQ1 1.940	32.436 ± 1.282	0.182 ± 0.008
MQ2 3.900	0.071 ± 0.003	0.205 ± 0.008
Gl1 2.027	2.559 ± 0.110	0.186 ± 0.008

[a]Equation (23).
[b]Equation (24).

Gl1. According to the theoretical prediction in Eqs. (12), all data points must fall on a straight line of unity slope and intersection s if plotted as the normalized velocity amplitude u_{a}/u_0 as function of the normalized particle radius squared $(a/a_0)^2$. The plot is shown in Fig. 9, showing good agreement with the theoretical prediction using $s_{\text{r}}^T \approx 0.194$.

D. Velocity ratios

In Table V we list velocity ratios for different particle sizes in the experiment series MQ1, MQ2, and Gl1. From Eqs. (12) we expect $u_{\text{a}} - u_{\text{a}}^{\text{str}} \propto a^2$, leading to the prediction $(u_{\text{a}}^{5\,\mu\text{m}} - u_{\text{a}}^{\text{str}})/(u_{\text{a}}^{10\,\mu\text{m}} - u_{\text{a}}^{\text{str}}) = (5/10)^2 = 0.25$. If we assume that the smallest 0.6-μm-diam particles are only influenced by the acoustic streaming, we have $u_{\text{a}}^{\text{str}} = u_{\text{a}}^{0.6\,\mu\text{m}}$. We can therefore test the just-mentioned hypothesis by calculating $(u_{\text{a}}^{5\,\mu\text{m}} - u_{\text{a}}^{0.6\,\mu\text{m}})/(u_{\text{a}}^{10\,\mu\text{m}} - u_{\text{a}}^{0.6\,\mu\text{m}})$. The results are listed in the fifth column in Table V, where we obtain values ranging from 0.27 to 0.29, or a deviation of 8–18%.

Assuming that the smallest 0.6-μm-diam particles and the largest 10-μm-diam particles are influenced only by the acoustic streaming and the acoustic radiation force, respectively, we can estimate the ratio of radiation- and streaming-induced velocities as $u_{\text{a}}^{\text{rad}}/u_{\text{a}}^{\text{str}} = u_{\text{a}}^{10\,\mu\text{m}}/u_{\text{a}}^{0.6\,\mu\text{m}}$, which are listed in the fourth column in Table V. First, we notice that the ratio increases by a factor of $88.4/49.6 = 1.8$ as we increase the frequency by a factor of $3.900/1.940 = 2.0$. This agrees well with a linear increase with frequency as predicted by Eq. (13). Second, we notice that the ratio increases by a factor of $48.6/16.4 = 3.0$ as we change the suspending medium from a 0.75:0.25 mixture of water and glycerol to pure water. According to Eq. (13), $u_{\text{a}}^{\text{rad}}/u_{\text{a}}^{\text{str}}$ increases linearly with ν/Φ and from Table II we obtain a predicted ratio increase of $16.8/5.25 =$

TABLE V. Relative particle velocities.

Suspension	Frequency (MHz)	$\dfrac{u_a^{0.6\,\mu m}}{u_a^{10\,\mu m}}$	$\dfrac{u_a^{10\,\mu m}}{u_a^{0.6\,\mu m}}$	$\dfrac{u_a^{5\,\mu m} - u_a^{0.6\,\mu m}}{u_a^{10\,\mu m} - u_a^{0.6\,\mu m}}$
MQ1	1.940	0.020	49.6	0.294
MQ2	3.900	0.011	88.4	0.291
Gl1	2.027	0.061	16.4	0.270

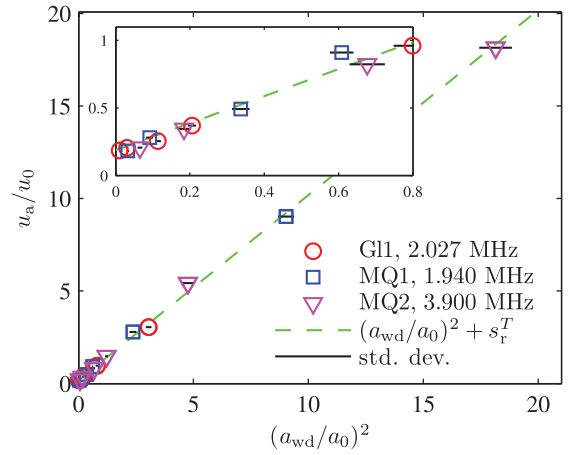FIG. 9. (Color online) Plot of the measured normalized acoustophoretic particle velocity amplitude u_{a}/u_0 versus the square $(a_{\text{wd}}/a_0)^2$ of the normalized wall-drag-corrected particle radius. The dashed line is a fit to Eqs. (12).

3.2, which matches well with the experimentally estimated ratio. With these results we have gained experimental support for the theoretical prediction of the velocity ratio given in Eq. (13).

V. DISCUSSION

Our results verify experimentally the theoretically predicted dependence of the magnitude of the acoustophoretic velocity in a microchannel on the viscosity of the suspending liquid, the acoustic contrast factor Φ, and the ultrasound frequency. For most situations involving cells, isotonic solutions are used such as phosphate-buffered saline, sodium chloride, or blood plasma. Direct manipulation of small particles such as bacteria in plasma or in buffers of high levels of protein is problematic, primarily due to the high viscosity of those media. When possible, these media should be exchanged prior to manipulation to increase the potential for success.

Increasing the frequency in the system would allow for a reduction of the critical diameter of particles. One adverse effect of a higher frequency is that the channel width must be narrowed down, which affects the throughput in the system. This problem can, however, be overcome by designing a channel of high aspect ratio, where the resonance occurs over the smallest dimension [41].

Another benefit of high-aspect-ratio channels was pointed out by Muller *et al.* [24]. Since the acoustic streaming emanates from the walls perpendicular to the wave propagation (here the top and bottom), a high channel leads to a weaker average streaming field in the center.

The measurements of particle velocities for polystyrene particles ranging from 0.6 to 10 μm give no support to previous measurements presented by Yasuda and Kamakura [42]. Their rather spectacular result was that particles below a certain size move faster than larger particles do. From the experiments reported herein it is clear, however, that the motion of particles indeed can be well described with the analyses presented by Rayleigh [23], Yosioka and Kawasima [17], and Gorkov [18].

The uncertainties in the measured particle velocities may in particular be due to the following four causes: (i) variations in particle density ρ_p and compressibility κ_p as a function of particle producer (Fluka and G. Kisker) or batch, (ii) deviations from normal distributed particle sizes as shown in Fig. 1 of Ref. [35], (iii) local fluctuations in the bead concentrations leading to particle-particle interactions, and (iv) viscosity variations induced by the suspended particles.

To better understand the nature of acoustic streaming in microchannels the streaming field should be mapped for the channel cross section and along the whole length of the channel. As reported by Hagsäter *et al.* [43] and Augustsson *et al.* [14], the acoustic field can deviate dramatically from the very uniform one-dimensional field reported herein. Nonsymmetrical acoustic fields can be expected to generate far more complex streaming fields.

VI. CONCLUSION

We have investigated the motion of microparticles due to acoustic radiation and acoustic streaming inside a liquid-filled long, straight rectangular channel of width w and height h driven by an ultrasound standing wave of wavelength λ. Fortuitously, the simple analytical expression derived by Lord Rayleigh for the streaming velocity in an isothermal liquid slab between two infinite parallel plates fulfilling $\lambda \gg h$ is a good approximation for the specific rectangular channel of Fig. 1 containing a thermoviscous liquid and fulfilling $\lambda \approx h$. The reduction in velocity obtained when replacing the parallel plates with the rectangular geometry is almost perfectly compensated for by the enhancement in velocity from replacing the isothermal liquid by the thermoviscous one.

A theoretical prediction was made [Eqs. (12)] for the dependence of the radiation- and streaming-induced velocities on the size of the particles, the ultrasound frequency, the viscosity of the suspending liquid, and the acoustic contrast factor. This prediction was found to be in excellent agreement with experimental findings as shown by the collapse after re-scaling of data from 22 different measurements on the same line in Fig. 9. The results have bearing on acoustophoretic manipulation strategies for submicrometer biological particles such as bacteria and vira, which are too small to be handled using the present manifestation of this technique. We can conclude that increasing the ultrasound frequency, increasing the channel aspect ratio, and lowering the viscosity of the suspending fluid is probably the most viable route to conduct such manipulation.

[1] J. Friend and L. Y. Yeo, Rev. Mod. Phys. **83**, 647 (2011).

[2] H. Bruus, J. Dual, J. Hawkes, M. Hill, T. Laurell, J. Nilsson, S. Radel, S. Sadhal, and M. Wiklund, Lab Chip **11**, 3579 (2011).

[3] J. J. Hawkes, R. W. Barber, D. R. Emerson, and W. T. Coakley, Lab Chip **4**, 446 (2004).

[4] F. Petersson, A. Nilsson, C. Holm, H. Jönsson, and T. Laurell, Analyst **129**, 938 (2004).

[5] P. Thevoz, J. D. Adams, H. Shea, H. Bruus, and H. T. Soh, Anal. Chem. **82**, 3094 (2010).

[6] P. Augustsson, C. Magnusson, M. Nordin, H. Lilja, and T. Laurell, Anal. Chem. **84**, 7954 (2012).

[7] X. Ding, S.-C. S. Lin, B. Kiraly, H. Yue, S. Li, I.-K. Chiang, J. Shi, S. J. Benkovic, and T. J. Huang, Proc. Natl. Acad. Sci. USA **109**, 11105 (2012).

[8] B. Vanherberghen, O. Manneberg, A. Christakou, T. Frisk, M. Ohlin, H. M. Hertz, B. Önfelt, and M. Wiklund, Lab Chip **10**, 2727 (2010).

[9] P. Augustsson and T. Laurell, Lab Chip **12**, 1742 (2012).

[10] M. Bengtsson and T. Laurell, Anal. Bioanal. Chem. **378**, 1716 (2004).

[11] L. A. Kuznetsova, S. P. Martin, and W. T. Coakley, Biosens. Bioelectron. **21**, 940 (2005).

[12] S. P. Martin, R. J. Towsend, L. A. Kuznetsova, K. A. J. Borthwick, M. Hill, M. B. McDonnell, and W. T. Coakley, Biosens Bioelectron **21**, 758 (2005).

[13] B. Hammarström, T. Laurell, and J. Nilsson, Lab Chip **12**, 4296 (2012).

[14] P. Augustsson, R. Barnkob, S. T. Wereley, H. Bruus, and T. Laurell, Lab Chip **11**, 4152 (2011).

[15] R. Barnkob, P. Augustsson, T. Laurell, and H. Bruus, Lab Chip **10**, 563 (2010).

[16] R. Barnkob, I. Iranmanesh, M. Wiklund, and H. Bruus, Lab Chip **12**, 2337 (2012).

[17] K. Yosioka and Y. Kawasima, Acustica **5**, 167 (1955).

[18] L. P. Gorkov, Sov. Phys.—Dokl. **6**, 773 (1962).

[19] M. Wiklund, R. Green, and M. Ohlin, Lab Chip **12**, 2438 (2012).

[20] J. F. Spengler, W. T. Coakley, and K. T. Christensen, AIChE J. **49**, 2773 (2003).

[21] S. M. Hagsäter, T. G. Jensen, H. Bruus, and J. P. Kutter, Lab Chip **7**, 1336 (2007).

[22] M. Settnes and H. Bruus, Phys. Rev. E **85**, 016327 (2012).

[23] L. Rayleigh, Philos. Trans. R. Soc. London **175**, 1 (1884).

[24] P. B. Muller, R. Barnkob, M. J. H. Jensen, and H. Bruus, Lab Chip **12**, 4617 (2012).

[25] A. Y. Rednikov and S. S. Sadhal, J. Fluid Mech. **667**, 426 (2011).

[26] H. Faxén, Ann. Phys. **68**, 89 (1922).

[27] H. Brenner, Chem. Eng. Sci. **16**, 242 (1961).

[28] J. Happel and H. Brenner, *Low Reynolds Number Hydrodynamics with Special Applications to Particulate Media* (Nijhoff Publishers, The Hague, 1983).

[29] *CRC Handbook of Chemistry and Physics*, 92nd ed. (Taylor and Francis, London, 2012), www.hbcpnetbase.com/.

[30] L. Bergmann, *Der Ultraschall und seine Anwendung in Wissenschaft und Technik*, 6th ed. (Hirzel, Stuttgart, 1954).

[31] P. H. Mott, J. R. Dorgan, and C. M. Roland, J. Sound. Vibr. **312**, 572 (2008).

[32] L. D. Landau and E. M. Lifshitz, *Theory of Elasticity. Course of Theoretical Physics*, 3rd ed. (Pergamon, Oxford, 1986), Vol. 7.

[33] N.-S. Cheng, Ind. Eng. Chem. Res. **47**, 3285 (2008).

[34] F. Fergusson, E. Guptill, and A. MacDonald, J. Acoust. Soc. Am. **26**, 67 (1954).

[35] See Supplemental Material at http://link.aps.org/supplemental/10.1103/PhysRevE.86.056307 for more details regarding the Coulter counter data, the acquisition table of logged experimental data, and all measured acoustophoretic velocity fields.

[36] G. K. Batchelor, J. Fluid Mech. **74**, 1 (1976).

[37] C. Mikkelsen and H. Bruus, Lab Chip **5**, 1293 (2005).

[38] C. Meinhart, S. Wereley, and M. Gray, Meas. Sci. Technol. **11**, 809 (2000).

[39] M. G. Olsen and R. J. Adrian, Exp. Fluids Suppl. **29**, S166 (2000).

[40] M. Rossi, R. Segura, C. Cierpka, and C. J. Kähler, Exp. Fluids **52**, 1063 (2012).

[41] J. D. Adams, C. L. Ebbesen, R. Barnkob, A. H. J. Yang, H. T. Soh, and H. Bruus, J. Micromech. Microeng. **22**, 075017 (2012).

[42] K. Yasuda and T. Kamakura, Appl. Phys. Lett. **71**, 1771 (1997).

[43] S. M. Hagsäter, A. Lenshof, P. Skafte-Pedersen, J. P. Kutter, T. Laurell, and H. Bruus, Lab Chip **8**, 1178 (2008).

Acoustic radiation- and streaming-induced microparticle velocities determined by micro-PIV in an ultrasound symmetry plane

Rune Barnkob[(a)]*, Per Augustsson[(b)], Thomas Laurell[(b,c)], and Henrik Bruus[(d)]

[(a)]*Department of Micro- and Nanotechnology, Technical University of Denmark*

DTU Nanotech Building 345 East, DK-2800 Kongens Lyngby, Denmark

[(b)]*Department of Measurement Technology and Industrial Electrical Engineering,*

Division of Nanobiotechnology, Lund University, Box 118, S-221 00 Lund, Sweden

[(c)]*Department of Biomedical Engineering, Dongguk University, Seoul, South Korea*

[(d)]*Department of Physics, Technical University of Denmark*

DTU Physics Building 309, DK-2800 Kongens Lyngby, Denmark

(Dated: 31 August 2012)

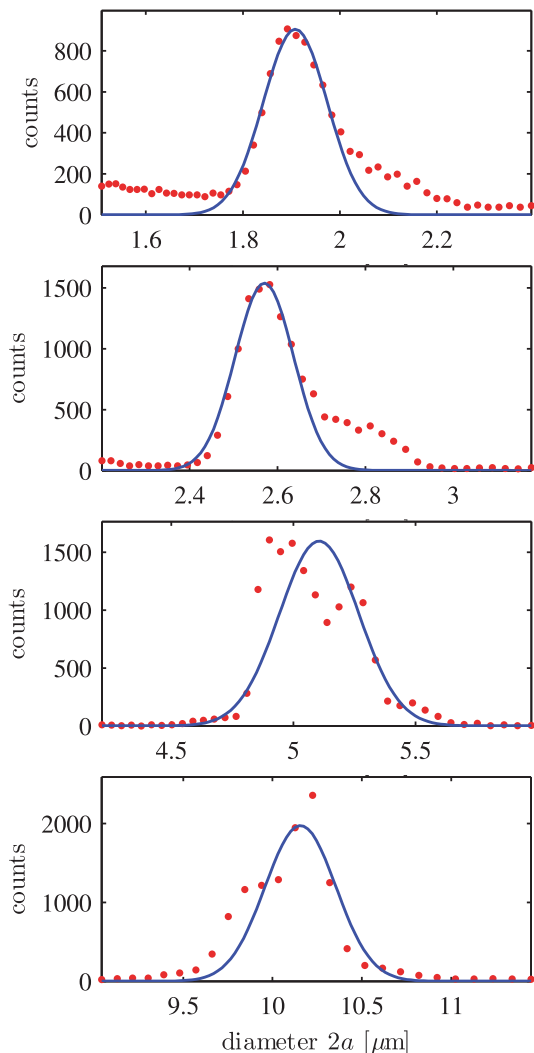## I. MEASUREMENT OF MICROPARTICLE DIAMETERS USING A COULTER COUNTER

In Fig. 1 we show the raw Coulter Counter data obtained for the particles of diameters 2-µm, 3-µm, 5-µm, and 10-µm. For each of the Coulter Counter distributions we fit a Gaussian profile from which we extract the particle diameters shown in Table I. Note, we were not able to measure the size distributions of the smallest 0.6-µm-diameter and 1.0-µm-diameter particles and we therefore use the diameters given by the producers.

TABLE I. Microparticle diameters extracted from fitting a Gaussian profile to the Coulter Counter data shown in Fig. 1.

Diameter	$2a$
591 nm, G. Kiosker Gbr [a],	(591 ± 30) nm
992 nm, G. Kiosker Gbr,[a]	(992 ± 50) nm
2.0 µm, G. Kiosker Gbr,[b]	(1.91 ± 0.07) µm
3.0 µm, G. Kiosker Gbr,[b]	(2.57 ± 0.07) µm
5 µm, Fluka,[b]	(5.11 ± 0.16) µm
10 µm, Fluka,[b]	(10.16 ± 0.20) µm

[a] Value from manufacturer and assumed 5 % standard deviation.
[b] Coulter Counter data, see Fig. 1.

II. ACQUISITION TABLE

In Table II we show all the logged experimental data including actuation frequencies, camera frame rates, number of acoustic focusing repeats, and piezo driving voltage.

III. ACOUSTOPHORETIC VELOCITIES

In Figs. 2, 3, 4, and 5, we show the acoustophoretic particle velocities for the four experimental measurement series MQ0, MQ1, MQ2, and GL1, respectively. Panels (a) shown the x (left) and y (right) components of the particle velocities, while panel (b) shows the x-average of the y velocity component $\langle u_y \rangle_x$.

FIG. 1. Coulter counter distributions for 2-µm, 3-µm, 5-µm, and 10-µm particles.

TABLE II. Acquisition

| Date	Time	2a [um]	Fps	Repeats	$U_{pp}*$ [V]
MQ0 series: MQ/PS, Freq. $f = 1.940$MHz					
24-05-2011	—	1	808	250	6.19
24-05-2011	—	2	808	250	6.25
24-05-2011	—	3	808	250	4.16
24-05-2011	—	5	808	250	2.51
MQ1 series: MQ/PS, Freq. $f = 1.940$MHz					
24-02-2012	16:08:43	5	808	101	3.936
24-02-2012	18:15:02	1	404	100	7.940
25-02-2012	11:10:08	2	404	100	6.334
25-02-2012	12:22:39	3	404	100	4.767
25-02-2012	13:39:10	10	404	100	1.951
25-02-2012	15:49:37	0.6	404	150	7.940
Gl1 series: Gl/PS, Freq. $f = 2.027$MHz					
25-02-2012	19:51:27	5	100	100	10.644
25-02-2012	21:27:04	0.6	100	150	17.251
25-02-2012	23:27:55	1	100	100	17.269
26-02-2012	00:53:12	2	100	150	14.824
26-02-2012	02:47:53	3	100	150	14.801
26-02-2012	04:50:21	10	100	250	6.375
26-02-2012	08:20:03	5	100	100	10.649
MQ2 series: MQ/PS, Freq. $f = 3.900$MHz					
26-02-2012	10:18:33	5	100	100	20.175
26-02-2012	12:04:42	0.6	25	150	31.179
26-02-2012	14:00:15	1	25	100	31.193
26-02-2012	15:08:42	2	25	100	25.718
26-02-2012	16:01:51	2	25	50	25.703
26-02-2012	16:51:17	3	25	60	20.129
26-02-2012	17:29:38	3	25	21	20.129
26-02-2012	18:10:58	3	25	50	20.129
26-02-2012	19:35:32	10	25	100	5.785
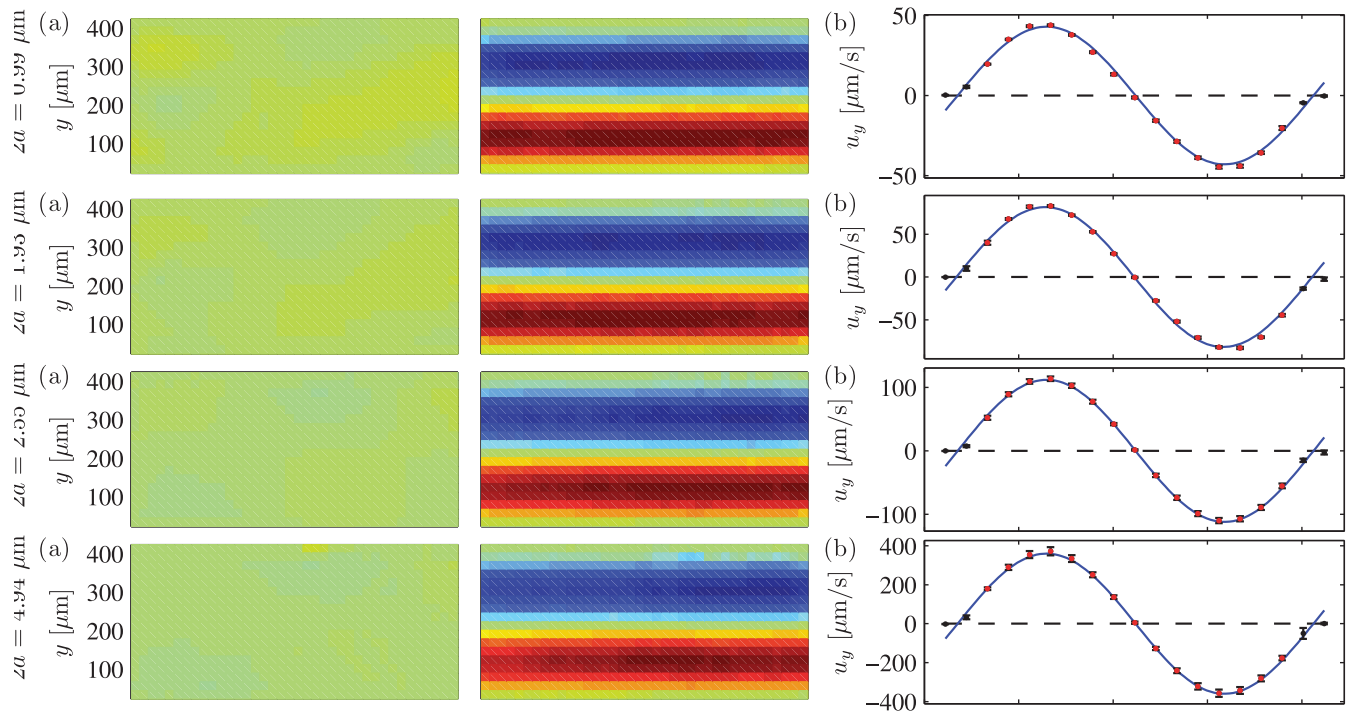
FIG. 2. MQ0-series: Milli-Q water, $f = 1.940$ MHz
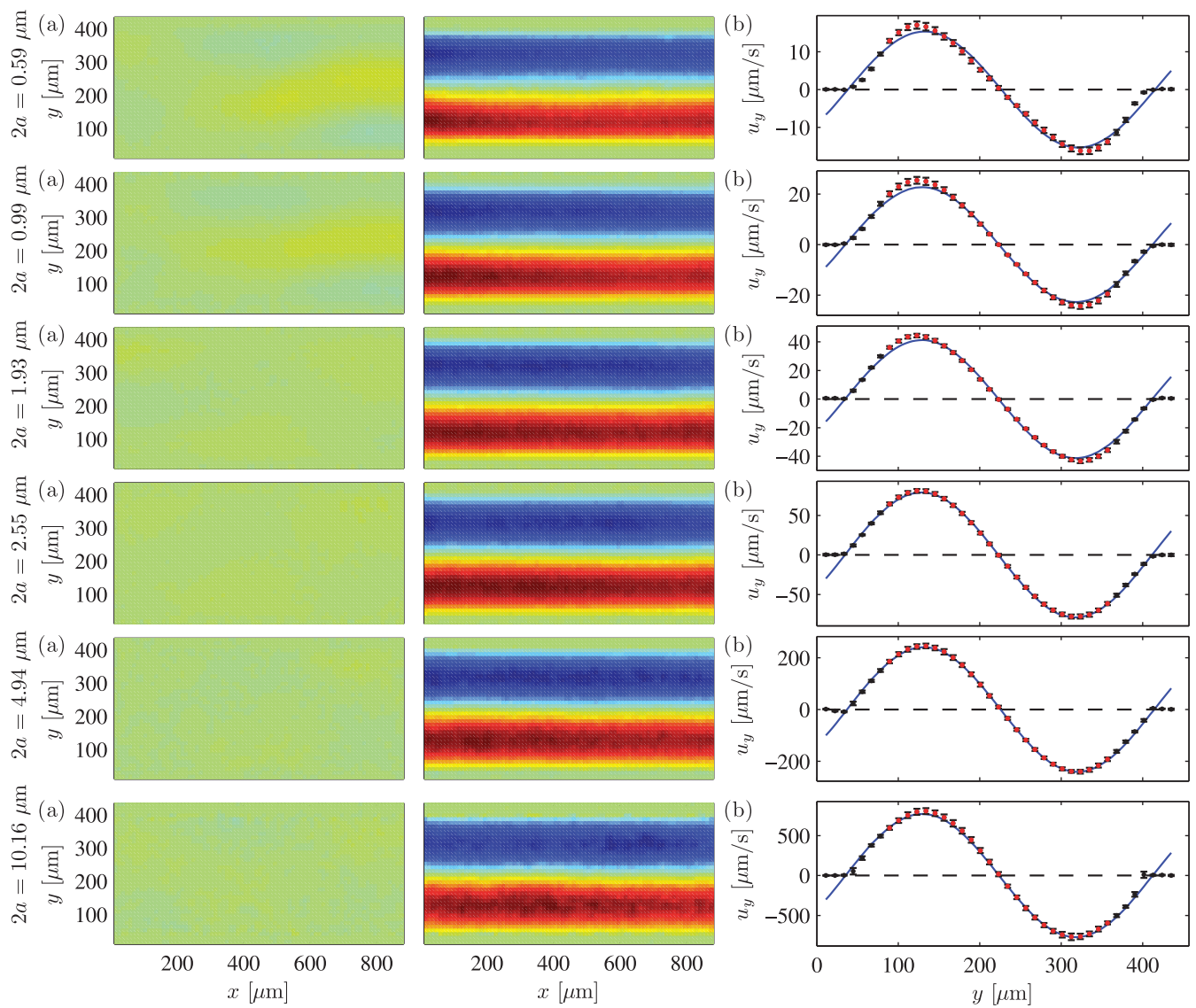
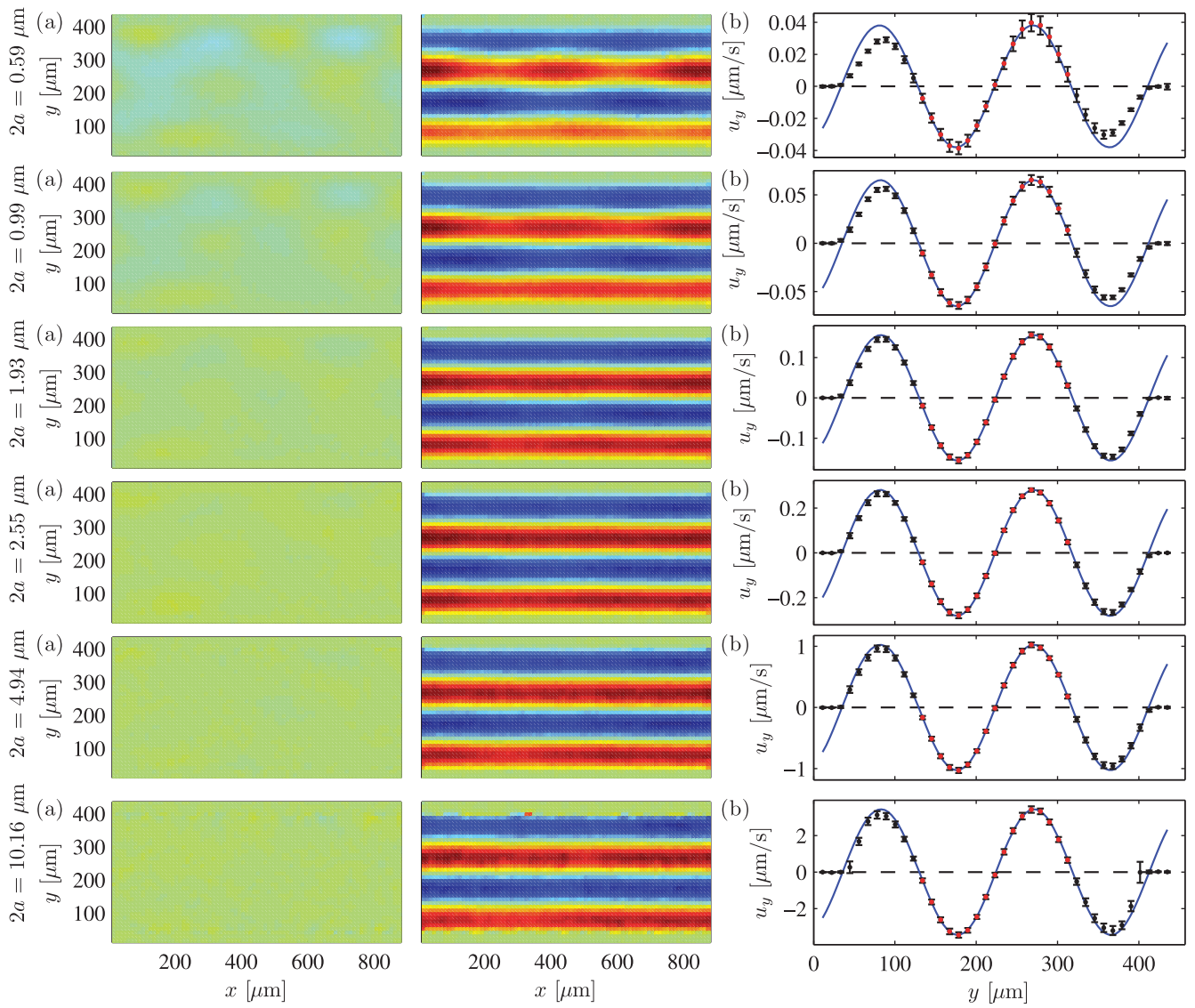FIG. 3.   MQ1-series: Milli-Q water, $f = 1.940$ MHz

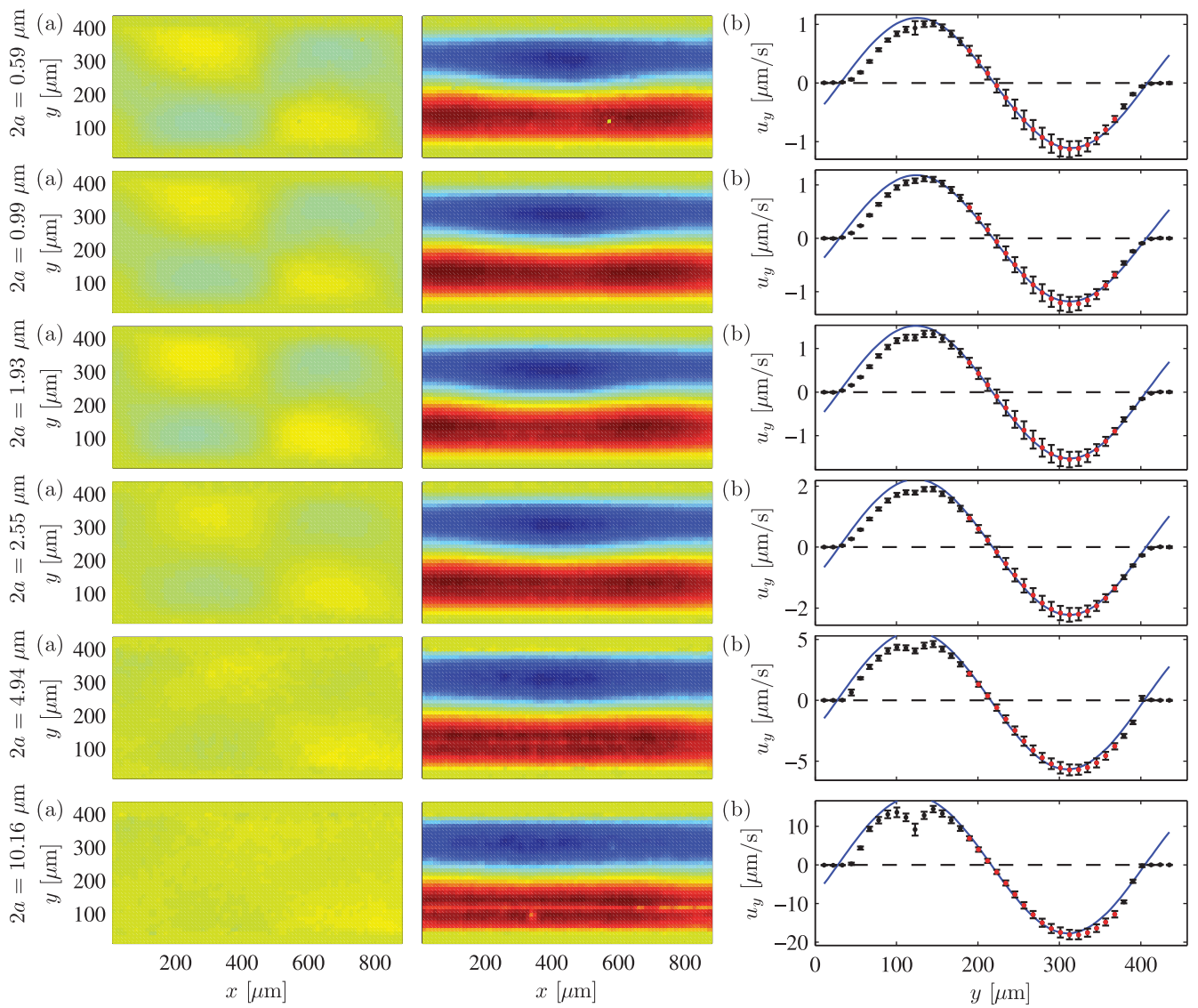FIG. 4. MQ2-series: Milli-Q water, $f = 3.900$ MHz

FIG. 5.   Gl1-series: 0.75:0.25 mixture of water and glycerol, $f = 2.027$ MHz

Bibliography

[1] CRCnetBASE Product, *CRC Handbook of Chemistry and Physics*, 92nd ed., (Taylor and Francis Group, www.hbcpnetbase.com/, 2012).

[2] L. Bergmann, *Der Ultraschall und seine Anwendung in Wissenschaft und Technik*, 6th ed., (S. Hirzel Verlag, Stuttgart, 1954).

[3] P. H. Mott, J. R. Dorgan, and C. M. Roland. *The bulk modulus and poissons ratio of incompressible materials.* J Sound Vibr **312**, 572–575 (2008).

[4] *COMSOL Multiphysics 4.2a, Material Library.*

[5] N.-S. Cheng. *Formula for the viscosity of a glycerol-water mixture.* Ind Eng Chem Res **47**, 3285–3288 (2008).

[6] F. Fergusson, E. Guptill, and A. MacDonald. *Velocity of sound in glycerol.* J Acoust Soc Am **26**, 67–69 (1954).

[7] O. Bates. *Thermal conductivity of liquids.* Ind Eng Chem **28**, 494–498 (1936).

[8] F. Gucker and G. Marsh. *Refrigerating capacity of 2-component systems - glycerol-water and propylene glycol water.* Ind Eng Chem **40**, 908–915 (1948).

[9] L. D. Landau and E. M. Lifshitz, *Theory of Elasticity. Course of Theoretical Physics*, vol. 7, 3rd ed., (Pergamon Press, Oxford, 1986).

[10] H. A. Stone, A. D. Stroock, and A. Ajdari. *Engineering flows in small devices: Microfluidics toward a lab-on-a-chip.* Annu Rev Fluid Mech **36**, 381–411 (2004).

[11] T. Squires and S. Quake. *Microfluidics: Fluid physics at the nanoliter scale.* Rev Mod Phys **77**, 977–1026 (2005).

[12] G. M. Whitesides. *The origins and the future of microfluidics.* Nature **442**, 368–373 (2006).

[13] Z. I. Mandralis, D. L. Feke, and R. J. Adler. *Transient response of fine particle suspensions to mild planar ultrasonic fields.* Fluid/Particle Sep J **3**, 3897–3905 (1990).

[14] Z. I. Mandralis and D. L. Feke. *Continuous suspension fractionation using acoustic and divided-flow fields.* Chem Eng Sci **48**, 3897–3905 (1993).

[15] K. Yasuda, S. Umemura, and K. Takeda. *Concentration and fractionation of small particles in liquid by ultrasound.* Jpn J Appl Phys **34**, 2715–2720 (1995).

[16] D. Johnson and D. Feke. *Methodology for fractionating suspended particles using ultrasonic standing wave and divided flow fields.* Separations Technology **5**, 251–258 (1995).

[17] J. Hawkes and W. Coakley. *A continuous flow ultrasonic cell-filtering method.* Enzyme Microb Tech **19**, 57–62 (1996).

[18] P. Augustsson. *On microchannel acoustophoresis — Experimental considerations and life science applications.* Ph.D. thesis, Lund University [http://lup.lub.lu.se/record/2203054/file/2203068.pdf] (2011).

[19] J. Friend and L. Y. Yeo. *Microscale acoustofluidics: Microfluidics driven via acoustics and ultrasonics.* Rev Mod Phys **83**, 647–704 (2011).

[20] H. Bruus, J. Dual, J. Hawkes, M. Hill, T. Laurell, J. Nilsson, S. Radel, S. Sadhal, and M. Wiklund. *Forthcoming lab on a chip tutorial series on acoustofluidics: Acoustofluidics-exploiting ultrasonic standing wave forces and acoustic streaming in microfluidic systems for cell and particle manipulation.* Lab Chip **11**, 3579–3580 (2011).

[21] J. J. Hawkes, R. W. Barber, D. R. Emerson, and W. T. Coakley. *Continuous cell washing and mixing driven by an ultrasound standing wave within a microfluidic channel.* Lab Chip **4**, 446–452 (2004).

[22] F. Petersson, A. Nilsson, C. Holm, H. Jönsson, and T. Laurell. *Separation of lipids from blood utilizing ultrasonic standing waves in microfluidic channels.* Analyst **129**, 938–43 (2004).

[23] J. Persson, P. Augustsson, T. Laurell, and M. Ohlin. *Acoustic microfluidic chip technology to facilitate automation of phage display selection.* Febs Journal **275**, 5657–5666 (2008).

[24] J. Svennebring, O. Manneberg, P. Skafte-Pedersen, H. Bruus, and M. Wiklund. *Selective bioparticle retention and characterization in a Chip-Integrated confocal ultrasonic cavity.* Biotechnol Bioeng **103**, 323–328 (2009).

[25] C. Grenvall, P. Augustsson, J. R. Folkenberg, and T. Laurell. *Harmonic microchip acoustophoresis: A route to online raw milk sample precondition in protein and lipid content quality control.* Anal Chem **81**, 6195–6200 (2009).

[26] A. Lenshof, A. Ahmad-Tajudin, K. Jaras, A.-M. Sward-Nilsson, L. Aberg, G. Marko-Varga, J. Malm, H. Lilja, and T. Laurell. *Acoustic whole blood plasmapheresis chip for prostate specific antigen microarray diagnostics.* Anal Chem **81**, 6030–6037 (2009).

[27] J. V. Norris, M. Evander, K. M. Horsman-Hall, J. Nilsson, T. Laurell, and J. P. Landers. *Acoustic differential extraction for forensic analysis of sexual assault evidence.* Anal Chem **81**, 6089–6095 (2009).

[28] P. Thevoz, J. D. Adams, H. Shea, H. Bruus, and H. T. Soh. *Acoustophoretic synchronization of mammalian cells in microchannels.* Anal Chem **82**, 3094–3098 (2010).

[29] P. Augustsson, C. Magnusson, M. Nordin, H. Lilja, and T. Laurell. *Microfluidic, label-free enrichment of prostate cancer cells in blood based on acoustophoresis.* Anal Chem **84**, 7954–7962 (2012).

[30] B. Vanherberghen, O. Manneberg, A. Christakou, T. Frisk, M. Ohlin, H. M. Hertz, B. Onfelt, and M. Wiklund. *Ultrasound-controlled cell aggregation in a multi-well chip.* Lab Chip **10**, 2727–2732 (2010).

[31] X. Ding, S.-C. S. Lin, B. Kiraly, H. Yue, S. Li, I.-K. Chiang, J. Shi, S. J. Benkovic, and T. J. Huang. *On-chip manipulation of single microparticles, cells, and organisms using surface acoustic waves.* PNAS **109**, 11105–11109 (2012).

[32] B. Hammarstrom, T. Laurell, and J. Nilsson. *Seed particle enabled acoustic trapping of bacteria and nanoparticles in continuous flow systems.* Lab Chip **12**, in press (2012).

[33] R. M. White. *Introductory lecture - acoustic interactions from faraday's crispations to mems.* Faraday Discuss **107**, 1–13 (1997).

[34] M. Rossi, R. Barnkob, P. Augustsson, Álvaro G. Marín, P. B. Muller, H. Bruus, T. Laurell, and C. J. Kähler. *Experimental and analytical characterization of the 3d motion of particles in acoustofluidic devices. Proceedings of the 3rd European Conference on Microfluidics - Microfluidics 2012 - Heidelberg, December 3-5* (, 2012).

[35] A. Lenshof, M. Evander, T. Laurell, and J. Nilsson. *Acoustofluidics 5: Building microfluidic acoustic resonators.* Lab Chip **12**, 684–695 (2012).

[36] P. Augustsson, R. Barnkob, S. T. Wereley, H. Bruus, and T. Laurell. *Automated and temperature-controlled micro-piv measurements enabling long-term-stable microchannel acoustophoresis characterization.* Lab Chip **11**, 4152–4164 (2011).

[37] R. Barnkob, P. Augustsson, T. Laurell, and H. Bruus. *Acoustic radiation- and streaming-induced microparticle velocities determined by microparticle image velocimetry in an ultrasound symmetry plane.* Phys Rev E **86**, 056307 (2012).

[38] S.-C. S. Lin, X. Mao, and T. J. Huang. *Surface acoustic wave (saw) acoustophoresis: now and beyond.* Lab Chip **12**, 2766–2770 (2012).

[39] M. Gedge and M. Hill. *Acoustofluidics 17: Surface acoustic wave devices for particle manipulation.* Lab Chip **12**, 2998–3007 (2012).

[40] A. D. Pierce, *Acoustics*, (Acoustical Society of America, Woodbury, 1991).

[41] J. Dual and D. Möller. *Acoustofluidics 4: Piezoelectricity and application to the excitation of acoustic fields for ultrasonic particle manipulation.* Lab Chip **12**, 506–514 (2012).

[42] J. Dual, P. Hahn, I. Leibacher, D. Möller, and T. Schwarz. *Acoustofluidics 6: Experimental characterization of ultrasonic particle manipulation devices.* Lab Chip **12**, 852–862 (2012).

[43] H. Bruus. *Acoustofluidics 2: Perturbation theory and ultrasound resonance modes.* Lab Chip **12**, 20–28 (2012).

[44] J. Dual and T. Schwarz. *Acoustofluidics 3: Continuum mechanics for ultrasonic particle manipulation.* Lab Chip **12**, 244–252 (2012).

[45] L. D. Landau and E. M. Lifshitz, *Fluid Mechanics*, vol. 6, Course of Theoretical Physics, 2nd ed., (Pergamon Press, Oxford, 1993).

[46] P. Marmottant and S. Hilgenfeldt. *Controlled vesicle deformation and lysis by single oscillating bubbles.* Nature **423**, 153–156 (2003).

[47] M. Wiklund, R. Green, and M. Ohlin. *Acoustofluidics 14: Applications of acoustic streaming in microfluidic devices.* Lab Chip **12**, 2438–2451 (2012).

[48] S. S. Sadhal. *Acoustofluidics 13: Analysis of acoustic streaming by perturbation methods.* Lab Chip **12**, 2292–2300 (2012).

[49] S. Sadhal. *Acoustofluidics 15: Streaming with sound waves interacting with solid particles.* Lab Chip **12**, 2600–2611 (2012).

[50] S. S. Sadhal. *Acoustofluidics 16: acoustics streaming near liquid-gas interfaces: drops and bubbles.* Lab Chip **12**, 2771–2781 (2012).

[51] H. Schlichting. *Berechnung ebener periodischer grenzeschichtströmungen.* Physik Z **33**, 327–335 (1932).

[52] L. Rayleigh. *On the circulation of air observed in Kundt's tubes, and on some allied acoustical problems.* Philosophical Transactions of the Royal Society of London **175**, 1–21 (1884).

[53] C. Mikkelsen and H. Bruus. *Microfluidic capturing-dynamics of paramagnetic bead suspensions.* Lab Chip **5**, 1293–1297 (2005).

[54] L. M. Andersen, A. Nysteen, and M. Settnes. *Forces acting on microparticles in acoustofluidic systems.* Master's thesis, BSc thesis, DTU Nanotech, Technical University of Denmark (2009).

[55] L. D. Landau and E. M. Lifshitz, *Statistical physics, Part 1*, vol. 5, 3rd ed., (Butterworth-Heinemann, Oxford, 1980).

[56] H. Bruus, *Theoretical Microfluidics*, (Oxford University Press, Oxford, 2008).

[57] P. M. Morse and K. U. Ingard, *Theoretical Acoustics*, (Princeton University Press, Princeton NJ, 1986).

[58] A. Y. Rednikov and S. S. Sadhal. *Acoustic/steady streaming from a motionless boundary and related phenomena: generalized treatment of the inner streaming and examples.* Journal of Fluid Mechanics **667**, 426–462 (2011).

[59] W. L. Nyborg. *Acoustic streaming due to attenuated plane waves.* J Acoust Soc Am **25**, 68–75 (1953).

[60] L. E. Kinsler, A. R. Frey, A. B. Coppens, and J. V. Sanders, *Fundamentals of Acoustics*, 4th ed., (John Wiley & Sons, Inc., 2000).

[61] L. V. King. *On the acoustic radiation pressure on spheres.* P Roy Soc Lond A Mat **147**, 212–240 (1934).

[62] K. Yosioka and Y. Kawasima. *Acoustic radiation pressure on a compressible sphere.* Acustica **5**, 167–173 (1955).

[63] L. P. Gorkov. *On the forces acting on a small particle in an acoustical field in an ideal fluid.* Soviet Physics - Doklady **6**, 773–775 (1962).

[64] M. Settnes and H. Bruus. *Forces acting on a small particle in an acoustical field in a viscous fluid.* Phys Rev E **85**, 016327 (2012).

[65] H. Bruus. *Acoustofluidics 7: The acoustic radiation force on small particles.* Lab Chip **12**, 1014–1021 (2012).

[66] H. Bruus. *Acoustofluidics 10: Scaling laws in acoustophoresis.* Lab Chip **12**, 1578–1586 (2012).

[67] P. B. Muller. *Acoustofluidics in microsystems: investigation of acoustic streaming.* Master's thesis, Technical University of Denmark, www.nanotech.dtu.dk/microfluidics (2012).

[68] J. Happel and H. Brenner, *Low Reynolds number hydrodynamics with special applications to particulate media*, (Martinus Nijhoff Publishers, The Hague, 1983).

[69] R. Barnkob, P. Augustsson, T. Laurell, and H. Bruus. *Measuring the local pressure amplitude in microchannel acoustophoresis.* Lab Chip **10**, 563–570 (2010).

[70] M. Kumar, D. Feke, and J. Belovich. *Fractionation of cell mixtures using acoustic and laminar flow fields.* Biotechnol Bioeng **89**, 129–137 (2005).

[71] M. S. Limaye and W. T. Coakley. *Clarification of small volume microbial suspensions in an ultrasonic standing wave.* J Appl Microbiol **84**, 1035–1042 (1998).

[72] R. Barnkob, I. Iranmanesh, M. Wiklund, and H. Bruus. *Measuring acoustic energy density in microchannel acoustophoresis using a simple and rapid light-intensity method.* Lab Chip **12**, 2337–2344 (2012).

[73] H. Faxén. *The resistance against the movement of a rigour sphere in viscous fluids, which is embedded between two parallel layered barriers.* Ann Phys **68**, 89–119 (1922).

[74] H. Brenner. *The slow motion of a sphere through a viscous fluid towards a plane surface.* Chem Eng Sci **16**, 242–251 (1961).

[75] COMSOL Multiphysics 4.2a, www.comsol.com (2012).

[76] M. B. Andersen. *Electrokinetics of nanochannels and porous membranes with dynamic surface charges.* Ph.D. thesis, Technical University of Denmark, Department of Micro- and Nanotechnology (2012).

[77] L. H. Olesen. *Computational Fluid Dynamics in Microfluidic Systems.* Master's thesis, Technical University of Denmark, Department of Micro- and Nanotechnology (2003).

[78] P. B. Muller, R. Barnkob, M. J. H. Jensen, and H. Bruus. *A numerical study of microparticle acoustophoresis driven by acoustic radiation forces and streaming-induced drag forces.* Lab Chip **12**, 4617–4627 (2012).

[79] M. Wiklund, P. Spégel, S. Nilsson, and H. M. Hertz. *Ultrasonic-trap-enhanced selectivity in capillary electrophoresis.* Ultrasonics **41**, 329–333 (2003).

[80] J. Hultström, O. Manneberg, K. Dopf, H. M. Hertz, H. Brismar, and M. Wiklund. *Proliferation and viability of adherent cells manipulated by standing-wave ultrasound in a microfluidic chip.* Ultrasound Med Biol **33**, 145–151 (2007).

[81] M. Ohlin, A. Christakou, T. Frisk, B. Önfelt, and M. Wiklund. *Controlling acoustic streaming in a multi-well microplate for improving live cell assays.* J. Landers, A. Herr, D. Juncker, N. Pamme, and J. Bienvenue (eds.), *Proc. 15th MicroTAS, 2 - 6 October 2011, Seattle (WA), USA,* 1612–1614, (CBMS, 2011).

[82] K. Sritharan, C. Strobl, M. Schneider, A. Wixforth, and Z. Guttenberg. *Acoustic mixing at low reynold's numbers.* Appl Phys Lett **88**, 054102 (2006).

[83] T. Frommelt, M. Kostur, M. Wenzel-Schaefer, P. Talkner, P. Haenggi, and A. Wixforth. *Microfluidic mixing via acoustically driven chaotic advection.* Phys Rev Lett **100**, 034502 (2008).

[84] S. M. Hagsäter, T. G. Jensen, H. Bruus, and J. P. Kutter. *Acoustic resonances in microfluidic chips: full-image micro-PIV experiments and numerical simulations.* Lab Chip **7**, 1336–1344 (2007).

[85] J. Santiago, S. Wereley, C. Meinhart, D. Beebe, and R. Adrian. *A particle image velocimetry system for microfluidics.* Experiments in Fluids **25**, 316–319 (1998).

[86] R. Adrian. *Twenty years of particle image velocimetry.* Experiments in Fluids **39**, 159–169 (2005).

[87] M. Raffel, C. E. Willert, S. T. Wereley, and J. Kompenhans, *Particle Image Velocimetry,* (Springer, New York, 2007).

[88] R. Lindken, M. Rossi, S. Grosse, and J. Westerweel. *Micro-particle image velocimetry (µpiv): Recent developments, applications, and guidelines.* Lab Chip **9**, 2551–2567 (2009).

[89] S. T. Wereley and C. D. Meinhart. *Recent advances in micro-particle image velocimetry.* Annual Review of Fluid Mechanics **42**, 557–576 (2010).

[90] C. Meinhart, S. Wereley, and J. Santiago. *A piv algorithm for estimating time-averaged velocity fields.* Journal of Fluids Engineering-Transactions of the AMSE **122**, 285–289 (2000).

[91] R. Adrian. *Image shifting technique to resolve directional ambiguity in double-pulsed velocimetry.* Applied Optics **25**, 3855–3858 (1986).

[92] C. Meinhart, S. Wereley, and M. Gray. *Volume illumination for two-dimensional particle image velocimetry.* Measurement Science and Technology **11**, 809–814 (2000).

[93] M. G. Olsen and R. J. Adrian. *Out-of-focus effects on particle image visibility and correlation in microscopic particle image velocimetry.* Exp Fluids **Suppl.**, S166–S174 (2000).

[94] M. Rossi, R. Segura, C. Cierpka, and C. J. Kaehler. *On the effect of particle image intensity and image preprocessing on the depth of correlation in micro-piv.* Experiments in Fluids **52**, 1063–1075 (2012).

[95] J. F. Spengler, W. T. Coakley, and K. T. Christensen. *Microstreaming effects on particle concentration in an ultrasonic standing wave.* AIChE J **49**, 2773–2782 (2003).

[96] C. Cierpka, R. Segura, R. Hain, and C. J. Kaehler. *A simple single camera 3c3d velocity measurement technique without errors due to depth of correlation and spatial averaging for microfluidics.* Meas Sci Technol **21** (2010).

[97] C. Cierpka and C. J. Kähler. *Particle imaging techniques for volumetric three-component (3d3c) velocity measurements in microfluidics.* Journal of visualization **15**, 1–31 (2012).

[98] R. Hain and C. Kähler. *Single camera volumetric velocity measurements using optical aberrations. 12th Int. Symp. Flow Visualization, 10-14 September, Göttingen, Germany (2006).*

[99] S. Chen, N. Angarita-Jaimes, D. Angarita-Jaimes, B. Pelc, A. H. Greenaway, C. E. Towers, D. Lin, and D. P. Towers. *Wavefront sensing for three-component three-dimensional flow velocimetry in microfluidics.* Exp Fluids **47**, 849–863 (2009).

[100] C. J. Kähler, S. Scharnowski, and C. Cierpka. *On the uncertainty of digital piv and ptv near walls.* Exp Fluids **52**, 1641–1656 (2012).

[101] A. Kumar, C. Cierpka, S. J. Williams, C. J. Kaehler, and S. T. Wereley. *3d3c velocimetry measurements of an electrothermal microvortex using wavefront deformation ptv and a single camera.* Microfluid Nanofluidics **10**, 355–365 (2011).

[102] K. Tschulik, C. Cierpka, A. Gebert, L. Schultz, C. J. Kaehler, and M. Uhlemann. *In situ analysis of three-dimensional electrolyte convection evolving during the electrodeposition of copper in magnetic gradient fields.* Anal Chem **83**, 3275–3281 (2011).

[103] C. Cierpka, M. Rossi, R. Segura, and C. J. Kaehler. *On the calibration of astigmatism particle tracking velocimetry for microflows.* Meas Sci Technol **22**, 015401 (2011).

[104] S. P. Martin, R. J. Towsend, L. A. Kuznetsova, K. A. J. Borthwick, M. Hill, M. B. McDonnell, and W. T. Coakley. *Spore and micro-particle capture on an immunosensor surface in an ultrasound standing wave system.* Biosens Bioelectron **21**, 758–767 (2005).

[105] M. Wiklund, C. Günther, R. Lemor, M. Jäger, G. Fuhr, and H. M. Hertz. *Ultrasonic standing wave manipulation technology integrated into a dielectrophoretic chip.* Lab Chip **6**, 1537–1544 (2006).

[106] P. Augustsson, R. Barnkob, C. Grenvall, T. Deierborg, P. Brundin, H. Bruus, and T. Laurell. *Measuring the acoustophoretic contrast factor of living cells in microchannels.* S. Verporte, H. Andersson, J. Emneus, and N. Pamme (eds.), *Proc. 14th MicroTAS, 3 - 7 October 2010, Groningen, The Netherlands*, 1337–39, (CBMS, 2010).

[107] R. Barnkob, P. Augustsson, C. Magnusson, H. Lilja, T. Laurell, and H. Bruus. *Measuring density and compressibility of white blood cells and prostate cancer cells by microchannel acoustophoresis.* J. Landers, A. Herr, D. Juncker, N. Pamme, and J. Bienvenue (eds.), *Proc. 15th MicroTAS, 2 - 6 October 2011, Seattle (WA), USA*, 127–129, (CBMS, 2011).

[108] D. Hartono, Y. Liu, P. L. Tan, X. Y. S. Then, L.-Y. L. Yung, and K.-M. Lim. *On-chip measurements of cell compressibility via acoustic radiation.* Lab Chip **11**, 4072–4080 (2011).

[109] R. Barnkob. *Acoustofluidics in microsystems: investigation of resonances.* Master's thesis, Technical University of Denmark, www.nanotech.dtu.dk/microfluidics (2009).

[110] O. Manneberg, B. Vanherberghen, B. Onfelt, and M. Wiklund. *Flow-free transport of cells in microchannels by frequency-modulated ultrasound.* Lab Chip **9**, 833–837 (2009).

[111] D. Bazou, L. A. Kuznetsova, and W. T. Coakley. *Physical enviroment of 2-D animal cell aggregates formed in a short pathlength ultrasound standing wave trap.* Ultrasound Med Biol **31**, 423–430 (2005).

[112] M. Koklu, A. C. Sabuncu, and A. Beskok. *Acoustophoresis in shallow microchannels.* J Colloid Interface Sci **351**, 407–414 (2010).